University of Southampton

Faculty of Medicine

Clinical and Experimental Sciences

Systemic Infections in Multiple Sclerosis

by

Aravinthan Varatharaj

ORCID ID 0000-0003-1629-5774

Thesis for the degree of Doctor of Philosophy

December 2020

University of Southampton

Abstract

Faculty of Medicine

Clinical and Experimental Sciences

Doctor of Philosophy

Systemic Infections in Multiple Sclerosis

by

Aravinthan Varatharaj

Infections outside the brain can affect the brain. These 'systemic infections' are very common and occur much more frequently than infections inside the brain itself. Despite the existence of a blood-brain barrier (BBB), the systemic immune system does communicate with the brain. In people with a neurological disease, such as multiple sclerosis (MS), the effect of systemic infections on the brain can be magnified, and harmful.

In the SIMS study (Systemic Infections in MS), 53 people with progressive MS were followed up for an average of two and a half years. In that time, over half of the group experienced progression in their level of disability. Systemic inflammatory episodes were common, occurring on average more than 3 times per year, most commonly infections. People with a high systemic inflammatory response, measured by urinary neopterin, experienced significantly faster brain atrophy than those people with a low response, and had nearly 10 times the chance of developing significant brain atrophy. This effect was particularly marked in those people with a high level of disability to start with.

People with MS have a leaky BBB. It may be that the BBB is disrupted during an inflammatory episode, and that this leads to disease progression. If this is the mechanism, then repairing or protecting the BBB may be a therapeutic target in MS. Dynamic contrast-enhanced magnetic resonance imaging (DCE-MRI) can be used to study the BBB in humans and test this hypothesis. In a series of experiments, a protocol for DCE-MRI was devised, refined, and tested. It was found that the marker of BBB permeability derived from DCE-MRI, K_i, behaves as expected, and that measurement variability could be significantly improved with a series of optimisations.

In the SIBIMS study (Systemic Infections and the BBB in MS), BBB permeability was measured using DCE-MRI in 12 individuals during a urinary tract infection (UTI) and again once fully recovered. There was strong evidence for an effect of UTI on the brain, with significant increases in symptoms. There was also modest evidence for BBB disruption during UTI, with a 53% increase in K_i during infection.

This thesis demonstrates two main points. Firstly, that DCE-MRI can be used to study the human BBB in health and disease. Secondly, that systemic infections can have both short- and long-term effects on the brain. BBB disruption may be one possible mechanism linking systemic events with the brain, and warrants further study.

Table of Contents

Table of Contents ..... **i**

Table of Tables ..... **vii**

Table of Figures ..... **xi**

Research Thesis: Declaration of Authorship ..... **xiii**

Acknowledgements ..... **xv**

Definitions and Abbreviations ..... **xvii**

Chapter 1 Background **1**

1.1 Introduction 1

1.2 Multiple sclerosis 2

1.3 Systemic infection and multiple sclerosis 5

1.4 Urinary tract infection 5

1.5 The blood-brain barrier 6

1.6 Systemic inflammation and the blood-brain barrier 7

1.7 Tracer kinetic theory 11

1.8 Dynamic contrast-enhanced magnetic resonance imaging 17

Chapter 2 Hypotheses and Aims **21**

2.1 Primary hypotheses 21

2.2 Aims 21

Chapter 3 Systemic Infections and Disease Progression in Multiple Sclerosis **23**

3.1 Introduction 23

3.2 Hypotheses 23

3.3 Research techniques 23

3.3.1 Clinical monitoring of systemic events 24

3.3.2 Laboratory monitoring of systemic events 24

3.3.3 Radiological measures of disease progression 27

3.3.3.1 Overview of radiological measures 27

3.3.3.2 Longitudinal brain atrophy measurement 28

3.3.3.3 Cross-sectional brain volume measurement 31

3.3.3.4 Cross-sectional brain lesion measurement 32

3.3.3.5 Cross-sectional spinal cord area measurement 33
3.3.3.6 Quality control of radiological data 34
3.3.4 Clinical measures of disease progression 35
3.4 Methods 36
3.4.1 Study design 36
3.4.2 Ethical approval 37
3.4.3 Participants 37
3.4.4 Sample size 38
3.4.5 Statistical analysis 38
3.4.6 Testing of SIENA-ZEFRAM 38
3.5 Results 38
3.5.1 Participants 38
3.5.2 Adverse events 39
3.5.3 Data quality 39
3.5.4 Baseline clinical and radiological data 41
3.5.5 Clinical and radiological progression during follow-up 47
3.5.6 Inflammatory episodes and systemic inflammatory response 50
3.5.7 Brain atrophy and systemic inflammation 54
3.5.8 Secondary clinical outcomes and systemic inflammation 56
3.5.9 Secondary radiological outcomes and systemic inflammation 58
3.6 Discussion 58
3.6.1 Key results 58
3.6.2 Strengths 59
3.6.3 Limitations 59
3.6.4 Interpretation 61
3.6.5 Implications and future directions 62

Chapter 4 Development and Validation of a Dynamic Contrast-Enhanced Magnetic Resonance Imaging Protocol 65

4.1 Introduction 65
4.2 Hypotheses 65
4.3 Methods 66

4.3.1 Initial protocol development....66
4.3.2 Protocol description....69
4.3.3 Analysis description....69
4.3.4 Participants....71
4.3.5 Statistical analysis....71
4.3.6 Ethical approval....71
4.4 Results....72
4.5 Discussion....74
4.5.1 Key results....74
4.5.2 Strengths....75
4.5.3 Limitations....75
4.5.4 Implications and future directions....76
Chapter 5 Optimisation of the Dynamic Contrast-Enhanced Magnetic Resonance Imaging Protocol....77
5.1 Introduction....77
5.2 Checking linearity of the RF transmitter....77
5.3 Establishment of a T_1 mapping phantom....78
5.4 Signal averaging....80
5.5 Flip angle choice....81
5.6 Correction for B1 inhomogeneity....82
5.7 Correction for incomplete spoiling....85
5.8 Motion correction....88
5.9 Measurement of signal drift....89
5.10 Improving input function measurement....90
5.11 Automated tissue segmentation....93
5.12 Final protocol and analysis pipeline....94
Chapter 6 Assessment of Measurement Variability in Dynamic Contrast-Enhanced Magnetic Resonance Imaging....97
6.1 Introduction....97
6.2 Aims....97
6.3 Background....97

6.4 Methods 100
6.4.1 Study design 100
6.4.2 Ethical approval 101
6.4.3 Study participants 101
6.4.4 Measurement of potential sources of biological variation 101
6.4.5 Measurement of asymptomatic systemic inflammation 101
6.4.6 Measurement of haematocrit 101
6.4.7 DCE-MRI protocol and analysis 102
6.4.8 Statistical analysis 103
6.5 Results 104
6.5.1 Participants 104
6.5.2 Effect of optimisation steps on measurement validity 104
6.5.3 Scan-rescan variability 106
6.5.4 Potential sources of biological variation 108
6.5.5 Sample size calculation using measured variability 109
6.5.6 Effect of haematocrit correction 109
6.6 Discussion 110
6.6.1 Key results 110
6.6.2 Limitations 110
6.6.3 Interpretation 111
6.6.4 Implications and future directions 114

Chapter 7 Systemic Infection and the Blood-brain barrier 117

7.1 Introduction 117
7.2 Hypotheses 117
7.3 Considerations in study design 118
7.4 Methods 120
7.4.1 Study design 120
7.4.2 Ethical approval 121
7.4.3 Participants 121
7.4.4 Research techniques 122
7.4.5 Sample size 123

7.4.6 Statistical analysis....124

7.5 Results....124

7.5.1 Participants....124

7.5.2 Baseline clinical and radiological data....125

7.5.3 Data quality....127

7.5.4 Evidence of infection and recovery....127

7.5.5 MS worsening associated with infection....128

7.5.6 BBB disruption associated with infection....129

7.5.7 Association of systemic inflammatory response and BBB disruption....132

7.5.8 Non-infection analyses of BBB permeability....133

7.6 Discussion....134

7.6.1 Key results....134

7.6.2 Limitations....135

7.6.3 Interpretation....137

7.6.4 Generalisability....140

Chapter 8 Discussion....141

8.1 Looking back....141

8.2 Looking forwards....142

Appendix A SIMS Study Infection Diary....145

Appendix B SIMS Study MRI Exam Card....149

Appendix C Clinical measures used in SIMS and SIBIMS....163

C.1 Expanded Disability Status Scale (EDSS)....163

C.2 Multiple Sclerosis Functional Composite (MSFC)....166

C.3 Multiple Sclerosis Impact Scale (MSIS)....166

C.4 Chalder Fatigue Scale (FS)....172

C.5 Beck Depression Inventory (BDI)....173

C.6 Activities of daily living (ADLs)....176

C.7 Patient Global Impression of Improvement (PGI-I)....177

C.8 Multiple Sclerosis Symptoms and Impact Diary (MSSID)....178

C.9 SicknessQ....182

C.10 Non-steroid anti-inflammatory drug (NSAID) score....183

C.11 Lower urinary tract symptom (LUTS) score 184
C.12 Spasticity self-score..... 186
C.13 Ashworth spasticity score 187

Appendix D Testing of ZEFRAM 189
Appendix E Protocol optimisations 191
Appendix F SIBIMS Study MRI Exam Card 193
List of References..... 219
Bibliography..... 243

Table of Tables

Table 1 Overview of methodological concepts for *in vivo* study of BBB disruption in humans. 10

Table 2 Outcome measures in the SIMS study 24

Table 3 Number (percent) of participants with complete data for outcome measures. 40

Table 4 Baseline demographic and clinical data for the SIMS study. 42

Table 5 Baseline radiological data for the SIMS study. 43

Table 6 Correlation matrix between baseline clinical measures of disability in the SIMS study. 44

Table 7 Multivariable regression of predictors of baseline brain volume. 45

Table 8 Correlation matrix between radiological and clinical measures of disability. 46

Table 9 Radiological progression during follow-up. 47

Table 10 Group values for annualised change in clinical progression measures. 48

Table 11 Proportion of participants with clinically important progression in secondary outcome measures. 49

Table 12 Correlation matrix between longitudinal clinical and radiological measures of progression. 50

Table 13 Annualised rate of reported systemic inflammatory events. 51

Table 14 Comparison of UNCR peak heights between systemic inflammatory episode categories. 52

Table 15 Comparison of baseline variables between high and low response groups. .. 53

Table 16 ANCOVA showing the effect of systemic inflammatory response group on brain atrophy rate. 55

Table 17 No associations between systemic inflammation and secondary clinical outcomes. 57

Table of Tables

Table 18 No associations between systemic inflammation and secondary radiological outcomes.....58

Table 19 Inclusion and exclusion criteria 71

Table 20 Results for BBB permeability calculations in normal-appearing white matter.73

Table 21 Calculated T_1 by inversion recovery (IR) for the T1MES phantom at 3T. 80

Table 22 Improvement in T_1 measurement accuracy by signal averaging in the variable-flip angle (VFA) mapping sequence. 81

Table 23 Significant improvement in T_1 measurement accuracy by adding B1 correction. 85

Table 24 Significant improvement in T_1 mapping accuracy by increasing TR. 86

Table 25 Significant improvement in T_1 mapping accuracy with correction for incomplete spoiling. 87

Table 26 Possible sources of analytical imprecision in BBB permeability measurement with DCE-MRI. 98

Table 27 Possible sources of biological variation in BBB permeability. 99

Table 28 Baseline demographics for participants in the variability study. 104

Table 29 Effect of optimisation steps on values of whole-brain K_i and measures of validity. 105

Table 30 Scan-rescan variability results for whole-brain K_i. 106

Table 31 Investigation of potential sources of biological variation in K_i.....109

Table 32 Sample sizes required to demonstrate a change in K_i in a longitudinal study.109

Table 33 Summary of studies reporting measurement variability in brain DCE-MRI. .114

Table 34 Considerations in study design for assessing within-participant change associated with infection. 119

Table 35 Baseline characteristics of the SIBIMS study population. 126

Table 36 Comparison of infection and inflammation markers during infection and non-infection timepoints. 128

Table 37 Changes in MS rating scales associated with infection. 129

Table 38 Changes in K_i associated with infection. 131

Table 39 Correlations between BBB disruption and systemic inflammatory response to infection. 132

Table 40 Comparison of BBB permeability between controls and people with MS, outside of infection. 133

Table 41 BBB permeability in control individuals according to presence of small vessel disease. 133

Table 42 Correlations of non-infection K_i and MS disease severity. 134

Table 43 Correlation of brain atrophy with clinical progression, by analysis method. 189

Table 44 Declarations regarding the optimisations described in Chapter 5. 191

Table of Figures

Figure 1 Spectrum of typical magnetic resonance imaging findings in multiple sclerosis. 4

Figure 2 Schematic of the blood-brain barrier. 7

Figure 3 Differences between and putative mechanisms of disruptive and non-disruptive blood-brain barrier (BBB) changes. 8

Figure 4 Four phases during a tracer kinetic experiment. 12

Figure 5 Schematic of compartments in the Patlak tracer kinetic model. 13

Figure 6 Example Patlak plot. 15

Figure 7 Graph of the function $y = 1 - e^{-x}$ 16

Figure 8 Pulse sequence diagram for 3D spoiled gradient echo. 18

Figure 9 Example of longitudinal UNCR and symptoms analysis for a single individual. 26

Figure 10 Example of longitudinal brain atrophy calculation by SIENA. 29

Figure 11 Black holes may be missed during tissue segmentation. 30

Figure 12 Zero-filling of black holes by ZEFRAM. 31

Figure 13 Example of automated legion segmentation. 33

Figure 14 Example of automated spinal cord segmentation. 34

Figure 15 Gantt chart showing SIMS study activities. 36

Figure 16 Path of all eligible and recruited participants through the SIMS study. 39

Figure 17 Examples of tissue and lesion segmentation. 70

Figure 18 Pairwise plots of K_i and CBV values in white matter (WM) and grey matter (GM), for individual control subjects. 72

Figure 19 Bland-Altman plot comparing K_i values by region-of-interest (ROI) and segmentation methods. 74

Table of Figures

Figure 20 Linear scaling of signal in relation to flip angle, in both the simulated and in measured data. 78

Figure 21 T_1 recovery curves for the nine tubes of the T1MES phantom at 3T. 79

Figure 22 Simulated effect of flip angle on sensitivity of MR signal to gadolinium concentration. 82

Figure 23 Simulated effect on flip angle error on T_1 calculation by the variable flip angle method. 83

Figure 24 Example of visual improvement in signal-time curves after motion correction.89

Figure 25 No evidence of linear signal drift over time....90

Figure 26 Scaling of arterial input function according to the venous outflow function. 92

Figure 27 Demonstration of automatic input function detection. 93

Figure 28 Image processing pipeline. 95

Figure 29 Example of voxelwise parameter maps. 96

Figure 30 Bland-Altman plot of scan-rescan K_i measurements. 107

Figure 31 Scan-rescan results for whole brain K_i, using all optimisations....108

Figure 32 Example B1 map from an individual in the measurement variability study. 112

Figure 33 Overview of final design for the SIBIMS study. 121

Figure 34 Path of recruited participants through the SIBIMS study. 125

Figure 35 Modest evidence for BBB disruption during infection. 130

Research Thesis: Declaration of Authorship

Print name: Aravinthan Varatharaj

Title of thesis: Systemic Infections in Multiple Sclerosis

I declare that this thesis and the work presented in it are my own and has been generated by me as the result of my own original research.

I confirm that:

1. This work was done wholly or mainly while in candidature for a research degree at this University;
2. Where any part of this thesis has previously been submitted for a degree or any other qualification at this University or any other institution, this has been clearly stated;
3. Where I have consulted the published work of others, this is always clearly attributed;
4. Where I have quoted from the work of others, the source is always given. With the exception of such quotations, this thesis is entirely my own work;
5. I have acknowledged all main sources of help;
6. Where the thesis is based on work done by myself jointly with others, I have made clear exactly what was done by others and what I have contributed myself;
7. Parts of this work have been published as:-

Varatharaj A, Galea I. The blood-brain barrier in systemic inflammation. Brain Behavior and Immunity. 2017; 60: 1-12.

Varatharaj A, Liljeroth ML, Darekar A, et al. Blood-brain barrier permeability measured using dynamic contrast enhanced magnetic resonance imaging: a validation study. Journal of Physiology. 2018; 597 (3): 699-709.

Signature: ..... Date: 11/12/2020

Acknowledgements

This thesis is dedicated to my wife Emily, who always supported me, and also to Harry and Penelope, who didn't help at all.

I would never have got here without the expert guidance of Ian Galea.

My co-supervisors – Angela Darekar, Mary Gawne-Cain, and Hugh Perry – and mentor – Karen Morrison – provided valuable guidance. Henrik Larsson and Stig Cramer were great collaborators and friends, as was James Malone-Lee.

Maria Liljeroth helped set up the initial DCE-MRI protocol. Charlotte Stuart shared the PhD journey with me. Elizabeth Jarman and Monica Fenn managed the SIMS study. Geoff Payne taught me much physics. Brigitte Vollmer and Tracey Newman gave useful feedback. Joanne Greenhalgh helped with the use of the MS symptom score. Alexander James Phillips taught me the language of computers.

I am especially grateful to the participants who kindly gave up their own time to take part in this research.

This research was funded by the Medical Research Council and by the University of Southampton's Research Management Committee.

All work in this thesis is my own, except for the following which are used with permission:

- Mass spectrometry for urinary neopterin measurements was performed by Charlotte Stuart and Faye Cornick (Research Technicians, University of Southampton).
- Clinical data in the SIMS study was largely collected by Monica Fenn and Elizabeth Jarman (R&D Department, University Hospital Southampton NHS Foundation Trust).
- Statistical analysis of the SIMS data was conducted jointly with Charlotte Stuart.
- All code was written by me, except where specified in the text.
- Chapter 5 includes a mix of original work and testing of previously reported methods. A detailed declaration is given in E.

Definitions and Abbreviations

9HPT.....9- hole peg test

AIF .....Arterial input function

ANCOVA .....Analysis of covariance

ANOVA .....Analysis of variance

BBB.....Blood-brain barrier

BDI .....Beck's depression inventory

BET .....Brain extraction tool

BMI.....Body mass index

CAMs.....Cell adhesion molecules

CBF .....Cerebral blood flow

CBV.....Cerebral blood volume

CNR .....Contrast-to-noise ratio

CNS.....Central nervous system

COV .....Coefficient of variation

COVID-19.....Coronavirus disease 2019

CRP.....C-reactive protein

CSA.....Cross-sectional area

CSF .....Cerebrospinal fluid

DCE-MRI.....Dynamic contrast-enhanced magnetic resonance imaging

DICOM.....Digital imaging and communications in medicine

EAE.....Experimental autoimmune encephalomyelitis

EDSS .....Expanded disability status scale

EMM .....Estimated marginal mean

ESR .....Erythrocyte sedimentation rate

FLAIR .....Fluid-attenuated inversion recovery

FLASH .....Fast low-angle shot

FS..... Fatigue scale

GBCA ..... Gadolinium-based contrast agent

GL ..... Glia limitans

GM ..... Grey matter

GRAPPA ..... Generalised autocalibrating partial parallel acquisition

GRE..... Gradient echo

ICA..... Internal carotid artery

ICC ..... Intraclass correlation coefficient

IR ..... Inversion recovery

K_i..... Influx constant (of tracer from whole blood)

K_{trans} ..... Transfer constant (of tracer from plasma)

LPS..... Lipopolysaccharide

LUTS ..... Lower urinary tract symptoms

LST..... Lesion segmentation tool

MMP..... Matrix metalloproteinase

MP-RAGE..... Magnetisation prepared – rapid gradient echo

MR..... Magnetic resonance

MRI..... Magnetic resonance imaging

MS ..... Multiple sclerosis

MSFC ..... Multiple sclerosis functional composite

MSIS ..... Multiple sclerosis impact scale

MSIS-Phys..... Physical sub-score of MSIS

MSIS-Psych ..... Psychological sub-score of MSIS

MSSIS..... Multiple sclerosis symptoms and impact diary

MSU..... Mid-stream urine

NAWM..... Normal appearing white matter

NEX..... Number of excitations

NIFTI ..... Neuroimaging informatics technology initiative

PASAT.....Paced auditory serial addition test

PBVC.....Percentage brain volume change

PGI-I .....Patient global impression of improvement

PPMS.....Primary progressive multiple sclerosis

PROM .....Patient-reported outcome measure

PS .....Permeability-surface area

pwMS .....People (or person) with multiple sclerosis (a preferred term)

R_1.....Longitudinal relaxation rate (inverse of T_1)

RF .....Radiofrequency

ROI .....Region of interest

ROS .....Reactive oxygen species

RRMS.....Relapsing-remitting multiple sclerosis

S_0.....Signal in the fully relaxed state

SD.....Standard deviation

SNR.....Signal-to-noise ratio

SPMS .....Secondary progressive multiple sclerosis

SS-Pre .....Slice-selective preparation pulse

SSS.....Superior sagittal sinus

SVD.....(Cerebral) small vessel disease

T_1.....Longitudinal relaxation time

T_2.....Transverse relaxation time

T_2*.....Effective transverse relaxation time

$T_2$5FW.....Timed 25-foot walk

TE .....Echo time

TNF.....Tumour necrosis factor

TR .....Repetition time

UNCR.....Urinary neopterin-to-creatinine ratio

UTI.....Urinary tract infection

VFA ..... Variable flip angle

VOF ..... Venous outflow function

WM ..... White matter

ZEFRAM ..... Zero Filled Robust Atrophy Measurement

Chapter 1 Background

1.1 Introduction

The motto of the Association of British Neurologists is 'the brain above all'. In this thesis I have set out to puncture this notion. The brain is not removed from the mundane concerns of the rest of the body. There is a bidirectional communication between the brain and the rest of the body, mediated by mechanisms that are not fully understood. This is apparent when there is an infection in the body ('systemic infection'). Systemic infections are common, for example colds, flu, and urinary tract infections (UTIs). We are currently living in a pandemic of a systemic infection; COVID-19. During systemic infection changes occur in the brain, and we feel sick. However, there is evidence that it is not infection itself which sends these signals, but rather the body's response to infection – inflammation. Systemic inflammation may communicate with the brain.

In people with neurological disease, the effects of systemic infection on the brain can be magnified. Multiple sclerosis (MS) is a common and ultimately incurable neurological disease, in which this pattern is often seen. Many attempts to halt or slow disability progression in MS by targeting brain inflammation have been unsuccessful. Could it be that common systemic infections drive disability progression in people with MS (pwMS)? This is an idea that comes straight from the bedside, and from the experiences of many pwMS. In this thesis I will present the results of a prospective observational study designed to address this question. If proven, then the prevention and treatment of systemic infection may become an important avenue to halt disability progression.

What is the mechanism that allows communication between the brain and rest of the body, and which transmits the signals of systemic infection? For a time, the blood-brain barrier (BBB) was thought to enforce a strict separation between the brain and rest of the body, and to keep the brain 'above all'. We now know that the BBB is a dynamic and responsive structure, rather than an absolute barrier. Could BBB changes be the link between the brain and the rest of the body? We already know that the BBB is affected in many brain diseases. Perhaps the diseased BBB responds differently to the healthy BBB? In this thesis I will use and refine quantitative MRI techniques to explore these issues in humans. Understanding this could provide novel targets for treating MS and other degenerative brain diseases.

In this chapter, I first review the pathology and clinical features of MS, and the possible link with systemic inflammation. I discuss UTI in more detail as this is a particular problem for people with

MS and will be the basis for a prospective study. Moving on to possible mechanisms, I outline the structure and function of the BBB, and review available evidence regarding the effects of systemic inflammation on the BBB. It becomes apparent that a robust technique is needed to study BBB disruption in humans; in this context I discuss tracer kinetic analysis and how it may be conducted using dynamic contrast-enhanced MRI (DCE-MRI).

1.2 Multiple sclerosis

MS is a common and incurable chronic inflammatory condition affecting the central nervous system (CNS), with an estimated UK prevalence of 127,000 (1). Common symptoms affect mobility, balance, and dexterity, as well as cognition and fatigue. The known causes of MS are combination of genetic susceptibility including female sex and HLA-DRB1*1501, and environmental exposure including Epstein-Barr virus infection, low ultraviolet type B exposure, low vitamin D levels, and smoking (2). The most common form is relapsing-remitting MS (RRMS), the hallmark of which is relapse; ‘a patient reported, or objectively observed, event typical of an acute inflammatory demyelinating event in the central nervous system, current or historical, with a duration of at least 24 hours’ (3). Usually, 10-15 years after the onset of RRMS the disease enters a secondary progressive phase (SPMS) characterised by the absence of relapses and inexorable disability progression (4). In a minority of cases relapses are never a feature and the picture is one of gradual progression from the start; this is primary progressive MS (PPMS). As has been described eloquently, progression is 'at the heart of the medical, social and economic impact of multiple sclerosis’ (5).

The pathology of MS is characterised by perivenular sclerotic plaques containing a T-cell predominant inflammatory infiltrate (6). Inflammation leads to oligodendrocyte loss and demyelination, conduction block, and eventually axonal damage and neuronal death. The symptoms of a lesion depend on its size and location relative to eloquent tissue. In progressive disease inflammatory lesions are less common (but not absent) and instead lesions tend to be surrounded by activated microglia and macrophages (7). It is increasingly recognised that B-cells and plasma cells also play a role, especially in progressive disease where ectopic lymphoid follicles form in the meninges and drive intrathecal antibody synthesis (8). There is much debate regarding the relative contributions and relationship between inflammatory and degenerative pathology, as relapses are only related to disability in the early phase of RRMS (5, 9). Though MS is often thought of as a neuroinflammatory condition, the most recent evidence suggests that disease onset is driven by an aberrant systemic inflammatory response (10).

MRI is a standard tool in the diagnosis and management of MS (11, 12). Focal lesions are seen as areas of high signal on T_2-weighted images and occur in characteristic locations, as shown in Figure 1. However, the number of lesions correlates poorly with clinical disability (13), suggesting that T_2 lesions do not provide a full picture of the pathological process (the 'clinico-radiological paradox'). Focal gadolinium enhancement is used to indicate BBB disruption during active inflammation and occurs in almost all new lesions, preceding appearance as a T_2 lesion (14). Areas of low signal on T_1-weighted images ('black holes') suggest severe tissue damage (15). Brain atrophy due to neuronal loss occurs at an accelerated rate compared to controls, and correlates better with disability (16).

BBB disruption is a key step in the development of experimental autoimmune encephalomyelitis (EAE; an animal model of MS) (17), and the clinical severity can be linked to the degree of BBB disruption (18). EAE involves loss of tight junction proteins (19) which contribute to BBB integrity. In humans, BBB disruption has also been demonstrated in MS (20). Up-regulation of miR-155 in active MS lesions (21), with corresponding down-regulation of BBB tight junction components (22), may be involved. Imaging studies show BBB disruption in normal-appearing white matter in MS (23), and BBB breakdown precedes the development of new lesions (14, 24).

The relative infrequency of enhancement in progressive forms of MS when using conventional contrast MRI (25, 26) has led to the impression that BBB disruption is less relevant in progressive MS than in RRMS. However, independent evidence from a number of groups using electrophoresis of cerebrospinal fluid (CSF) proteins (27), the CSF-serum albumin ratio (28, 29), and immunohistochemistry for dysferlin (30) suggests the converse; that BBB leakage is overall greater in progressive MS. This apparent discrepancy may reflect the measurement threshold of conventional contrast MRI; focal areas of high-level leakage in RRMS are visualised, whereas diffuse low-level leakage in progressive MS may be invisible. Biochemical techniques such as these reflect the permeability of the whole brain in aggregate. Histological study in progressive MS does suggest diffuse pathology in the radiologically normal-appearing brain tissue, with loss of tight junction proteins (31, 32), and this has been demonstrated using dynamic susceptibility contrast MRI (33). There is also evidence from RRMS that individuals with greater BBB leakage accrue disability faster (34, 35).

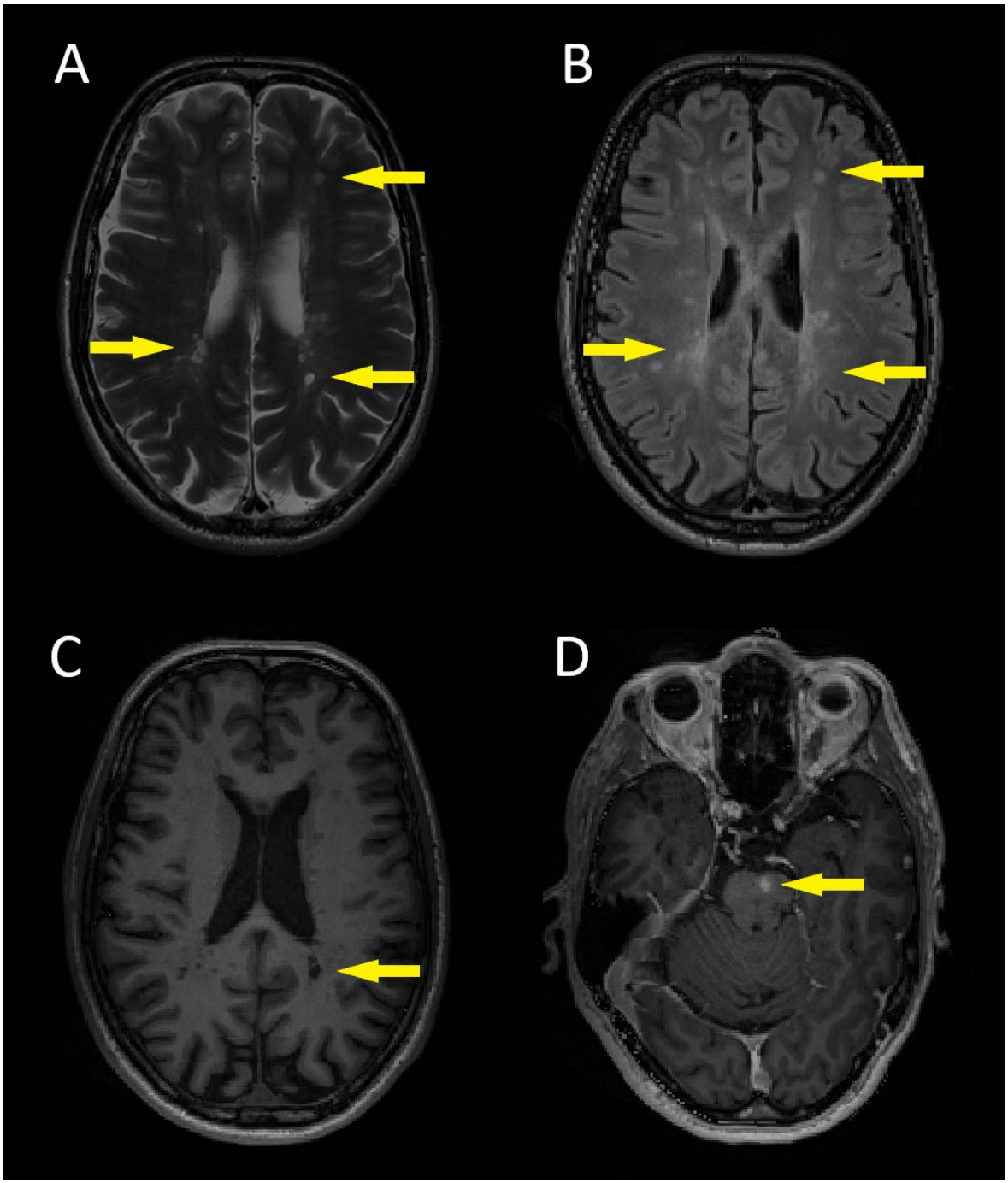

Figure 1 Spectrum of typical magnetic resonance imaging findings in multiple sclerosis.

A. T_2-weighted image showing periventricular white matter lesions and surrounding normal-appearing white matter (NAWM).

B. Fluid-attenuated inversion recovery (FLAIR) image allowing better appreciation of white matter lesions.

C. T_1-weighted image showing T_1-hypointense lesions (so-called 'black holes').

D. T_1-weighted post-contrast image showing an enhancing lesion in the pons.

Images are from an individual examined as part of this thesis.

1.3 Systemic infection and multiple sclerosis

It is a common observation of pwMS and their clinicians that episodes of systemic inflammation may be associated with symptom exacerbation. Infections are a frequent cause of episodic systemic inflammation; trauma, surgery, and vaccinations are other examples. Also, pwMS have a higher incidence of systemic infections than controls (36). Studies in RRMS have shown that systemic infections are associated with subsequent relapses by examining the frequency of relapses relative to 'at-risk periods' defined around reported infections; relative risk of relapse during the at-risk period has been variably reported as 1.3 (37), 2.1 (38), 4.1 (39) (using a 4 week period), 2.5 (40) (6 week period), 2.3 (41) and 2.8 (42) (both 7 week period). Other studies have also examined serological markers of infection and shown similar findings, with greater relative risk (37, 38). Two studies also reported that exacerbations associated with infection were more likely to lead to sustained impairment than those unrelated to infection (39, 41). However, it remains to be shown whether systemic infections impact long-term disability accumulation in progressive MS.

A study in EAE suggests that this association may be causal, as in this model systemic inflammation leads to symptom relapse, cerebral perivascular macrophage/microglia and T-cell infiltration, and axonal injury (43). Degree of axonal injury correlated with markers of microglial activation, suggesting that the switch to a pro-inflammatory phenotype may play a role. Whether BBB changes play a role in this interaction remains unclear, and disruptive change was not seen in this study. Likewise, no evidence of BBB disruption associated with infection was seen in two studies using conventional contrast-enhanced MRI in people with RRMS (38, 41). However, another study in RRMS did suggest BBB leakage (39), as did a different EAE model (44). Study design, techniques for detecting subtle BBB disruption, and timing relative to infection are likely to be key factors.

1.4 Urinary tract infection

UTI is one of the most common bacterial infections (45). Typical symptoms are urinary urgency, frequency, nocturia, and pain. UTIs can be classed as uncomplicated, in a healthy individual, or complicated, in an individual with compromise of the urinary tract or host defence. Many neurological diseases, including MS, cause incomplete bladder emptying and retention, predisposing to complicated UTIs (46). The lifetime risk of UTI for pwMS is estimated to be 13-80% (47) and increases with disability (48). In RRMS, UTIs are associated with relapses (41). Though often thought of as non-severe, UTIs are one of the most common reasons for hospital

admission in MS (49), and are a significant risk factor for death in MS (48). Therefore, although UTI severity encompasses a broad spectrum, the burden for people with MS is significant.

UTI has long been defined as 'bacteriuria associated with clinical, histologic, or immunologic evidence of host injury', in contrast to colonisation which is simply 'replication of bacteria in urine without evidence of tissue invasion' (50). Urine culture alone only identifies the presence of bacteria, and is also insensitive as some pathogens are difficult to grow (51). Colonisation must be discriminated from infection by evidence of host injury, or response to injury. This can be provided by symptoms and objective laboratory evidence. Symptoms have been proven to be a good predictor of infection (52). In terms of objective laboratory evidence, urine dipstick is widely used though mounting evidence suggests that this performs poorly (53). Instead, the current best test is urine microscopy to directly visualise the inflammatory response, in the form of pyuria (leukocytes in the urine) (54). This has the benefits of being cheap, easy, and fast. Since pyuria is a direct marker of inflammation in the urinary tract, it is most relevant to the present investigation. Samples are examined fresh and unspun, as storage and centrifugation cause unpredictable cell loss, and staining is of no additional benefit (53). A threshold pyuria value of 10^7 cells/L is widely used and is based on a number of observations (50, 55) and endorsed by national guidelines (56).

1.5 The blood-brain barrier

The BBB exists at the level of capillaries of the cerebral microcirculation (57). The most apparent BBB function is a physical barrier to ions, molecules, and cells. This arises from a number of structural specializations of the gliovascular complex including tight junctions between adjacent endothelial cells which block paracellular flux (58). A schematic of key BBB elements is shown in Figure 2. However, as well as the physical barrier the BBB has several other functions:

- Transport, including facilitated diffusion, active transport, and vesicular transport (57).
- Metabolism, by ecto- and endo-enzymes (59).
- Secretion, which may be polarised (60).
- Responsiveness to CNS or systemic stimuli, including inflammatory mediators (61).

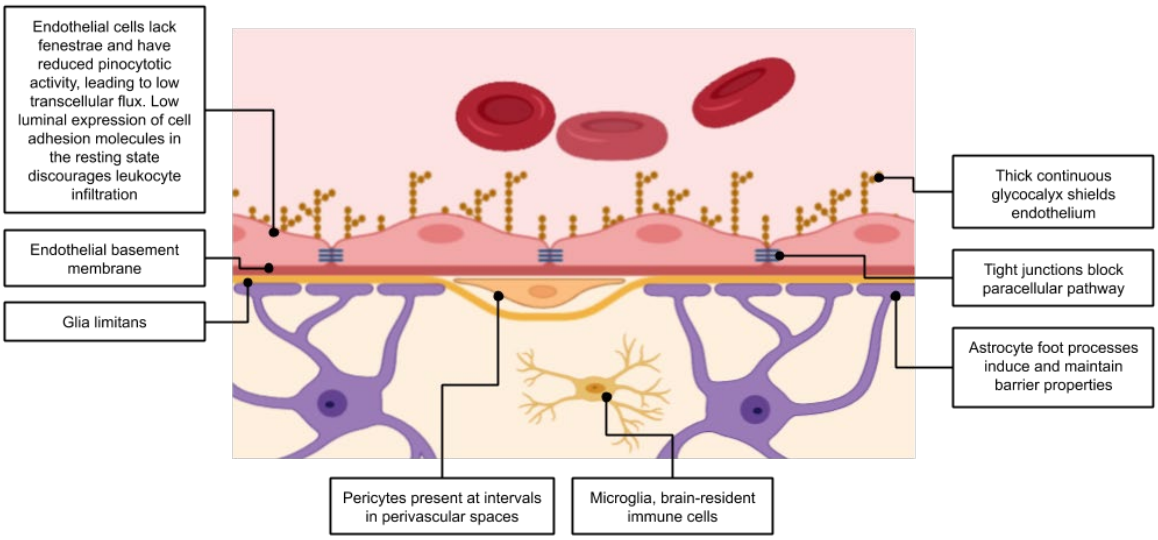

Figure 2 Schematic of the blood-brain barrier.

Elements are not shown to scale. Created using biorender.com.

BBB responsiveness can be disruptive or non-disruptive, reflecting the presence or absence of structural disruption of the BBB (62). Disruptive change occurs at the histological level, while non-disruptive change occurs at the molecular level. Studying the BBB using inert substances will detect disruptive BBB change, but is unlikely to detect non-disruptive BBB change. It is disruptive change which can be most easily conceptualised in terms of a change in permeability, due to loss of a physical barrier. Figure 3 illustrates the anatomical context and possible mechanisms of disruptive and non-disruptive BBB change. Both may have important consequences on the brain's microenvironment and function.

1.6 Systemic inflammation and the blood-brain barrier

Much of the data on the effect of systemic inflammation on the BBB comes from models involving challenge with lipopolysaccharide (LPS), an immunogenic component of Gram-negative bacteria. *In vitro* studies have shown that LPS challenge results in disruptive BBB change to ions (63) as well as solutes such as albumin (64). However, *in vivo* the effect of LPS on BBB function is highly variable. In a systematic review of animal studies examining disruptive BBB change after LPS challenge *in vivo* (62), species differences accounted for a significant amount of variance in results. This is unsurprising as inter-species BBB differences are well documented (65).

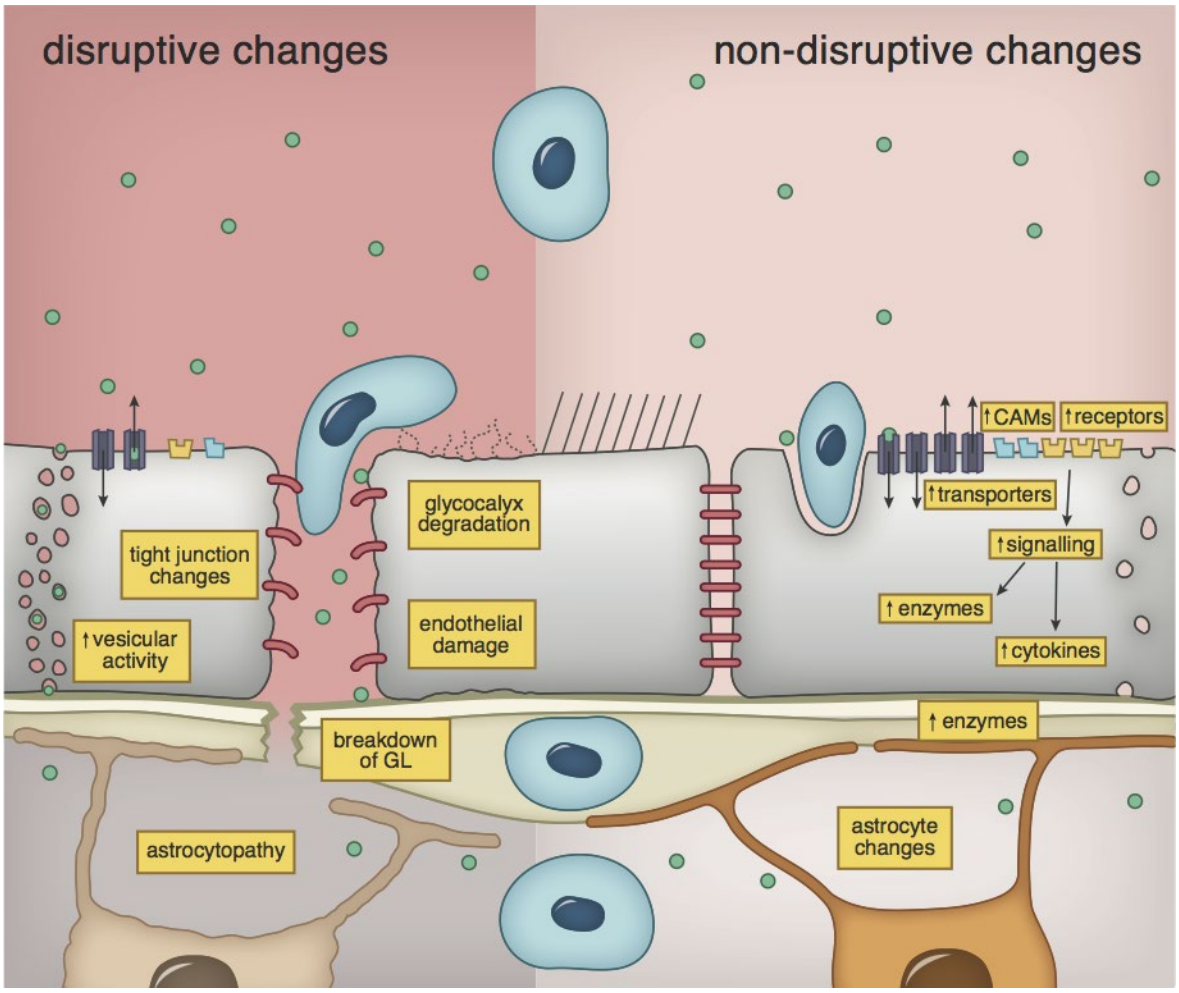

Figure 3 Differences between and putative mechanisms of disruptive and non-disruptive blood-brain barrier (BBB) changes.

CAMs = cellular adhesion molecules, GL = glia limitans.

I am grateful to Stephanie Suddell for the illustration.

Despite the mixed outcomes, LPS studies in animals have shown valuable insights into the possible mechanisms of BBB disruption during system inflammation. A central role emerges for prostanoids and nitric oxide (66), both of which are synthesized by the LPS-stimulated cerebrovascular endothelium and surrounding cells (67, 68). Important mechanisms include damage to and down-regulation of:

- Tight junctions, mediated by prostanoids (63), nitric oxide (69), matrix metalloproteinases (MMPs) (70), and reactive oxygen species (ROS) (71).
- Endothelial cells, including induction of apoptosis mediated by MAP kinase (72).
- Glycocalyx, which may be mediated by tumour necrosis factor-α (TNF-α) (73), heparanase (74), ROS (75), MMPs (76), and thrombin (73).
- Glia limitans, mediated by MMPs (77).
- Astrocytes, which may be lost (78) or transcription patterns altered to favour pro-inflammatory and cytotoxic pathways (79).

It has also been reported that neurodegenerative disease can magnify the response of the BBB to LPS (80), which may have relevance to the vulnerability of pwMS. Priming of microglia in neurodegenerative disease may be relevant (81), as recent evidence suggests that during systemic inflammation microglia can migrate to the cerebral endothelium and disrupt the BBB (82).

However, in the absence of compelling human data and the limited applicability of animal data, there is ongoing doubt as to the *in vivo* effects of systemic inflammation on the BBB in humans. This leads to a consideration of how the BBB can be studied in humans. An overview of relevant concepts in is shown in Table 1. There is some human data to suggest a link between systemic inflammation and BBB disruption, as shown in one study using the CSF/serum albumin ratio (83). Importantly, this study also highlighted that this effect may be magnified during neurological disease.

Imaging techniques based on the detection of an injected tracer have the advantage of being relatively non-invasive and well-tolerated by participants, as well as providing spatial information on BBB disruption which cannot be captured by CSF/serum measurements. In this context, the analysis of tracer studies is discussed in more detail in the next section.

Table 1 Overview of methodological concepts for *in vivo* study of BBB disruption in humans.

Not included in this table are techniques used in post-mortem study, for example immunohistochemistry for albumin in brain tissue to detect ante-mortem leakage (84).

Concept	**Method**	**Example**
The CNS concentration of a plasma protein not usually synthesised within the CNS correlates with BBB permeability	Paired cerebrospinal fluid (CSF) and serum analysis to estimate the ratio of CSF to serum concentration of plasma protein	CSF/serum albumin ratio (Q_{alb}) (83)
The serum concentration of a CNS protein not usually synthesized outside the CNS correlates with BBB permeability	Serum analysis of the CNS protein	Serum S100β (85)
Intravital injection of tracers	Injection of low molecular weight paramagnetic tracer before magnetic resonance imaging	Gadolinium contrast enhanced magnetic resonance imaging (23)
	Injection of radiolabelled tracer before nuclear imaging	Gallium positron emission tomography (86)
	Injection of fluorescent tracer before spectroscopic imaging	Indocyanine green near-infrared spectroscopy (87)
	Injection of radiolabelled test and BBB-impermeable reference tracers into brain arterial supply, and detection in brain venous drainage	Double indicator diffusion technique (88)
Water diffusion across the BBB is usually restricted	Labelling of blood water to detect exchange across BBB	Arterial spin labelled magnetic resonance imaging (89)

1.7 Tracer kinetic theory

If a bolus of tracer[1] is injected into the body and its path followed, one can use the kinetics of the tracer to draw inferences about the properties of biological systems. In compartmental analysis, the tracer is considered to be distributed throughout the system in discrete entities. The idea of a compartment is that it possesses instantaneous equilibrium, i.e. within the compartment at any time the concentration at any point is representative of the concentration within the compartment as a whole. We can then think of the tissue compartment as a system which takes inputs and delivers outputs in a reproducible way. By measuring the input function (arterial concentration-time curve) and output function (tissue concentration-time curve) we can derive a mathematical function for the behaviour of the tissue. In this sense tracer kinetic theory makes some fundamental assumptions regarding a system, namely of:

- Causality. There is no output without an input.
- Stationarity. If the input is delayed by time *t*, the output is also delayed by time *t*.
- Linearity. Twice the input gives twice the output (the amount of tracer should not affect how the system works).
- Conservation of indicator mass. Indicator is neither created nor destroyed inside the system (here the difference between a tracer and an indicator becomes more than terminological; a biologically-active tracer may well undergo metabolism within the system.

A model obeying these assumptions can be fitted to the measured data. The Patlak model (90) is widely used and makes some additional assumptions, namely that the tissue contains:

- A vascular compartment, of volume v_p, which is in instantaneous equilibrium with plasma.
- An irreversible compartment, of infinite capacity, in which tracer can be trapped.

The rate of diffusion into the irreversible compartment is governed by the transfer constant, K_{trans}. In this model there is no back-diffusion; tracer cannot leave the irreversible compartment. In a tissue where permeability is expected to be low (such as the brain), the assumption of irreversible trapping may be reasonable, and independent groups have shown the Patlak model to be superior for the analysis of low-permeability states (91, 92). The Patlak model is used extensively in this work and so a more detailed explanation is given here, and in diagrammatic form below.

[1] Technically a 'tracer' is a substance which normally operates within a system but has been labelled for detection. A substance introduced *de novo* for the purposes of detection is an 'indicator'. Injection of an exogenous non-biological contrast agent would fall into the latter category. However, 'tracer kinetics' is universally used as a catch-all term to refer to both, and has been used as such in this thesis.

Before introducing equations, it is helpful to think about what is happening during four phases of the experiment, as described in Figure 4.

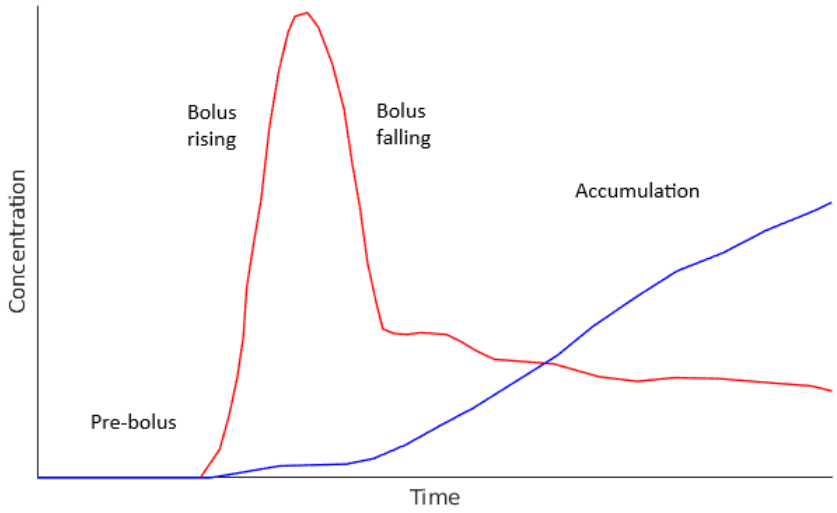

Figure 4 Four phases during a tracer kinetic experiment.

Red indicates contrast in plasma, blue is contrast irreversibly trapped in the tissue. This plot is a schematic derived from real data which has been highly simplified and exaggerated for demonstration purposes. A fifth washout phase is not included in the Patlak model and so is not shown here. The four phases are:

Pre-bolus: There is no contrast, so the plasma and tissue amounts are zero.

Bolus rising: The bolus is injected, and the plasma concentration sharply rises. Contrast diffuses into the tissue along the concentration gradient and is trapped, at a rate determined by the gradient and K_{trans}. The concentration of trapped contrast increases. However, this phase is very brief.

Bolus falling: The plasma concentration sharply falls. The concentration of trapped contrast stops rising. Since the bolus lasted only a small fraction of the measurement time, even though the plasma amount was high the amount of contrast trapped during the bolus was negligible.

Accumulation: The plasma concentration gradually falls as contrast is distributed throughout the body and excreted. The plasma concentration is not changing rapidly during this phase. Contrast is gradually trapped in the tissue at a rate determined by K_{trans} and the concentration gradient. If K_{trans} is small, or if the plasma concentration is low, then it will take a long time for an appreciable amount of contrast to be trapped. Therefore, continuing the measurement for a long time and giving a large bolus both mean that a large amount of contrast will be trapped overall, which makes it easier to detect.

Compartmental analysis of this system can be performed using the components of the Patlak model, as shown in Figure 5.

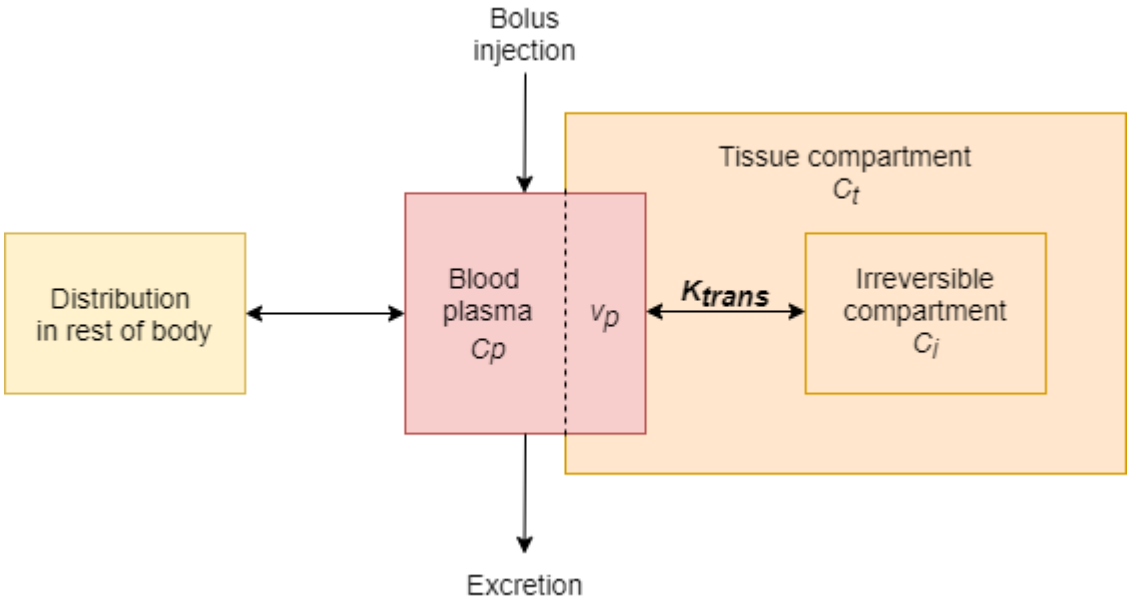

Figure 5 Schematic of compartments in the Patlak tracer kinetic model.

K_{trans} = transfer constant, C_p = contrast in plasma, C_t = contrast in tissue, C_i = contrast irreversibly trapped in tissue, v_p = volume of plasma in tissue.

These concepts can be parameterised to derive the value of K_{trans}. The simplest starting equation is

Equation 1

$$C_t(t) = C_i(t) + v_p C_p(t)$$

This states that, at any particular time (t), contrast in the tissue (C_t) is the sum of the contrast trapped irreversibly (C_i) plus contrast in the plasma (C_p), which is weighted by the volume of plasma in the tissue (v_p). So, in a very vascular tissue, the tissue will closely follow the time course of contrast in plasma, whereas in a less vascular tissue, the contrast in tissue will depend more closely on how much is trapped. It then follows that

Equation 2

$$\frac{dC_i}{dt} = K_{trans}\, C_p(t)$$

Meaning that, at any particular time, the rate of change in the concentration of trapped contrast (differential with respect to time) is equal to plasma concentration multiplied by the transfer constant. K_{trans} is also tissue clearance; the volume of plasma from which contrast is completely

removed in a given time. The commonly used units of K_{trans} are ml/100g/min or ml/100ml/min. The former is used here out of convention, though if tissue density is assumed to be 1 g/ml (93), then these units are interchangeable. K_{trans} of 1 ml/100g/min means that 100 g of tissue clears contrast from 1 ml of plasma in 1 minute.

Integration of Equation 2 gives

Equation 3

$$C_i(t) = K_{trans} \int_0^t C_p dt$$

This states that, at any particular time, the amount of trapped contrast is equal to the total amount of contrast that the plasma has delivered to the tissue by that time, multiplied by the transfer constant. If Equation 3 is inserted into Equation 1, the concentration in the tissue, at any particular time, can then be expressed as

Equation 4

$$C_t(t) = K_{trans} \int_0^t c_p(\tau) d\tau + v_p C_p(t)$$

Where τ in the integrand refers to the period between time zero and time *t*. To isolate the tissue component this is divided by the plasma concentration, to give

Equation 5

$$\frac{C_t(t)}{C_p(t)} = K_{trans} \frac{\int_0^t c_p(\tau) d\tau}{c_p(t)} + v_p$$

This equation can be solved graphically by recognising that it takes a linear form, if

Equation 6

$$x = \frac{\int_0^t C_p(\tau) d\tau}{C_p(t)}$$

Equation 7

$$y = \frac{C_t(t)}{C_p(t)}$$

So, it is $C_p(t)$ and $C_t(t)$ which must be measured; the input function and the tissue function. In this way x and y values can be calculated for every timepoint and plotted as shown in Figure 6. A line is then fitted, and the slope will be K_{trans} and the intercept v_p. The Patlak plot is only linear once

the plasma concentration has reached a steady state, a short time after the bolus. Hence the initial points are excluded from the fitting. The plasma volume v_p reflects cerebral blood volume (CBV) (94).

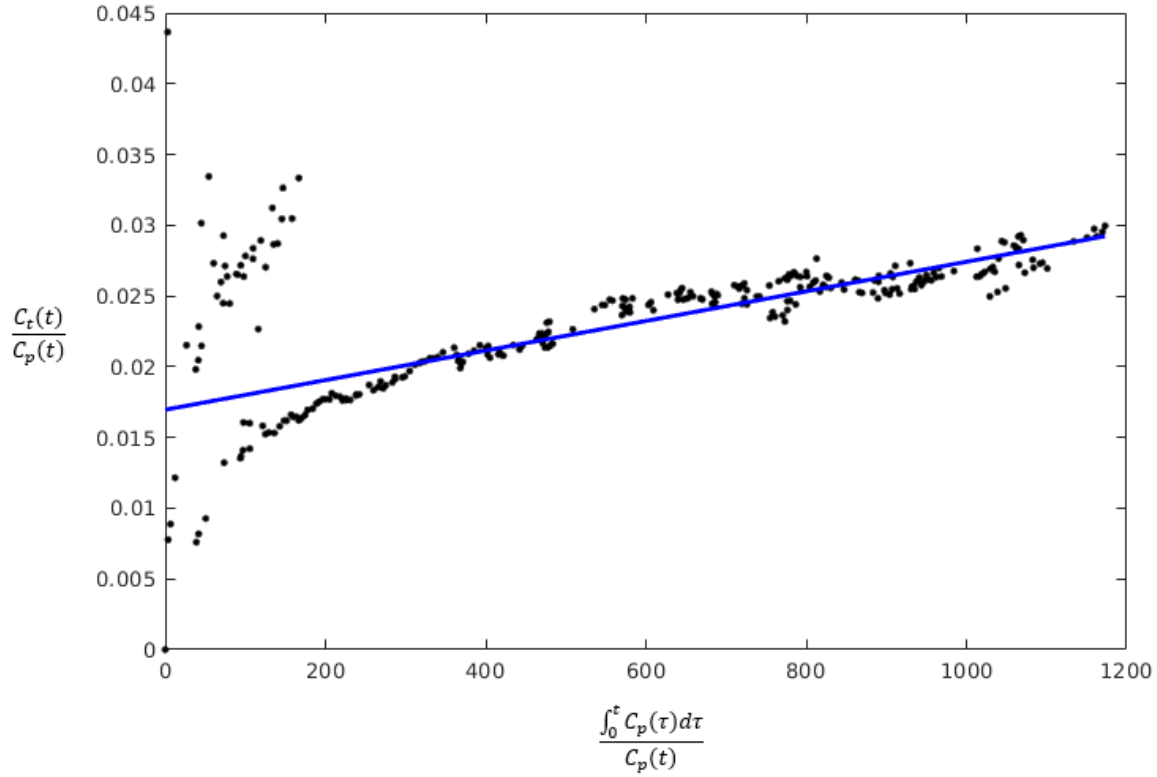

Figure 6 Example Patlak plot.

This was generated from a region of white matter in the same individual in Figure 1. The values for x and y are those generated from Equations 6 and 7. The initial points reflect rapid concentration changes during bolus passage and are excluded from the fitting.

The x-axis of the Patlak plot is not intuitive. The units are in time since the values of x are those calculated by Equation 6. The x variable is not meant to be intuitive, and it purely reflects the result of a mathematical rearrangement of equations to be able to easily calculate K_{trans} as the slope of a linear plot of the form y = mx + c.

The meaning of K_{trans} is demonstrated in the Crone-Renkin equation (95, 96), which describes the relationship between perfusion (F) and the permeability-surface area product (PS). The usual form is

Equation 8

$$K_{trans} = F(1 - e^{-\frac{PS}{F}})$$

Which can be rearranged to

Equation 9

$$\frac{K_{trans}}{F} = 1 - e^{-\frac{PS}{F}}$$

This takes the form $y = 1 - e^{-x}$, where $y = K_{trans}/F$ and $x = PS/F$. Figure 7 is a plot of $y = 1 - e^{-x}$, which shows that when x is very small, $y \cong x$. Therefore, if PS is much less than F (a 'permeability-limited' scenario, as in the brain) then K_{trans} approximates to PS.

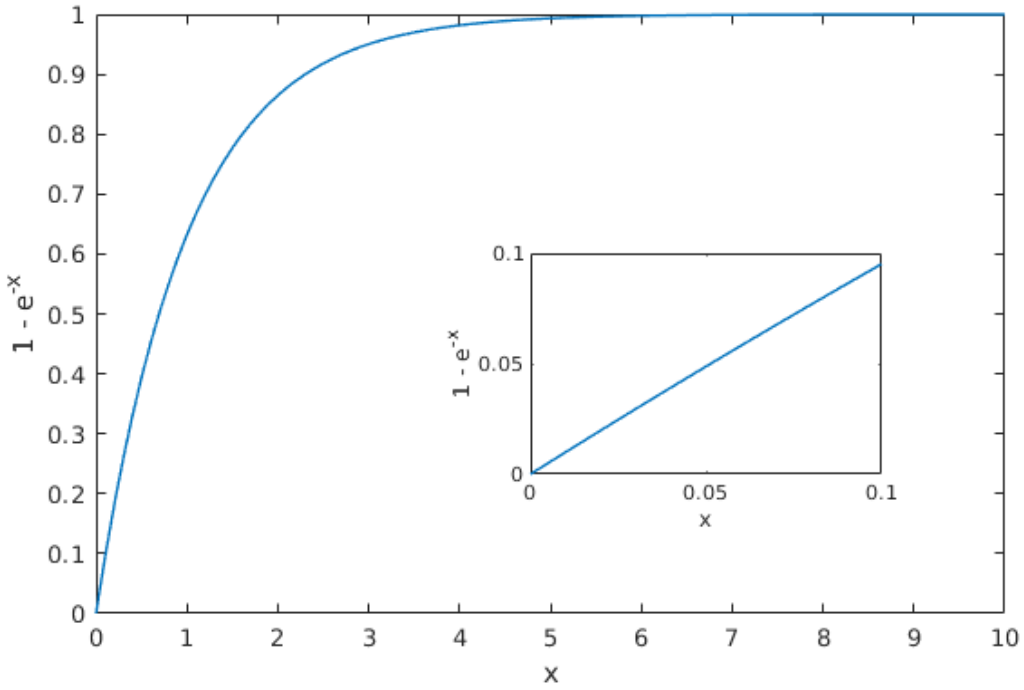

Figure 7 Graph of the function $y = 1 - e^{-x}$.

The inset shows that at very low values of x, $y \cong x$.

Therefore, it is important to remember that K_{trans} measured in the brain is a compound marker of permeability and surface area. This is intuitive; influx will be faster if either the tissue is more leaky, or if there is a greater surface area available for exchange. Surface area may depend on factors such as vessel density, radius, or tortuosity. Therefore, if two tissues are compared within an individual, a difference in K_{trans} could arise from differences in either P or S.

The Patlak model is only one of a large family of models, which notably includes the Tofts (97) and extended Tofts models (98). All tracer kinetic models involve some degree of simplification of a complex biological system. Issues such as interstitial fluid drainage, which may be impaired by ageing and pathology (99), will likely impact the observed kinetics. However, the addition of free parameters to a model can increase the risk of over-fitting (92). As with any model, the aim of

tracer kinetics is ultimately to deliver useful insights into the system under study, whilst maintaining an awareness of weaknesses.

1.8 Dynamic contrast-enhanced magnetic resonance imaging

In dynamic contrast-enhanced magnetic resonance imaging (DCE-MRI), changes in MR signal in response to a contrast agent (acting as an indicator) are used to provide the data for tracer kinetic analysis. The contrast agent in DCE-MRI is usually based on gadolinium (Gd), a rare earth metal which is strongly paramagnetic at room temperature and induces relaxation in adjacent nuclei. The effect on relaxation rate ($R_1 = 1/T_1$) is quantified by the constant of relaxivity (r, in L/mmol/s), which describes the linear relationship between concentration and relaxation rate. Gadolinium-based contrast agents (GBCAs) are largely excluded from the brain parenchyma by the healthy BBB, and hence can be used for the detection of BBB disruption.

To do this requires knowledge of the input and tissue functions as concentration-time curves. The tissue function must be measured, and the input function can either be measured from a feeding artery or values from the literature may be used. Concentration-time curves can be derived from the MR signal change with time. At each timepoint, the change in T_1 from baseline can be converted to concentration, using the known relaxivity of contrast agent. The fundamental technical challenge of DCE-MRI is to measure T_1 changes over time, with an acceptable spatial and temporal resolution.

Spoiled gradient echo (GRE) sequences are commonly used in DCE-MRI due to their speed in producing heavily T_1-weighted images. A short repetition time (TR) produces a pulsed steady state of magnetisation, but the build-up of transverse magnetisation is prevented ('spoiled'). Several methods are available, the most effective of which is radiofrequency (RF)-spoiling where the phase of the RF pulse is offset every time (Figure 8). The offset is determined by a quadratic schedule which after every excitation favours phase cancelling of transverse magnetisation from previous excitations.

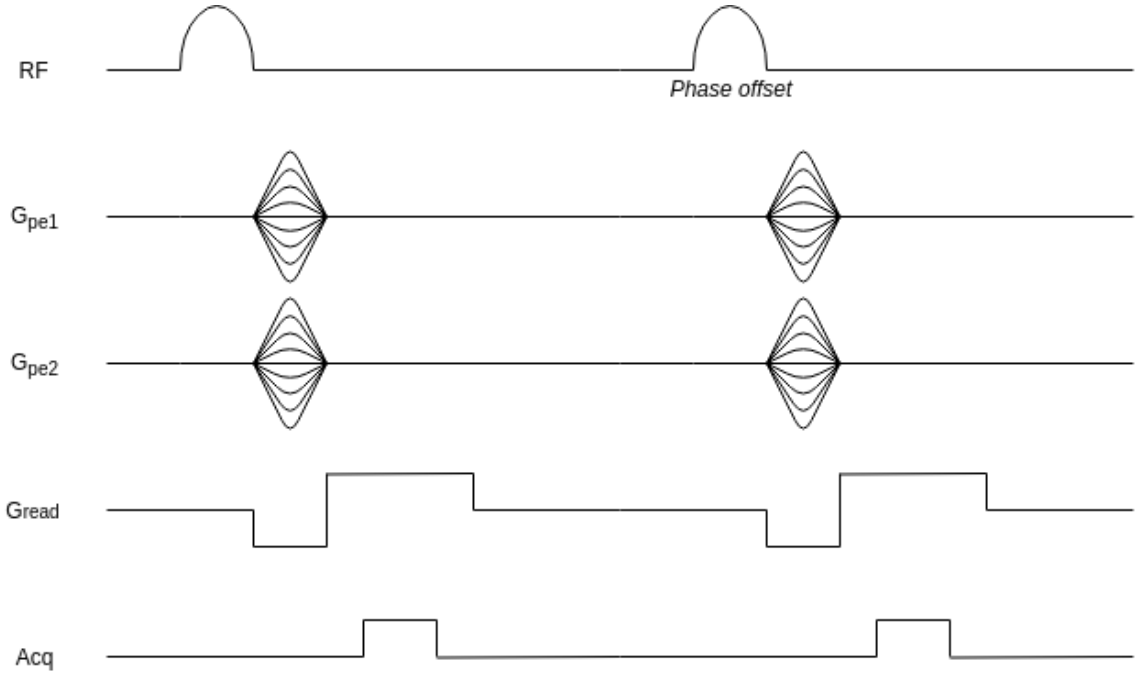

Figure 8 Pulse sequence diagram for 3D spoiled gradient echo.

RF = radiofrequency transmit field, G_{pe1} and G_{pe2} = gradients in the first and second phase encoding directions. G_{read} = gradient in the readout direction. Acq = signal acquisition.

For a spoiled gradient echo sequence in the longitudinal steady-state and with perfect spoiling such that there is no steady-state magnetisation in the transverse plane, the signal can be formulated algebraically as follows:

Equation 10

$$S = S_0 \sin \alpha_1 \frac{1 - E_1}{1 - (\cos \alpha) E_1}$$

Equation 11

$$E_1 = e^{-TR/T1}$$

Where α = flip angle, TR = repetition time, T_1 = longitudinal relaxation time. S_0 is the signal obtained from a fully relaxed acquisition, and is a function of equilibrium magnetisation (M_0, which relates to proton density) and scanner gain. As demonstrated in later chapters, these equations [2] can be used to convert the MR signal into T_1, and then the constant of relaxivity can

[2] The signal equation in full also contains a term for weighting by T2*, the effective transverse relaxation time. However, this term is removed by setting echo time (TE) to be very short, and so is not included here.

be used to convert T_1 into the concentration of contrast, thereby providing the data for tracer kinetic analysis.

The scheme described above is one of the most commonly-used methods for DCE-MRI, and though recommendations have been published (100, 101), there is significant variation in the acquisition and processing protocols used by individual centres. The starting point for the protocol used in this thesis was that used by the Larsson group (University of Copenhagen), as theirs was the first to reveal the abnormality in the normal-appearing brain tissue of pwMS (23). In the literature, various techniques have been used to improve DCE-MRI data collection and analysis, but many have not been clearly shown to add value and hence are inconsistently applied. For example, most centres create a manual input function per scan, which has considerable difficulties in practice, whereas automated detection may have benefits for useability, accuracy, and precision. Likewise, a very short TR is often used to enable a fast temporal resolution, though the effect of this on K_i has not been clearly reported. This and other optimisations are discussed in detail in Chapters 5 and 6, where some of the difficulties of DCE-MRI are addressed systematically.

There are other challenges in conducting tracer kinetic analysis using MRI. Most of the MR signal comes from water molecules, and so water exchange can blur the delineation of compartments in tracer kinetic analysis. GBCA induces relaxation in adjacent water molecules, and hence it is tempting to think that the effect is confined to the compartment containing contrast molecules, i.e. the plasma. However, the exchange rate of water molecules between plasma and red blood cells is very fast (102), and so when the MR signal is used to derive the concentration in a feeding artery, the resulting concentration will be that in whole blood, even though contrast is confined to the plasma. If the volume fraction of red blood cells is measured as the haematocrit (Hct), then plasma concentration (C_p) can be derived from whole blood concentration (C_b) according to the formula

Equation 12

$$C_p = C_b/(1 - Hct)$$

For the purposes of tracer kinetic analysis, it is convenient to leave this correction until the end (103). Thus, the analysis is completed to give the influx constant K_i for whole blood. This can then be converted to the transfer constant K_{trans} according to the formula

Equation 13

$$K_{trans} = K_i(1 - Hct)$$

There is variation in the literature, with some favouring K_{trans} (100, 104) and others K_i (23, 105, 106). If a fixed value is assumed for haematocrit (0.45 is often used) then both parameters scale, and the difference is one of accuracy. Alternatively, an individual haematocrit can be measured, however, this is typically sampled from a large vein and is not constant throughout the vascular tree. The haematocrit is significantly lower in smaller blood vessels such as capillaries (the Fähraeus effect), and a factor of 0.85 is often cited (107, 108), though lower values have been reported (109), as has an effect of pathology (110). This adds another source of measurement uncertainty. Since the Fähraeus effect is dependent on blood flow rate, it is possible that small vessel haematocrit varies across brain regions and in pwMS, where abnormalities of perfusion have long been reported (111-114). There is also an issue of whether an individual's historical haematocrit values can be used, as in some studies (92). Within an individual, the day-to-day variation in haematocrit is fairly small (115), but ideally measurements should be contemporaneous (100). This could be particularly important if serial tracer analyses are conducted to assess the response to some event; for example, haematocrit falls during severe sepsis (116).

In summary, DCE-MRI provides a method for the measurement of BBB permeability in humans, by deriving the influx constant K_i for a gadolinium-based contrast agent. With a suitable setup, this technique can be used to probe BBB disruption which may occur in association with systemic inflammation. This forms part of a larger question, as to how systemic inflammation affects the brain in people with neurological disease, such as MS. This leads to the hypotheses for this thesis.

Chapter 2 Hypotheses and Aims

2.1 Primary hypotheses

Hypothesis 1: The host inflammatory response to systemic events such as infections is associated with the rate of brain atrophy in people with MS.

Hypothesis 2: K_i as measured by DCE-MRI conforms to the expectations of a BBB permeability marker.

Hypothesis 3: An episode of systemic infection, specifically UTI, is associated with BBB disruption detectable by DCE-MRI.

2.2 Aims

Hypothesis 1 was addressed by the SIMS Study (Systemic Infection and Multiple Sclerosis). Individuals with progressive MS were followed-up over a period of 2.5 years, with robust longitudinal measures of clinical and radiological progression. Over the same period, detailed clinical and biochemical characterisation of systemic infections and the host inflammatory response was conducted. The aim was to examine these data for signals of a possible association between the host inflammatory response to systemic events and brain atrophy, a surrogate marker of MS disease progression.

Hypothesis 2 was addressed during the development and optimisation of DCE-MRI. The aim was to set out biological expectations of a BBB permeability marker and test the behaviour of K_i as measured by DCE-MRI in accordance with these expectations. In doing so, the aim was to validate K_i as a marker of BBB permeability, suitable for further human studies.

Hypothesis 3 was addressed by the SIBIMS Study (Systemic Infection and the BBB in MS). Unlike previous human studies, a within-participant design was used to maximise power and account for between-participant variation. DCE-MRI was used for the detection of subtle BBB disruption, and extensive optimisation work was conducted with this purpose in mind. The study was focused on UTI specifically, as focussing on this common infection removed another source of variation. The aim was to determine whether BBB disruption could be a mechanism linking systemic infection and disease activity.

Chapter 3 Systemic Infections and Disease Progression in Multiple Sclerosis

3.1 Introduction

In this chapter I describe the SIMS (Systemic Infections and Multiple Sclerosis) study. Understanding the role of systemic infection in progression may advance our understanding of disease biology, and potentially open a new path towards a long-sought goal; an effective treatment to delay or prevent progression. 53 individuals with progressive MS were followed over 2.5 years, with detailed clinical and laboratory monitoring of systemic inflammatory events. Disease progression over this timeframe was captured by brain atrophy, as well as secondary clinical and radiological measures. The relationships of these markers were examined for signals of a possible association between the host inflammatory response to systemic events and brain atrophy.

3.2 Hypotheses

The primary hypothesis is that systemic infections and other inflammatory stimuli are associated with the rate of disability progression in people with MS. The secondary hypothesis is that the magnitude of host inflammatory response to systemic infections is associated with MS disease progression. Due to sample size considerations discussed below, the primary outcome measure of progression is longitudinal brain atrophy.

3.3 Research techniques

SIMS was a longitudinal prospective cohort study examining the relationship between brain atrophy and the host inflammatory response to systemic events such as infections, in people with progressive MS over 2.5 years. The study outcomes measures are shown in Table 2. As far as possible all clinical, laboratory, and radiological assessments were conducted blind to each other.

Table 2 Outcome measures in the SIMS study

EDSS = expanded disability status scale, MSFC = multiple sclerosis functional composite, MSIS = multiple sclerosis impact scale, FS = fatigue scale, BDI = Beck's depression inventory short form.

Primary outcome	Brain atrophy	
Secondary outcomes	Radiological	Spinal cord atrophy
		Lesion measures (volume and number)
	Clinical	Physician: EDSS and MSFC
		Patient-reported: MSIS-29, FS, BDI

3.3.1 Clinical monitoring of systemic events

Episodic infections (or other inflammatory events such as surgery, major injuries, or vaccinations) were recorded using a weekly electronic diary supplied to all participants, capturing the onset, duration, localisation, and treatment (copy in Appendix A). This method was chosen to provide the most comprehensive record of self-reported infection episodes. Compliance was encouraged with weekly reminders by text or phone as preferred. In the analysis, reported episodes were categorised as infections, vaccinations, or other. Infections were subcategorised as visceral infections (defined as those affecting bladder or chest), and infections requiring antibiotic treatment. If multiple infection sites were reported during a single episode, the episode was still treated as single. However, reported infection sites were also enumerated separately to ascertain the frequency of different infections (with one exception: if upper and lower respiratory tract infections were reported together, the site was classed as lower respiratory tract). Clinical management of inflammatory episodes was at the discretion of the participant and their healthcare team, not the study team.

3.3.2 Laboratory monitoring of systemic events

Host response to systemic infection may differ according to the infective stimulus as well as host factors. Hence a robust measure of the inflammatory response was needed to control for this. A method enabling regular sampling was preferable since this allows for trends to be studied within the individual and relative to their own baseline; in practice this necessitates that the sampling method be highly tolerable to participants. Longitudinal measurement of urinary neopterin was chosen as it provides a non-invasive, reliable, and non-specific marker of systemic inflammation,

with the ability to integrate inflammatory status over a long period of time (117). Neopterin is produced by activated macrophages in response to stimulation by interferon-γ, a master checkpoint of the immune response (118), and hence provides a non-specific marker irrespective of inflammatory stimulus. Systemic levels are not influenced by CNS inflammation (119). Since neopterin has a high renal clearance it is suitable for measurement in urine, and measurements were normalised to urinary creatinine to correct for hydration status and expressed as the urinary neopterin-to-creatinine ratio (UNCR). Participants collected weekly midstream urine samples at home and were given training and materials to store samples in their home freezer, shielded from light (neopterin degrades in light). Batches of samples were periodically transferred to the laboratory freezer. Urine was first stored at −20°C, then thawed and centrifuged at 10°C and 2000g for 5 min, before aliquoting and long-term storage at −80 °C.

Samples were analysed by ultraperformance liquid chromatography-mass spectrometry, using an ACQUITY UPLC system coupled to a Xevo triple quadrupole mass spectrometer (both Waters, Milford, MA, USA); method described in detail elsewhere (117). Samples were assayed in duplicate or triplicate. Urinary creatinine and neopterin concentrations were calculated as μm/L and mg/dL; UNCR was expressed in micromole per mole. This method has high test-retest precision (inter-day coefficient of variation 5.6%, intra-day 2.0%) and low limits of both detection (0.3 μg/L) and quanitification (1 μg/L) (117).

Analysis of longitudinal UNCR and infection data was performed using a custom-built script in MATLAB (Mathworks, Natick, MA, USA). For each participant, the infection and UNCR time-series were aligned and episodes marked. At-risk periods were defined as 2 weeks prior and 5 weeks following an episode (41, 42), except for planned events such as vaccination or surgery where the at-risk period began on the day of the event. The linear regression line passing through all points outside at-risk periods was calculated and used as the baseline (see example in Figure 9). For each episode, peak height was calculated as the maximum difference between measured UNCR and regression baseline during the at-risk period, expressed as a percentage of the regression baseline value (Figure 9). Reported episodes without a peak above baseline were discarded, on the basis that such episodes would reflect either genuine infection without systemic inflammatory response, or over-reporting of perceived infection symptoms – both scenarios with the potential to confound the analysis. For each participant, the output of analysis was the annualised rate of episodes and the mean percentage UNCR peak height during episodes. In addition, mean UNCR was calculated for each participant by taking the mean of all UNCR values over the study period. The adjusted mean was calculated by excluding those values within at-risk periods from the calculation, to give a better idea of baseline UNCR outside of discrete inflammatory episodes.

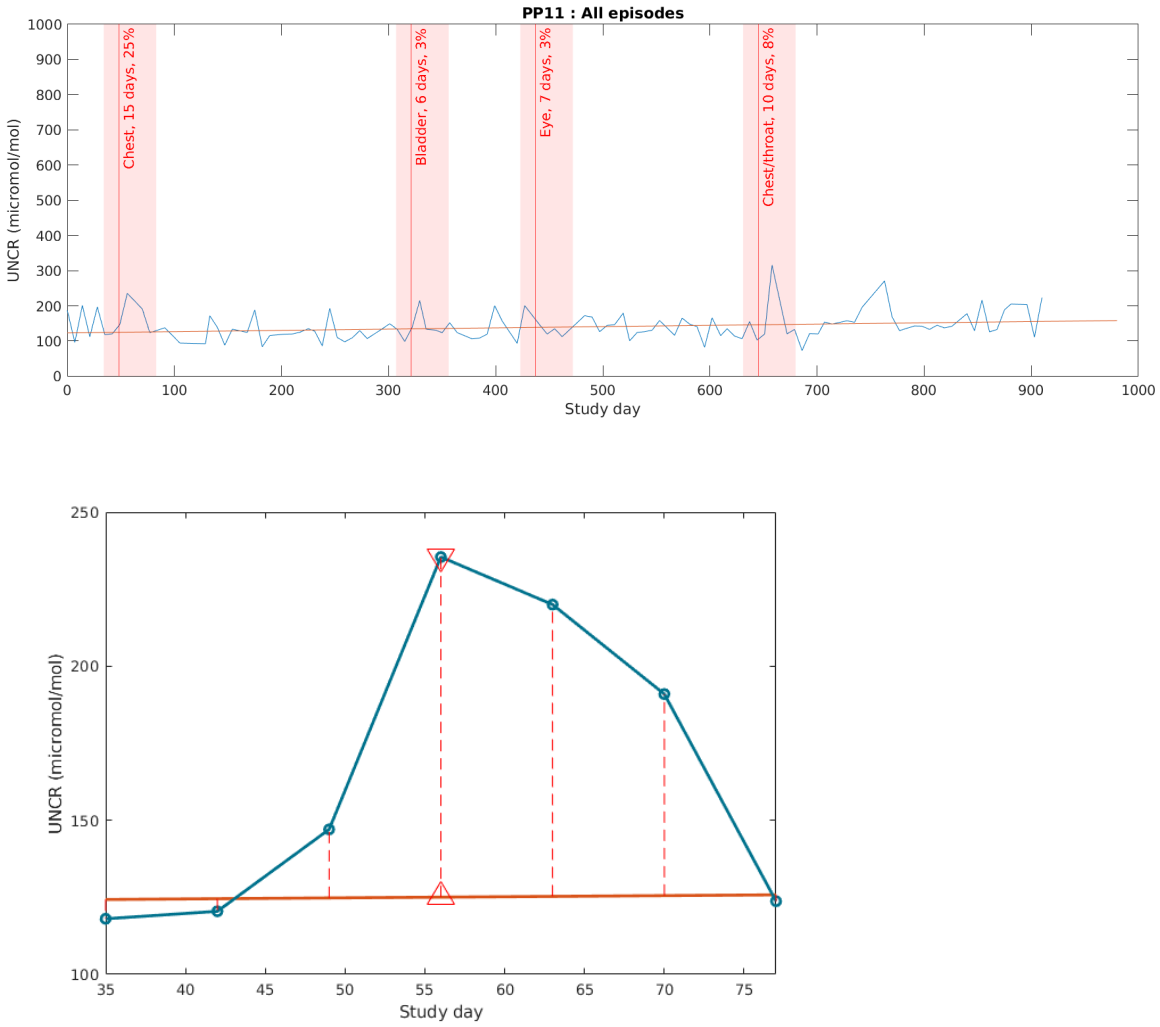

Figure 9 Example of longitudinal UNCR and symptoms analysis for a single individual.

The top panel shows UNCR data plotted as a time-series (blue). Episodes of participant-reported infection were marked (red lines) with surrounding at-risk periods (pink bars). A regression line (orange) was fitted, excluding points within the at-risk periods. This represents the participants' own baseline, which may vary over time.

The bottom panel is an expansion of the first at-risk period. At each point, the difference was calculated between measured UNCR (blue) and the corresponding regression baseline (orange, differences marked with dashed lines), and expressed as a percentage of the regression baseline value. Conceptually, this reflects UNCR elevation over the expected value at that time. The maximum difference (bounded by orange triangles) is taken to represent the peak height, and the inflammatory response to the episode. The process was repeated for each at-risk period, and the summary value for each participant was the mean of peak heights.

3.3.3 Radiological measures of disease progression

3.3.3.1 Overview of radiological measures

Radiological measures provide an objective and sensitive marker of disease progression. Since progression in MS is slow, reliance on clinical measures alone requires a prohibitively large sample size or study duration (120). Primary outcomes based on imaging are widely accepted in MS clinical trials (121), and brain atrophy was the primary outcome for the SIMS study.

All imaging was conducted on the 3T MR unit (Skyra, Siemens, Erlangen, Germany) at University Hospital Southampton NHS Foundation Trust, using a 20-element phased-array head and neck coil. Due to the long duration of the study, scans at entrance and exit were naturally interleaved. The imaging protocol comprised (detailed protocol information in Appendix B):

- 3D magnetization prepared-rapid gradient echo (MP-RAGE) covering the whole brain: TR = 2200 ms, TE = 2.45 ms, TI = 900 ms, flip angle = 8°, GRAPPA (GeneRalised Autocalibrating Partial Parallel Acceleration) undersampling with parallel imaging factor =2, field-of-view 250 × 250 × 176 mm^3, voxel size 1.0 × 1.0 × 1.0 mm^3. Chosen to provide structural imaging with isotropic voxels and excellent grey-white matter contrast, suitable for volume and atrophy estimation and tissue classification (122).
- Axial turbo spin echo T_2-weighted sequence covering the whole brain: TR = 4400 ms, TE = 9/90 ms, field-of-view 250 × 203 ×149 mm3, voxel size 1.0 × 1.0 × 3.0 mm3, 45 slices (distance factor = 10%). Chosen as standard in the assessment of MS lesions (11).
- Axial fluid-attenuated inversion recovery (FLAIR) covering the whole brain: TR = 5000 ms, TE = 397 ms, TI = 1800 ms, field-of-view = 256 × 248 × 194 mm3, voxel size 1.0 × 1.0 × 1.1 mm3, 176 slices. Chosen to facilitate MS lesion detection and automated segmentation (122).
- 3D MP-RAGE covering the spinal cord from fourth ventricle to T4: TR = 2200 ms, TE = 2.45 ms, TI = 900 ms, flip angle = 8°, GRAPPA undersampling with parallel imaging factor = 2, field of view 176 x 250 x 250 mm3, voxel size 1.0 x 1.0 x 1.0 mm3.

The analysis pipeline was developed in MATLAB and optimised for parallel execution on an 8-core workstation running Linux Red Hat 7 (Red Hat Inc, Raleigh, NC, USA). Images were exported from the scanner in DICOM (Digital Imaging and Communications in Medicine) format and converted to

NIFTI (Neuroimaging Informatics Technology Initiative) format using *dicm2nii* (open source code from Xiangui Li, Ohio State University).

3.3.3.2 Longitudinal brain atrophy measurement

Brain atrophy reflects irreversible axonal loss (123). Whole-brain atrophy was quantified using SIENA (124), part of the software package FSL (125), as the percentage whole brain volume change (PBVC) between the two imaging timepoints, and then annualised. Negative values for volume change represent atrophy. Many methods are available for longitudinal brain atrophy calculation, but SIENA is widely used and has been demonstrated to be accurate and robust, with reported 0.15% error (124). SIENA starts by extracting brain and skull images from the two-timepoint whole-head input data (126). Settings of the brain extraction tool (FSL-BET) were modified from default according to optimisation recommendations for MS (127), namely by cropping of the field of view (using the FSL tool 'RobustFOV'), and use of option '-B' with a fractional intensity threshold of 0.1 (the same optimisation was applied to all uses of BET in this work). Standard-space masking was also applied to improve removal of non-brain tissue, as this has previously been shown to improve SIENA output (128). The two brain images were then aligned to each other using the skull images to constrain the registration scaling (129), and both brain images were resampled into the space halfway between the two. Next, tissue-type segmentation was carried out using FSL-FAST (130) to find brain/non-brain edge points, and then perpendicular edge displacement (between the two timepoints) was estimated at these edge points. Finally, the mean edge displacement was converted into a (global) estimate of PBVC between the two timepoints. An example of the SIENA output is shown in Figure 10.

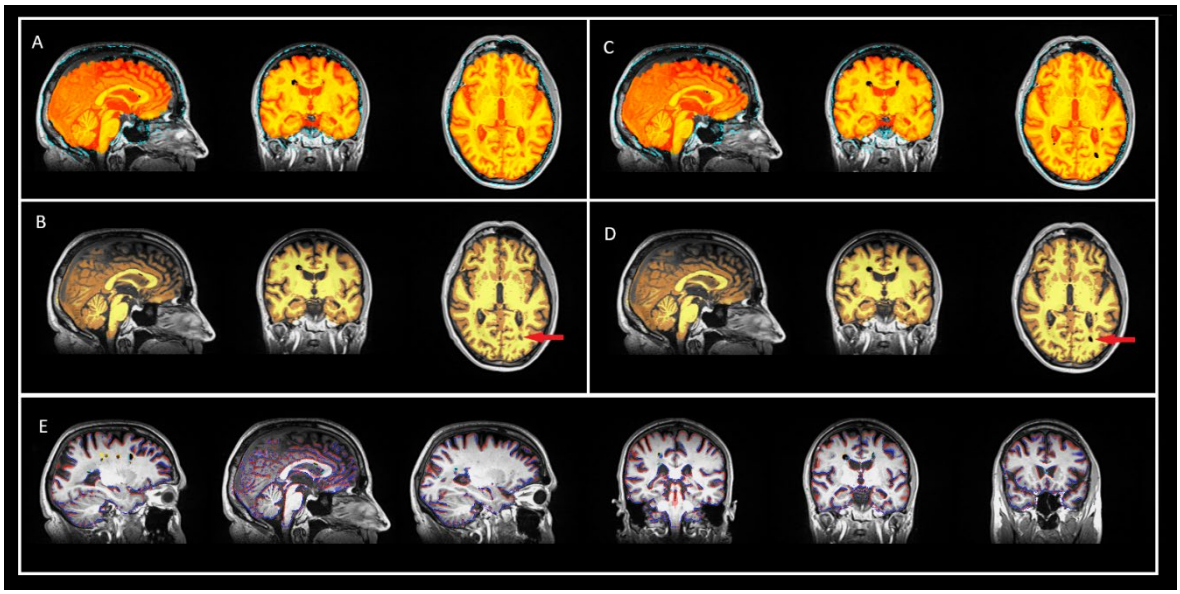

Figure 10 Example of longitudinal brain atrophy calculation by SIENA.

The baseline scan is brain extracted (panel A), and tissue-type segmented (B) to identify the edges of brain and non-brain tissue. The same operations are performed on the follow-up scan (C and D). Perpendicular edge motion between the two images is then calculated (E, atrophy shown in blue). There is actually a small error in this randomly-selected example, as a black hole lesion in the left parieto-occipital white matter has been labelled as brain in the baseline scan (B, arrow), but as non-brain in the follow-up scan (D, arrow).

In preliminary analyses errors were found in the conventional implementation of SIENA due to the presence of so-called 'black holes'. Black holes are T_1-hypointense MS lesions which reflect areas of axonal destruction; in fact T_1 intensity in a black hole correlates with axonal density (131). Tissue segmentation in FSL-FAST is a forced choice between grey matter (GM), white matter (WM), CSF, and non-brain. The classification of GM vs WM is irrelevant as both are counted as brain tissue. However, the classification of GM or WM vs CSF or non-brain is crucial, as this is the basis for edge detection. Since FAST makes use of signal intensity and neighbourhood information (130), black holes surrounded by normal-appearing WM can be misclassified as WM, and if so will be incorrectly counted as brain tissue (an example is shown in Figure 11). Out of 53 participants paired scans later analysed with conventional FAST, 43 (81%) had at least one scan with at least one misclassified black hole lesion. Other studies have dealt with lesions by performing lesion-filling before performing SIENA (132); areas within the lesion mask are filled with signal matched to surrounding brain tissue. However, valuable information is lost in this process, as black holes are then segmented as brain tissue by FAST, and a change in black hole volume is therefore incorrectly excluded from the calculation of change in brain volume.

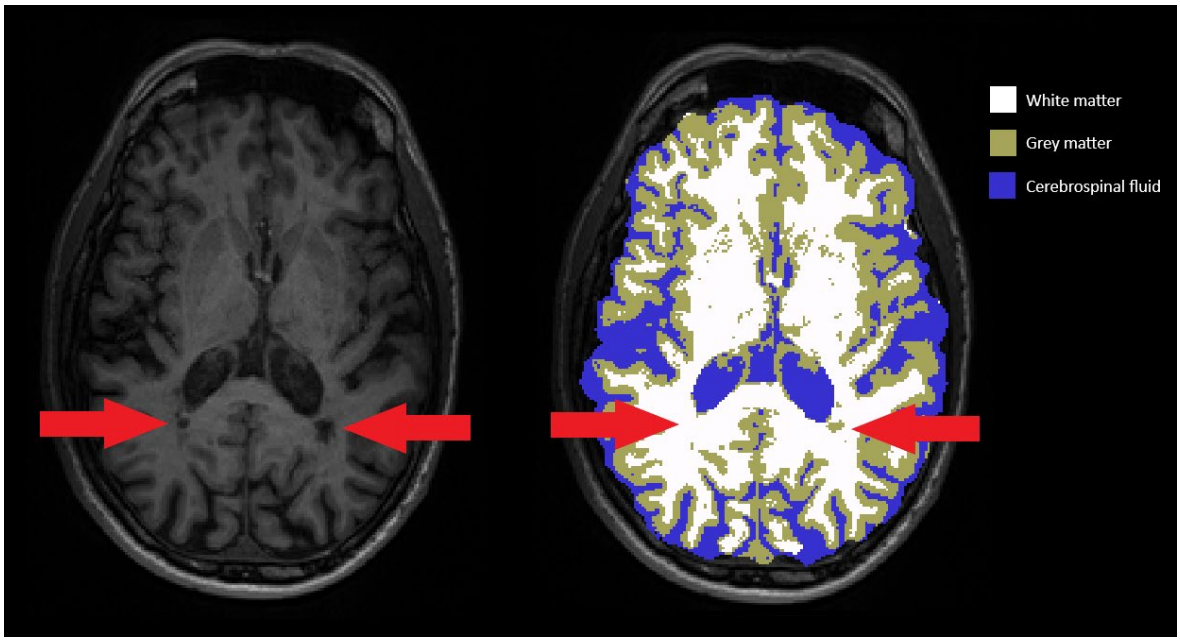

Figure 11 Black holes may be missed during tissue segmentation.

A T_1-weighted image (left) has been tissue-type segmented (right) using FSL-FAST. Black hole lesions are visible in next to the posterior horns of both lateral ventricles (arrowed). These have signal intensity comparable to CSF. However, in the segmentation these are classed as brain tissue.

A new method for dealing with black holes was developed and named ZEFRAM (ZEro-Filled Robust Atrophy Measurement). This method makes use of the robust perpendicular edge motion detection capabilities of SIENA, which makes no distinction between internal and external edges. Black holes were defined as T_2/FLAIR-hyperintense lesions with corresponding T_1 signal intensity less than GM, as in previous studies (133-135). The T_1 image was first segmented using FAST, and the mean signal intensity of GM computed. The WM map and lesion map (see Section 3.3.3.4 below) were then used to fill holes in the T_1 image, using the 'lesion filling' command in FSL. The lesion map was then registered into T_1 space; each lesion voxel was classed as a black hole voxel if the (unfilled) T_1 signal intensity were less than the mean value for GM. The resulting black hole map was then inverted and multiplied with the filled T_1 image, resulting in a new synthetic T_1 image with non-black hole lesions filled with surrounding NAWM, and black holes 'zero-filled', i.e. with signal intensity set to zero (as shown in Figure 12).

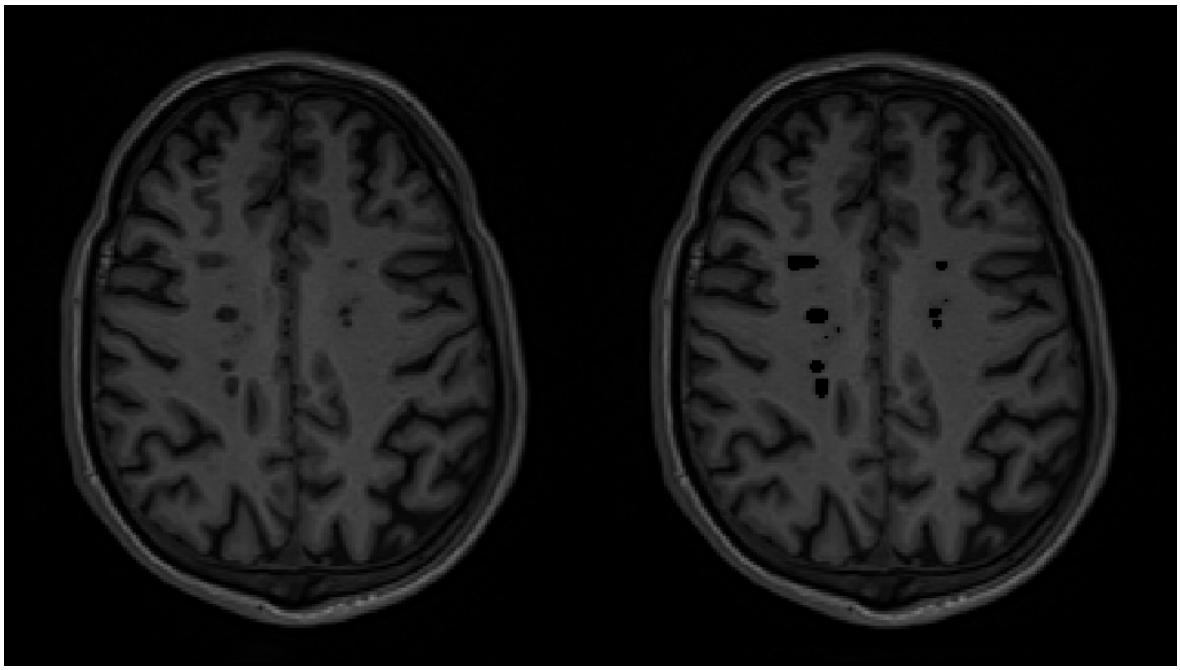

Figure 12 Zero-filling of black holes by ZEFRAM.

Black holes in the raw T_1-weighted image (left) have been zero-filled (right), only if their signal intensity is less than that of grey matter.

When passed into SIENA, this modification forces FAST to treat the zero-filed black holes as non-brain, as their signal intensity is markedly different from any other structures. The edge between a black hole and surrounding brain tissue is examined for perpendicular motion, along with other internal and external edges. Meanwhile the filling of non-black hole lesions prevents their misclassification as non-brain. The additional advantage of this method is that a separate metric of black hole change can be obtained. The volume of black hole voxels at each timepoint was measured and corrected for head size using the normalisation factor derived from SIENAX (see Section 3.3.3.3 below); the percentage volume change of black holes can then be calculated.

3.3.3.3 Cross-sectional brain volume measurement

Cross-sectional measurements of brain tissue volumes, normalised for subject head size (NBV), were quantified by SIENAX (124), also part of FSL. The lesion-filled and black hole erased T_1 images synthesised for SIENA were used for this analysis; the significant confounding effect of lesions on SIENAX has previously been reported (136, 137). SIENAX starts by extracting brain and skull images from the single whole-head input data using BET (126). The brain image is then affine-registered (129) to MNI152 standard space (138) using the skull image to determine the registration scaling; this is primarily in order to obtain the volumetric scaling factor, to be used as a normalisation for head size. Next, tissue-type segmentation with partial volume estimation is carried out (130) to calculate total volume of brain tissue. This includes separate estimates of

volumes of GM, WM, cortical GM, and ventricular CSF. The change in regional volumes between timepoints was expressed as the annualised percentage change from baseline.

The advantage of SIENAX over SIENA is that it is possible to estimate tissue-specific volumes, and thus assess tissue-specific atrophy. Grey matter atrophy, for example, is associated with disability accumulation in MS (139). The disadvantage of SIENAX, however, is that measurements of change across serial cross-sectional measurements are less precise than longitudinal measurements, as normalisation and segmentation introduce sources of error. Total error is reported as 0.5-1% for SIENAX, compared to 0.15% for SIENA (124). Hence the measurements of whole brain atrophy were taken from SIENA, not SIENAX.

3.3.3.4 Cross-sectional brain lesion measurement

Brain MS lesions were segmented by the lesion growth algorithm (140) from the lesion segmentation toolbox (LST) version 20.0.15, operating within the software package SPM version 12, in MATLAB. This method has been validated in MS (141) and is fully automated. The algorithm first segments the isotropic T_1 image into tissue classes, and then combines the information with co-registered FLAIR intensities to calculate lesion belief maps. These maps are binarised with a cut-off ($\kappa = 0.3$) determined by visual inspection, to produce an initial binary lesion map. This is then grown along voxels that appear hyperintense in the FLAIR image, to produce a lesion probability map. The probability map is binarised with a final threshold of 1, and the total lesion volume and number of lesions extracted. An example is shown in Figure 13. The process was repeated for both imaging timepoints, and the change in both lesion volume and number was computed (as difference).

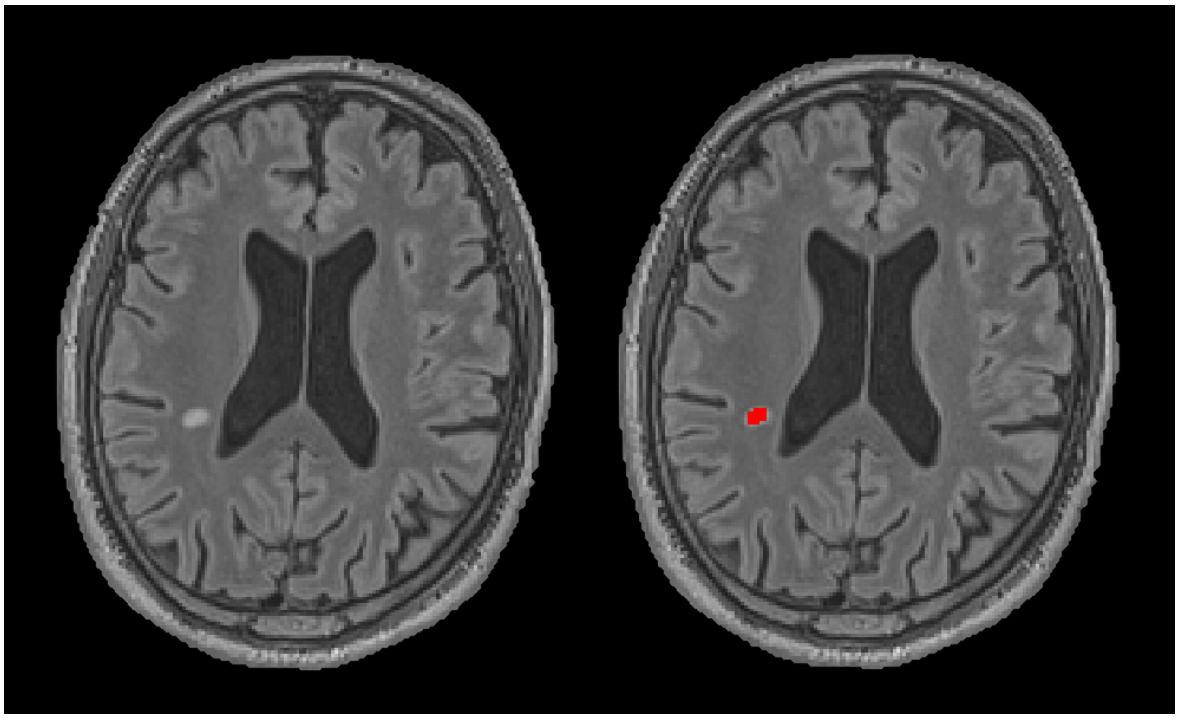

Figure 13 Example of automated legion segmentation.

The FLAIR image (left) has been segmented to create a mask of lesions (right).

3.3.3.5 Cross-sectional spinal cord area measurement

MRI often reveals abnormalities of the spinal cord in MS, especially in the cervical region, and these are likely involved in the development of mobility and bladder symptoms which contribute significantly to the disability of MS (142). Atrophy of the spinal cord is seen over time, and this likely reflects axonal loss (143). Several studies have shown that measurements of spinal cord atrophy are accurate, reproducible, sensitive to change, and correlate well with clinical disability (144-147). Longitudinal studies have reported a cervical cord atrophy rate in MS of around 2-3% per year (148-152). High-resolution 3D T_1-weighted images with 1mm isotropic voxels are usually used (153), and several techniques for semi-automated (147, 153, 154) and automated analysis are available. The automated method *PropSeg* (155), part of the Spinal Cord Toolbox (156), was chosen for this study as it has excellent scan-rescan reliability, correlates with clinical disability (157), and minimises operator bias. The method relies on propagation and iterative improvement of a deformable model, with adaptation to local differences in contrast-to-noise as is often the case in the large field-of-view in a spinal cord image. The mean cross-sectional area (CSA) between C2-C5 levels was computed (see Figure 14). Since spinal cord area varies according to subject size a number of normalisation methods have been discussed (158), but in this case where serial within-participant measurements are compared normalisation is not required as the participant is their own control. For each individual the change in CSA between timepoints was expressed as the annualised percentage change from baseline.

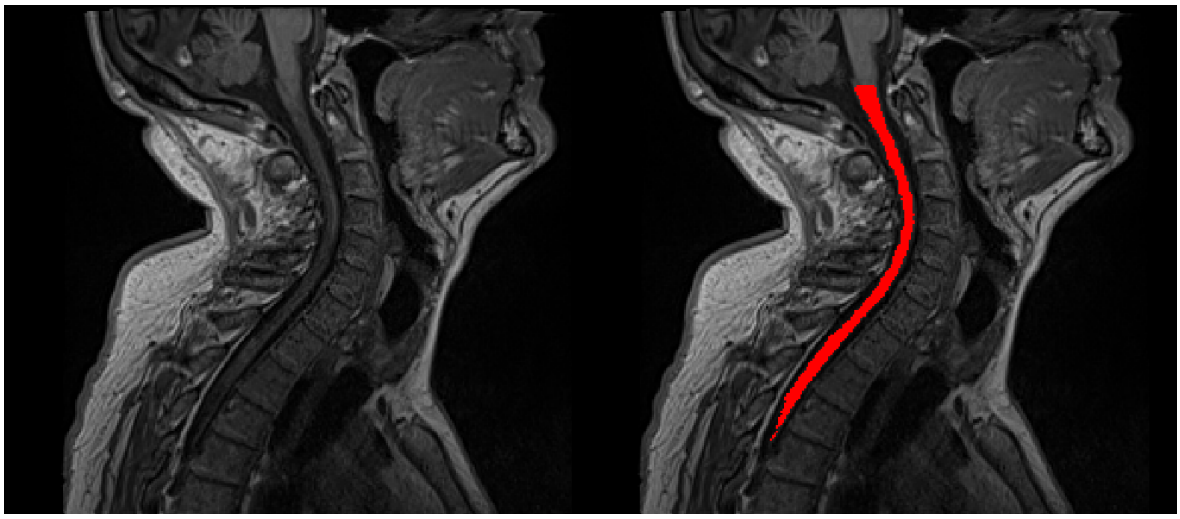

Figure 14 Example of automated spinal cord segmentation.

The T_1-weighted image (left) has been segmented to create a mask of the spinal cord (right).

3.3.3.6 Quality control of radiological data

All raw images were visually inspected by an experienced neuroradiologist (Janine Domjan, University Hospital Southampton NHS Foundation Trust); subjects with inadequate image quality (due to movement artefact, for example) were recalled for repeat imaging as soon as possible. Intra-rater reliability was not analysed since the report of visual inspection was not a study outcome.

For SIENA and SIENAX: the intermediate results of brain extraction, image registration, and segmentation were visually examined in all cases, blinded to the result of analysis. In the case of incomplete segmentation or poor registration the brain mask was manually adjusted, either by incremental modification of BET settings or by manual editing. Manual adjustment has been shown to improve the accuracy of fully automated SIENA without introducing significant variability (159). In any cases where BET was adjusted in SIENA, the same modifications were made in SIENAX.

For LST: The lesion map was visually examined in combination with the FLAIR to ensure the appropriateness of classification. In the case of inappropriate classification, the initial threshold value was manually adjusted, and the adjustment applied to both timepoints.

For PropSeg: the segmented spinal cord mask was visually examined in all cases, and manually edited where required.

3.3.4 Clinical measures of disease progression

Clinical data collection was performed by trained examiners at recruitment and every 6 months thereafter. The majority by of assessments were conducted by Monica Fenn (Research Nurse) and Elizabeth Jarman (Research Physiotherapist, both R&D Department, University Hospital Southampton NHS Foundation Trust), and a smaller number of assessments were conducted by me. These comprised a range of validated assessments chosen to capture the breadth of MS disability (more details in Appendix C):

- Expanded Disability Status Scale (EDSS), the most widely used scale for this purpose (160), though heavily biased towards spinal disease and ambulation restriction (161). Higher scores reflect greater disability due to MS. Scores 0-3.5 reflect full ambulation, 4.0-6.5 independent ambulation with restriction, and ≥7.0 inability to walk.
- Multiple Sclerosis Functional Composite (MSFC), combining the 9-hole peg test (9HPT), timed 25-foot walk (T25FW), and Paced Auditory Serial Addition Test (PASAT), and providing a more global picture of upper limb function, lower limb function, and cognition, respectively (162). Values are standardised as z-scores according to the group baseline mean, where the units are standard deviations from the group mean. More negative scores reflect greater relative disability.
- Multiple Sclerosis Impact Scale (MSIS-29), a patient-reported scale designed to capture the physical (20 questions) and psychological (9 questions) impact of MS (163). Each set of questions has five response options, and the summed result of each set is scaled to give a score out of 100. Higher scores reflect greater impact.
- Chalder fatigue scale (FS), a patient-reported scale measuring the severity of both physical and mental fatigue (164), disabling symptoms in MS. 11 items are scored on a scale with up to 3 points each, giving a combined maximum score of 33. Higher scores reflect greater fatigue.
- Beck Depression Inventory (BDI) was also performed as depression is common in MS (165) and can affect performance on other tests, especially cognitive. 21 items are scored on a scale with up to 3 points each, giving a combined maximum score of 63. Higher scores reflect greater severity of depressive symptoms.

For the above clinical scores, change variables were computed as:

- Annualised difference between value at study entrance and exit.
- Presence or absence of a clinically meaningful change. For EDSS, defined as an increase by 1 point if baseline EDSS ≤5.5 or by 0.5 points if baseline EDSS >5.5, which is the standard definition used in clinical trials for example that of ocrelizumab (166); for MSFC a decrease of 20% in combined score or in an individual component (167); for MSIS-physical an increase of 7 points (168); for MSIS-psychological an increase of 6 points (169). To control for between-participant differences in follow-up duration, all scores were normalised to a per-protocol duration of 2.5 years before binarisation.

3.4 Methods

3.4.1 Study design

Participant flow through the study is outlined in Figure 15. Baseline activities in the first month were split over three separate visits to increase tolerability. After screening, eligible participants were invited to a clinic visit (week 1) to receive detailed verbal and written information about the study. If happy to proceed the participant returned one week later (week 2) to complete: written consent, baseline clinical data collection (split over two weeks), weekly online diary, and urine collection, MRI safety screening, and practice of visit procedures. At the week 3 clinic visit remaining clinical data collection was completed, and the urine collection kit was provided to begin weekly collection. Participants returned at 3-monthly intervals for return of stored urine samples and provision of new kit, and at 6-monthly intervals for repeat clinical data collection (detailed description in Section 3.3.3; again, split over two weeks for tolerability).

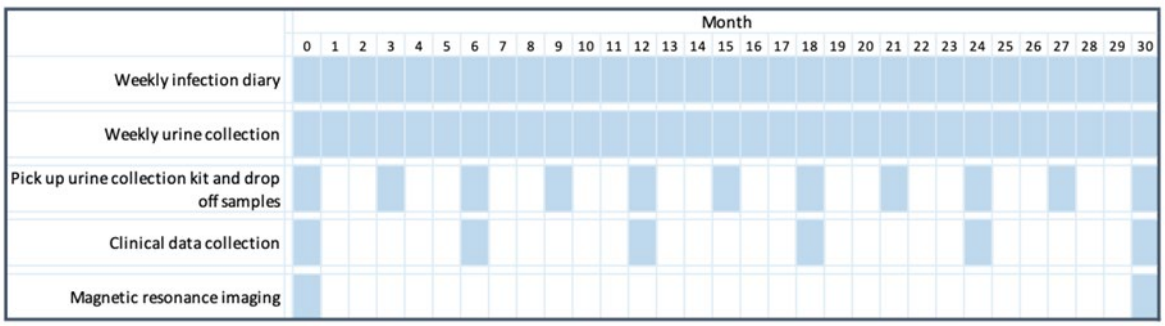

Figure 15 Gantt chart showing SIMS study activities.

Clinical data collection comprised the clinical measures of disease progression (detailed above) in addition to the following: age, sex, ethnicity, MS disease classification, MS disease duration, weight (kg), height (cm), handedness, smoking history, drug history especially usage of statins, which have been shown to slow brain atrophy (170), past medical history including detailed inventory of chronic inflammatory conditions, and urine symptom questionnaire.

The study entrance MRI was performed shortly after recruitment, and the study exit MRI at 2.5 years. For participants withdrawing from the study early, the study exit MRI was performed before withdrawal if possible. Participants who wished to remain on the study for a 6-month extension could do so.

3.4.2 Ethical approval

The study was approved by the National Research Ethics Service Committee South Central – Hampshire B (reference 12/SC/0176) and by the institutional review board (ERGO 5562). Experiments were conducted in accordance with the Declaration of Helsinki and all subjects gave informed written consent.

3.4.3 Participants

Eligible participants were adults aged >18 with a diagnosis of progressive MS according to the 2017 revisions of the McDonald criteria (171) (primary progressive MS or secondary progressive MS without superimposed relapses), and availability of a home freezer for storing urine samples. To minimise skewing of recruitment to an older and more disabled cohort (and thus maximise the chances of detecting significant changes in measures of disease progression), eligible participants aged ≥60 or with EDSS score ≥6.0 were initially held in reserve. Exclusion criteria were use of disease-modifying or immunosuppressive treatment in the last 6 months, or pregnancy.

The study setting was the Wessex region of southern England (the counties of Hampshire, Dorset, Wiltshire, and West Sussex), with a combined population of approximately 3.2 million (172). According to the latest UK prevalence figures (173) this would suggest a population of just under 6000 individuals with MS in the study region. Participants were recruited by (1) referrals from neurologists and MS nursing teams in hospital and community settings, and (2) advertisement through local branches of the MS Society, MS Trust, and MS therapy centres as well as through electronic media. All study visits were conducted at either University Hospital Southampton NHS Foundation Trust or Poole Hospital NHS Foundation Trust.

3.4.4 Sample size

As this was a pilot study addressing a novel hypothesis, an estimate of effect size could not be obtained from the literature. However, pooled data for brain atrophy in progressive MS indicated that if the cohort were divided into two equal-sized groups based on exposure one would require a sample size of 56 over 2 years to detect a 50% difference with 80% power (174).

3.4.5 Statistical analysis

The pre-specified primary outcome was brain atrophy, while the other outcomes were secondary. A priori, the data was to be analysed by grouping of study participants into high and low inflammatory responders to enable between-group comparisons of outcome measures.

$P < 0.05$ was used to reject the null hypothesis though individual P values in the region of 0.05 were considered modest degrees of evidence, whichever side of the threshold (175).

All statistical analyses in this and further chapters were conducted using SPSS version 24 (IBM Corp., Armonk, NY, USA). Frequency distributions, normal probability plots and Kolmogorov–Smirnov testing were used to test for normal distribution of raw or logarithmically transformed data.

3.4.6 Testing of SIENA-ZEFRAM

In a sub-study, the performance of the ZEFRAM modification to SIENA was tested by examining the correlation of brain atrophy progression to clinical progression. Atrophy measurements by the SIENA-ZEFRAM method were compared against the two methods commonly used in the literature, namely SIENA with the Popescu optimisations alone (127), or with Popescu optimisations and lesion filling (132). The results are shown in Appendix D.

3.5 Results

3.5.1 Participants

In total 53 participants completed the study and were included in the final analysis. Eligible participants were recruited from April 2013 to September 2017. The last visit of the last participant was in August 2020. One participant completed the study but was excluded from the analysis as they developed aggressive relapsing MS shortly after study exit and their eligibility was revised. The STROBE diagram (176) for the study is shown in Figure 16.

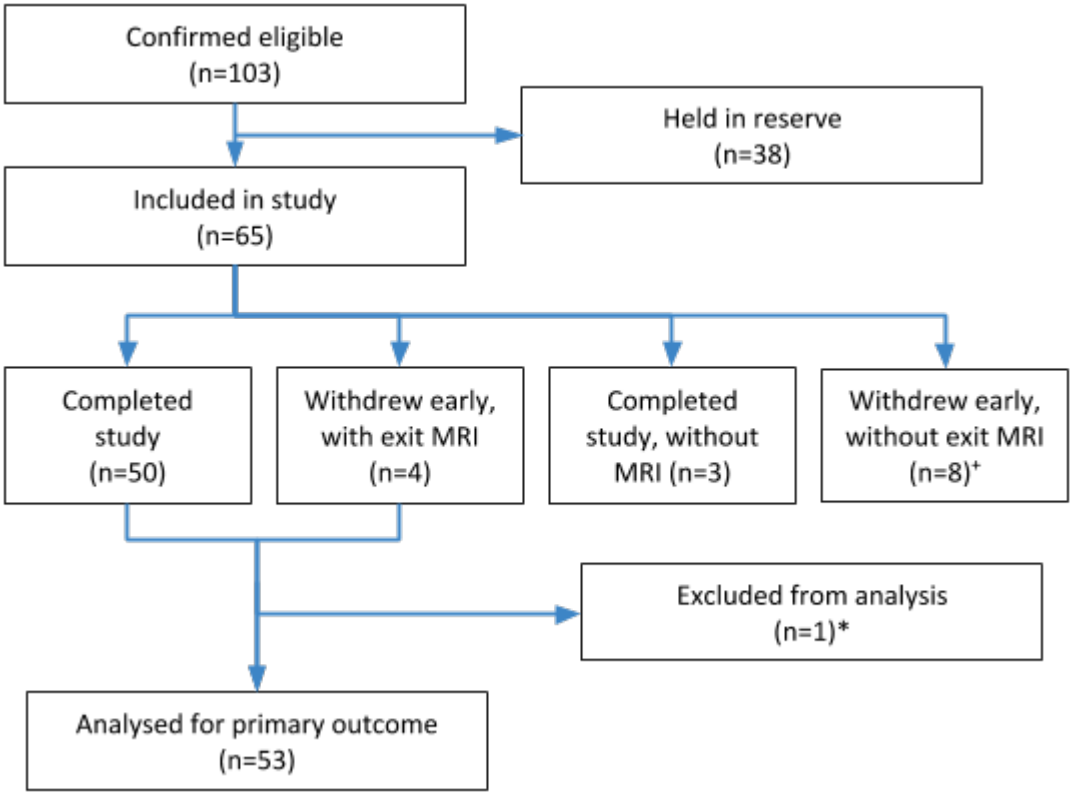

Figure 16 Path of all eligible and recruited participants through the SIMS study.

* 1 participant developed aggressive relapsing MS shortly after study exit and was excluded from the analysis due to revision of their eligibility. + includes one participant who died.

3.5.2 Adverse events

One participant died unexpectedly after one month on the study. This was classed as an unrelated serious adverse event, and their data was not included in the analysis.

3.5.3 Data quality

Since the primary outcome was brain atrophy, study entrance and exit dates for each participant were determined according to dates of baseline and follow-up MRI scans. Mean follow-up duration was 2.5 years (range 1.3-3.2 years). 50 (94%) participants achieved at least 2 years of follow-up, and 39 (74%) participants achieved at least 2.5 years of follow-up. The completion rates for all outcome measures are outlined in Table 3, and described in more detail below.

Table 3 Number (percent) of participants with complete data for outcome measures.

For clinical measures missing data were imputed from recent assessment if available; the number imputed in this way is shown in square brackets. In the 'both timepoints' column participants with imputed data are counted as complete.
EDSS = Expanded Disability Status Scale, MSFC = Multiple Sclerosis Functional Composite, MSIS = Multiple Sclerosis Impact Scale, FS = Fatigue Scale, BDI = Beck Depression Inventory.

Data source	**Baseline**	**Follow-up**	**Both timepoints**
Radiological progression measures			
Brain atrophy	n/a	n/a	53 (100%)
Regional brain volumes	53 (100%)	53 (100%)	53 (100%)
Lesion measures	53 (100%)	53 (100%)	53 (100%)
Spinal cord area	52 (98.1%)	52 (98.1%)	51 (96.2%)
Clinical progression measures			
EDSS	50 (94.3%) [3]	50 (94.3%) [1]	51 (96.2%)
MSFC	53 (100%)	51 (96.2%) [2]	53 (100%)
MSIS-29	52 (98.1%) [1]	53 (100%)	53 (100%)
FS	53 (100%)	53 (100%)	53 (100%)
BDI	53 (100%)	53 (100%)	53 (100%)

71.7% of participants achieved the target diary completion rate of 75%. Mean diary completion rate was 80.0%. 90.6% of participants achieved the target urine collection completion rate of 75%; mean collection rate was 87.4%.

2 participants required recall for a repeat imaging session, in both cases for repeat spinal cord imaging.

SIENA/SIENAX: Grey-white matter contrast was good in all MP-RAGE images. The Popescu (127) recommendations for BET require extreme tolerances, and in this cohort 32 (60%) of cases were found to be sub-optimal during manual quality control. In all these cases brain extraction was too conservative, leaving large amounts of non-brain tissue which later confounded FAST

segmentation, and therefore atrophy measurement. All cases achieved satisfactory results after manual adjustment.

LST: CSF suppression and lesion contrast were good in all FLAIR images. The recommended initial threshold (κ= 0.3) was suitable in all cases. During initial study set-up FLAIR sequences were omitted in 6 participants at the first timepoint; in these cases, a lesion mask was manually created on the T_2 image using FSLeyes (177) and used for lesion filling and black hole detection. For consistency, in these cases manual lesion segmentation was used at both timepoints (even though FLAIR images were available for all cases at the second timepoint). Manual lesion masking was conducted in a randomised order, maintaining blinding as to subject and timepoint. A comparison of cases with manual versus automatic lesion segmentation showed no significant difference in baseline lesion volume (4.2 vs 6.2 ml, P=0.54, t-test) but a trend to lower lesion count (11.2 vs 20.1, P=0.06, t-test) in manual cases.

PropSeg: In a randomly selected sample of spinal cord images (n=5), contrast-to-noise ratio (CNR) between spinal cord and surrounding CSF was approximately 5:1, less than in other reports (153) though the algorithm performed well overall. The quality of segmentation was good in 51 (96%) cases, however, in 2 (4%) cases an acceptable segmentation could not be achieved; one due to poor CNR and one due to movement artefact. In 31 (58%) cases manual editing was required, and in 9 (17%) cases the automating vertebral labelling failed and was done manually.

3.5.4 Baseline clinical and radiological data

Baseline descriptive data for the study group are given in Table 4 and Table 5. Values for MSFC are not shown in Table 4, as this measure was expressed as a z-score calculated using the baseline mean. Hence the whole group mean z-score was by definition zero and conveys no information. There was no significant difference in group means between PPMS and SPMS (P = 0.62, t-test).

Compared to the PPMS group, the SPMS group had significantly more females (36.7 vs 82.6%, P = 0.0008, Fisher's exact test) and longer disease duration (9.4 vs 16.8 years, P = 0.001, t-test). The SPMS group also experienced greater psychological impact (MSIS-Psych 19.8 vs 16.0, P = 0.02, t-test) and fatigue (FS 17.3 vs 14.0, P = 0.05, t-test), and there was a trend for greater depression scores (BDI, 6.4 vs 4.1, P = 0.08, t-test). There were also trends for higher EDSS (5.4 vs 6.0, P = 0.07, t-test), lesion count (17.2 vs 22.8, P = 0.10, t-test), and black hole volume in SPMS (2.9 vs 5.8 ml, P = 0.06, t-test), and lower WM volume (0.68 vs 0.66 litres, P =0.10, t-test).

Table 4 Baseline demographic and clinical data for the SIMS study.

For scalar variables, values are mean (SD). Percentages are rounded.
PPMS = primary progressive multiple sclerosis, SPMS = secondary progressive multiple sclerosis, EDSS = Expanded Disability Status Scale, MSFC = Multiple Sclerosis Functional Composite, MSIS = Multiple Sclerosis Impact Scale, FS = Fatigue Scale, BDI = Beck Depression Inventory.

Variable	**PPMS group (n=30)**	**SPMS group (n=23)**	**Whole group (n=53)**	**P-value for PPMS vs SPMS**
Demographics				
Age (years)	54.0 (9.9)	53.3 (4.6)	53.7 (8.0)	0.73
Sex (% female)	36.7	82.6	56.6	0.0009
MS disease duration (years)	9.4 (8.1)	16.8 (7.4)	12.6 (8.6)	0.001
Body mass index (kg/m2)	28.3 (5.2)	28.1 (6.9)	28.2 (5.9)	0.88
Smoker (%)	16.7	8.7	13.2	0.92
Statin use (%)	33.3	26.1	30.2	0.75
Co-morbidities (%)	20.0	21.7	20.8	0.57
Clinical measures				
EDSS (points)	5.4 (1.6)	6.0 (0.8)	5.9 (1.3)	0.07
MSIS-Phys (points)	46.6 (14.1)	50.1 (12.0)	48.2 (13.2)	0.33
MSIS-Psych (points)	16.0 (5.4)	19.8 (5.7)	17.7 (5.8)	0.02
FS (points)	14.0 (6.3)	17.3 (5.6)	15.5 (6.2)	0.05
BDI (points)	4.1 (4.2)	6.4 (4.8)	5.1 (4.6)	0.08

Table 5 Baseline radiological data for the SIMS study.

Values are mean (SD).

Variable	**PPMS group (n=30)**	**SPMS group (n=23)**	**Whole group (n=53)**	**P-value for PPMS vs SPMS**
Normalised brain volumes (l)				
- Whole brain	1.43 (0.07)	1.42 (0.06)	1.43 (0.07)	0.65
- Grey matter	0.75 (0.06)	0.76 (0.05)	0.76 (0.05)	0.63
- White matter	0.68 (0.03)	0.66 (0.03)	0.67 (0.03)	0.10
- Cortical grey matter	0.59 (0.05)	0.60 (0.04)	0.60 (0.04)	0.63
- Ventricles	0.06 (0.03)	0.06 (0.02)	0.06 (0.03)	0.76
Lesion count	17.2 (11.4)	22.8 (12.2)	19.7 (12.0)	0.10
Lesion volume (ml)	4.2 (6.5)	7.1 (7.0)	5.5 (6.8)	0.13
Black hole volume (ml)	2.9 (4.6)	5.8 (6.2)	4.2 (5.5)	0.06
Cervical cord area (mm^2)	59.7 (7.9)	60.9 (5.8)	60.2 (7.0)	0.55

Both physician- and patient-reported clinical measures of disability correlated well with each other, as shown in Table 6.

Table 6 Correlation matrix between baseline clinical measures of disability in the SIMS study.

Values are correlation coefficient and *P*-value, all by Spearman's rank test. All values were significant ($P < 0.05$); cells are colour-coded according to the strength of correlation (at intervals of r > 0.3, 0.5, or 0.7). EDSS = Expanded Disability Status. MSFC = Multiple Sclerosis Functional Composite. MSIS = Multiple Sclerosis Impact Scale (-Phys = Physical subscore, -Psych = Psychological subscore). FS = Fatigue Scale. BDI = Beck's Depression Inventory. For MSFC, more negative scores reflect more severe disability.

Variable	EDSS	MSFC	MSIS-Phys	MSIS-Psych	FS	BDI
EDSS		-0.48 0.0003	0.616 <10-6	0.36 0.007	0.34 0.01	0.34 0.01
MSFC	-0.48 0.0003		-0.61 10-6	-0.38 0.004	-0.44 0.001	-0.30 0.03
MSIS-Phys	0.62 <10-6	-0.61 10-6		0.65 <10-6	0.61 10-6	0.59 <10-5
MSIS-Psych	0.36 0.007	-0.38 0.004	0.65 <10-6		0.74 <10-9	0.75 <10-9
FS	0.34 0.01	-0.44 0.001	0.61 10-6	0.74 <10-9		0.53 <10-4
BDI	0.34 0.01	-0.30 0.03	0.59 <10-5	0.75 <10-9	0.53 <10-4	

Median brain volume was significantly lower in smokers compared to non-smokers (1.37 vs 1.44 litres, P = 0.02, t-test). Lesion volumes and counts were significantly negatively correlated with brain volume (for lesion volume: ρ = -0.43, P = 0.001, for lesion count: ρ = -0.35 , P = 0.01, all Spearman's). In a multiple linear regression 41% of the variance in brain volume could be explained by age, gender, EDSS, lesion volume, and disease duration (see Table 7).

Table 7 Multivariable regression of predictors of baseline brain volume.

Unadjusted r^2 of the whole model was 0.41. Regression method was 'enter'.
EDSS = Expanded Disability Status Scale.

Predictor	**β**	**P-value**
Age, per year	-0.30	0.02
Female sex	0.32	0.02
Lesion volume, per ml	-0.37	0.004
EDSS, per point	-0.08	0.53
Disease duration, per year	-0.15	0.27
Whole model		0.0001

Total brain volume or spinal cord area were not correlated with any of the clinical measures of disability. There were trends for cortical volume correlation with MSFC, MSIS-Phys, and FS. In contrast, lesion measures were strongly correlated with many clinical measures of disability, including MSFC, MSIS-Phys, and MSIS-Psych , as shown in Table 8.

Mean BMI was significantly higher in statin users than in non-users (31.7 vs 26.7, P = 0.004, t-test).

Statin use itself was not associated with any significant difference in brain volume (P = 0.34, t-test), though there was modest evidence for slightly lower cortical grey matter volume in statin users (0.58 vs 0.60 litres, P = 0.07, t-test);

Table 8 Correlation matrix between radiological and clinical measures of disability.

Values are correlation coefficient and P-value, all by Spearman's rank test. Significant correlations (P<0.05) are flagged in red. EDSS = Expanded Disability Status. MSFC = Multiple Sclerosis Functional Composite. MSIS = Multiple Sclerosis Impact Scale (-Phys = Physical subscore, -Psych = Psychological subscore). FS = Fatigue Scale. BDI = Beck's Depression Inventory.

Radiological measure	**EDSS**	**MSFC**	**MSIS-Phys**	**MSIS-Psych**	**FS**	**BDI**
Brain volume	-0.18 0.20	0.20 0.23	-0.16 0.24	-0.06 0.24	-0.21 0.14	-0.05 0.72
GM volume	-0.19 0.23	0.21 0.13	-0.22 0.12	-0.13 0.36	-0.21 0.13	-0.14 0.33
WM volume	-0.10 0.49	0.03 0.83	0.02 0.91	0.07 0.63	-0.09 0.52	0.06 0.67
Cortical volume	-0.17 0.22	0.23 0.09	-0.26 0.06	-0.13 0.37	-0.24 0.09	-0.18 0.21
Lesion count	0.13 0.34	-0.42 0.002	0.33 0.02	0.29 0.04	0.23 0.10	0.16 0.25
Lesion volume	0.14 0.32	-0.42 0.002	0.30 0.03	0.27 0.05	0.28 0.05	0.20 0.16
Black hole volume	0.14 0.34	-0.44 0.001	0.30 0.03	0.26 0.06	0.27 0.06	0.17 0.23
Spinal cord area	-0.07 0.64	0.09 0.53	-0.09 0.56	0.20 0.17	0.06 0.67	0.07 0.63

3.5.5 Clinical and radiological progression during follow-up

The study group was examined for evidence of brain atrophy during the follow-up period, as well as evidence of progression in the secondary outcome measures. The group mean annualised brain volume change was -0.43%, and significantly less than zero ($P = 10^{-10}$, one sample t-test). Based on the reported pathological cut-offs for brain atrophy rate (178), 25 (47.2%), 20 (37.7%), and 16 (30.2%) of participants were in the pathological range at specificity levels of 80%, 90%, and 95% respectively. The group means for the other radiological measures are shown in Table 9. There were no differences between groups for any of the measures.

Table 9 Radiological progression during follow-up.

All values are annualised group mean (standard deviation).

Radiological measure of change	**PPMS group (n=30)**	**SPMS group (n=23)**	**Whole group (n=53)**	**P-value for PPMS vs SPMS**
Brain volume (%/year)	-0.43 (0.39)	-0.42 (0.37)	-0.43 (0.38)	0.97
Lesion volume (ml/year)	0.19 (0.37)	0.16 (0.70)	0.17 (0.53)	0.86
Lesion count (lesions/year)	0.40 (2.10)	0.02 (1.59)	0.23 (1.89)	0.46
Black hole volume (ml/year)	0.07 (0.31)	0.11 (0.68)	0.09 (0.50)	0.80
Spinal cord cross-sectional area (%/year)	-2.1 (2.0)	-2.4 (1.8)	-2.3 (1.9)	0.63

For the cross-sectional measures, pairwise testing (t-test) of entrance and exit values (uncorrected for between-participant differences in follow-up duration) showed significant increases in ventricular volume (56.1 vs 58.4 ml, $P < 10^{-5}$) and lesion volume (5.5 vs 6.8 ml, $P = 0.02$), and a decrease in spinal cord area (60.2 vs 56.8 mm^2, $P < 10^{-10}$). There was a trend for a decrease in grey matter volume (0.76 vs 0.75 litres, $P = 0.07$). Similarly, the annualised percentage change in these measures was significantly different from zero (one-sample t-test) for ventricular volume ($P < 10^{-5}$), lesion volume ($P = 0.02$), and spinal cord area ($P < 10^{-10}$).

In a stepwise multivariable linear regression with brain atrophy rate as outcome and age, gender, disease duration, disease category, smoking, BMI, and statin use as predictors, and either baseline EDSS, MSFC, or brain volume as predictors representing disease severity, only baseline MSFC ($\beta = 0.22$, $P = 0.003$, i.e. less severe disability predicts slower brain atrophy) remained in the final model, which explained 16% of the variance in atrophy rate.

Group values for the annualised change clinical progression measures are shown in Table 10.

Table 10 Group values for annualised change in clinical progression measures.

Values are mean (SD). For MSFC and SC, negative values reflect worsening. EDSS = Expanded Disability Status Scale, MSFC = Multiple Sclerosis Functional Composite, MSIS = Multiple Sclerosis Impact Scale, FS = Fatigue Scale, BDI = Beck Depression Inventory.

Clinical measure	**PPMS group (n=30)**	**SPMS group (n=23)**	**Whole group (n=53)**	**P-value for PPMS vs SPMS**
EDSS (points)	0.2 (0.3)	0.0 (0.4)	0.1 (0.3	0.22
MSFC (z-score)	-0.4 (0.7)	-0.1 (0.3)	-0.3 (0.6)	0.04
MSIS-Phys (points)	1.2 (3.3)	0.5 (3.5)	0.9 (3.4)	0.50
MSIS-Psych (points)	0.7 (2.1)	0.1 (2.0)	0.4 (2.1)	0.32
FS (points)	0.9 (2.5)	-0.1 (2.2)	0.5 (2.4)	0.12
BDI (points)	0.3 (1.5)	-0.3 (1.5)	0.0 (1.5)	0.17

Progression in MSFC was significantly worse in the PPMS group compared to the SPMS group (change in z-score -0.4 vs -0.1, P = 0.04, t-test, Cohen's d = 0.57).

Clinically important progression in EDSS (as defined in Section 3.3.4) occurred in 30 (56.6%) participants. The number of participants with a clinically important progression in clinical measures is shown in Table 11.

Table 11 Proportion of participants with clinically important progression in secondary outcome measures.

Values are number (%).
EDSS = Expanded Disability Status Scale, MSFC = Multiple Sclerosis Functional Composite, MSIS = Multiple Sclerosis Impact Scale, FS = Fatigue Scale, BDI = Beck Depression Inventory.

Clinical measure	**PPMS group (n=30)**	**SPMS group (n=23)**	**Whole group (n=53)**	**P-value for PPMS vs SPMS**
EDSS	18 (60.0)	12 (52.2)	30 (56.6)	0.72
MSFC	19 (63.3)	11 (47.8)	30 (56.6)	0.72
MSIS-Phys	7 (23.3)	4 (17.4)	11 (20.8)	0.78
MSIS-Psych	5 (16.7)	2 (8.7)	7 (13.2)	0.88
FS	16 (53.3)	11 (47.8)	27 (50.9)	0.69
BDI	4 (13.3)	2 (8.7)	6 (11.3)	0.83

As shown in Table 12, there was a significant positive correlation between brain atrophy and MSFC progression rate (for both variables, more negative values imply faster progression). There was also a trend for correlation between spinal cord atrophy and EDSS progression rate (for spinal cord atrophy more negative values imply faster progression, whereas for EDSS the converse is true).

Table 12 Correlation matrix between longitudinal clinical and radiological measures of progression.

All variables are annualised measured of change over time.
Values are correlation coefficient and P value, all by Spearman's.
EDSS = Expanded Disability Status Scale, MSFC = Multiple Sclerosis Functional Composite, MSIS = Multiple Sclerosis Impact Scale, FS = Fatigue Scale, BDI = Beck Depression Inventory.

	Brain atrophy	**Lesion volume change**	**Lesion count change**	**Black hole volume change**	**Spinal cord area change**
EDSS change	0.02 0.88	-0.05 0.71	0.04 0.76	0.09 0.54	-0.26 0.07
MSFC change	0.38 0.005	0.14 0.33	-0.02 0.89	0.15 0.30	0.09 0.53
MSIS-Phys change	-0.07 0.64	-0.08 0.55	0.13 0.37	0.007 0.96	0.04 0.76
MSIS-Psych change	-.11 0.45	-0.14 0.31	-0.05 0.72	-0.09 0.54	0.11 0.45
FS change	-0.13 0.36	0.35 0.01	0.14 0.33	0.31 0.03	0.03 0.83
BDI change	-0.15 0.28	-0.24 0.09	0.07 0.63	-0.07 0.62	-0.04 0.80

3.5.6 Inflammatory episodes and systemic inflammatory response

A total of 463 unique inflammatory episodes were recorded, an average of 8.7 per participant. After correcting for differences in follow-up duration, the mean annualised episode rate was 3.3

(SD = 2.1) per year. Infections were the most frequent episodes (365 reported episodes, 78.8% of total). The breakdown of episode types and their annualised rates are shown in Table 13. There were no significant differences between PPMS and SPMS groups, apart from a trend for more frequent vaccination in the PPMS group (0.7 vs 0.5 per year, P = 0.07, t-test, Cohen's d = 0.5). When classified by site, the most frequent infections were upper respiratory (35.8%), lower respiratory (14.8%), skin (12.6%), bladder (11.2%), and gastrointestinal (10.4%).

Table 13 Annualised rate of reported systemic inflammatory events.

Values are group mean (SD). Visceral infections are lower respiratory tract or bladder.

Episode type	PPMS group (n=30)	SPMS group (n=23)	Whole group (n=53)	P-value for PPMS vs SPMS
All episodes	3.2 (2.0)	3.4 (2.2)	3.3 (2.0)	0.73
Infections	2.4 (1.8)	2.9 (2.3)	2.6 (2.0)	0.37
Visceral infections	0.6 (0.9)	0.8 (0.9)	0.7 (0.9)	0.66
Antibiotic infections	0.3 (0.4)	0.4 (0.8)	0.3 (0.6)	0.56
Vaccinations	0.7 (0.5)	0.5 (0.4)	0.6 (0.5)	0.07
Other	0.1 (0.2)	0.0 (0.1)	0.2 (0.2)	0.40

In the analysis of longitudinal UNCR data, mean (SD) peak height during at-risk periods (considering all episode types and excluding reported episodes without peaks) was 99.4% (78.0%). There was no significant difference between PPMS and SPMS groups (93.6 vs 102.6, P = 0.68, t-test).

In a one-way ANOVA there was no significant difference in mean peak height between categories of systemic inflammatory episode (P = 0.08), however for categories other than infections, most participants reported no episodes during the study period. Although the mean peak height was higher for infections requiring antibiotics compared to all episodes, this was not significant (203.0 vs 99.4%, P = 0.10, Tukey's post-hoc test).

Mean (SD) baseline UNCR (outside at-risk periods) was 189.7 (49.9) µmol/mol. In a linear regression, baseline UNCR was found to increase with age (P = 0.04, β = 0.27), with a trend for an additional effect of disease severity (assessed by MSFC, P = 0.06, β = -0.26).

Table 14 Comparison of UNCR peak heights between systemic inflammatory episode categories.

There was no significant difference between categories in a one-way ANOVA (P = 0.08). P-values shown here are from a Tukey post-hoc test comparing episode categories to all episodes.

Episode type	**Mean (SD) peak height (%)**	**P-value for comparison to all episodes**	**Number (%) of participants reporting at least one episode**
All episodes	99.4 (78.0)	-	49 (92.5)
Infections	110.5 (88.2)	0.99	49 (92.5)
Visceral infections	139.1 (158.5)	0.82	25 (47.2)
Antibiotic infections	203.0 (293.3)	0.10	14 (26.4)
Vaccinations	88.8 (129.2)	0.99	25 (47.2)
Other	45.1 (20.2)	0.95	6 (11.3)

Participants were divided into two equal-sized groups based on peak height, with a cut-point at the median value (73.1%), resulting in two groups with high and low inflammatory responses. There were no significant differences in baseline variables between the 'high response' and 'low response' groups, as shown in Table 15. There was no significant difference in baseline MSFC between the two groups (0.0 vs 0.1, P = 0.35, t-test).

Table 15 Comparison of baseline variables between high and low response groups.

Continuous variables by t-test, categorical by Fisher's exact test.
EDSS = Expanded Disability Status Scale, MSFC = MS Functional Composite, MSIS = MS Impact Scale, FS = Fatigue Scale, BDI = Beck Depression Inventory.

Variable	**Low response (n = 27)**	**High response (n = 26)**	**P-value**
Age (years)	55.3	52.0	0.15
Sex (% female)	55.6	57.7	0.55
Disease category (% SPMS)	52.2	47.8	0.55
MS disease duration (years)	12.0	13.3	0.60
Body mass index (kg/m2)	27.9	28.5	0.74
Smoker (%)	18.5	7.7	0.42
Statin use (%)	37.0	23.1	0.37
Inflammatory co-morbidities (%)	22.2	19.2	0.53
EDSS (points)	5.5	5.8	0.50
MSIS-Phys (points)	47.3	49.0	0.65
MSIS-Psych (points)	16.6	18.8	0.18
Fatigue score (points)	15.4	15.5	0.97
BDI (points)	5.5	4.8	0.57
Whole brain volume	1.43	1.43	0.81
Grey matter volume	0.76	0.76	0.71
White matter volume	0.68	0.67	0.28
Cortical grey matter volume	0.59	0.60	0.40
Ventricular volume	0.06	0.06	0.77
Lesion count	17.1	22.3	0.11
Lesion volume (ml)	5.0	6.0	0.58
Black hole volume (ml)	3.6	4.7	0.49
Cervical cord area (mm^2)	59.1	61.4	0.23

The frequency of visceral (versus non-visceral) infection was not significantly higher in the high response group compared to the low response group (0.45 vs 0.32 episodes/year, P = 0.46, 95% CI for difference -0.53-0.24), though there was a trend for more frequent antibiotic-requiring infections in the high response group (0.35 vs 0.10 episodes/year, P = 0.08, 95% CI 0.53-0.02; both t-test).

3.5.7 Brain atrophy and systemic inflammation

The primary hypothesis was tested using a factorial ANCOVA with annualised brain atrophy rate as the outcome (Table 16). The exposure variables were the host systemic inflammatory response (high or low responder) and the annualised rate of systemic inflammatory episodes (discounting reported episodes without UNCR peaks, as discussed in Section 3.3.2). To adjust for confounding the following variables were also included in the model: statin use, smoking, gender, baseline MSFC, and age. MSFC was chosen (over EDSS) to represent baseline disability due to the superior predictive value for longitudinal brain atrophy in this dataset.

Adjusted for confounders, brain atrophy rate was significantly faster in the high response group compared to the low response group (-0.59 vs -0.37 %/year, P =0.02, partial η^2 = 0.12). The adjusted difference between groups was 0.23%/year (95% CI 0.04 to 0.42%). This equates to a 62% faster brain atrophy rate in the high response group. There was no significant effect of episode rate (P = 0.56). The final model explained 20% of the variance in brain atrophy. There was also a highly significant effect of baseline disability measured by MSFC (P = 0.004, partial η^2 = 0.17). Restricting the analysis to the high response group only, episode rate remained non-significant but showed a trend towards greater brain atrophy with more frequent episodes (P = 0.07, partial η^2 = 0.16).

The model was robust to removing all non-significant confounding variables; in an ANCOVA with brain atrophy as outcome, exposure variables of response group and episode rate, and baseline MSFC as covariate, response group remained significant (P = 0.03, partial η^2 = 0.09) as did baseline MSFC (P = 0.003, partial η^2 = 0.16, overall model r^2 = 0.19). The estimated marginal mean difference between groups in this model was 0.21%/year (95% CI 0.02-0.39).

Table 16 ANCOVA showing the effect of systemic inflammatory response group on brain atrophy rate.

Adjusted r^2 of the model was 0.20.

MSFC = Multiple Sclerosis Functional Composite.

Variable	**P-value**	**Partial η^2**
High/low inflammatory response group	0.02	0.12
Episode rate	0.56	0.008
Age	0.99	$<10^{-7}$
Gender	0.30	0.02
Baseline MSFC	0.004	0.17
Statin use	0.35	0.02
Smoking	0.74	0.002

In a sensitivity analysis, the study group was divided into brain atrophy progressors and non-progressors according to the reported cut-off (-0.40%/year) at the 80% specificity level (178). In a binary logistic regression with brain atrophy progression status as dependent and including the same variables as in the full model above, response group significantly predicted progression status (P = 0.01, method 'enter'). The odds ratio for progression in the high response group compared to the low response group was 9.6 (95% CI 1.7-53.8, model Nagelkerke pseudo-r^2 = 0.47). Baseline MSFC remained a significant predictor of progression status (P = 0.006). The analysis was repeated adjusting the cut-off to the 90 and 95% specificity levels (-0.46 and 0.52%/year respectively); the effect of response group was greater at the 90% level (P = 0.01, OR = 11.1) and greater still at the 95% level (P = 0.004, OR = 21.6). No other variables were significant.

Mean baseline UNCR (outside of at-risk periods) did not predict brain atrophy rate when used instead of response group in the primary analysis, either as a continuous variable (P = 0.49, partial η^2 = 0.01), or when dichotomised (P = 0.16, partial η^2 = 0.04). There was no significant difference in mean baseline UNCR between brain atrophy progressors and non-progressors (P =0.82, t-test).

In another sensitivity analysis, the study population was divided into two subgroups by disease severity (using the customary EDSS threshold of greater than or equal to 6.0, the level above which individuals require assistance with walking), and the primary analysis was repeated within

each subgroup. In individuals with restricted walking, brain atrophy was more pronounced in people with a high (versus low) inflammatory response (n= 41, P = 0.02, partial η^2 = 0.15), whereas this effect was not seen in less disabled people (n = 12, P = 0.52, partial η^2 = 0.11). Raising the EDSS threshold to 6.5 (requirement for constant bilateral walking assistance) made the effect more pronounced (n = 19, P = 0.004, partial η^2 = 0.55). In these individuals, being in the high response group was associated with a 2.4-fold increase in brain atrophy rate (estimated marginal means -0.74 vs -0.31 %/year). Mean baseline UNCR was not significantly higher in individuals with restricted walking at either the EDSS 6.0 (177.8 vs 193.2, P = 0.32,) or EDSS 6.5 (181.8 vs 203.9, P = 0.15, both t-test) thresholds. Mean peak height was also no different in the more disabled individuals (by EDSS 6.0 threshold 93.3 vs 91.5%, P = 0.92; by EDSS 6.5 threshold 85.4 vs 103.5%, P = 0.49, both t-test).

3.5.8 Secondary clinical outcomes and systemic inflammation

The analysis was repeated replacing brain atrophy rate with the secondary clinical outcomes. Response group did not have a significant effect on any of the clinical outcomes in any of these analyses (Table 17).

Table 17 No associations between systemic inflammation and secondary clinical outcomes.

Change in the clinical scores was examined against systemic inflammatory response group and episode rate. All episodes were considered. In the logistic regression, progression status was binarized according to the cut-off of -0.52%/year.
EDSS = Expanded Disability Status Scale, MSFC = Multiple Sclerosis Functional Composite, MSIS = Multiple Sclerosis Impact Scale, FS = Fatigue Scale, BDI = Beck Depression Inventory.

Change variable	**ANCOVA with dependent as brain atrophy rate**		**Logistic regression with dependent as progression status**	
	P-value for response group	**Partial η^2**	**P-value for response group**	**OR**
EDSS	0.22	0.03	0.59	0.59
MSFC	0.84	0.01	0.66	1.3
MSIS Phys	0.70	0.003	0.50	1.7
MSIS Psych	0.92	$<10^{-4}$	0.65	0.7
FS	0.77	0.002	0.84	1.1
BDI	0.40	0.02	0.68	1.9

3.5.9 Secondary radiological outcomes and systemic inflammation

The analysis was repeated replacing brain atrophy rate with the secondary radiological outcomes. No significant associations were found, as shown in Table 18.

Table 18 No associations between systemic inflammation and secondary radiological outcomes.

Change variable	P-value for response group	Partial η^2
Grey matter volume	0.29	0.03
White matter volume	0.09	0.06
Cortical grey matter volume	0.29	0.01
Lesion volume	0.26	0.03
Lesion count	0.90	0.003
Black hole volume	0.32	0.02
Cervical cord atrophy	0.28	0.03

3.6 Discussion

3.6.1 Key results

This study found signals of an association between systemic inflammatory episodes and brain atrophy in MS, in that the magnitude of the host inflammatory response was associated with atrophy. 53 individuals with progressive MS were followed-up for a mean duration of 2.5 years, over which time 56.6% of the group experienced clinically meaningful EDSS progression. Systemic inflammatory episodes occurred with a mean annual frequency of 3.3, the vast majority infections (78.8%). UNCR elevations associated with reported episodes were highly variable, with a mean peak height of 99.4%, i.e. roughly twice as high as baseline. The cohort was split into 'high response' and 'low response' groups of equal size, according to peak height. The high response group experienced a 62% faster rate of brain atrophy, and nearly 10-fold increased odds of significant brain atrophy. The effect was seen predominantly in those individuals with more severe MS and restricted walking, in whom a high inflammatory response was associated with more than a doubling in the rate of brain atrophy.

3.6.2 Strengths

This study had a prospective design and was *a priori* powered to address the primary hypothesis. The study protocol minimised experimenter bias and all radiological measures including the primary outcome were obtained on the same MR scanner. Internal validity was supported by the correlations between study measures of progression. Potential confounders for brain atrophy were included in the analysis, namely age (179), sex (180), baseline disability (181), statin use (170), and smoking (182), which was robust to the presence or absence of confounders. When participants were dichotomised according to high or low systemic inflammatory response, there was no evidence of selection bias in baseline variables between the two groups. The key finding was robust to different statistical approaches. External validity was demonstrated by several findings which recapitulated previously reported data. Brain and regional volumes were similar to literature values for progressive MS (183), though measured lesion volumes were slightly lower (184). The effect of smoking on brain volume has previously been reported (185). As expected, individuals with a greater lesion burden demonstrated greater brain atrophy (186), and the factors predicting brain volume were in concordance with a regression model previously reported (183). The association between lesion measures and clinical disability was more clear-cut and has also been reported previously (187).

3.6.3 Limitations

The enumeration of inflammatory episodes in this study relied on self-reporting by participants. Differences in symptom perception, healthcare-seeking behaviour, and cognition may have influenced reporting. Self-reported episodes such as vaccination or surgery are binary, but self-diagnosed infection is more subjective. Independent clinical corroboration of self-reported infection was not routinely sought, creating the potential for over-reporting. The design was pragmatic; to perform clinical assessment of every self-reported infection would have required significant resources. However, reported episodes without an associated UNCR peak were excluded from analysis, mitigating the effect of over-reporting. Data was also collected on antibiotic use, with the assumption that prescription of antibiotics implied confirmation of infection by a clinician. However, infection episodes requiring antibiotics were rare (no episodes in 73.6% of participants), and hence were unsuitable for detailed analysis. Categorisation of infection episodes by site was difficult based solely on self-report, though since the aim of this study was to study the host inflammatory response to reported episodes, the breakdown by specific infection types was not important for addressing the primary hypothesis. However, it is likely that certain infections generate a more potent systemic inflammatory response and may therefore be more relevant for MS disease progression.

As well as over-reporting, there may have been under-reporting. UNCR peaks without reported symptoms were seen and may have represented un-recognised or under-reported episodes, which may have blunted the sensitivity of the analysis. Diary reporting was encouraged with regular reminders and review of the diary at every face-to-face visit. The mean diary completion rate was 80%. The 28.3% of participants who did not complete the target 75% completion rate were included in this analysis. There was the potential for diary data to have been missing not-at-random, in that participants may have been more likely to forgo diary completion during acute illness. However, participants were sent weekly reminder texts and study staff offered help when diaries were not completed. However, the diary was supplemented by a detailed questioning for acute episodes during the six-monthly visits, and participants could (and did) report episodes retrospectively in a following diary entry.

UNCR was chosen to assay systemic inflammation as it has previously been shown to be a simple and robust measure that is well-tolerated by participants (117). Since the interferon (IFN)-γ pathway is a master checkpoint for many cytokines in the inflammatory response (118), UNCR theoretically integrates inflammatory stimuli regardless of type. However, studies have shown differential responsivity to bacterial and viral infections (188), for example. Weekly sampling was chosen over daily in consideration of tolerability and practicality, however, UNCR fluctuations between days are common (117) and so short-lasting peaks may have been missed or biological variation over-interpreted. The rationale for using the maximum above-baseline UNCR value during the at-risk period was to best capture the peak as a measure of the intensity of inflammatory response, as far as possible. This method of analysing the combined clinical and laboratory longitudinal record of inflammatory events was one of several considered. However, condensing the history of an individual over many years into just two variables (peak height and episode rate) is necessarily a simplification. In individuals with multiple peaks, heights often varied between peaks, hence expressing a combined value using the mean may have given undue prominence to outliers. Also, by using the maximum peak height during episodes no weight was given to the duration of the inflammatory response, which may be of importance.

Whole-brain, tissue, and lesion volumes were used as the radiological outcomes in this study, however, there is increasing evidence for the utility of more specialised volumetrics of GM atrophy in the brain and spinal cord (189) and especially in the deep GM (139), as well as other measures such as diffusion tensor imaging (190) and proton magnetic resonance spectroscopy (191). Lesions were examined in the brain, but spinal cord lesions are also of value (192). The reliance on only start- and end-point imaging in this study was a limitation, as multiple imaging time-points over a longitudinal study improve power (174), and also ameliorate the effect of drop-out (12 participants in this study). With two time-points it is also impossible to discern a

possible non-linear trajectory of atrophy (174). Imaging at multiple time-points would also have allowed examination of progression rates during epochs with and without inflammatory episodes.

Although the group mean was significantly less than zero, positive values of brain atrophy (i.e. increase in brain volume over time) were seen in 2 (3.8%) cases, the highest value being 0.17%/year. Both cases underwent the same quality control as the others and were judged acceptable. Previous studies have reported similar outlying cases of a similar or greater magnitude, for example in about 2% of people with MS in one study (178). Technical variation may occur due to gradient distortion effects associated with inconsistent subject positioning along the z-axis (193), as well as processing errors in SIENA. This may be particularly relevant for subjects with little or no atrophy during the measurement interval; in one study, it was reported that technical sources of variability are the dominant factor at levels of volume change below -0.7% (194). However, biological variation in brain volume may also contribute; the effect of hydration status on brain volume, for example, is well-documented and can be in the order of disease-related changes (195). In the absence of a validated method, no attempt was made to measure and correct for hydration status. Inflammation and oedema as part of MS lesion evolution may also lead to an increase in brain volume (196). Hence cases with apparent brain volume increase were included in the final analysis, without manipulation.

The primary exposure variable, UNCR peak height, was dichotomised to provide two equal-sized groups to examine for the primary outcome, as the study was powered for this method of analysis. However, this dichotomisation has a cost in information loss and may inflate the type 1 error rate (197). Since the dichotomisation was made using the median, the cut-point is neither meaningful nor generalizable.

3.6.4 Interpretation

This study was adequately powered for the primary outcome. A cautious interpretation would be that higher host responses to systemic inflammatory episodes are associated with faster brain atrophy.

If a high host response to inflammatory stimuli is associated with brain atrophy, one might expect individuals with more frequent episodes to atrophy faster. However, episode rate was not significant in the main analysis, though there was a trend (P = 0.07) when examining the high response group alone. This suggests that the frequency of episodes is more relevant in those individuals with a high host response. There may be a threshold effect, whereby any inflammatory stimulus above the threshold leads to an effect on the brain. This would be in keeping with the

finding that the effect of the host response on brain atrophy was more pronounced in individuals with more severe MS, in whom the threshold might be lower.

The subgroup analysis suggested than individuals with more severe MS (and restricted walking) were more susceptible to the effects of a high inflammatory response. These individuals had neither higher baseline UNCR nor higher UNCR peaks with reported episodes, but the effect of systemic inflammation on their brains was heightened. This echoes a common clinical finding, and may be linked to the concept of 'microglial priming', whereby in response to neurodegeneration microglia proliferate and enter an activated state in which their response to systemic inflammation is exaggerated (81). Microglial priming contributes to exacerbation of EAE triggered by systemic inflammation (198) and there is evidence for their activation in MS (199).

It is also important to consider reverse causation. For example, an active systemic inflammatory process which is part and parcel of MS, characterised by Th17 and B-cells (200), may cause heightened responses to infective stimuli. However, baseline UNCR (outside of at-risk periods) did not predict brain atrophy.

3.6.5 Implications and future directions

Although brain atrophy is reported to correlate well with clinical outcomes (201), and correlated well with MSFC change in this study, it is appropriate to be cautious about a radiological outcome without confirmation of clinical benefit. A definitive study is needed to confirm or refute the findings of this study.

A key question is whether the high response status is modifiable. As discussed, the nature of this study precludes a conclusion as to whether the high response status reflects a high burden of inflammatory episodes, or other factors. However, there may be relatively simple opportunities for the prevention of systemic infection in pwMS which are currently under-utilised, and which at the least this study should draw attention to. For example, UTI was common in this cohort, as is typical (47); and yet UTI is reported to be under-diagnosed and under-treated in pwMS (202). Simple interventions have been suggested in consensus guidance (203), and there is modest evidence for the benefit of cranberry tablets for UTI prevention in individuals with spinal cord injury (204). Other infections such as gingivitis are also common in pwMS (205), as in the general population, and gingivitis has been implicated in neuroinflammation and BBB disruption (206). Infections remain a leading cause of mortality (48) and morbidity (49) for pwMS, and so there is an existing rationale for their prevention and treatment.

A wide variation in host inflammatory response was seen in this study and future work should examine the factors behind this. The response to an inflammatory stimulus is determined by both host and stimulus factors. It is possible that individuals in the high response group experienced more potent inflammatory stimuli, for example more severe or longer infections, or received sub-optimal treatment of episodes. It is also possible that individuals in the high response group possessed a more potent systemic inflammatory response (or vice versa), perhaps driven through genetic variation (207). Immunosenescence has been reported to affect both adaptive and innate immunity (208), though the low response group was not significantly younger than the high response group. Other host factors could have contributed variation in the response to inflammatory stimuli, for example vitamin D deficiency, which is common in MS (209). Most proliferating immune cells express the vitamin D receptor, including macrophages (210) where vitamin D is required for the production of the antimicrobial peptide cathelicidin (211). Understanding the factors which determine the host response will help translate the findings of this study into clinical benefit.

This study was designed to look for an association, but further work is needed to examine the mechanisms which mediate possible interplay between the host response to systemic inflammation and brain atrophy. The remainder of this thesis examines whether BBB disruption during systemic inflammation may be a relevant mechanism.

Chapter 4 Development and Validation of a Dynamic Contrast-Enhanced Magnetic Resonance Imaging Protocol

4.1 Introduction

The previous chapter described a study of the association between systemic inflammation and disease progression in MS. BBB disruption during inflammatory episodes is suggested as a possible mechanism. To probe this idea further, a method is required for non-invasive study of BBB permeability in human subjects. In this chapter I describe the initial development of a DCE-MRI protocol. Hypotheses derived from biological expectations are used to the validate the protocol.

4.2 Hypotheses

If K_i derived from DCE-MRI truly equates to the permeability-surface area product (PS), it is a compound marker of BBB permeability and surface area, in which case the following hypotheses can be stated, in order to validate the protocol:

1. That K_i is higher in areas with a higher vascular surface area available for tracer exchange. This can be tested by comparing K_i within-subject between grey and white matter in controls, as it has been histologically established that vascular density in GM is higher than in WM (212). Since GM and WM are easily identifiable, this gives a useful way to test assumptions about K_i. Assuming a very simple vascular architecture model comprising cylindrical vessels with constant radius, both surface area and cerebral blood volume (CBV) scale with vessel density, and CBV should then predict K_i.
2. That there is no correlation between cerebral blood flow (CBF) and K_i. This can be tested in controls across grey and white matter. According to the Crone-Renkin equation, when CBF is much greater than PS (which is expected at the BBB), there should be no correlation between CBF and PS.
3. That K_i is higher in areas with gross pathological BBB disruption. This can be tested by comparing K_i in active MS plaques, identified as visibly contrast-enhancing lesions (CELs), with normal-appearing brain tissue of the same type.

4. That K_i is higher in areas with subtle pathological BBB disruption. This can be testing by comparing K_i in the normal-appearing white matter (NAWM) of people with MS with that of healthy controls, as BBB disruption which is undetectable by conventional contrast MRI has been demonstrated histologically in MS NAWM (31, 213).

In addition, for future analysis it is desirable to reduce operator dependence in region of interest (ROI) placement and facilitate batch processing. Automated tissue segmentation can enable this whilst also allowing diffuse abnormalities to be captured. As previous authors have used ROI methods, an additional hypothesis is:

5. That there is good agreement between K_i measured from ROI and segmentation methods. This can be tested by comparing results for NAWM within-subject according to method.

4.3 Methods

4.3.1 Initial protocol development

The initial protocol was developed based on expert opinion. In particular, the work of the Larsson group in Copenhagen was a strong influence, as their protocol was the first to detect subtle BBB disruption in the normal-appearing white matter (NAWM) of pwMS (23) where previous studies with technical and modelling differences had not (214-216). The following features were given priority during method development:

- Whole-brain coverage, as it is not known where BBB changes during infection may localise. Other groups have sacrificed coverage in favour of resolution when the hypothesis is targeted to a specific region (217), but this would be unsuitable for the current study.
- Adequate resolution to discriminate important regions of interest (ROIs) such as lesions without significant partial volume effect. Unfortunately, signal is proportional to voxel volume and so increasing resolution decreases signal-to-noise ratio (SNR).
- Baseline T_1 mapping, rather than using literature values. T_1 error leads to significant error in the estimation of pharmacokinetic parameters (218) and so subject-specific measurement is preferable, though this requires that the measurement be accurate. Since T_1 values in MS are prolonged relative to controls (219) the use of a literature value would likely lead to significant errors.
- Input function measurement from the MR signal itself, rather than using literature values. Individual measurement has the advantage of capturing within-subject and between-subject differences which may be related to factors such as age, sex, health, and

haematocrit. The trade-off is that measurement of the AIF necessitates a fast time resolution of the dynamic sequence to capture bolus passage. This method was preferred to the alternatives, namely (1) using population average values, for reasons of capturing variation, or (2) analysing sequential blood samples taken from an arterial catheter during the DCE-MRI sequence, for reasons of subject tolerability and practicality.

- Minimal overall acquisition time, to improve subject tolerability. This is particularly relevant given the intention to scan acutely unwell subjects, some with disability.

To achieve these requirements a fast low-angle shot (FLASH) spoiled gradient echo sequence was selected. FLASH was a natural choice as it delivers fast acquisition times for whole brain volumes and has a long history in DCE-MRI (220). The principle of FLASH is that a low flip angle ensures that some longitudinal magnetisation remains after each excitation; a short TR is then feasible as despite the incomplete relaxation in the steady-state there is a reasonable amount of longitudinal magnetisation remaining.

3D imaging was selected in preference to 2D. In a multi-slice 2D acquisition, each slice is selected through a combination of a gradient in the z-axis and a slice-selective excitation pulse. In a 3D acquisition, the whole volume is excited by a single non-selective pulse, and position in the z-axis is encoded through an additional phase encoding direction. Therefore, a 3D acquisition takes longer due to the additional phase encoding steps, each of which takes one TR. FLASH allows the use of an extremely short TR (much shorter than T_1). This makes it practical to acquire a whole-brain 3D volume within a reasonable time. The other benefits of 3D acquisition are (1) the absence of slice gaps, (2) the absence of cross-talk between slices, as they are encoded rather than excited, (3) inherently higher SNR, as the data is re-sampled by phase encoding in the third dimension, (4) ability to reformat in different orientations. A downside is that any motion artefact will tend to be propagated along two axes, as there are two phase encoding directions.

Imaging was conducted on a 3 Tesla (T) platform. The benefit of 3T over 1.5T is an increase in MR signal, which increases linearly with magnetic field strength (221). This is important when considering the relatively small signal changes that may occur with subtle BBB disruption. The main downside of imaging at higher field strengths is radiofrequency (RF) field inhomogeneity. Recalling the Larmor equation, the resonance frequency is dictated by the gyromagnetic ratio and the field strength. At 1.5T this is approximately 64 MHz, compared to 128 MHz at 3T. At this increased frequency, the wavelength in water at 3T becomes about 26 cm (compared to 52 cm at 1.5T). As the wavelength becomes closer to the diameter of body structures (e.g. the head), RF waves become increasingly prone to complex shielding and interference effects, which leads to an

inhomogeneous field. This is of crucial importance for flip angle accuracy, as discussed in depth later.

T_1 mapping was achieved using the variable flip angle (VFA) method with FLASH sequences. The gradient echo signal equation (Equation 10) can be rearranged into linear form as

Equation 14

$$\frac{\mathrm{S}}{\sin \alpha} = E_1 \frac{\mathrm{S}}{\tan \alpha} + S_0(1 - E_1)$$

Therefore, if signals are acquired at more than one flip angle, with all other factors held constant, and plotted on axes of x = S/sin(α) and y = S/tan(α), then the fitted line allows calculation of both T_1 (from the slope) and S_0 (from the intercept). In this work, T_1 mapping by the VFA method was implemented using MATLAB code written and kindly provided by Professor David Atkinson, University College London.

Once baseline T_1 has been established by the VFA method, the dynamic sequence requires one flip angle only. It is assumed that proton density and scanner gain remain constant between acquisitions, and hence the baseline value of S_0 can be used in the calculation of T_1 during dynamic imaging. For each dynamic image, T_1 can then be calculated voxelwise by solving Equation 10 for T_1, using the measured signal S and the baseline S_0. The signal-time curve for each voxel can be converted to a T_1-time curve, and then to a concentration-time curve using the known relaxivity of contrast agent. Several other methods for T_1 mapping are available but were considered impractical given the desired temporal resolution (222). The inversion-recovery (IR) and saturation-recovery methods are well-established, but time-consuming.

Any of the standard paramagnetic contrast agents could in theory be used for DCE-MRI. Newer macrocyclic agents are used in favour of older linear agents, given the concerns regarding potential gadolinium deposition (223). Gadovist (Gd-DO3A-butrol, Gadobutrol; Bayer; Newbury, UK) was chosen as it is widely used in our institution, has a relatively high relaxivity (224), and is formulated with a relatively high concentration (1 mM, double that of most other agents) which allows a small volume for rapid bolus injection. Half the standard clinical dose was used to avoid truncation artefacts of the bolus peak and provide an adequate washout curve (215). The bolus injection was given at a rate fast enough to ensure a sharp peak with high arterial concentration with the first pass, which is at least 2-4 ml/s (101).

In addition to the DCE sequence the protocol also included imaging of structure and pathology to aid interpretation. A T_1-weighted MP-RAGE sequence was used for structural imaging as it provides excellent contrast between grey and white matter and is widely used for tissue

classification (225). The inclusion of a high-resolution anatomical image was also desirable for potential image registration. Finally, standard clinical T_2-weighted and 2D FLAIR sequences were included to aid identification of MS lesions and other pathology (11).

4.3.2 Protocol description

Imaging was performed on the 3T MR platform (Skyra, Siemens, Erlangen, Germany) at Southampton General Hospital, using a 20-element phased-array head and neck coil.

The dynamic sequence used a 3D spoiled gradient echo sequence (FLASH) with TR = 2.48 ms, TE = 0.99 ms, flip angle = 15°, linear phase ordering, GRAPPA undersampling with parallel imaging factor = 2, acquired matrix = 192 × 144 × 30, voxel size = 1.3 × 1.3 × 5.0 mm^3, field of view = 250 × 188 × 150 mm^3, reconstructed into 30 slices of thickness = 5.0 mm. The dynamic sequence comprised 300 dynamic frames at a time resolution of 3.2 s, giving a total scan duration of 16 min. The parameters were selected to give the maximum coverage and resolution with an acceptable time resolution.

Intravenous contrast injection was given after the 10^{th} time point using an automated injector (Medrad; Newbury, UK), with speed 3 ml/s, followed by a 30 ml saline flush at the same rate. Contrast agent was Gadovist at a dose of 0.05 mmol/kg.

Data for T_1 mapping by the VFA method was acquired prior to the DCE sequence using a 3D gradient echo sequence with identical coverage and matrix, with a series of flip angles (5, 10, 15 and 18°). Prior to the dynamic acquisition the following sequences were also performed:

- 3D MP-RAGE sequence (TR = 2200 ms, TE = 2.45 ms, TI = 900 ms, flip angle = 8°, field-of-view 263 × 350 × 350 mm^3, voxel size 1.0 × 1.0 × 1.0 mm^3).
- Axial T_2-weighted sequence (turbo spin echo; TR = 3600 ms, TE = 9.4 ms, field-of-view 263 × 350 × 350 mm^3, voxel size 0.3 × 0.3 × 4.0 mm^3, 35 slices).
- Coronal fluid-attenuated inversion recovery (FLAIR) sequence (TR = 9000 ms, TE = 81 ms, TI = 2500 ms, field-of-view = 186 × 220 × 160 mm^3, 40 slices).

After the dynamic acquisition, a post-contrast MP-RAGE with identical parameters to the pre-contrast image was also performed.

4.3.3 Analysis description

Lesions were segmented by the lesion growth algorithm from LST (140), as detailed in the previous chapter. CELs were identified through visual inspection of the post-contrast T_1 image. In

each subject four NAWM ROIs were drawn in the centrum semiovale on the axial FLAIR image and then applied to the dynamic sequence after registration. In controls, grey matter ROIs were drawn in the thalami, one in each hemisphere. The operator could not be blinded to group due to the obvious presence of lesions in the RRMS cases, but the K_i values were only calculated after finalization of ROI placement, to minimize the potential for bias. The high-resolution T_1 image was first brain-extracted using BET (126). Tissue-type segmentation was then performed using FAST (130) and the resulting tissue probability map was transformed into dynamic space and binarised with a 100% threshold. For RRMS cases, lesion filling was performed prior to segmentation using the LST toolbox. NAWM voxels were defined as those within the WM mask with a zero value in the lesion probability map (Figure 17).

Figure 17 Examples of tissue and lesion segmentation.

All images are the same slice from a single individual with RRMS.

An analysis pipeline was constructed in MATLAB to extract a signal–time series for each voxel. The mean behaviour of voxels within either ROI (for the manual ROI method) or tissue mask (for the segmentation method) was used for further analysis. Baseline T_1 and S_0 combined with contrast agent relaxivity was used to convert the signal–time series into a concentration–time series. The arterial input function (AIF) was measured for each subject by determining the maximal signal change within an axial ROI drawn manually over the supraclinoid segment of the right internal carotid artery. The same AIF was used for both ROI and segmentation methods. K_i and CBV were calculated from the AIF and tissue concentration curve using the Patlak model (MATLAB code written and kindly provided by Professor Henrik Larsson, University of Copenhagen). The linear part of the Patlak plot, i.e. the last two-thirds of the data points, were included in the fitting procedure, to allow for steady state arterial concentration. Perfusion estimation was done by Tikhonov deconvolution of the tissue concentration with the AIF (using all data points), which is a general form of singular value decomposition having a regularization term (226). Values of K_i were reported as ml/100g/min. In the ROI method, the mean of ROIs was quoted for each subject.

4.3.4 Participants

Healthy adult individuals without systemic or neurological disease (including migraine) were recruited by advertisement. Adults with RRMS were recruited from the MS service at the Wessex Neurological Centre, Southampton, UK. Inclusion and exclusion criteria are shown in Table 19. All participants had normal renal function according to the institutional cut-off for contrast administration (estimated glomerular filtration rate above 60 ml/min/1.73m^2). Scans were performed in an interleaved fashion to prevent the possibility of systematic bias due to longitudinal scanner drift.

Table 19 Inclusion and exclusion criteria

Inclusion criteria for healthy controls	**Inclusion criteria for people with MS**	**Exclusion criteria for all**
Healthy adult without known systemic or neurological disease.	Adult with diagnosis of relapsing-remitting MS by a neurologist.	Inability to have an MRI scan (incompatible metal implants, claustrophobia, morbid obesity) or gadolinium-based contrast (renal failure, history of contrast allergy).

4.3.5 Statistical analysis

Appropriate two-tailed tests were used to detect significance between groups for parametric or non-parametric data. ANCOVA was used to compare RRMS and control K_i, to enable inclusion of covariates. Multivariate linear regression was employed to examine CBV, CBF and tissue type as predictors of ROI-determined K_i. A p-value of <0.05 allowed rejection of the null hypothesis. Bland–Altman analysis was used to assess agreement between the ROI and segmentation methods, as this has been shown to be the most appropriate tool for this purpose (227). The intraclass correlation coefficient (ICC) was used to assess reliability, incorporating both agreement and correlation (228).

4.3.6 Ethical approval

The study was approved by the National Research Ethics Service Committee South Central (reference 12/SC/0176) and the institutional review board (ERGO 46018). Experiments were

conducted in accordance with the Declaration of Helsinki and all subjects gave informed written consent.

4.4 Results

13 control individuals and 12 patients with RRMS were recruited. The RRMS group was older (P = 0.01, t-test), and age was therefore factored into all further analyses comparing groups, since BBB permeability increases with age (83). The gender ratio between groups was not significantly different (P = 0.673, Fisher's exact test). All RRMS subjects had typical MS lesions, and three patients had a total of four visibly contrast-enhancing lesions (CELs). Tolerability of the scanning protocol was good, except for one RRMS subject who experienced discomfort towards the end of the session and required omission of the post-contrast MP-RAGE; for this subject all pre-contrast sequences and the full DCE sequence were acquired and included in the analysis, but the presence of CELs could not be assessed.

Hypothesis 1: In controls, K_i was significantly higher in GM than in WM (P = 0.001, Wilcoxon). CBV was significantly higher in grey than white matter (P = 0.005, Wilcoxon), with a mean pair-wise grey/white matter CBV ratio of 1.9 (range 1.0–3.6). The results are shown in Figure 18. A multivariate linear regression including ROI-derived CBV, CBF and tissue type was performed to ascertain the extent to which these could explain K_i. All variables were included in the final model, which explained 82% of the variance in K_i (r^2 = 0.816). Only CBV predicted K_i (β = 0.036, P < 10−8).

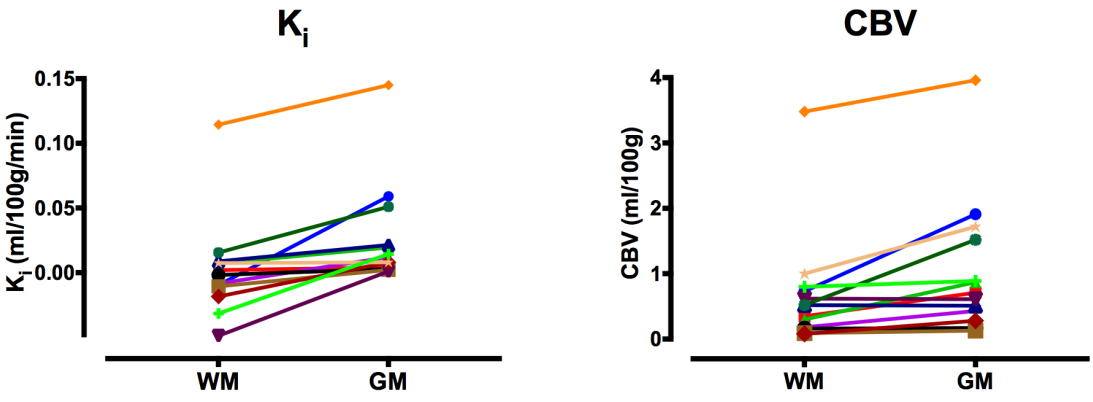

Figure 18 Pairwise plots of K_i and CBV values in white matter (WM) and grey matter (GM), for individual control subjects.

Hypothesis 2: CBF did not correlate with K_i (Spearman's ρ = 0.32, P = 0.111).

Hypothesis 3: Mean K_i in CELs (ROI method) was 0.139 ml/100g/min, significantly higher than NAWM in either RRMS (0.052 ml/100g/min, P = 0.002, t-test) or controls (0.020 ml/100g/min, P = 0.005, Mann–Whitney).

Hypothesis 4: K_i in NAWM was significantly higher in RRMS than controls by both the ROI method (P = 0.014, ANCOVA, no effect of age) and the segmentation method (P = 0.019, ANCOVA, no effect of age). The results are shown in Table 20.

Table 20 Results for BBB permeability calculations in normal-appearing white matter.

Values are mean (standard deviation). Analysis is by ANCOVA incorporating age as a covariate. HC = healthy control, RRMS = relapsing-remitting multiple sclerosis, ROI = region of interest, EMM = estimated marginal mean.

	Measured values		**p-value for group**	**Partial-ε^2 for group**	**p-value for age**	**EMM**	
K_i (ml/100g/min)	**HC (n = 13)**	**RRMS (n = 12)**				**HC (n = 13)**	**RRMS (n = 12)**
ROI	0.020 (0.038)	0.052 (0.037)	0.014	0.246	0.789	0.003	0.051
Segmentation	0.003 (0.027)	0.059 (0.045)	0.019	0.226	0.090	0.010	0.052

Hypothesis 5: A Bland–Altman plot comparing ROI and segmentation methods showed no clear difference or proportional bias between the calculated K_i values for NAWM (Figure 19). The difference in values by each method was not significantly different from zero (P = 0.638, one-sample t-test). Linear regression (with difference in K_i between the two methods as dependent, and mean K_i as predictor variable) confirmed absence of proportional bias (P = 0.859). The two-way mixed intra-class correlation coefficient showed good single measure consistency (0.610).

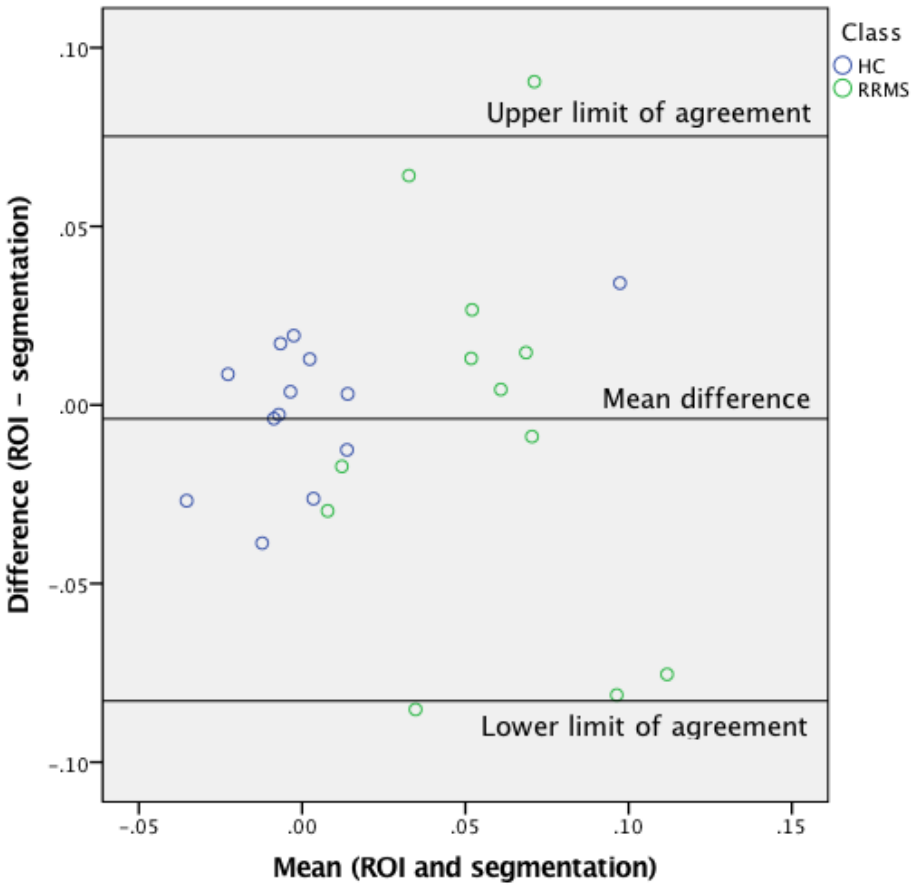

Figure 19 Bland-Altman plot comparing K_i values by region-of-interest (ROI) and segmentation methods.

HC = controls, RRMS = relapsing-remitting multiple sclerosis.

4.5 Discussion

4.5.1 Key results

This pilot study confirms the validity of K_i as measured by DCE-MRI as a marker of BBB permeability. The test of hypotheses 1-4 support the idea that K_i as measured by DCE-MRI does correspond with the PS product, and therefore is a marker of BBB permeability. The test of hypothesis 4 suggests that DCE-MRI can detect BBB leakage more than an order of magnitude below the level found in CELs by conventional imaging. In addition, the test of hypothesis 5 shows how automated tissue segmentation can replace the need for manual ROI placement, capturing more diffuse abnormality whilst reducing operator dependence and providing ease of batch processing.

4.5.2 Strengths

Since its inception there has been some concern over the exact meaning of parameters measured by DCE-MRI, though correlation of K_i with an established measure of permeability by PET has previously been demonstrated (229). This study used a novel approach, instead comparing K_i to the biological expectations of the PS product. Histological study in the human brain has shown that vascular volume is higher in GM than WM, with a mean GM/WM ratio of 2.9 (212). Other histological (230) as well as imaging studies (231, 232) support this finding. If one assumes that the mean vessel radius is the same in GM and WM (in the absence of any evidence to the contrary), the GM/WM CBV ratio should be equal to the GM/WM vascular surface area ratio. If K_i truly corresponds to the PS product, the larger vascular surface area in GM should contribute to a higher K_i in GM versus WM in the healthy brain. The above results support this and show that CBV, which scales with surface area, predicts K_i. When controlling for CBV, neither CBF nor tissue type predict K_i.

This study was also able to replicate the finding of abnormal BBB permeability in the NAWM of individuals with RRMS (23), in a different population and setting, and using a different protocol. Given concerns of a 'replication crisis' in the neuroimaging field (233), this is a reassuring finding.

4.5.3 Limitations

This MRI protocol in this study was developed based on expert guidance, however, it is possible that elements were sub-optimal for the detection of subtle leakage. No attempt was made to correct for B1 inhomogeneity, which can lead to errors in T_1 measurement and propagate into tracer kinetic analysis (234). A manually drawn carotid AIF was used, which is prone to artefacts of partial volume and flow-related enhancement. The half-dose of contrast agent used may have impaired the detection of signal enhancement (11).

Age was significantly higher in RRMS versus control groups. Increasing age is associated with higher BBB permeability (83, 217), so this was a possible confounder. However, age was included as a covariate, and a significant effect of age on K_i was not observed in this small dataset (see Table 20).

Although ROI and segmentation methods gave similar results, if we take the mean difference between controls and RRMS to be meaningful, then the difference between 95% limits of agreement exceeded this level, so the ROI and segmentation methods cannot be used interchangeably. However, the two methods showed good agreement in ratio of change, as evidenced by the ICC.

4.5.4 Implications and future directions

This study demonstrates that DCE-MRI is an appropriate tool for measuring subtle BBB permeability changes. Whilst *in vitro* and animal models are of limited applicability to the human BBB (65, 235), this study provides increased confidence in the use of DCE-MRI as a validated non-invasive method for clinical and research applications in humans.

To maximise the performance of the technique for the detection of subtle BBB leakage, a systematic approach is needed to investigate and optimise each element of the acquisition and analysis pathway. Some elements likely to be of importance are discussed briefly in the Limitations section above. Therefore, this study led to a dedicated optimisation study designed to explore these issues in detail. This is the focus of the next chapter.

Chapter 5 Optimisation of the Dynamic Contrast-Enhanced Magnetic Resonance Imaging Protocol

5.1 Introduction

It is anticipated that if disruptive BBB change occurs during systemic infection, it may be subtle. In this chapter I describe a series of experiments conducted to optimise several aspects of the protocol (previously described in Chapter 4) to maximise sensitivity to detect an effect. A systematic approach was taken to identify and correct potential major sources of error during acquisition and processing. As with most MR sequence development, the final acquisition protocol must include trade-offs to balance the desired properties with the inevitable penalties. In this case the fast time resolution required for dynamic imaging imposes a limit on acquisition time. However, through judicious selection of parameters it is possible to balance the trade-offs favourably. Based on participant feedback and scanner logistics total scan time was capped at 60 minutes, and competing needs were balanced against this threshold. To analyse the large image datasets, an automated software pipeline was developed incorporating several features designed to improve parameter estimation, reduce operator-dependence, and maximise the extraction of useful information. Since the optimisations described in this chapter includes a mix of those which are novel and those which have been previously described, a specific declaration is given in Appendix E.

5.2 Checking linearity of the RF transmitter

A specified flip angle is achieved by adjusting the RF transmitter amplitude whilst keeping the duration fixed. One potential source of error is if the transmitter does not scale linearly. An experiment was conducted to test the linearity of amplitude scaling, using a homogenous spherical phantom (T_1 = 374ms, T_2 = 287ms) and the same 3D FLASH sequence from the DCE-MRI protocol. Parameters were set to remove the effects of both T_1- and T_2*-weighting (TR = 1500 ms, TE = 0.99 ms). The RF pulse duration was fixed, and amplitude varied to achieve nominal flip angles of 5, 10, 15, 20°. Signal was measured from a fixed circular ROI in the centre of the object.

Simulation using the signal equation (Equation 10) shows that in this range the relationship between flip angle and signal is expected to be linear (Figure 20). Therefore, if transmitter amplitude scales linearly then the measured signal in this flip angle range should also scale linearly. The absolute values of signal calculated depend on S_0, but the relationship between flip

angle and signal should hold true as S_0 is fixed between acquisitions (proton density and scanner gain do not change). Therefore, the signal can be expressed as a fraction of the signal from a 20° acquisition. As expected, the graph of measured data is also linear. Therefore, flip angle, and transmitter amplitude, must be scaling as expected.

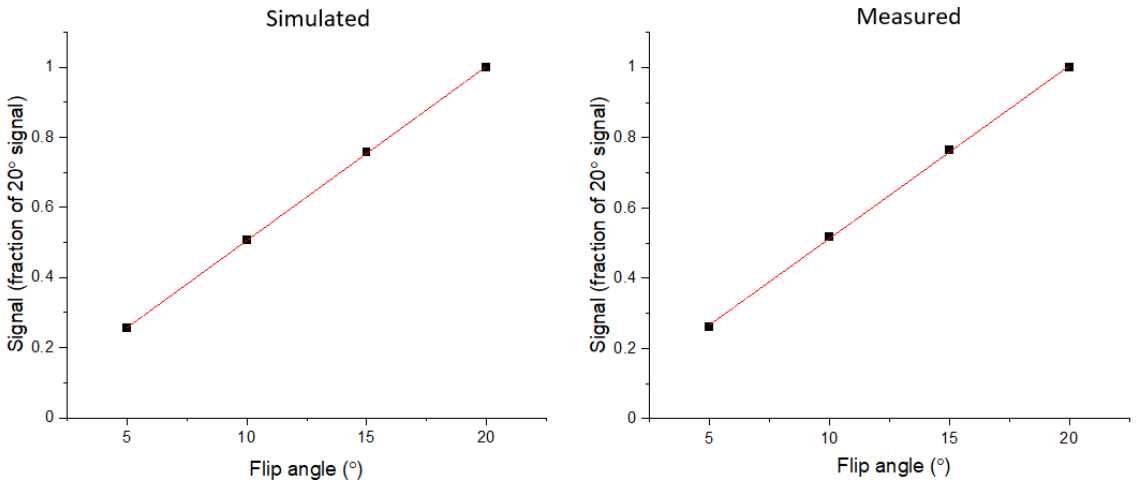

Figure 20 Linear scaling of signal in relation to flip angle, in both the simulated and in measured data.

5.3 Establishment of a T_1 mapping phantom

For further studies it was essential to have a reference standard for T_1 measurements. Experiments were conducted using the validated and CE-marked T1MES phantom comprising nine agarose gel tubes doped with nickel chloride (236). T_1 values were established using the reference method of inversion recovery (IR) (222). This is comprised of a spin echo sequence with a preceding 180° inversion pulse, separated by an inversion time (TI). The 180° pulse tips longitudinal magnetisation so that it is pointing in the opposite direction to B0. After the pulse magnetisation gradually regrows to the equilibrium value, in the same direction as B0. The spin echo sequence reads out whatever magnetisation has recovered by time TI, which is dependent on T_1. Signals are acquired at a range of TI and plotted. A curve can then be fitted to the data to solve the following equation for T_1 (222):

Equation 15

$$S = M_0(1 - 2e^{-TI/T1})$$

Acquisition was performed at TI = [25, 50, 100, 200, 500, 800, 1300, 2000, 3000, 4000, 6000] ms, TR = 8000 ms, TE = 25 ms. The long TR (several times longer than T_1) ensures full relaxation in between successive inversion pulses. Due to the very long acquisition time, images were acquired

from one slice only. Standardised circular ROIs were drawn in the centre of each tube and the mean signal value extracted. Signal was plotted along a range of TI times and the T_1 recovery curve fitted by least-squares (Figure 21).

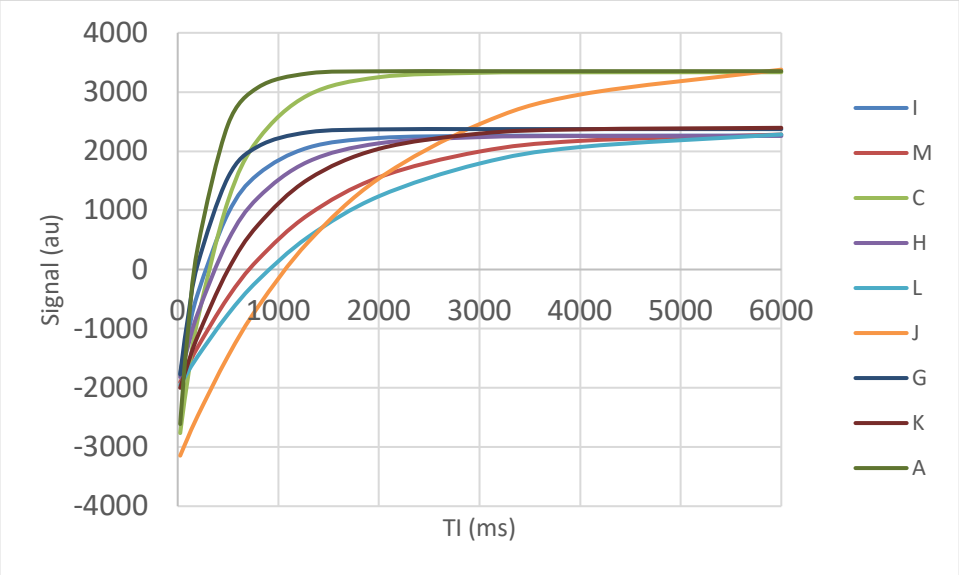

Figure 21 T_1 recovery curves for the nine tubes of the T1MES phantom at 3T.

The letter designations of the tubes are those given by the manufacturer. Signal is measured in arbitrary units (au).

The resulting T_1 values are shown in Table 21, with the corresponding manufacturer's value where available. There was good agreement between the calculated values and the available values from the manufacturer. The measured values were used as reference for further experiments.

Table 21 Calculated T_1 by inversion recovery (IR) for the T1MES phantom at 3T.

The letter designations of the tubes are those given by the manufacturer.

Tube	**Manufacturer's quoted T_1 (ms)**	**Measured T_1 by IR (ms)**
I	424	425
M	n/a	1140
C	451	461
H	555	569
L	n/a	1464
J	n/a	1645
G	294	292
K	n/a	787
A	250	251

5.4 Signal averaging

SNR can be improved by signal averaging, that is collecting and averaging together several images. The signals are present in each of the averaged images so their contributions to the final image are additive. Noise is random so it does not add but instead cancels as more signals are averaged. The SNR improvement from signal averaging is proportional to the square root of the number of images averaged (NEX = number of excitations). Due to the increase in acquisition time, it would not be possible to average signals in the dynamic run, as to do so would significantly compromise the time resolution. However, time is less of a factor during T_1 mapping, and these sequences are relatively short to begin with (roughly 5 seconds per flip angle). Hence the impact of increasing NEX during T_1 mapping was tested. The phantom was imaged with the existing T_1 mapping protocol (flip angle = [5, 10, 15, 18°], TR = 2.48 ms), with NEX = 1 and NEX = 4. T_1 was calculated using the VFA method and quoted as the mean per ROI in the centre of each tube. T_1 accuracy was reported as the percentage error from the reference IR measurement. As shown in Table 22, signal averaging was associated with a significant improvement in mean percentage error with T_1 consistently under-estimated (-21.4 ± 3.3% vs. -29.9 ± 5.2%, P = 0.006, paired t-test). The improvement in T_1 measurement is worthwhile since it is directly carried forward into the calculation of contrast agent concentration.

Table 22 Improvement in T_1 measurement accuracy by signal averaging in the variable-flip angle (VFA) mapping sequence.

NEX = number of excitations. P = 0.006 for a paired t-test of mean percentage error.

Reference T_1 (ms)	**NEX = 1**		**NEX = 4**	
	T_1 (ms)	**Error (%)**	**T_1 (ms)**	**Error (%)**
425	309	-27.4	339	-20.2
1140	826	-27.5	963	-15.5
461	290	-37.0	350	-24.1
569	428	-24.8	464	-18.4
1464	1057	-27.8	1124	-23.2
1645	1257	-23.6	1340	-18.5
292	208	-28.9	221	-24.3
787	492	-37.5	597	-24.1
251	165	-34.4	191	-23.8
Mean (SD) error		*-29.9 (5.2)*		*-21.4 (3.3)*

5.5 Flip angle choice

A simulation was conducted in MATLAB to determine the optimum flip angle for the dynamic acquisition, using the signal equation (Equation 8) and TR = 2.48, T_1 = 1000 ms (a rough estimate for brain tissue), and flip angles = [5, 10, 15] °. The effect of a range of gadolinium concentrations was considered, within the range likely to be encountered (Figure 22). Even though a smaller flip angle gives higher signal at low concentrations (because it is closer to the Ernst angle), it is seen that the greatest sensitivity and dynamic range to changing concentration is achieved with the higher flip angle. This is important to maximise the detection of subtle permeability changes. Therefore, a flip angle of 15° was chosen for the dynamic acquisition.

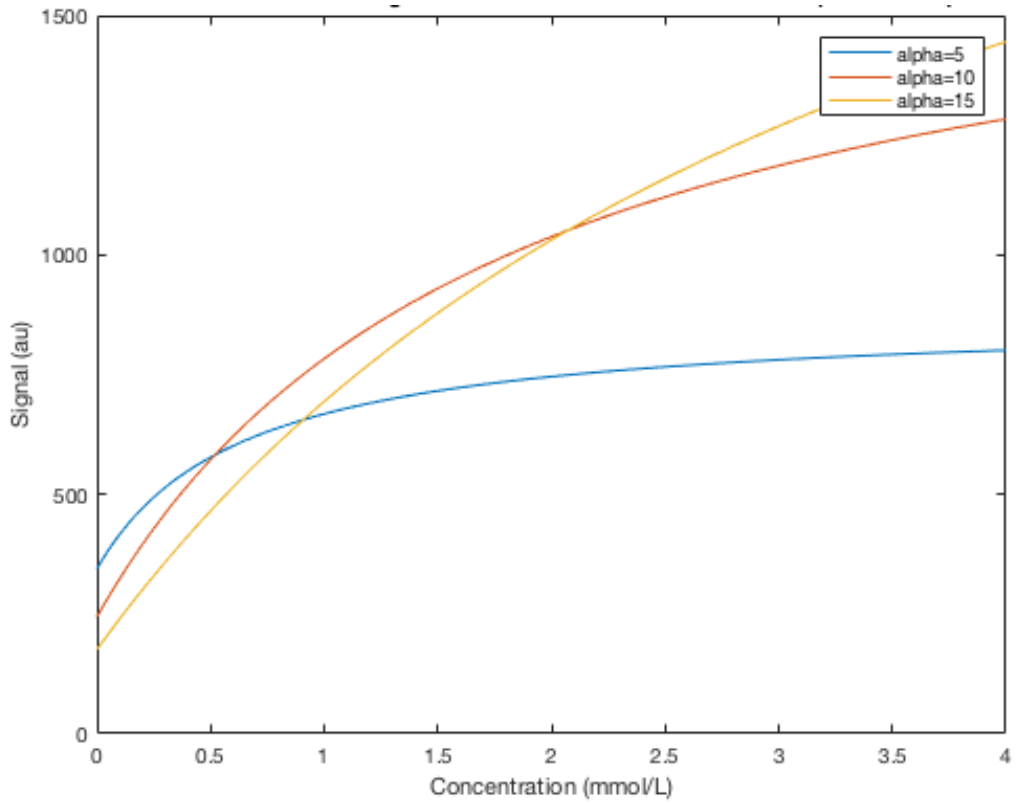

Figure 22 Simulated effect of flip angle on sensitivity of MR signal to gadolinium concentration.

A formula for determining the optimum angles for VFA T_1 mapping has previously been published (237), and on this basis flip angles in the VFA sequence were revised to [5, 7, 15].

5.6 Correction for B1 inhomogeneity

Flip angle is determined by the amplitude, duration, and shape of the RF pulse. These parameters are calculated by the scanner to achieve the nominal flip angle for all spins within the field of view. However, in practice this is confounded by spatial inhomogeneity of the transmit field, due to penetration and interference (dielectric resonance[3], particularly at 3T and higher, causes the RF field to be higher near the centre of the object than near its periphery), coil geometry, and non-ideal slice profiles. The VFA method of T_1 mapping is especially sensitive to misrepresentation of flip angle. The nominal flip angle (set by the user) can differ from the true flip angle (experienced by the voxel). The effect can be simulated. Values of signal were simulated in MATLAB for a hypothetical tissue (T_1 = 1000 ms) at a range of flip angles, and T_1 calculated using the VFA

[3] Biological tissues may be dielectric materials, poor conductors which become polarised in an electric field. Complex reflection and refraction effects occur as electromagnetic radiation encounters tissues and tissue boundaries.

method with two angles. For each flip angle pair, an error was then introduced whereby the nominal flip angle used in the VFA calculation deviated from the true flip angle by a prescribed amount. As shown in Figure 23, a relatively small error in flip angle can lead to a large error in T_1 calculation. Errors in T_1 are propagated to errors in calculating concentration of contrast agent which leads to errors in kinetic analysis (234).

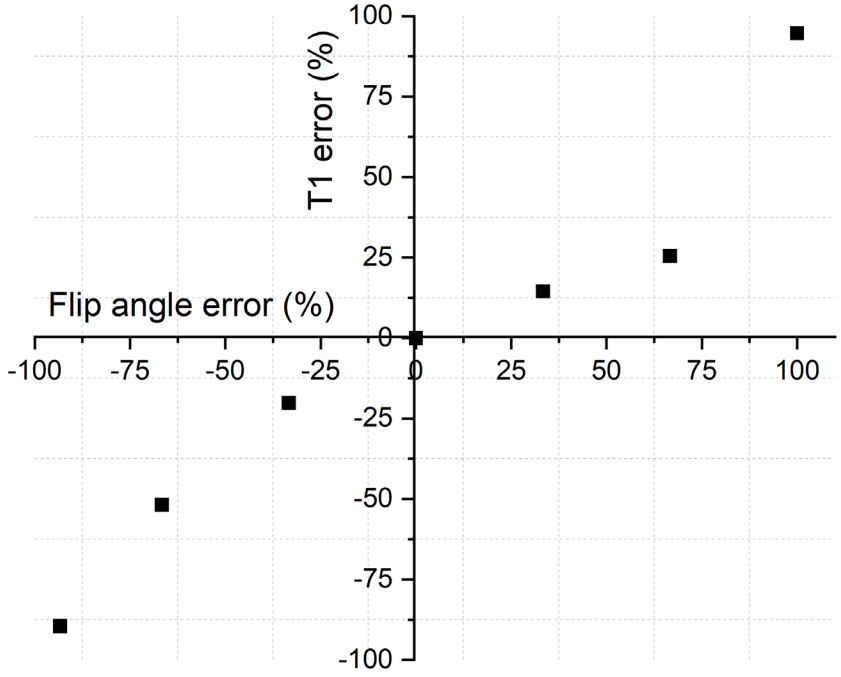

Figure 23 Simulated effect on flip angle error on T_1 calculation by the variable flip angle method.

Values are for a hypothetical tissue with T_1 = 1000 ms. The true flip angle deviates from the nominal value by a percentage error and gives rise to an error in calculated T_1.

Therefore, a method of determining and correcting for voxel-wise values of true flip angle is desirable [4]. The double-angle method is considered a reference technique for flip angle mapping

[4] Some confusion in terminology arises because in much of the literature the terms B1+, B1, and actual/true/measured flip angle are used interchangeably. Generally, 'B1' is used to refer to a scaling factor which relates actual to nominal flip angle and is used as such in this work. If there were no inhomogeneity, B1 would be 100% throughout the field of view, and the flip angle experienced by every voxel would be exactly that which was specified on the scanner console.

but is slow (238). The slice-selective preparation pulse method (SS-Pre) (239) is of particular interest as it is one of the few methods which allows whole-brain mapping in the order of 10 seconds, with excellent agreement with the double-angle method. A slice-selective sinc preparation pulse (relatively robust to off-resonance) is used, with a nominal flip angle ($\alpha_{nominal}$). After this excitation, residual transverse magnetisation is spoiled. Immediately afterwards, a TurboFLASH sequence is performed to readout the residual longitudinal magnetisation (M_Z, giving signal S_{SSPre}). A proton density image with the same imaging parameters but without a preparation pulse is also acquired (capturing fully recovered longitudinal magnetisation, M_0, giving signal S_{PD}). The relationship between M_Z and M_0 is given by:

Equation 16

$$\frac{S_{SSPre}}{S_{PD}} = \frac{M_Z}{M_0} = \cos(B_1 \cdot \alpha_{nominal})$$

Equation 17

$$B_1 = \cos^{-1}\left(\frac{S_{SSPre}}{S_{PD}}\right) / \alpha_{nominal}$$

Ideally $\alpha_{nominal}$ of the pre-pulse should be close to 90° (to maximise the effect on the cosine), but not 90° as in that case there would be no residual longitudinal magnetisation and the readout would just be of noise. Hence a value of 80° is sensible.

The SS-Pre method was tested in the phantom and acquired with the same coverage as the T_1 mapping and dynamic sequences, but with a reduced matrix size of 64 x 64 x 15 (acquisition time = 12 seconds). Mapping is usually performed at low resolution, as spatial variation in flip angle is expected to be low in frequency (240). VFA data was collected with flip angle = [5, 7, 15]°, TR = 2.48 ms, NEX = 4. The SS-Pre data were then interpolated with a cubic spline to match the geometry of the VFA data (192 x 144 x 30). Most authors also apply a filter to reduce noise. Based on a published method (240), the interpolated maps were filtered by a 3D Gaussian kernel (σ= 4.2, size = 10 mm) within an intensity-based mask of the phantom (or a skull-stripped brain mask in further human imaging). For each voxel, the scaling factor B1 was then calculated between the measured flip angle and the nominal flip angle (80°) and expressed as a percentage. T_1 was then calculated by the VFA method, either with or without the additional voxel-wise B1 correction factor. Instead of using a single circular ROI in each tube, 3D cylindrical ROIs were used to better capture the effects of spatial variation in all axes. T_1 accuracy was calculated as in Section 5.4. As shown in Table 23, B1 correction was associated with a significant improvement in accuracy (mean error -13.6 ± 5.6 vs. 21.6 ± 5.2%, $P < 10^{-8}$, paired t-test). Hence B1 correction by this method was included in the final protocol.

Table 23 Significant improvement in T_1 measurement accuracy by adding B1 correction.

$P < 10^{-8}$ for a paired t-test of mean percentage error. T_1 values were calculated from the same acquisition as in Table 22; the reported values without B1 correction differ slightly as different ROIs were used.

Reference T_1 (ms)	**Without B1 correction**		**With B1 correction**	
	T_1 (ms)	**Error (%)**	**T_1 (ms)**	**Error (%)**
425	350	-17.6	384	-9.6
1140	830	-27.2	916	-19.6
461	376	-18.4	419	-9.1
569	440	-22.7	487	-14.4
1464	1039	-29.0	1160	-20.8
1645	1230	-25.2	1356	-17.6
292	245	-16.1	268	-8.2
787	603	-23.4	650	-17.4
251	215	-14.3	237	-5.6
Mean (SD) error		*-21.6 (5.2)*		*-13.6 (5.6)*

5.7 Correction for incomplete spoiling

As discussed previously (Section 1.8), the signal for a spoiled gradient echo sequence such as FLASH can be formulated algebraically (Equation 10), but this requires the assumption that transverse magnetisation returns completely to zero in between consecutive pulses. If the assumption holds, then signal depends only on the steady state of longitudinal magnetisation; in a balance of reduction by excitation and recovery described by T_1. If TR is much longer than T_2 (the time constant for decay of transverse magnetisation), then this assumption is met through relaxation alone. At shorter TRs, however, a method of spoiling transverse magnetisation is required. In FLASH (and most other spoiled sequences) this is achieved through RF-spoiling. The phase of sequential RF-pulses is offset every time, which after every excitation favours phase cancelling of transverse magnetisation from previous excitations. It has been recognised for some time that the accuracy of T_1 measurement using FLASH is contingent on perfect spoiling (220).

Most published brain DCE-MRI studies have used a TR of <10ms, and published guidelines suggest that a TR <3ms is 'ideal' (101). T_2 of brain tissue is in the region of 80-110 ms (241). It has previously been demonstrated that incomplete spoiling occurs as TR becomes very short (242, 243). As a result, the measured signal may be different to that predicted from the signal equation, and if so the VFA method fails to produce an accurate T_1.

An experiment was conducted to test the effect of increasing TR on the accuracy of T_1 estimation. The phantom was imaged with the familiar 3D FLASH sequence, flip angle = [5,7, 15]°, and TR = [2.48, 10, 25, 40] ms. T_1 was calculated and compared to the reference IR method. Results are shown in Table 24. In a one-way repeated measures ANOVA there was a significant difference in T_1 error according to TR ($P < 10^{-6}$), and in the post-hoc test with Bonferroni correction significant differences were seen when increasing TR to 10 ms and longer. These results suggest a breakdown of T_1 mapping accuracy at very short TRs, which may be due to incomplete spoiling. Though significant the improvement on increasing TR further than 10 ms was relatively small, and any improvement must be weighed against the significant increase in acquisition time.

Table 24 Significant improvement in T_1 mapping accuracy by increasing TR.

There was a significant effect of TR in a repeated measures ANOVA ($P < 10^{-6}$). P-values shown here are for the post-hoc test with Bonferroni correction.

TR (ms)	**Mean (SD) T_1 error (%)**	***P*-value for comparison to TR = 2.48**
2.48	21.7 (2.4)	-
10	4.4 (3.0)	$<10^{-7}$
25	3.4 (2.3)	$<10^{-5}$
40	3.6 (3.0)	$<10^{-5}$

Increasing TR to 10 ms is acceptable in the T_1 mapping sequence, as it is still possible to image a whole brain volume in 25 seconds. However, TR cannot be increased in the dynamic sequence within the constraints of the desired time resolution. This poses a problem. In the DCE-MRI analysis, T_1-time (and then concentration-time) curves are calculated by passing measured signal in the dynamic acquisition into the gradient echo signal equation (Equation 10) together with the other known parameters: signal in the fully relaxed state (S_0) which is carried forward from the VFA measurement, flip angle, and TR. The error in the dynamic signal measured at shorter TR still propagates into the T_1 calculation.

One solution is to correct the signal from the dynamic sequence for the error potentially introduced by incomplete spoiling. A correction method has previously been proposed by Baudrexel et al (243), in which a factor (C) is used to modify the flip angle ($\alpha \rightarrow \alpha'$) term in the signal equation in order to offset the error due to incomplete spoiling. It was shown that C is independent of T_1, but dependent on flip angle and TR according to the parameters of a two-dimensional polynomial. Using these calculated parameters C and therefore α' can be calculated for any combination of flip angle and TR and passed into the signal equation.

The applicability of the Baudrexel correction was tested in a phantom experiment. VFA data was collected with flip angle = [5, 7, 15]° and TR = 2.48 or 10ms. B1 mapping and correction was applied as in Section 5.6. 2D ROIs were drawn in each tube. The actual flip angle calculated using B1 correction was further corrected by the Baudrexel method, and then used for VFA calculation. Percentage absolute error from reference was calculated. As shown in Table 25 the Baudrexel correction significantly reduced error at TR = 2.48ms (26.1 vs 13.4%, P = 0.0003, paired t-test) and to a smaller degree at TR = 10ms (9.8 vs 7.9%, P = 0.02, paired t-test). Despite correction, error was still significantly reduced with the longer TR (13.4 vs 7.9%, P = 0.0001, paired t-test).

Table 25 Significant improvement in T_1 mapping accuracy with correction for incomplete spoiling.

Values are percentage error from the reference value.

Reference T_1 (ms)	**TR = 2.48ms**		**TR = 10ms**	
	Uncorrected	**Corrected**	**Uncorrected**	**Corrected**
425	20.7	12.0	3.3	1.6
1140	34.0	17.4	18.3	14.7
461	14.5	5.4	3.7	5.5
569	20.3	9.6	1.9	0.6
1464	30.4	8.6	11.9	7.5
1645	25.7	3.4	4.4	0.2
292	46.2	40.8	34.3	33.9
787	27.7	14.2	9.4	6.2
251	15.3	9.3	1.4	1.1
Mean (SD) error	*26.1 (10.0)*	*13.4 (11.1)*	*9.8 (10.7)*	*7.9 (10.8)*

Considering these results, it was decided to apply the Baudrexel correction to the dual TR DCE-MRI protocol in combination with voxelwise B1 correction (first using the B1 map to find the actual flip angle, then correcting this for incomplete spoiling). Firstly, it is shown that the most accurate VFA T_1 mapping is achieved by combining the longer TR (10ms) with the Baudrexel correction. Secondly, in the dynamic sequence the flip angle for each voxel can be corrected for the shorter TR (2.48ms).

As discussed in the start of this section, since the effect of incomplete spoiling becomes more prominent as TR becomes shorter than T_2, one would expect some variation in the completeness of spoiling in tissues with different values of T_2, such as GM and WM (241). This is potentially important if the Baudrexel correction is used in the comparison of different tissues or brain regions. However, it has been demonstrated that the correction is valid to within 2% for the range of T_2 values likely to encountered in the brain (243). Also, since the Baudrexel correction did not perfectly correct the T_1 values, it is likely that though incomplete spoiling is an important source of error, it is not the only one. In particular, the effect of longitudinal relaxation during the excitation pulse itself may become relevant at a very short TR, and should be examined in future work.

5.8 Motion correction

Subject tolerability of the lengthy dynamic acquisition is variable, and in preliminary work some datasets were corrupted by motion artefact. More subtle motion artefact could alter the signal-time curves measured from static ROIs, and lead to errors in kinetic analysis. There could also be bias due to differences in motion between groups (244), for example people with MS might be less able to tolerate lying still for the duration of the scan, and therefore move more. For these reasons it is desirable to implement motion correction of the dynamic time-series. Prospective methods were considered (245) but deemed infeasible due to logistical constraints. Retrospective motion correction was achieved offline by rigidly registering all dynamic images to the first VFA image using FSL-FLIRT (129). Two-step registration via the high-resolution MP-RAGE image was used to provide superior results for two registering relatively low-resolution images. All other images (remaining VFA images, B1 maps) were also registered to the first VFA image in this way. Visual inspection of the dynamic time-series after motion correction demonstrated improved image alignment and removal of gross subject head motion. Correspondingly, visual inspection of sample signal-time curves showed smoothing, and a reduction in rapid non-physiological signal changes during the washout phase (see Figure 24).

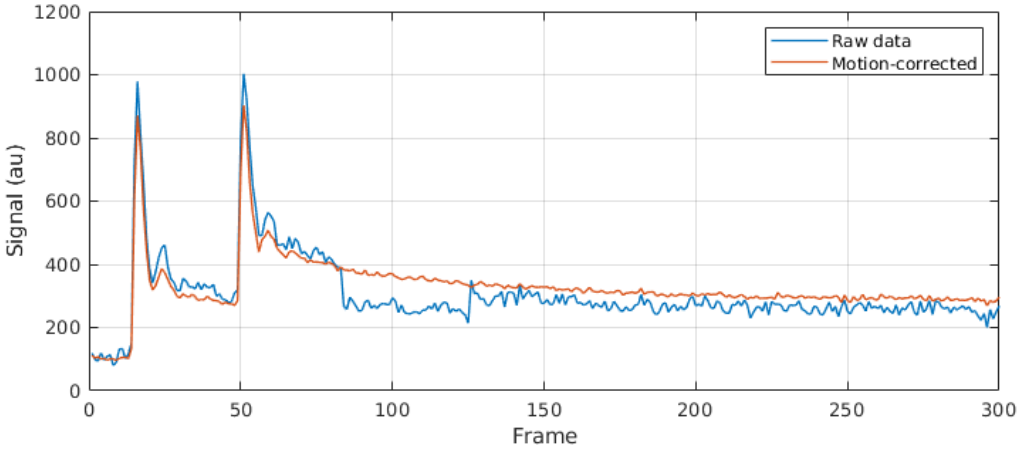

Figure 24 Example of visual improvement in signal-time curves after motion correction.

This is signal in the internal carotid artery over time, in an individual who visibly moved during the acquisition. There is a sudden change in signal during the washout phase, which is removed by motion correction. The two large peaks in signal in the initial phase reflect two bolus injections of contrast and are followed by dampened recirculation peaks.

In addition to the qualitative evaluation, motion correction was also evaluated quantitatively. After the initial rapid signal changes of bolus passage and recirculation (here defined arbitrarily as the first 100 time points), it is expected that changes in signal over time be gradual, reflecting distribution and elimination. Hence the standard deviation of the second derivative of the latter part of the signal-time curve provides a measure of temporal noise (246). Noise measured in this way can be divided by mean signal over the same period, to give SNR. 37 scans (acquired throughout the project) were re-analysed, and SNR calculated for the carotid AIF with or without motion correction. The AIF was chosen as this had previously been found to be particularly sensitive to noise and artefact related to motion. Motion correction gave a small but significant improvement in mean SNR (42.5 to 47.3, P = 0.003, paired-t-test). There was modest evidence for a greater absolute SNR improvement in MS cases versus controls (2.8 vs 8.8, P = 0.06, t-test), compatible with greater noise attributable to subject motion in MS cases.

5.9 Measurement of signal drift

Signal drift is a poorly understood phenomenon whereby signal intensity in a voxel changes during the measurement period simply as a function of time. This can arise through heavy cycling of the RF fields during operation, and heating (247). Since these changes are independent of contrast, if unaccounted for these can have a significant effect on pharmacokinetic analysis (92). To assess the presence of signal drift in the MR scanner, a healthy control individual was imaged with the

dynamic sequence (as described in Section 3.2), but without the injection of contrast. Ten ROIs were drawn in white and grey matter and for each drift was calculated as the weighted least-squares slope of mean signal over time, expressed as a percentage per second of mean baseline signal over the first 10 time points. There is no standardised method for reporting drift but this incorporates a possible effect of baseline signal and is similar to a published method (92). By this method mean drift was <10-7 % per second, and not statistically different from zero (P = 0.62, one sample t test). Visual examination of the signal-time curves also suggested the absence of significant drift (example shown in Figure 25). On this basis further attempts to measure and correct for signal drift were not pursued in this study.

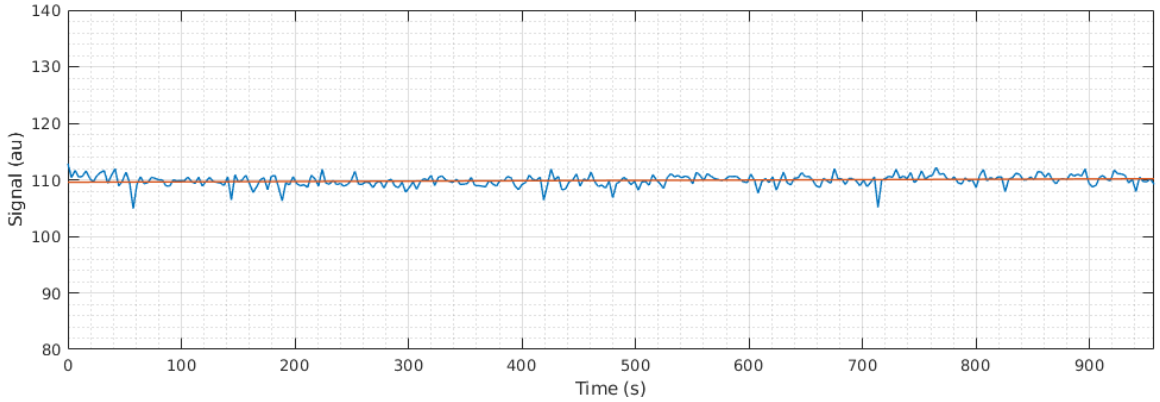

Figure 25 No evidence of linear signal drift over time.

This is an example case. The plot shows signal from a region of white matter over the duration of the dynamic acquisition (blue), and the regression line (orange). Signal is measured in arbitrary units (au); for reference, the signal difference between white and grey matter is in the region of 100-200 au.

5.10 Improving input function measurement

Based on the literature, the bolus injection protocol was changed from a single half-dose injection of 0.05 mmol kg−1 Gadovist, to a double half-dose injection scheme, with 0.05 mmol kg−1 Gadovist given at the 10th and 45th time points. This scheme has the benefit of maximising total contrast dose, to improve the contrast-to-noise ratio (11), whilst minimising the peak blood contrast concentration during bolus first-pass, which contributes to AIF measurement errors due to truncation artefact and T_2* effects (94, 248) (though truncation artefact would tend to affect measurements of perfusion rather than permeability). This injection protocol has been tested by the Larsson group at the University of Copenhagen (unpublished data), and hence was not examined in detail in this work.

Measuring an AIF from the internal carotid artery (ICA) has several pitfalls, most importantly:

- Partial volume artefact: since the artery is a relatively small structure, voxels located peripherally in the ROI will not just consist of blood (voxel size here is 1.3 x 1.3 x 5 mm). The contribution of these non-vascular voxels dampens the measured arterial waveform. Also, low-level subject motion can easily displace the artery from the ROI entirely if the ROI location is fixed between sequential images.
- Flow-related enhancement (also known as inflow artefact): spins within the imaging volume develop a new steady-state equilibrium magnetisation. Therefore, less magnetisation can be tipped into the transverse plane, and signal is lower than otherwise. A voxel in the artery, however, will contain fewer or none of these spins, as its contents are continually replenished by unsaturated spins from outside the volume. These spins contribute to an artefactually higher signal from the artery. This makes the T_1 measurement artificially low, which propagates through the analysis.

To address these difficulties manual AIF ROIs were drawn with great care, making sure to examine the frames just prior to and during contrast arrival, and selecting a region in which pre-contrast enhancement (flow-related) was minimal. The supraclinoid segment of the ICA was usually most suitable for this purpose. Baseline T_1 of the ROI was checked, to ensure that the value was reasonable for blood (or as good as possible). However, this process was time-consuming and dependent on the operator.

A potential solution to flow-related enhancement in other contexts is to extend the imaging volume so that spins entering the artery are not unsaturated. However, in healthy adults the peak systolic velocity in the internal carotid artery can approach 125 cm/second (249), and the mean lengths of the common and internal carotid arteries are 13 cm and 8.5 cm respectively (250). Therefore even if the volume were extended to the aortic arch, acquisition time were 1 second, and the AIF were created in the most distal ICA segment, unsaturated spins from outside the volume could still easily enter the ROI during acquisition.

A venous outflow function (VOF) obtained from the superior sagittal sinus (SSS) near the torcula is less susceptible to both artefacts, as it is larger, and the vessel proximal to the ROI lies within the imaging volume, and hence spins entering the ROI should be saturated. In this region the vein also tends to be easy to identify, straight, and perpendicular to the imaging volume. Many studies have used a venous input function in favour of an arterial one, and there is evidence that the choice makes little difference (251). The theoretical downside is that the shape and timing of the venous function will not exactly match the arterial function (it will be dampened), and this may affect parameter calculation, especially of CBF. As a compromise a rescaling approach was

employed. It is an established principle of tracer kinetics that the time integral of the concentration-time curve is conserved throughout the vascular tree. Hence the carotid AIF was rescaled to a venous function derived from the SSS using a derivative-free method in MATLAB to minimise the difference in area under the curve (252) (code adapted from that written and kindly provided by Professor Henrik Larsson, University of Copenhagen). An example is shown in Figure 26.

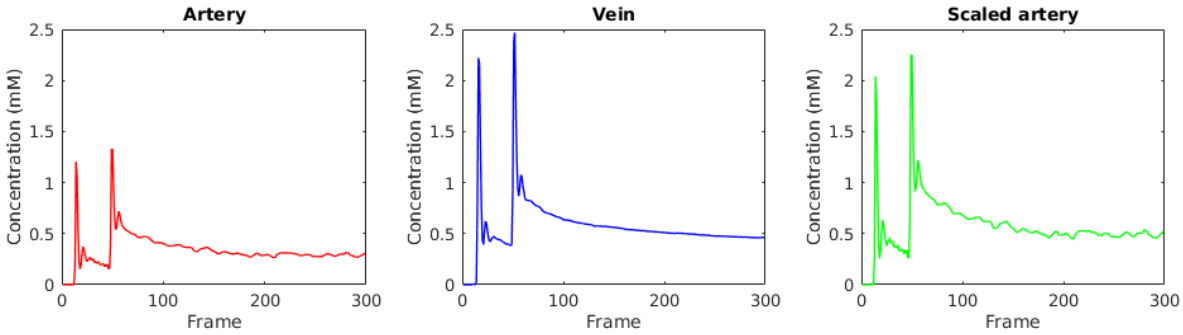

Figure 26 Scaling of arterial input function according to the venous outflow function.

The arterial function is scaled to match the area under the curve of the venous function.

Next, the process of identifying AIF and VOF voxels was automated, to reduce operator-dependence and enable seamless batch processing. High-resolution atlases of brain arterial (253) and venous (254) anatomy were used to manually generate standard binary masks of the ICA and SSS respectively. Using a two-step process, each mask was transformed from MNI space to subject T_1 MP-RAGE space using FSL's non-linear registration tool FNIRT (255), and then to dynamic space using FLIRT. The signal-time curves of all voxels within either artery or vein mask were then evaluated according to criteria based on those suggested by Mouridsen et al (256), by choosing voxels (1) with rapid signal changes shortly after the known times of bolus injection, (2) in the top decile of area-under-the-curve, (3) in the bottom quartile of roughness. Visual inspection of the resulting masks showed good results (see Figure 27). The median signal-time curves from ICA and SSS masks were then used for AIF and VOF respectively.

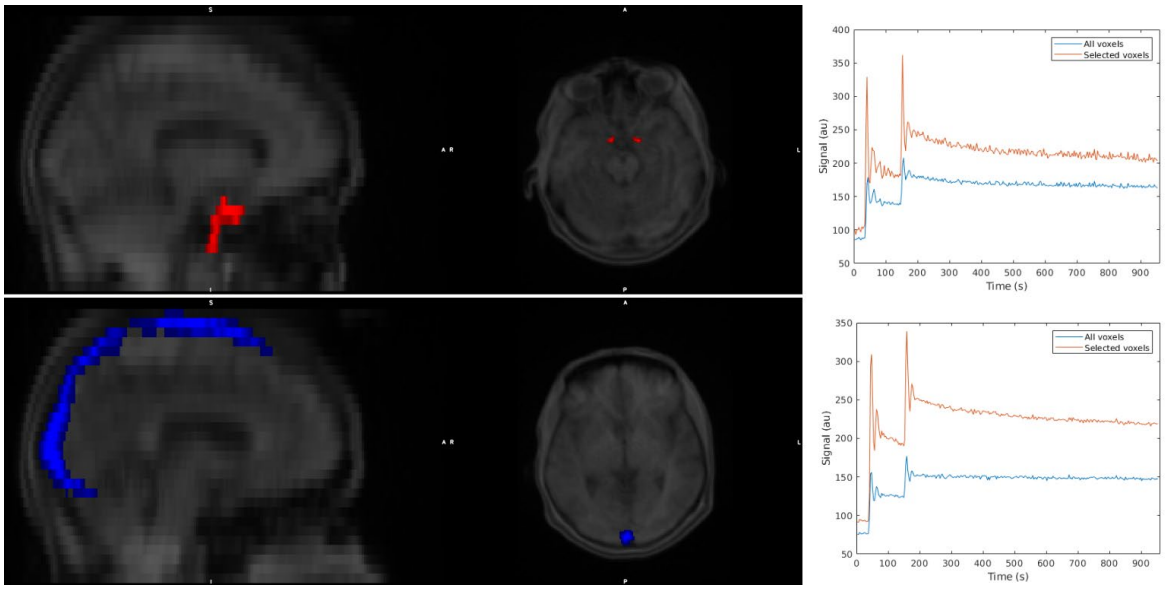

Figure 27 Demonstration of automatic input function detection.

Standard masks of internal carotid artery (top panel) and superior sagittal sinus (bottom panel) are transformed into the space of the dynamic images. Signal-time curves from all masked voxels (blue lines) are refined by selection of voxels meeting expectations of signal behaviour from knowledge of typical signal-time curves (orange lines).

5.11 Automated tissue segmentation

Tissue-type segmentation was performed using FSL-FAST to generate probabilistic maps of WM, GM, and CSF. Automated lesion segmentation was performed using the lesion growth algorithm from LST version 20.0.15 (140) as previously described (Section 3.3.3.4). FLAIR imaging was changed from a 2D to a 3D sequence (TR = 5000 ms, TE = 397 ms, TI = 1800 ms, field-of-view = 256 × 248, voxel size 1.0 x 1.0 x 1.1 mm^3, 176 slices) which is superior for the detection of MS lesions (257) and the acquisition for which this technique has been best validated (140, 258). LST also performs well with age-related WM lesions (259, 260); this is useful as the algorithm can be applied uniformly to all cases (MS or control). In cases with lesions, lesion filling of the MP-RAGE image was also conducted using LST and the prepared lesion mask, prior to tissue-type segmentation with FAST. The lesion mask was subtracted from the WM mask to give a NAWM mask. The mask of all lesions was combined with the tissue masks to give masks of WM and GM lesions, as well as all lesions. All masks were then transformed into dynamic space using FSL-FLIRT and binarised with a pre-specified threshold (0.95). Since K_i measurement is prone to outlier

results in non-brain tissue (without a BBB), vessels, or CSF, the median value of voxels within each mask was quoted as the representative value for that tissue.

5.12 Final protocol and analysis pipeline

The final protocol incorporated all of the incremental advances described above. Total acquisition time was 40 minutes. The detailed exam card with all sequence parameters is given in Appendix F.

The analysis pipeline was developed in MATLAB and optimised for parallel execution on an 8-core workstation running Linux Red Hat 7. The development of an automated pipeline enabled high-throughput analysis of a large volume of scans by a single operator. Figure 28 outlines the flow through the pipeline. Execution time was approximately 2 hours per case; the majority occupied with motion-correction (c. 20 minutes) and voxel-wise parameter fitting (c. 60 minutes). All intermediate files of analysis were stored and available for manual quality control. An example of voxelwise parameter maps is given in Figure 29.

This protocol was optimised for the detection of subtle BBB leakage. However, there is limited evidence regarding the measurement variability of DCE-MRI (261). Certain of the optimisations described here might be expected to reduce variability, by removing effects dependent on the scanner (such as B1 inhomogeneity), subject (such as motion), or operator (such as manual ROI creation). If the aim is to use DCE-MRI to study change in K_i within a subject over time, then a study of the measurement variability of this protocol is essential. This is dealt with in the next chapter.

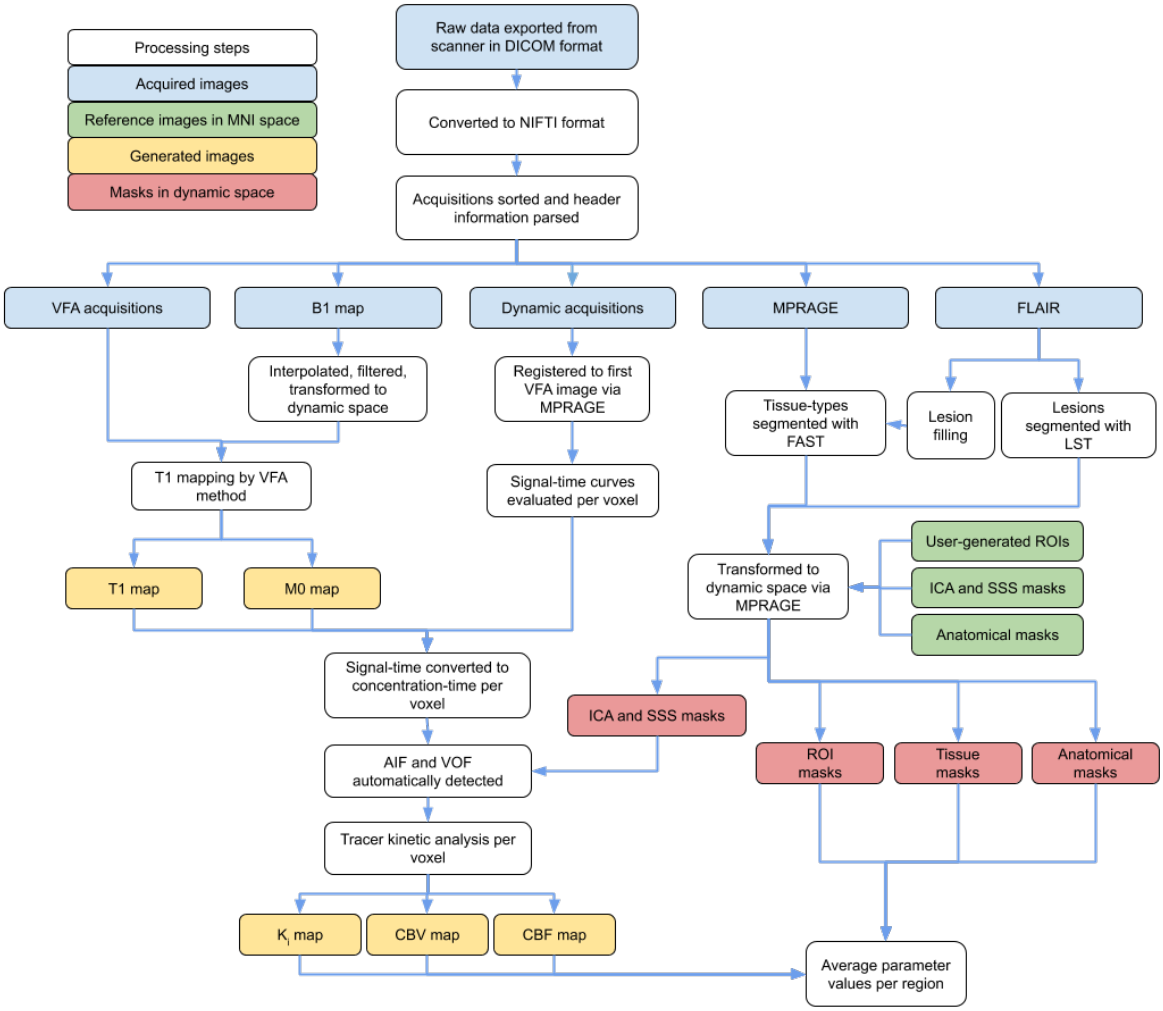

Figure 28 Image processing pipeline.

'Dynamic space' refers to the shared space of dynamic and VFA acquisitions.

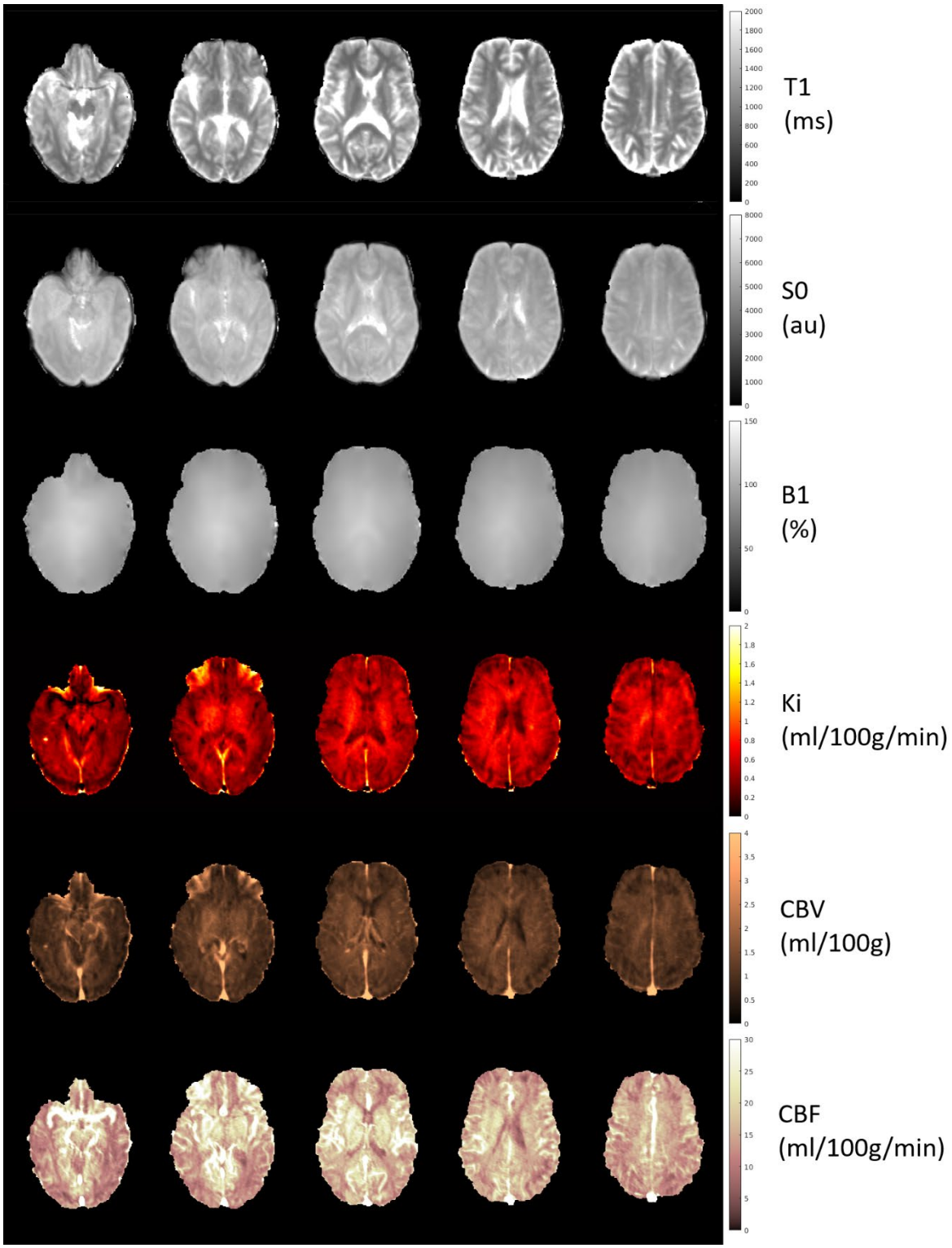

Figure 29 Example of voxelwise parameter maps.

From left to right, these are five slices from a single individual with MS. The B1 map has been interpolated, but the other maps have not been altered in any way.

Chapter 6 Assessment of Measurement Variability in Dynamic Contrast-Enhanced Magnetic Resonance Imaging

6.1 Introduction

The previous chapters covered the development and optimisation of DCE-MRI. The SIBIMS Study (Chapter 7) will use DCE-MRI to perform BBB permeability measurements at two timepoints, to address the hypothesis of BBB disruption during systemic infection. If DCE-MRI is to be used for this purpose, it is crucial to quantify measurement variability over the relevant time interval.

6.2 Aims

1. Establish the minimum detectable effect size for the SIBIMS study, by quantifying measurement variability over the relevant time interval (two months) and in the relevant population (adults aged 40-80).
2. Establish a dataset to test and refine the optimisation strategies outlined in Chapter 5, to maximise robustness of the protocol to detect subtle BBB changes.

6.3 Background

Within a subject, the measured value of any biomarker will fluctuate over time due to two components: analytical imprecision and biological variation. Analytical imprecision reflects inherent variation in the measurement method itself. For K_i measurement by DCE-MRI there are several sources of analytical imprecision, outlined in Table 26. As per the definition of precision (262), these factors influence the closeness of repeated independent measurements of K_i obtained under a stipulated set of conditions, and assuming that the 'ground truth' value of K_i is invariant. In this context, 'a stipulated set of conditions' means that the acquisition hardware, protocol, and analysis pipeline remain constant. 'Independent' means that each sequential measurement is taken such that it is not influenced by the previous measurement(s); importantly this means leaving an adequate time interval for complete washout of contrast agent.

Table 26 Possible sources of analytical imprecision in BBB permeability measurement with DCE-MRI.

AIF = arterial input function, ROI = region of interest.

Source of analytical imprecision		**Possible countermeasures**
Subject	Motion	Ensure subject comfort; software motion-correction; prospective motion-correction
	Body temperature	Measurement of subject temperature
	Contrast agent pharmacokinetics	Measurement of individual AIF per subject
Hardware	Noise, which arises in the MR signal from sources including Johnson noise[5] from the human body, coil and receiver electronics, and extraneous RF fields.	Select acquisition parameters to optimise SNR (coil selection, voxel size, field of view, bandwidth, number of excitation); post-acquisition filtering; averaging of signals from multiple voxels in ROI
	B1 inhomogeneity	Shimming; B1 mapping and correction
Environment	Ambient temperature	Control of ambient temperature; measurement of temperature
Operator	Operator-dependent components of analysis, for example placement of ROIs for AIF or tissue function extraction	Automated AIF extraction (or use of a standard AIF); automated tissue ROI placement or voxel-wise analysis

As with any biomarker, K_i is also subject to biological variation. This reflects intrinsic changes in the true value occurring in the absence of any change in health or disease state. The most

[5] Johnson noise (or thermal noise) arises because the charge carriers within a conductor (usually electrons) experience random motion as a function of temperature.

important source of biological variation is usually fluctuation around a 'set point' as part of normal homeostasis. For some biomarkers, important biological variation may also occur over the lifecourse or in a cyclical fashion; these may also be relevant for K_i (217, 263). Possible factors which may influence BBB permeability without any apparent change in health or disease state are outlined in Table 27. These are all hypothetical, as there is limited human evidence for the relevance of these factors or the strength of each effect.

Table 27 Possible sources of biological variation in BBB permeability.

Source of biological variation	**Possible countermeasures**
Systemic inflammation, which may increase permeability (62). Episodes of systemic inflammation can occur in healthy individuals without overt symptoms (117).	Screening for symptoms of systemic inflammation; biochemical indices of systemic inflammation.
Medication, for example non-steroidal anti-inflammatory drugs (NSAIDs) may reduce permeability (63).	Drug history; avoidance of acute medications before scanning.
Menstrual cycle, for example oestrogen may reduce permeability (263).	Menstrual history; synchronise repeated scans to same point in cycle.
Diet, for example chronic saturated fat intake may increase permeability (264), whereas caffeine may reduce it (265).	Dietary history.
Physical exercise, which may reduce permeability (266).	Record physical activity.
Shear stress on vascular endothelium, which may increase permeability (267). Shear stress is dependent on blood flow and viscosity, which are themselves subject to biological variation (268, 269).	Measure plasma viscosity.

The total random variation in serial within-subject measurements is therefore a combination of both analytical imprecision and biological variation. Any change must exceed the likely bounds of random variation to be considered significant. When a new method is developed for the measurement of some biomarker its analytical imprecision should be determined experimentally, usually by performing replicate analyses on a stable sample according to recognised protocols

(270). Serial measurements from healthy volunteers can then be used to determine what component of random variation reflects biological variation (271).

There are challenges in transferring this gold-standard methodology from the laboratory to DCE-MRI. It is impossible to measure the same 'sample' in simultaneous replicate. A scan-rescan study can be used to estimate analytical imprecision, and when the interval between scans is short it is assumed that the effect of biological variability is minimised. However, for measurements to be independent the interval must be long enough to allow for complete washout of contrast agent, as residual contrast may alter the pharmacokinetics. For gadobutrol this is 72 hours (272). As there is no data on biological variation in BBB permeability (by DCE-MRI or any other method) it is impossible to know whether this interval is appropriate. Many of the possible factors described in Table 27 could conceivably operate within an interval of days.

Another approach is to study analytical imprecision using a phantom, in which the effects of biological variation are removed. Perfusion phantoms are available (273). However, not all sources of imprecision operate within a phantom, and therefore it is difficult to apply the findings to *in vivo* measurements. While it would be ideal to be able to quantify the relative contribution of technical and biological components to the total variability between two repeated measurements with a defined interval, the most pressing need is to quantify the total variability itself, in order to enable sample size calculations for studies such as SIBIMS (Chapter 7). The pragmatic approach, which is most applicable to the intended use case, is to study within-subject scan-rescan variation over the duration of interest. This is essential since a comprehensive study of this kind has not been performed and would be of use to investigators worldwide. In one study, most subjects were scanned with an interval of 1 day, which raises the possibility that the measurements were not independent due to inadequate contrast washout (274). In another study, the median interval was 16.5 months (275), a timescale over which the effects of disease progression are difficult to untangle from biological variation.

6.4 Methods

6.4.1 Study design

Participants were scanned in two separate sessions, as close as possible to two months apart. The rationale for this time interval was to mirror the protocol of the SIBIMS study (Chapter 7), as the results of this study will directly inform the calculation of the minimum detectable effect size in SIBIMS. First and second scans were performed in an interleaved fashion to prevent the possibility of systematic bias due to longitudinal scanner signal drift.

6.4.2 Ethical approval

The study was approved by the National Research Ethics Service Committee London Surrey (reference 18/LO/2015) and the institutional review board (ERGO 46018). Experiments were conducted in accordance with the Declaration of Helsinki and all subjects gave informed written consent.

6.4.3 Study participants

Healthy adult individuals were recruited by advertisement. Inclusion criteria were as follows: age 40-80 (comparable to the age of the progressive MS population to be studied), no systemic or neurological disease (including migraine), no regular medication use, and no family history of MS. All subjects were examined by a neurologist (me) prior to inclusion. Baseline demographic and clinical data was collected at inclusion.

6.4.4 Measurement of potential sources of biological variation

Evidence of systemic inflammation was sought at each scanning session through clinical questioning, temperature measurement, and SicknessQ (276), a validated questionnaire which records the incidence and severity of sickness behaviour symptoms. In the event of a symptomatic episode (such as infection) the scan was deferred until complete symptomatic recovery. A drug history including NSAID score (277) was also recorded.

6.4.5 Measurement of asymptomatic systemic inflammation

In addition to the above urinary neopterin was also measured by UPLC-MS of a morning urine sample from each session (method detailed in Section 3.3.2). Blood samples were also taken at each session and analysed for the inflammatory markers C-reactive protein (CRP) and erythrocyte sedimentation rate (ESR).

6.4.6 Measurement of haematocrit

Haematocrit was measured in a venous blood sample taken from an arm vein at each scanning session and scaled for the effect of vessel size using the factor 0.85 (107, 108). The effect on variability of converting K_i to K_{trans} using the contemporaneous small vessel haematocrit was examined.

6.4.7 DCE-MRI protocol and analysis

DCE-MRI was performed to calculate voxel wise whole-brain K_i according to the optimised protocol detailed in Chapter 5, though for logistical reasons the following non-essential acquisitions were omitted: FLAIR, T_2, short TR VFA mapping, post-contrast MP-RAGE. The following optimisation steps were testable *in silico*:

- B1 correction (see Section 5.6)
- Baudrexel correction for incomplete spoiling (see Section 0)
- Motion correction (see Section 5.8)
- Automatic AIF detection (see Section 5.10)
- AIF rescaling (see Section 5.10)

As previously described, these optimisation steps have all been tested in terms of their effects on components of the analysis pipeline (Chapter 5). However, the ultimate purpose is to improve the accuracy and precision of K_i measurement, not, for example, T_1 or SNR *per se*, and so it is important to know the effect of these optimisations on the parameter of final interest. Therefore, the analysis was repeated with (1) no optimisations, (2) each optimisation in turn, (3) all optimisations. K_i, CBV, and CBF were calculate for the whole brain, GM, and WM. The effect of the Baudrexel correction was tested alongside the other optimisations, though since this is a systematic correction post-acquisition an obvious effect on K_i was expected.

Importantly, an *a priori* decision was made regarding negative K_i values, which sometimes arise in Patlak fitting. Random noise can be positive or negative. Although it is theoretically impossible for the true value of BBB permeability to be negative, if the true value is close to zero (as is likely in the healthy brain), then negative K_i values may be measured because of noise. In other studies, negative values have been removed by a positivity constraint (92), upper percentile (274), positive threshold (275), or instead by reporting the volume fraction of detectable leaking tissue (278). However, since the object of this study is to account for analytical imprecision including random noise components, no positivity constraint was applied to the data (neither to K_i values nor to concentration-time curves).

6.4.8 Statistical analysis

The validity of K_i measured by DCE-MRI was tested against the biological expectations set out in Section 4.2. Briefly, these are that:

- CBV (and K_i) should be higher in GM than WM, due to the higher vascular density in GM. This was tested using a pairwise within-subject comparison. The GM/WM CBV (or K_i) ratio was reported. Histological study suggests that the GM/WM CBV ratio should be approximately 2.9 (212).
- CBV should predict K_i, since K_i is a compound marker of vascular permeability and surface area. In other words, the higher K_i in GM should be explained by the higher CBV in GM. This was tested in a multivariate linear regression with K_i as dependent, and CBV, CBF, and tissue type as predictors. The β coefficient and P value were quoted for CBV.
- K_i should not correlate with CBF, as predicted by the Crone-Renkin equation for a low permeability tissue. This was tested in the regression in the point above.

In addition, summary K_i values (whole brain, WM, or GM) were examined, as well as the percentage of voxels with negative K_i values, out of all voxels analysed. These tests were performed on only the first scans of all participants to ensure independence of observations (chosen arbitrarily).

Paired scan-rescan data was used to calculate metrics for variability analysis, using published guidance (279). Within-subject coefficient of variation (COV) is widely used for this purpose. The within-subject COV derived from this study was used to derive sample sizes for future studies, according to published methods (280). The 95% limits of agreement for the within-subject differences were also calculated and used to indicate the minimum detectable change. In addition, Bland-Altman analysis was used to assess agreement between scanning sessions.

To determine the effect of the optimisation steps, analyses were conducted with either no optimisations, each optimisation in turn, or all optimisations. Results were compared between these methods using one-way repeated measures ANOVA with post-hoc tests using Bonferroni correction where appropriate.

In an exploratory analysis to investigate the possible effect of potential sources of biological variation, correlations were examined between inter-session differences in K_i and inter-session differences in the potential source measures. The effect of time of day on K_i values and variability was also examined.

$P < 0.05$ was used to reject the null hypothesis.

6.5 Results

6.5.1 Participants

Recruitment began in August 2019 and was halted by the COVID-19 pandemic in March 2020. 7 participants completed the study. An additional 3 participants had the first scan but were unable to complete the study due to the pandemic. Baseline demographics are shown in Table 28.

Table 28 Baseline demographics for participants in the variability study.

Continuous variables are given as mean (SD).

N	7
Age (years)	56.0 (7.3)
Sex (% female)	85.7%
Ethnicity (% White British)	100%
Body mass index (kg/m^2)	24.6 (2.3)
Smoker (%)	0%
Handedness (% right-handed)	100%

6.5.2 Effect of optimisation steps on measurement validity

For the first scans of all participants, the effect of optimisation steps on the value of whole-brain K_i, individually or in combination, is reported in Table 29. Optimisations significantly decreased mean K_i ($P = 0.03$) and increased the GM/WM CBV ratio ($P = 0.01$) and percentage of negative voxels ($P = 0.02$). In the post-hoc tests the only single optimisations with a significant effect versus no optimisation were the B1 and Baudrexel corrections. B1 correction significantly increased the GM/WM K_i ratio ($P = 0.0003$) and CBV ratio ($P = 0.0004$). Baudrexel correction significantly decreased K_i ($P = 0.03$) and increased the percentage of negative voxels ($P = 0.01$).

Table 29 Effect of optimisation steps on values of whole-brain K_i and measures of validity.

P-value is from a one-way repeated measures ANOVA with analysis method as the within-subject factor.

Regression parameters are from a multivariate linear regression with K_i as dependent, and CBV, CBF, and tissue type as predictors. CBF or tissue type did not predict K_i in any model.

	No optimisations	**Motion correction**	**B1 correction**	**Baudrexel correction**	**Auto-input function**	**Input function scaling**	**All optimisation**	**P-value for method in ANOVA**
Mean (SD) K_i (ml/100g/ml)	0.54 (0.41)	0.52 (0.39)	0.56 (0.43)	0.28 (0.20)	0.50 (0.20)	0.30 (0.12)	0.11 (0.06)	0.03
Mean (SD) K_i difference from analysis with no optimisations (ml/100g/min)	n/a	-0.02 (0.09)	0.02 (0.03)	-0.27 (0.30)	-0.04 (0.48)	-0.26 (0.33)	-0.43 (0.42)	n/a
Voxels with negative K_i values (%)	5.67 (7.86)	1.34 (1.84)	5.67 (7.86)	15.21 (11.31)	9.44 (7.63)	5.70 (7.90)	19.97 (9.00)	0.02
Mean (SD) within-subject GM/WM K_i ratio	1.05 (0.35)	0.80 (0.17)	1.48 (0.39)	1.95 (1.22)	0.96 (0.46)	1.06 (0.35)	1.74 (1.97)	0.25
Mean (SD) within-subject GM/WM CBV ratio	1.14 (0.23)	1.00 (0.16)	1.51 (0.28)	2.10 (0.99)	1.15 (0.23)	1.14 (0.23)	2.12 (1.06)	0.01
β coefficient for CBV to predict K_i (P-value)	0.37 (0.21)	0.28 (0.34)	0.34 (0.26)	0.38 (0.19)	0.71 (0.007)	-0.04 (0.91)	0.62 (0.04)	n/a

Given the significant effect of the B1 correction on the GM/WM CBV (and K_i) ratios, a further investigation was conducted into potential B1 differences between GM and WM. For each of the scans analysed above, mean B1 was calculated in GM or WM segments. B1 was higher in WM compared to GM (103.41 vs 101.33%, P = 0.04, t-test).

In an ANCOVA with K_i (using all optimisations) as outcome, individual participants as factors, and time of day as covariate, there was no effect of time of day on measured values of K_i (P = 0.38).

6.5.3 Scan-rescan variability

The mean (SD) interval between scan-rescan sessions was 10.0 (2.2) weeks. The within-subject variability metrics are reported in Table 30, including the effect of optimisation steps individually or in combination. COV improved from 79% to 32% with the use of all optimisation steps, but in a one-way repeated measures ANOVA there was no significant difference in COV between the different methods (P = 0.27). In the post-hoc tests, no single optimisation had a significant effect compared to no optimisations.

Table 30 Scan-rescan variability results for whole-brain K_i.

	No optimisations	**Motion correction**	**B1 correction**	**Baudrexel correction**	**Auto-input function**	**Input function scaling**	**All optimisation**
Mean (SD) within-subject difference in repeated K_i measurements (ml/100g/min)	-0.17 (0.68)	-0.12 (0.58)	-0.16 (0.70)	-0.27 (0.29)	-0.03 (0.35)	-0.07 (0.16)	-0.01 (0.07)
Mean within-subject coefficient of variation	79%	78%	81%	56%	39%	38%	32%
95% limits of agreement (ml/100g/min)	-1.49-1.16	1.25-1.02	-1.53-1.21	-0.84-0.30	-0.71-0.65	-0.38-0.25	-0.12-0.14
Difference between 95% limits of agreement (ml/100g/min)	2.66	2.27	2.73	1.14	1.37	0.62	0.26

The data analysed with all optimisations was taken forward for Bland-Altman analysis (Figure 30). There was no evidence of proportional bias on the plot or by linear regression (P = 0.26).

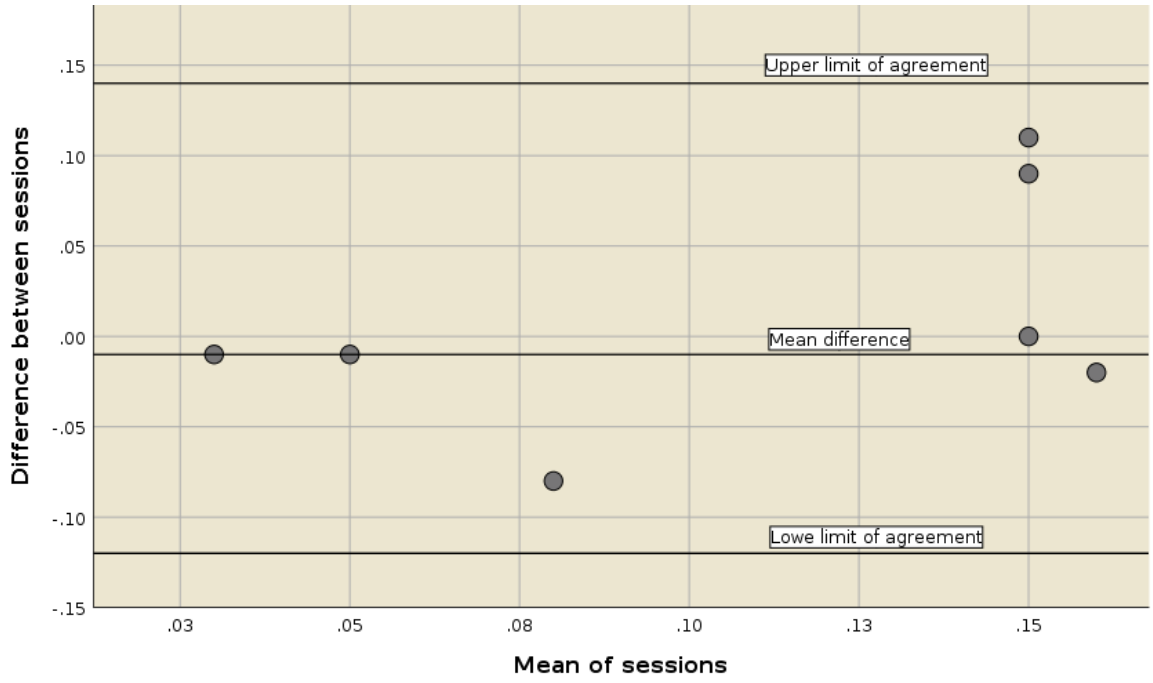

Figure 30 Bland-Altman plot of scan-rescan K_i measurements.

Values are from the analysis with all optimisations.

Figure 31 shows the scan-rescan K_i values in the analysis with all optimisations. Four participants had inter-session differences very close to zero (mean COV 14%), whereas three participants had more substantial differences (mean COV 56%). These two groups did not differ in any baseline parameters, though there was modest evidence that the group with greater variability were scanned with a shorter interval (8.3 vs 11.3 weeks, P = 0.06, t-test). For all participants, there was no correlation between the scan-rescan K_i difference and the difference in time of day that scans were performed (P = 0.84, Pearson's).

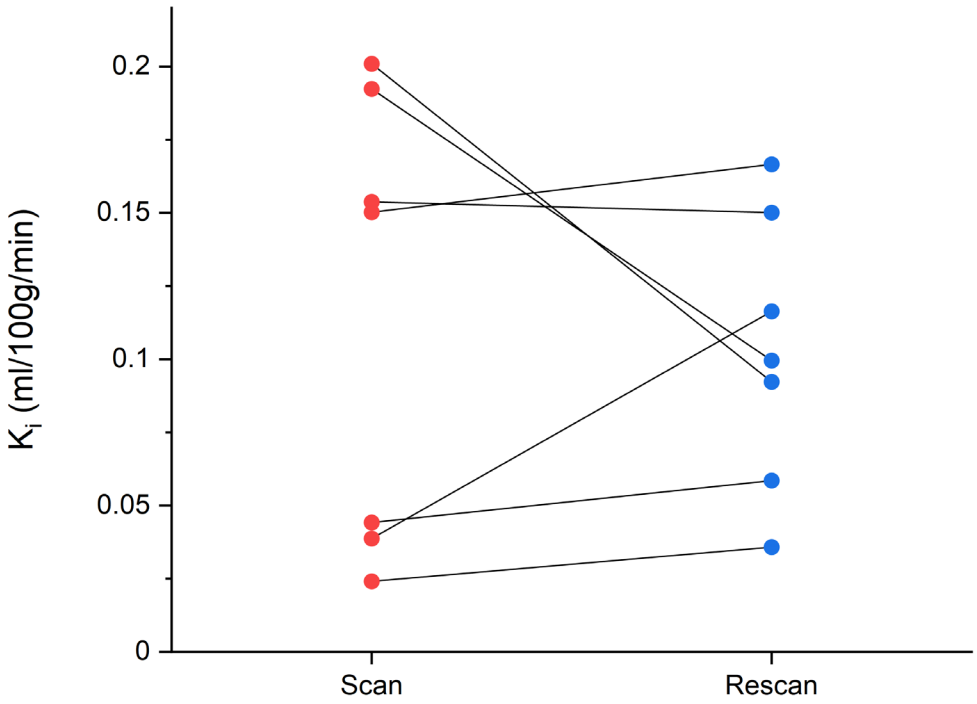

Figure 31 Scan-rescan results for whole brain K_i, using all optimisations.

Each line represents an individual.

The analysis was repeated using all optimisations but restricting to WM or GM voxels; COV was 42% or 90% respectively (no significant difference by paired t-test, P = 0.18).

6.5.4 Potential sources of biological variation

There were minimal differences between measurements of potential sources of biological variation at each scanning session, as shown in Table 31. There were no significant correlations between inter-session differences in K_i (by the fully optimised method) and inter-session differences in these variables. Neither was there any correlation between inter-session K_i difference and inter-session interval (P = 0.29, Pearson's).

Table 31 Investigation of potential sources of biological variation in K_i.

Values are mean (SD). P-values are from a paired t-test comparing sessions.
* For all but one participant, CRP was below the lower limit of detection at both sessions.
NSAID = non-steroidal anti-inflammatory drug, UNCR = urinary neopterin-to-creatinine ratio, CRP = C-reactive protein, ESR = erythrocyte sedimentation rate.

Measure	**First session**	**Second session**	**P-value**
SicknessQ	0 (0)	0 (0)	n/a
NSAID score	0 (0)	0 (0)	n/a
Temperature	36.7 (0.2)	36.7 (0.2)	0.44
UNCR (µmol/mol)	126.54 (62.35)	135.12 (43.61)	0.65
CRP	4*	4*	n/a
ESR	3.0 (1.5)	3.3 (2.2)	0.18

6.5.5 Sample size calculation using measured variability

Using the measured variability in within-subject K_i over a relevant timeframe, it is possible to calculate the sample sizes required to demonstrate an estimated change in means. Results are shown in Table 32. The fully optimised method (COV = 32%) is used here.

Table 32 Sample sizes required to demonstrate a change in K_i in a longitudinal study.

Based on a two-sample two-sided test with type 1 error 0.05 and 80% power.

% change in mean	5	10	15	20	25	30	35	40
N per group	626	148	62	33	20	13	9	6

6.5.6 Effect of haematocrit correction

There was a trend for a small difference in venous haematocrit between scanning sessions (0.39 vs 0.41, P = 0.10, paired t-test, mean within-subject COV 2.9%). However, converting K_i to K_{trans} (using the method with all optimisations) had no effect on variability (mean COV 32.1% vs 32.4%, P = 0.77, paired t-test).

6.6 Discussion

6.6.1 Key results

Within-subject COV of whole-brain K_i measured using paired DCE-MRI in healthy control subjects over 2 months was 79%, but reduced to 32% with the optimisation steps discussed in Chapter 5. At this level of measurement variability, a sample size of 33 would be required to detect a 20% change in K_i in repeated measurements, with type 1 error 0.05 and 80% power. The combination of optimisation steps also significantly lowered the values of K_i measured, and increased in the GM/WM K_i and CBV ratios in line with biological expectations. None of the proposed sources of biological variation explained K_i variability in this dataset.

6.6.2 Limitations

The sample size of this study was unfortunately limited by the pandemic but, since systematic study of measurement variability for quantitative imaging biomarkers is a relatively emergent field, it is not dissimilar to some published reports (281, 282). The potential for type 2 error may have been high, and some statistical tests were difficult to interpret in the small sample. However, trends were observed which are compatible with the theoretical underpinnings.

This study was designed pragmatically to capture measurement variability, without attempting to separate components of biological variation and analytical imprecision. An exploratory analysis of potential sources of biological variation did not yield any confirmation of effects for these sources. However, these sources were hypothesised based largely on the pre-clinical literature of animal and *in vitro* studies, this study was likely under-powered to detect a true effect, and the range of variation within these potential sources was small. Moreover, no attempt was made to account for analytical imprecision within the measurements of these potential sources themselves. An additional measurement timepoint would have been useful; for example, if participants were scanned at both a short and a long interval, the difference in variability between interval durations could give an indication as to the relative effects of analytical imprecision and biological variability.

The precision profile of a biomarker may vary within the range of the measurand or within different subpopulations (279). In this study, there was no evidence of proportional bias in the Bland-Altman plot, but in a larger sample it would have been appropriate to compare COV between males and females or older and younger individuals, for example.

The rationale for the choice of participants was to provide a group comparable to that in the SIBIMS study (Chapter 7). However, only healthy controls were included, not people with MS. This decision was made since biological variation of K_i – intrinsic changes in the true value occurring in the absence of any change in health or disease state – would be impossible to distinguish from pathological changes in people with MS, a condition in which BBB disruption is an integral feature of disease (24).

6.6.3 Interpretation

This study provides a rationale for using the optimisation steps tested here. These analysis steps cannot influence biology, and hence the reduction in COV from 79% to 32% by their application suggests the presence of significant analytical imprecision. The effect seems to be synergistic, as the combination of all optimisations gives a greater reduction in variability than any one step in isolation. The two steps with greatest effect (though not significant in the post-hoc tests) are both concerned with improving input function measurement; this is perhaps unsurprising, as deriving an input function from a small ROI susceptible to partial volume and inflow artefacts is challenging, and prone to operator-dependence (282). In analyses using different optimisations (or none), the within-subject GM/WM K_i ratio was always greater than 1, as expected and recapitulating previous results (see Section 4.4). When using all optimisations, the GM/WM CBV ratio came closer to the value of 2.9 reported from histological study (212), and CBV was able to predict K_i, demonstrating the expected behaviour of the PS product.

In particular, B1 correction significantly increased the GM/WM K_i (and CBV) ratios. Examining a typical B1 map (Figure 32), it is apparent that B1 is higher in the brain centre compared to the edge. This is a characteristic distribution, attributed to constructive interference of standing waves induced from dielectric resonance (283). Hence WM will tend to experience a higher flip angle than cortical GM. A systematically higher flip angle in WM will give rise to a positive bias in signal relative to GM. This positive bias will inflate K_i in WM, and erode the GM/WM difference. This highlights the importance of B1 correction when using DCE-MRI for regional measurements.

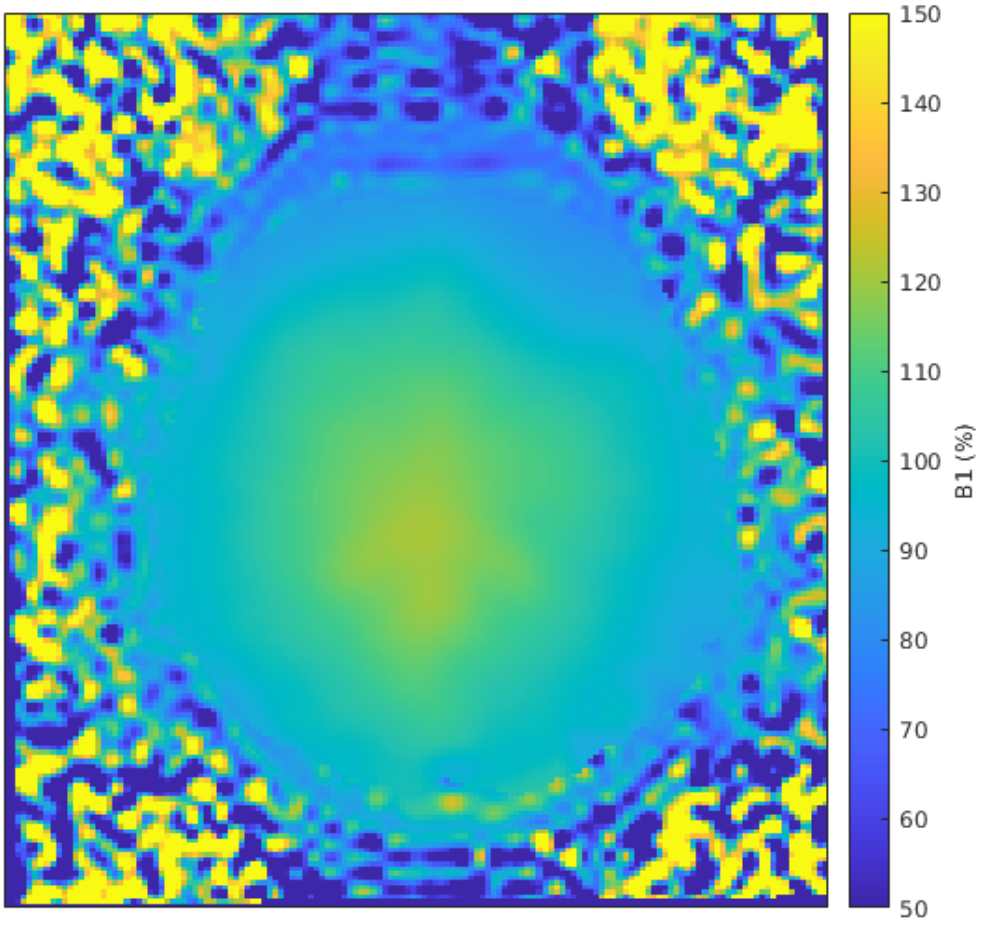

Figure 32 Example B1 map from an individual in the measurement variability study. B1 is higher in the brain centre compared to the edges.

There was a suggestion of greater measurement variability in GM compared to WM, a finding which has been reported before (274). This may be due to the smaller number of GM voxels available for analysis, and the higher likelihood of partial volume artefact for cortical GM, which may include CSF and pial microvessels (despite the strict threshold enforced here). Alternatively, there may be greater biological variation in GM permeability related to neurovascular coupling to activity and metabolism, as is reported for perfusion (284).

The optimisation steps also influenced K_i values measured, in general bringing the values down. It is reassuring that the values for K_i measured when using all optimisations were broadly similar to those in other DCE-MRI studies, using different protocols and scanners (23, 91, 105, 106). The greatest effect for an individual step was seen with the Baudrexel correction, supporting the work done in Section 0. An effect with this optimisation was to be expected since this is a systematic correction post-acquisition. A full factorial analysis was not conducted here given the small sample, but there is likely to have been an interaction between B1 and Baudrexel corrections, since the latter relies on the flip angles measured by the former. Since there is no 'gold-standard'

method for determining BBB permeability in humans, it is not possible to compare K_i measured by DCE-MRI to ground truth and comment on the accuracy. For example, the effect of optimisation steps was to bring the group mean K_i value closer to 0.03 ml/100g/min, the reported K_i value in healthy control individuals using positron emission tomography and the tracer ^{68}Ga-EDTA (285). However, the behaviour of ^{68}Ga-EDTA is unlikely to be directly comparable to that of gadobutrol due to differences in molecular mass (360 vs 605 Daltons) and other physiochemical properties including protein binding (286), and so a direct comparison is not possible.

As well as bringing down K_i values, optimisation steps also tended to increase the proportion of voxels with negative values. Dealing with negative values, which are common in DCE-MRI, is an unresolved issue (261). Other studies have imposed constraints to remove the effect of such voxels, though recent consensus guidance recommends against this (100). If the true value of K_i in the healthy brain is close to zero, then it is likely that negative values will arise due to random noise, especially when measurements are made at a voxelwise level with low contrast-to-noise ratio. If these voxels are excluded, then the reported value of K_i will be biased. Hence in this study a simple average (median) of all voxels was used, as recommended.

Within the study group, four participants had very little variation whereas three had more substantial variation. Group comparison did not reveal any baseline factors to distinguish these groups. The finding that the group with higher variation tended to have a shorter inter-session interval is difficult to explain and is likely to be a chance finding. Also, there was no evidence of a time of day effect on variability. Time of day could influence K_i values either through analytical imprecision, for example through gradient coil heating during scanner use (287), or biological variation, as many physiological processes display diurnal variation. However, no effect of time of day on K_i values was seen in this study.

Of the remaining 32% variation, it is difficult to determine what component is biological and what is analytical variation. None of the potential sources of biological variation explored here were proven to be relevant, though none showed significant within-subject variation. Other factors as outlined in Table 27 may be relevant.

Other studies have examined the measurement variability of DCE-MRI in the brain and are summarised in Table 33. Reported COVs are lower, however, significant methodological differences are relevant. Importantly, previous studies have used a much shorter timeframe, days rather than months, which may reduce the impact of some sources of biological variation. Also, these studies tended to use small regions of interest rather than the whole brain or tissue segments, and many used constraints on K_i values to limit the effects of random noise. Also, B1 inhomogeneity was likely less of a problem with the lower field strengths used in earlier studies.

Table 33 Summary of studies reporting measurement variability in brain DCE-MRI.

For comparison, whole brain volume is approximately 1.3 litres.

Author	**Participants**	**Field strength (Tesla)**	**Inter-session interval**	**Region of interest**	**Constraints**	**COV**
Jackson et al, 2003 (281)	Glioma (n = 9)	1.5	36-56 hours	Tumour (~70ml)	Voxels constrained by K_i, v_e, and fit quality	7.7%
Roberts et al, 2006 (282)	Glioma (n =4)	1.5	36 hours	Tumour (~50ml)	Only visibly-enhancing voxels included	8%
Wong et al, 2017 (274)	Cerebrovascular disease (n = 16)	3	1-8 days (1 day for most)	Periventricular white and grey matter (~250ml)	75^{th} percentile	WM = 11.6%, GM = 14.4%

DCE-MRI has also been extensively studied in the oncology field, and though there are differences with brain DCE-MRI, there are findings of relevance to the current study. For example, the COV of K_i is reported as 19.1% (288) or 24% (289) for visceral tumours over one week, and around 40% for neck muscle over two weeks (290).

The within-subject COV of haematocrit found here was very similar to the reported value of 2.8% (115). Since measurements were made at each scanning session, it was possible to correct each individual's K_i values to K_{trans} at each timepoint. However, this correction had no effect on the variability of BBB permeability measurements. There may have been an improvement in accuracy, though as discussed above this is difficult to prove.

6.6.4 Implications and future directions

There is an unmet need for technical and biological validation of DCE-MRI (261). With the increasing use of quantitative imaging biomarkers, knowledge of measurement variability is needed to allow meaningful interpretation of serial measurements. This is relevant to both research and clinical practice; serial BBB permeability measurements have shown value in

predicting treatment response in MS (106), but also other conditions such as CNS lymphoma (291). For some imaging techniques, within-subject COV of repeated measurements is reported to be excellent, for example only 5% for fractional anisotropy measurements with diffusion tensor imaging (292), which is useful for longitudinal study of white matter integrity. However, such studies are usually conducted with healthy volunteers aged 20-30, typically male, and over a timeframe of days. Therefore, it is debatable whether metrics of variability derived in this way can be applied to different demographic groups, and to studies conducted over a longer time interval.

Separating the effects of biological variation and analytical imprecision is inherently challenging in a human imaging study, but the former cannot be ignored when imaging biomarkers are used to assess change over time. This study answers a specific question, namely the minimum detectable effect for the SIBIMS study (Chapter 7). However, the finding that analytical imprecision can be reduced by the optimisation steps demonstrated is applicable to other studies using DCE-MRI, and the possible role of biological variation warrants further study.

Chapter 4, Chapter 5, and Chapter 6 have dealt with the development, optimisation, and testing of the DCE-MRI protocol, and the aim throughout has been to hone a technique suitable for detecting subtle BBB permeability changes which may occur during systemic infection. The use of DCE-MRI for this purpose is described in the next chapter.

Chapter 7 Systemic Infection and the Blood-brain barrier

7.1 Introduction

The SIMS Study, detailed in Chapter 3, sought evidence of an association between systemic infection and disease progression in MS. In subsequent Chapters, DCE-MRI has been developed and validated as a tool for the assessment of subtle BBB disruption. Could BBB disruption link systemic infection with changes in the brain? Animal studies have shown mixed results. Homing in on one infection removes a source of variation. UTI is a good exemplar of systemic infection to study, as it is common in people with MS (47), and participants are likely to be able to tolerate a DCE-MRI scan (unlike respiratory tract infections, which lead to coughing). SIBIMS (Systemic Inflammation and the Blood-brain barrier in Multiple Sclerosis) is a prospective observational study of the BBB changes associated with UTI, in people with and without MS. The optimised DCE-MRI protocol is used to study BBB disruption occurring during UTI in humans.

7.2 Hypotheses

1. The primary hypothesis is that an episode of UTI is associated with BBB disruption detectable by DCE-MRI.

The secondary hypotheses are that:

2. During UTI, the magnitude of BBB disruption is associated with the magnitude of the systemic inflammatory response, as characterised by blood and urine markers of inflammation. Individuals with a high inflammatory response will experience greater BBB disruption than those with a low response.
3. During UTI, disruptive BBB changes in the brain of a person with MS are magnified compared to a healthy individual. People with MS will, all other things being equal, experience greater BBB disruption during infection than healthy controls.
4. During UTI in people with MS, the magnitude of BBB disruption is associated with the severity of symptom exacerbation. People with MS who have greater BBB disruption during infection will also have more severe symptom exacerbation.

7.3 Considerations in study design

The hypotheses could have been addressed by collecting data at a single time point from a range of participants, with and without infection, and correlating the two measures. However, such a method intrinsically lacks statistical power as there is likely to be large between-participant variation at each time point (as was seen in Chapter 6). This is reduced by a within-participant design, where data is collected at two time points from each participant: one infection and non-infection. The non-infection time point therefore acts as each participant's own control against their infection time point. There are number of possible study designs to achieve this, outlined in Table 34.

The most practical study design was to scan participants with current infection, and then re-scan again once fully recovered. The difference in K_i between the two imaging time points represents disruptive BBB change associated with UTI (with the caveats outlined above). This design has been used to investigate BBB changes associated in a study of migraine aura (293), a similarly spontaneous and unpredictable acute event.

Table 34 Considerations in study design for assessing within-participant change associated with infection.

BBB = blood-brain barrier, LPS = lipopolysaccharide.

Design	**Disadvantages**
Identify a population in whom infection is likely; collect data at the point of recruitment and then again when spontaneous infection occurs.	Inefficient use of resources; assuming likelihood of infection in the population is not 100%, then some participants will have data only from the first time point. Also, the interval between the two points is unpredictable and will vary between participants, allowing longitudinal changes in the measures to become confounders (e.g. if BBB permeability increases with age (83)).
Identify participants with current infection; collect data at the point of recruitment and then again once fully recovered.	Assumes that the post-infection state is identical to the pre-infection state. Potential confounding effect of impaired recovery (e.g. if BBB permeability increases during infection and then fails to recover, the apparent BBB change will be minimal).
Controlled human infection model; collect data, provoke infection (e.g. influenza), collect data again.	Ethically challenging, especially in people with MS in whom infection is believed to cause deterioration.
Experimental inflammation model; collect data, provoke experimental inflammation (e.g. lipopolysaccharide challenge, vaccination), collect data again. Alternatively identify participants who are scheduled to receive an inflammatory stimulus for clinical reasons (e.g. vaccination, elective surgery) and collect data before and after.	Relevance to naturalistic infection is debatable. Ethically challenging if provoking an inflammatory state purely for research purposes, especially in participants with MS.

7.4 Methods

7.4.1 Study design

The timing of each scan was critical to maximise the difference between states. For the infection scan, this was based on a robust case definition of UTI, comprising both (1) acute lower urinary tract symptoms (LUTS), and (2) pyuria > 10^{-7} cells/L. Pyuria has been shown to be the single best marker of UTI (53). For the non-infection scan, this was (1) resolution of acute LUTS, (2) completion of antibiotic treatment (if deemed appropriate by the clinical team), (3) normalisation of pyuria. The minimum interval between scans was set at eight weeks, based on the observation that the 'at-risk period' for infection-associated symptom exacerbation extends to five weeks after infection onset (41), and that UNCR may remain elevated for six weeks after infection onset (294). These criteria were pragmatic, balancing the need to separate the scan time points as much as possible to allow fully recovery, whilst avoiding too long an interval which could bring into play possible long-term BBB changes over time.

Given that UTI is a spontaneous and unpredictable event, recruitment was maximised by operating two streams in parallel: participants with a tendency to recurrent UTI recruited in anticipation of developing acute UTI in the future ('cold'), and participants with acute UTI at the time of recruitment ('hot'). An overview of the final study design, and flow of participants through the study, is shown in Figure 33.

In the 'cold' recruitment stream: Participants attended an initial visit to complete informed consent procedures and clinical data collection. A urine sample was collected to enable comparison with future samples. Participants were educated in the symptoms of UTI and instructed to report episodes, with regular reminders. In the event of a reported UTI, the participant was assessed (usually at home) and urine microscopy was performed. Upon meeting the case definition of UTI, DCE-MRI was performed as soon as possible. Urine sample collection and clinical data collection were also repeated. After eight weeks and once the criteria for recovery were met (recovery of LUTS and pyuria and completion of treatment), DCE-MRI, urine sample collection, and clinical data collection were repeated.

In the 'hot' recruitment stream: Participants followed the same pathway, with the initial visit omitted. Informed consent was obtained during the acute infection.

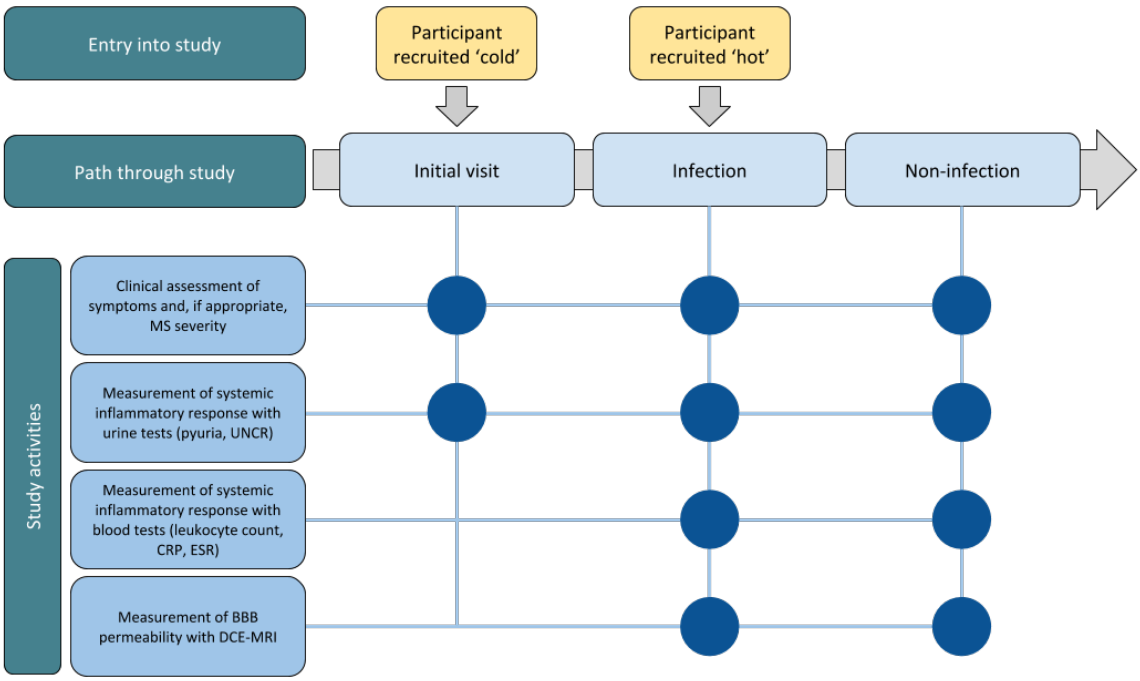

Figure 33 Overview of final design for the SIBIMS study.

Participants recruited through 'hot' or 'cold' streams enter at different points but otherwise undertake the same study activities. The path through the study and the activities are identical for participants with MS and for controls, except for MS-specific clinical assessments which are omitted in controls.

7.4.2 Ethical approval

The study was approved by the National Research Ethics Service Committee London Surrey (reference 18/LO/2015) and the institutional review board (ERGO 46018). Experiments were conducted in accordance with the Declaration of Helsinki and all subjects gave informed written consent.

7.4.3 Participants

Both people with and without MS were studied, allowing this study to examine whether BBB responses to systemic inflammation are abnormal in MS. Both groups followed the same pathway. The study was focussed on progressive forms of MS, where insights into the biology of disease progression are desperately needed (295). Relapsing forms of MS were excluded to avoid the confounding effects of relapses on BBB permeability (24). Healthy control individuals had no known significant neurological disease or symptoms. All potential participants (MS or control) were examined by a neurologist (me) prior to inclusion.

People with MS were recruited from the population served by the Wessex Neurological Centre, Southampton, UK, as well as from local patient groups and advertisement. Neurologically healthy control individuals without MS were recruited from urology and gynaecology clinics as well as from general practice and by advertisement. The age range was 18-80. Controls under the age of 40 were held in reserve as it was anticipated that most individuals with MS would be above the age of 40. General exclusion criteria were inability to have an MRI scan (incompatible metal implants, claustrophobia, morbid obesity) or gadolinium-based contrast (renal failure, history of contrast allergy).

7.4.4 Research techniques

The primary outcome was BBB permeability measured as whole-brain K_i by DCE-MRI, according to the protocol detailed in Chapter 5. Secondary outcomes were regional measurements of K_i. All DCE-MRI scans were quality-controlled by (1) examination of images during acquisition, and repetition of sequences during the imaging session if necessary, (2) post-acquisition review of all images by an experienced neuroradiologist, (3) visual inspection of key intermediate steps of analysis, including input functions, Patlak plots, T_1 maps, and tissue and lesion masks. The presence of CELs was assessed on the post-contrast MP-RAGE image by an experienced neuroradiologist, for all scans at all time points. A mask of CELs was created manually.

In the study of measurement variability, the use of K_{trans} did not improve precision (Section 6.5.6). Since there was no strong reason to prefer one over the other, and since haematocrit represents another source of measurement uncertainty, K_i was used in preference to K_{trans}.

Systemic inflammatory response to UTI was measured in several different ways, to maximise robustness to change. The following measurements were made at both infection and non-infection timepoints, at the same time as DCE-MRI:

1) Body temperature.
2) Blood leukocyte count, C-reactive protein (CRP), and erythrocyte sedimentation rate (ESR).
3) UNCR in a morning sample, as detailed in Section 3.3.2. In subjects attending an initial visit an additional sample was collected prior to UTI.

Microscopy for pyuria was performed by a single operator using a counting chamber (Glasstic 10, Kova International, Garden Grove, CA, USA) and a fresh unspun sample of urine. Each sample was also tested with a standard dipstick (Multistix 10 SG, Siemens, Erlangen, Germany). A sample taken during the acute UTI was also sent for standard culture and reported according to the

standard Kass criteria (296). Microscopy was chosen as the objective arbiter of infection as it is immediate and effective (53), whereas culture automatically adds a delay of at least 48 hours, and the predictive value of dipstick is limited, especially for ruling out infection (297).

Clinical and demographic data were collected at the first study visit, comprising: demographics, MS disease classification, MS disease duration, weight, height, handedness, smoking history, drug history, and past medical history (MS-specific questions omitted in controls). At every study visit a detailed inventory of LUTS and sickness behaviour symptoms were collected using validated questionnaires (54, 276). For people with MS, a comprehensive assessment of disease severity was also performed using validated metrics as described in detail in Section 3.3.4 (EDSS, MSFC, FS, and BDI), as well as a self-assessment (298) and physician assessment of spasticity (modified Ashworth scale) (299). In addition, at the infection time point all participants recorded the effect of the infection on activities of daily living, and at the non-infection time point recorded their overall perception of recovery using the Patient Global Impression of Improvement (PGI-I) (300).

In pwMS, the MSSID (MS Symptom and Impact Diary) was used to capture MS symptoms and detect possible changes association with infection (301). The first part of the MSSID asks about fourteen common MS symptoms and their effect on function, broadly grouped as factors of mobility, emotional/physical fatigue, and overall impact. Higher scores reflect better functioning; the maximum score of 15 means no MS symptoms (or MS symptoms present but with not even slight functional impact) and no overall impact of MS, whereas the minimum score is 1. To increase sensitivity to detect symptom change, the MSSID was modified by the inclusion of an additional question at repeat sittings. Participants were asked '*Last time you completed this questionnaire you mentioned some symptoms. Have any of these symptoms changed compared to usual?*'. Answers for each symptom were given as a five-point Likert scale ranging from 'a lot worse' (-2 points) to 'a lot better' (+2 points) and including the option of 'no change' (0 points), and the average quoted for each participant. All of the above mentioned clinical assessments are shown in Appendix C.

Brain, tissue, and lesion volumes were also calculated as previously described (Sections 3.3.3.3 and 3.3.3.4) using the non-infection reference point.

7.4.5 Sample size

The effect size was estimated from a study which examined the CSF/serum albumin ratio around the time of systemic inflammation in hospital patients (83). A moderate infection (with a five-fold rise in CRP) gave rise to a three-fold increase in CSF/serum albumin ratio. The means and standard deviations from this study were used for the power calculation. Correcting for a paired design

(eliminating between-participant variation), the power is 96% with a sample size of 27. Accounting for 10% dropout, the sample size was set at 30 in each group (i.e. 30 people with MS and 30 controls). The study of measurement variability performed in Chapter 6 has so far confirmed this sample size for an effect size of 20%.

7.4.6 Statistical analysis

The primary hypothesis was tested using an appropriate parametric or non-parametric paired test to compare whole brain K_i between infection and non-infection timepoints. To test for a difference in BBB response to infection between control and MS groups, a mixed ANOVA was performed with group as the between-subject factor and timepoint (infection or non-infection) as the within-subjects factor. Secondary hypotheses were tested using correlation methods to examine the changes in K_i in relation to markers of inflammation and symptoms. Exploratory outcomes examined K_i changes in selected brain regions (WM, GM, or lesions).

$P < 0.05$ was used to reject the null hypothesis though individual P values in the region of 0.05 were considered modest degrees of evidence, whichever side of the threshold (175).

7.5 Results

7.5.1 Participants

Recruitment began in March 2019 and was halted by the COVID-19 pandemic in March 2020. The path of recruited participants is shown in Figure 34.

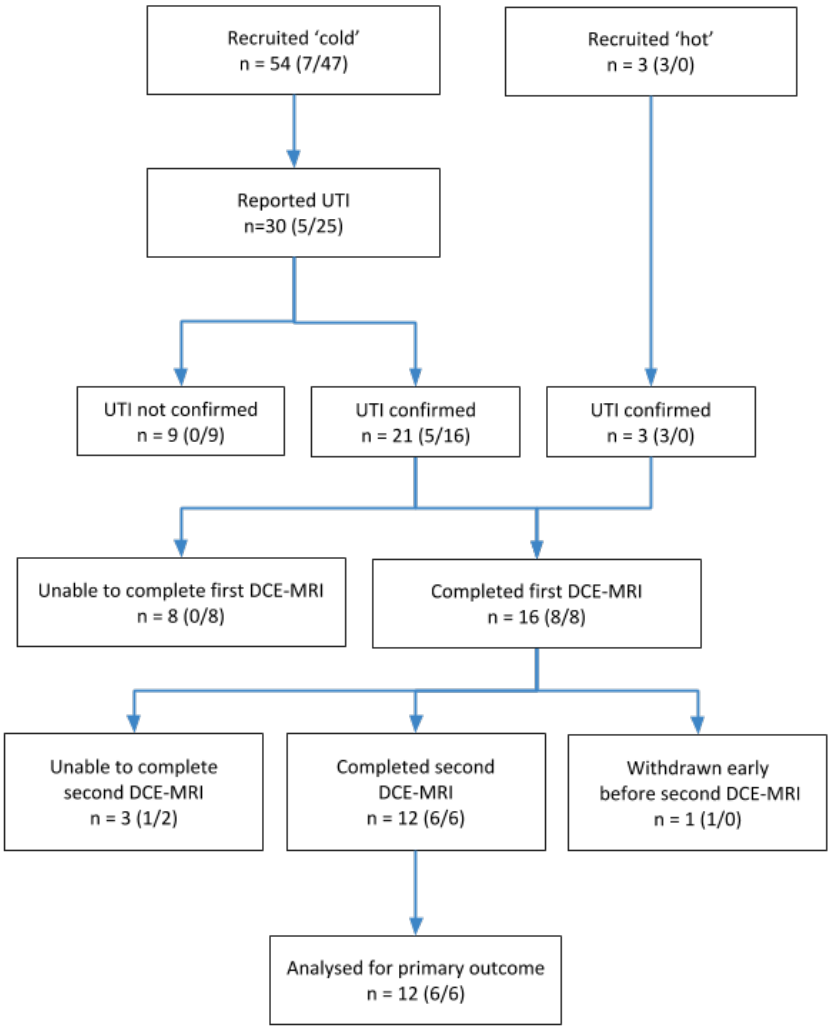

Figure 34 Path of recruited participants through the SIBIMS study.

'Cold' recruitment was of participants in anticipation of developing a UTI in future. 'Hot' recruitment was of participants with current acute UTI. Numbers in each group are given as total (controls/MS). Of those unable to complete the first DCE-MRI, this was due to unavailability of either the participant (4 cases), scanner (3 cases), or researcher (1 case). For those unable to complete the second DCE-MRI this was due to pandemic restrictions. One participant withdrew from the study for personal reasons.

7.5.2 Baseline clinical and radiological data

12 participants completed the study and were analysed for the primary outcome. Baseline demographic data and disease characteristics for these participants are shown in Table 35.

Table 35 Baseline characteristics of the SIBIMS study population.

Values are mean (SD). P-value is for a t-test between control and MS groups (Fisher's exact test for categorical variables). * The lesion measures in the control group were strongly influenced by the presence of small vessel disease, as discussed below. BMI = body mass index, EDSS = expanded disability status scale, SPMS = secondary progressive multiple sclerosis.

Variable	**Controls (n = 6)**	**MS (n = 6)**	**P-value**
Age (years)	59.8 (17.7)	51.0 (7.8)	0.30
Sex (% female)	50	83.3	0.55
BMI (kg/m^2)	26.4 (1.6)	27.9 (5.5)	0.55
Smoker (%)	0	0	n/a
Catheterisation (%)	66.7	16.7	0.50
MS disease category (% SPMS)	n/a	83.3	n/a
MS disease duration (years)	n/a	17.8 (8.4)	n/a
EDSS (points)	n/a	6.5 (0.8)	n/a
Lesion count	10.2 (9.5) *	20.8 (11.1)	0.11
Lesion volume (ml)	2.87 (5.24) *	3.40 (3.45)	0.84
Black hole volume (ml)	0.80 (1.27) *	1.85 (2.09)	0.33
Normalised brain volumes (l)			
- Whole brain	1.44 (0.09)	1.39 (0.04)	0.32
- White matter	0.72 (0.04)	0.67 (0.02)	0.03
- Grey matter	0.72 (0.06)	0.72 (0.04)	0.91
- Cortical grey matter	0.59 (0.04)	0.57 (0.04)	0.50
- Ventricles	0.08 (0.05)	0.05 (0.01)	0.26

7.5.3 Data quality

There was no missing data for any of the key study measures. One participant recruited 'cold' attended an initial visit but was unable to provide a urine sample. A blood sample during infection was not obtainable for one participant due to difficulties with venepuncture. Haemolysis compromised the analysis of one sample for CRP (during infection) and three samples for ESR (all during infection).

All scans passed the quality control steps described in Section 7.4.4. One participant required repetition of T_1 mapping sequences during acquisition due to obvious motion artefact, and one participant required repetition of the dynamic sequence due to malfunction of the contrast injector (both repetitions during the same imaging session).

The calculation of MSFC requires conversion of component data into z-scores, usually based on the group means and standard deviations of the study population. However, the sample size was smaller than anticipated and normality could not be demonstrated on either the raw or transformed data. Hence MSFC z-scores were calculated using group means and standard deviations from the SIMS study (Chapter 3).

7.5.4 Evidence of infection and recovery

All participants met the case definition for UTI, with both subjective and objective evidence in the form of symptoms and pyuria respectively. As shown in Table 36, group values for urine leukocyte count and LUTS score were significantly higher during infection compared to non-infection (for urine leukocyte count 362.7 vs 0.6 cells/µl, P = 0.04; for LUTS 16.1 vs 4.8 points, P = 0.0002, both paired t-test). There was also evidence of effects on the brain during infection, with sickness behaviour symptoms detected by SicknessQ (11.6 vs 2.3 points, P = 0.0003, paired t-test). Other blood and urine markers including UNCR were relatively insensitive to the presence of infection.

4 (33.3%) participants had a positive MSU culture during defined infection, in 2 cases with *E.coli* and in 2 with mixed growth. 11 (91.7%) participants had initiated antibiotic treatment prior to collection of the MSU sample. Pyuria during infection was significantly greater in those with positive MSU culture compared to those without (988.8 vs 49.6 cells/µl, P = 0.04, t-test). 11 (91.7%) of participants received antibiotic treatment during UTI at the discretion of their own physician. 3 (27.3%) of these individuals required a second course of antibiotics. No participants were hospitalised during infection.

Table 36 Comparison of infection and inflammation markers during infection and non-infection timepoints.

Values are mean (SD). The lower limit of detection for CRP is 1 mg/l, and many values were reported as <1 mg/l. These were treated as zero for the purposes of analysis as a continuous variable.
LUTS = lower urinary tract symptoms, UNCR = urinary neopterin-to-creatinine ratio, ESR = erythrocyte sedimentation rate.

Variable	**Infection**	**Non-infection**	**P-value**
Urine leukocyte count (cells/µl)	362.7 (543.2)	0.6 (2.0)	0.04
LUTS score (points)	16.1 (8.7)	4.8 (5.1)	0.0002
SicknessQ (points)	11.6 (7.3)	2.3 (3.5)	0.0003
UNCR (µmol/mol)	182.1 (54.3)	162.3 (58.9)	0.30
Blood leukocyte count (10^{-9} cells/l)	7.7 (3.4)	7.0 2.7)	0.48
C-reactive-protein (mg/l)	4.1 (4.6)	2.0 (2.6)	0.20
ESR (mm/hour)	12.8 (9.3)	6.6 (8.5)	0.12
Temperature (°C)	37.1 (0.4)	37.0 (0.3)	0.32

In those participants recruited 'cold' where assessments had been performed prior to the onset of UTI, paired comparison of values between the non-infection timepoint and those prior to UTI onset showed no differences in urine leukocyte count (P = 0.21), UNCR (P = 0.17), LUTS (P = 0.16), or SicknessQ (P = 0.52, all paired t-test). According to the PGI-I, all participants rated their recovery from UTI as either 'much better' (33.3%) or 'very much better' (66.7%).

7.5.5 MS worsening associated with infection

Participants with MS uniformly experienced symptom worsening associated with UTI, reflected in a significant difference in MSSID between infection and non-infection timepoints (4.7 vs 8.3, P = 0.001, paired t-test). This was also reflected in the dedicated MSSID change score which had a mean value of -1.59 +/- 0.28 (a score of -2 implies that all symptoms are 'a lot worse') and was significantly less than zero (P = 0.0003, one-sample t-test). Similar changes were also seen in the

self-rating of spasticity (see Table 37). However, no significant changes were seen in the physician-reported outcome measures (see Table 37). People with MS were more likely than controls to report impairment of one or more ADLs during infection (66.7 vs 16.7%, $\chi^2 = 3.1$, P = 0.08, Chi-square test).

Table 37 Changes in MS rating scales associated with infection.

Values are mean (SD). In controls, Beck's depression inventory did not show a significant change during infection (P = 0.39)
MSSID = Multiple Sclerosis Symptoms and Impact Diary, BDI = Beck Depression Inventory, EDSS = Expanded Disability Status Scale, MSFC = Multiple Sclerosis Functional Composite.

Score	**Infection**	**Non-infection**	**P-value**
Patient-reported outcome measures			
MSSID (points)	4.7 (1.4)	8.26 (1.4)	0.001
Spasticity (points)	7.2 (2.8)	4.83 (0.4)	0.005
Fatigue (points)	25.7 (7.4)	11.5 (5.8)	0.07
BDI (points)	6.7 (4.5)	3.8 (5.8)	0.06
Physician outcome measures			
EDSS (points)	6.5 (0.8)	6.5 (0.8)	n/a
MSFC (z-score)	-0.60 (2.58)	-0.86 (2.35)	0.44
Ashworth (points)	15.8 (8.5)	12.0 (4.5)	0.17

7.5.6 BBB disruption associated with infection

DCE-MRI was performed at the infection timepoint at a mean (SD) of 3.9 (1.9) days after onset of UTI symptoms, with no difference between control and MS groups (4.2 vs 3.7 days, P = 0.67, t-test). The mean (SD) interval between infection and non-infection scans was 11.7 (5.0) weeks, again with no difference between groups (11.1 vs 12.4 weeks, P = 0.66, t-test).

The primary hypothesis was tested by comparing mean whole brain K_i between paired infection and non-infection scans. There was modest evidence of BBB disruption associated with infection (0.58 vs 0.38 ml/100g/min, P = 0.12, paired t-test, see Figure 35). This was a 52.6% increase in K_i

at the time of infection. The effect size was moderate (Cohen's d = 0.64). There was no correlation between time from infection onset to scan and BBB disruption (r = 0.06 P = 0.98, Pearson's).

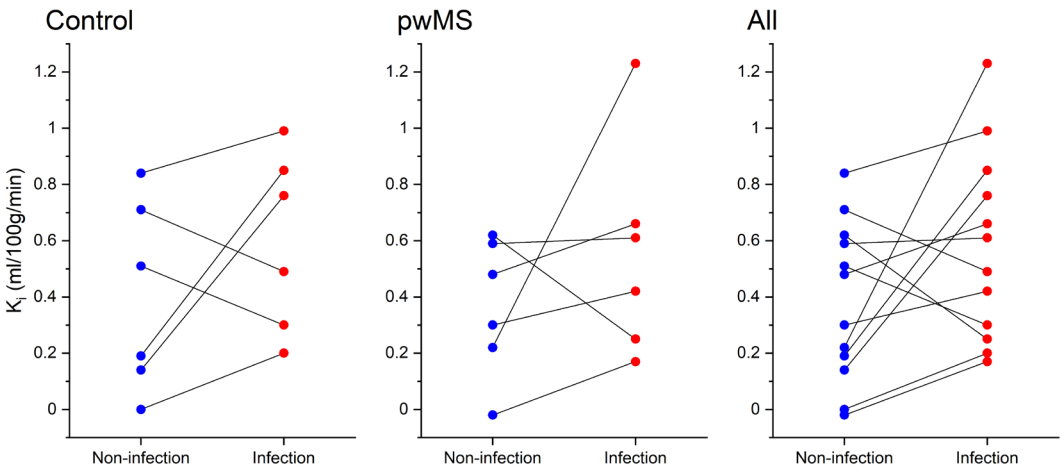

Figure 35 Modest evidence for BBB disruption during infection.

The non-infection timepoint is shown to the left of the infection timepoint, for readability.

To test for a difference in BBB permeability change to infection between control and MS groups, a mixed ANOVA was performed with group as the between-subject factor and timepoint (infection or non-infection) as the within-subject factor. There was no significant interaction between timepoint and group (P = 0.97). Neither was there a significant interaction when considering BBB permeability in GM-only (P = 0.55) or WM-only (P = 0.94) tissues.

BBB disruption during infection was not strongly correlated with age (r = -0.43, P = 0.17), nor were there any differences between males and females (0.14 vs 0.22, P = 0.74, t-test).

Table 38 Changes in K_i associated with infection.

Values for grey matter lesions are not shown as very few suitable voxels were identified.

NAWM = normal-appearing white matter, WM = white matter.

K_i (ml/100g/min)	**Infection**	**Non-infection**	**P-value**
Whole brain	0.58 (0.36)	0.38 (0.28)	0.12
Grey matter	0.54 (0.32)	0.39 (0.30)	0.22
NAWM	0.58 (0.34)	0.38 (0.28)	0.12
All lesions	0.48 (0.42)	0.33 (0.24)	0.31
WM lesions	0.48 (0.42)	0.33 (0.24)	0.31

CELs were identified in five scans, all in people with MS. One individual had CELs only during infection, which had resolved in the non-infection scan. Two individuals had CELs during infection which again had resolved in the non-infection scan, but new CELs had appeared in different locations. Mean K_i in CELs was significantly higher than the individuals own NAWM from the same timepoint in a pair-wise comparison (0.97 vs 0.52 ml/100g/min, P = 0.04, paired t-test). Total lesion volume did not change between infection and non-infection timepoints, either in controls (2.87 vs 2.96 ml, P = 0.34) or people with MS (3.40 vs 3.43, P = 0.78, paired t-test).

BBB disruption during infection did not correlate with sickness behaviour symptoms (r = -0.17, P = 0.59, Pearson's).

There was no significant difference in haematocrit between sessions (0.41 vs 0.042, P = 0.31, paired t-test).

7.5.7 Association of systemic inflammatory response and BBB disruption

There were no correlations between the magnitude of whole brain BBB disruption during infection and the magnitude of the systemic inflammatory response assessed by several measures, as shown in Table 39. The urothelial inflammatory response, assessed by the pyuria count, also did not correlate with BBB disruption (r = 0.06, P = 0.86, Pearson's).

Table 39 Correlations between BBB disruption and systemic inflammatory response to infection.

For each measure, change between infection and non-infection timepoints was taken to be the response to infection.
All by Pearson's.
UNCR = urinary neopterin-to-creatinine ratio.

Measure of change	**Correlation coefficient**	**P-value**
Temperature	-0.21	0.51
UNCR	-0.09	0.79
White cell count	-0.05	0.88
C-reactive protein	-0.19	0.60
Erythrocyte sedimentation rate	-0.20	0.64

7.5.8 Non-infection analyses of BBB permeability

Whole brain K_i was not significantly different between control and MS groups at the non-infection timepoint (0.40 vs 0.37 ml/100g/min, P = 0.85, t-test). There were no significant differences in regional analyses, shown in Table 40.

Table 40 Comparison of BBB permeability between controls and people with MS, outside of infection.

All by t-test.

K_i (ml/100g/min)	**Controls (n = 6)**	**MS (n = 6)**	**P-value**
Whole brain	0.40 (0.34)	0.37 (0.25)	0.85
Normal-appearing white matter	0.40 (0.34)	0.37 (0.25)	0.86
Grey matter	0.46 (0.34)	0.31 (0.26)	0.43
Lesions	0.19 (0.26)	0.40 (0.22)	0.31

However, five out of six (83.3%) control individuals had undiagnosed small vessel disease (SVD). When stratified by Fazekas grade (302), cases with more severe SVD had higher K_i than those without, as shown in Table 41. Except for the individual with Fazekas grade 2 SVD, who had treated hypertension, none of the other control individuals were known to have had conventional vascular risk factors (other than age).

Table 41 BBB permeability in control individuals according to presence of small vessel disease.

Values are mean (SD).

Fazekas grade	**n**	**Age**	**Whole brain K_i**
0 (absent)	1	38	0.19
1 (mild)	4	62.0 (17.3)	0.42 (0.41)
2 (moderate)	1	73	0.51

In the whole study group, there was no correlation between age and whole brain K_i (r = 0.06, P = 0.85, Pearson's, not controlling for group). There was evidence for higher K_i in WM lesions compared to normal-appearing white matter in people with MS (0.40 vs 0.37, P = 0.08, paired t-test), but not in the subgroup of control individuals with SVD lesions (0.19 vs 0.22, P = 0.36, paired-test).

In people with MS, non-infection K_i did not correlate with any clinical or radiological measures of disease severity, as shown in Table 42.

Table 42 Correlations of non-infection K_i and MS disease severity.

All by Pearson's.
EDSS = Expanded Disability Status Scale, MSFC = Multiple Sclerosis Functional Composite.

Measure	**Correlation coefficient**	**P-value**
Clinical measures		
EDSS	0.28	0.59
MSFC	0.31	0.52
Disease duration	-0.09	0.87
Radiological measures		
Brain volume	-0.14	0.79
Lesion volume	-0.66	0.16
Lesion count	-0.24	0.65

7.6 Discussion

7.6.1 Key results

This study examined individuals during UTI and again once fully recovered. There was both subjective and objective evidence that the infection and non-infection states were clearly delineated. There was strong evidence for an effect of UTI on the brain, with a significant increase in sickness behaviour symptoms during UTI (P = 0.0003). There was modest evidence to address the primary hypothesis, as a 53% increase in K_i was seen at the time of infection (P = 0.12),

suggesting BBB disruption. The effect size was moderate (0.64). People with MS uniformly experienced symptom worsening during UTI, though there was no correlation with BBB disruption.

7.6.2 Limitations

Unfortunately, recruitment to this study was significantly impacted by the COVID-19 pandemic, and as a result the analysis presented here is under-powered for the primary outcome. More complexes analyses including covariates were planned but not suitable for this small sample.

The limitations of this study design have been discussed previously (Section 7.3). The apparent difference between infection and non-infection states may have been blunted if recovery was incomplete, though evidence is presented against this. Alternatively, the difference may have been blunted if long-lasting BBB impairment occurred (i.e. if infection recovery was complete, but BBB recovery was incomplete). It is difficult to disprove this possibility. The fact that neurological symptoms recovered well points away from a long-lasting CNS response. That the MS group as a whole did not accrue new lesions after infection also suggests that the effect on the brain was transient. However, two individuals with MS did have persistent evidence of CNS inflammation even once fully recovered from UTI (discussed further below). Ideally it would have been useful to measure BBB permeability at multiple time points before, during, and after infection, but this was not practical in this study.

The main outcome for this study was whole brain K_i and measures were also examined in pre-defined tissue segments. Lesions were also examined though GM lesions were not well-identified in the absence of specific sequences (303). However, a significant change may have been missed without a more fine-grained regional analysis. It is possible that BBB disruption occurs predominantly in defined neuroanatomical or neurovascular regions or is spatially stochastic. There is animal evidence which suggests that regional vulnerabilities do exist (304). Such focal changes would be diluted out by examining the whole brain or large tissue segments. This could be overcome in an unbiased fashion by co-registering K_i maps from both timepoints and examining differences at the level of voxels or clusters, as is familiar in functional MRI (305); though a robust correction for multiple comparisons is needed with such an approach (306). Also, imaging was restricted to the brain, though a large burden of MS activity is in the spinal cord, especially in progressive disease (142), and it is possible that BBB disruption during infection occurs here. DCE-MRI in the spinal cord poses unique challenges due to the constrained anatomy but can be done (307). This may be particularly relevant to explain the increase in spasticity during infection that was seen in people with MS in this study.

DCE-MRI was performed as promptly as possible after the onset of infection (mean 3.9 days), and the possibility remains that BBB changes occurring at the peak of infection were missed. In a study using DCE-MRI to examine changes during migraine attacks, imaging was performed on average within 8 hours of symptom onset (293), though such rapidity was not feasible in this study. Conversely, BBB disruption might be delayed, as shown in an animal model (304) and in one study in people with MS (39). On balance it was felt that scanning as soon as possible was pragmatic, and in the final analysis there was no correlation between the delay in scanning and the BBB disruption observed.

The measures of systemic inflammation used in this study did not detect any significant change associated with UTI, except for ESR, which is a good non-specific marker of the acute phase response (308). One possibility is that UTI is a weak systemic inflammatory stimulus, as the response is confined largely to the bladder. Since participants in this study had to be well enough to have an MRI scan at the time of infection, there was a bias towards less severe infections without systemic upset. There were no cases where a participant reported an infection but was judged too unwell to proceed to scanning, though such cases likely self-excluded. If this is the case, the finding of BBB disruption during UTI is even more relevant to other infections. However, the lack of a clear systemic inflammatory response made it difficult to correlate inflammation with BBB disruption, and so this hypothesis could not be clearly addressed. It is also possible that the chosen markers of inflammation were not optimal. Neopterin was chosen since it has good evidence as a non-specific marker of systemic inflammation, though there is evidence that it is better in viral than bacterial infections (188), and serum levels are not raised in children with UTIs (309). This has implications for the interpretation of the SIMS study (Chapter 3), where UTIs were common and neopterin was the sole marker of inflammation. Since pro-inflammatory cytokines such as TNF-α are implicated in BBB disruption (310), further analyses should explore correlations with these markers. Also, if it is the case that UTI does not induce significant systemic inflammation, then it remains to be explained why in this study UTI was strongly associated with sickness behaviour in the whole group, and with symptom exacerbation in the MS group. It could be that the mechanisms are independent of systemic inflammation, for example direct activation of the neural pathway by urothelial inflammation. Most work on the neural pathway (311) of neuro-immune communication has focussed on the vagus nerve, which can be stimulated by inflammatory cytokines (312), and potentially also directly by pathogens via Toll-like receptors (313). However, the bladder is richly innervated but by spinal afferents rather than the vagus (314).

As discussed previously (Section 1.6) and recently reviewed (315), BBB change may be disruptive or non-disruptive. DCE-MRI using an inert tracer can only comment on BBB disruption, and so it is not possible to determine whether non-disruptive BBB changes occurred during UTI.

7.6.3 Interpretation

There was modest evidence to address the primary hypothesis, that UTI is associated with BBB disruption. In addition, there was strong evidence for an effect of UTI on the brain, as across all participants there was a highly significant increase in sickness behaviour symptoms during infection, and in people with MS there were significant changes in all patient-reported outcome measures (PROMs), reflecting global worsening of MS symptoms.

There was robust evidence for a clear delineation between infection and non-infection states, by subjective and objective measures of UTI. This is essential to the interpretation of the primary study outcome. MSU culture was only positive in one-third of individuals during infection, though most individuals had already taken antibiotics by the point of sample collection, which may have influenced the results (UTI treatment was entirely at the discretion of the individual and their clinical team, as to alter this for research purposes would have been unethical). Markers of systemic inflammation showed little change during UTI, though there was modest evidence for a rise in ESR.

The worsening of MS symptoms found in PROMs was not reflected in physician-reported outcome measures. For EDSS, this may be due to a ceiling effect: EDSS is heavily biased towards ambulation, and many of these individuals were already non-ambulant prior to their infection. MSFC provides a much more holistic assessment of disability, though this also did not mirror the reported symptom exacerbation. It has previously been recognised that an individual's perception of their own changing disability with MS can vary significantly from a physician's assessment, for EDSS (316) and also MSFC (317), and as a result there has recently been a drive to recognise the unique added value of PROMs (318).

There was no evidence for a differential BBB response between MS and control groups, though the sample was small. MS and control groups were well-matched in terms of age, which is known to affect BBB permeability (83). There were no significant differences in how the two groups progressed through the study.

27/47 (53.2%) of people with MS reported UTI during their time on the study, which varied greatly between participants. Of reported UTIs, 30% were not confirmed according to the pre-specified case definition, all in people with MS. The definition was intentionally strict, to maximise the

signal of a potential effect. These episodes may have been mild infections, or exacerbations or day-to-day fluctuations in MS symptoms affecting the bladder, as are common (3). There is evidence that individuals with spinal cord injury such as MS are better at predicting the absence rather than the presence of infection (319).

Three out of six people with MS had a visible CEL during infection, and all CELs seen during infection resolved by the time of the baseline scan. This is in keeping with the reported average duration of visible enhancement in an active MS lesion of 3 weeks (320). However, in two of these three individuals, distinct new CELs appeared at the time of the baseline scan. Both individuals had an established diagnosis of progressive MS, where CELs are relatively uncommon (321), and both had previous clinical imaging showing no contrast enhancement. One possible interpretation is that UTI triggered a self-sustaining inflammatory response within the CNS. If so, this phenomenon could have caused a long-lasting BBB disruption, and so minimised the apparent change between infection and baseline. This was identified as a weakness of this study design in in the planning phase (Section 7.3). The presence of CELs during infection also supports the idea of BBB disruption associated with infection, though suggests that this may be focal rather than diffuse (an argument for future regional analyses as discussed above).

There was a low incidence of missing data for the key study measures. However, many ESR samples were missing due to haemolysis. Since this occurred exclusively during infection this raises the possibility of infection-associated haemolysis, which may be explained by several mechanisms (322); some of which may also be relevant for this study. Some pathogens, such as *Plasmodium falciparum*, directly infect red blood cells, while others, notably *Clostridium perfringens*, produce haemolytic toxins. Infections may also lead to antibody-mediated autoimmune haemolysis or increase oxidative stress on red cells. Whether these mechanisms are relevant for bacteria causing UTI is debatable. The enterohaemorrhagic strain of E.coli (EHEC) does produce the Shiga toxin, which binds to glycosphingolipids on human endothelial cells, primarily in the gut but also in the brain (323), and may lead to BBB disruption (324, 325). EHEC rarely causes UTI (326), however the genome of *E.coli* is notoriously changeable and haemorrhagic virulence factors can be seen in uropathogenic (UPEC) strains (327). In fact, UPEC does produce α-haemolysin which can lyse red cells (328), though this is not thought to be relevant clinically. Antibody-mediated haemolysis is unlikely during UTI, as these rarely produce a significant humoral response (329). There is little literature on oxidative stress during UTI, though this has been linked to BBB disruption in other pathologies (330).

There was no significant difference in non-infection K_i between people with MS and controls, which is surprising given the histological and biochemical evidence for a disrupted BBB in

progressive MS (31, 32, 331). However, the mean value for controls was higher than that found in the variability study (0.40 vs 0.11 ml/100g/min, P = 0.04, t-test), which would have obscured this difference. Controls in SIBIMS were a similar age to those in the variability study (58.9 vs 56.0 years). Therefore, it is unexpected that K_i values were so different. It is possible that these individuals had not fully recovered from their infections by the time of the non-infection scan, though all met the pre-specified criteria for resolution. Another possibility is that the populations differed in some respect. The control population in SIBIMS had no manifest neurological disease, however, white matter lesions were seen in this group. In all cases these were determined by an experienced neuroradiologist to be (previously undiagnosed) small vessel disease. Therefore, it is debatable whether this can be considered a true control group. However, since the control group was age-matched to the progressive MS population, such findings were likely to be unavoidable as small vessel disease is highly prevalent with increasing age (332). This could be an important confounder, as BBB disruption is evident (using DCE-MRI) in people with small vessel disease (333). Since neither FLAIR nor T_2-weighted images were acquired in the variability study, it is possible that asymptomatic small vessel disease was missed in these individuals. However, white matter lesions of vascular origin may appear T_1-hypointense (334), and no such areas were identified by an experienced neuroradiologist.

In the MS group all lesions were interpreted as 'MS lesions', though it is possible if not likely that these individuals had co-existent small vessel disease, as people with MS have a higher risk for cerebrovascular disease than age-matched controls (335). In this study no attempt was made to discriminate individual lesions by aetiology, as though there are distinguishing features (336) this is difficult within an individual, and especially when lesion burden is high and tending to confluence. It is possible that BBB disruption occurred in MS lesions during infection, but that this effect was diluted out by the admixture of MS and vascular lesions. Even within MS lesions, there may have been heterogeneity in the BBB response to infection, as is reported in EAE (44). These are arguments for more focused regional analyses, as discussed previously. In fact, DCE-MRI itself may be a useful tool for discriminating MS lesions from vascular lesions, as this study demonstrated higher K_i in lesions than NAWM in people with MS but not those with small vessel disease (even though the difference may have been blunted due to the same dilution effect).

Though this hypothesis of this study related to BBB disruption, it is possible that the underlying issue may be one of BBB repair after an insult. The Wnt/β-catenin signalling pathway plays a key role in maintaining barrier function (337), may be activated during neuroinflammation (338), and plays an important role in driving BBB repair (339). Further work should examine not only BBB disruption during infection but also the timeline of following repair, in both health and disease.

7.6.4 Generalisability

It is important to determine whether the finding of BBB disruption during UTI is more broadly applicable. Since BBB disruption is reported with increasing age (83), it is possible that these changes would not be reproducible in a younger cohort, though no effect of age was seen in this sample. Whether these changes may occur during other infections or inflammatory stimuli also needs to be answered. UTI was chosen as a model infection, but since significant inflammation was not seen there is no evidence to prove or disprove the idea that BBB changes are driven by inflammation regardless of stimulus. However, other studies using different methods have shown evidence of BBB disruption in humans during post-operative delirium (340) and fatal sepsis (341). Since UTI in this study was generally non-severe (no participants were hospitalised, and all recovered) it is reasonable to suggest that the BBB changes seen here may be at the milder end of the spectrum.

This study recruited a typical cohort of individuals with progressive MS. Individuals had established disability interfering with ambulation, slightly more so than in SIMS (mean EDSS 6.5 vs 5.9). The sample was biased towards individuals with recurrent UTI, as these were more likely to be recruited. There is also the possibility that a subset of individuals with MS are more susceptible to the effects of infection on their disease, and that these individuals were more likely to enrol in the study (given its premise).

The control population was also biased towards individuals with recurrent UTI. The finding that over 80% of the control population had incidental cerebral small vessel disease was unexpected but potentially important. Asymptomatic cerebral vascular disease is a common incidental finding in imaging studies, though the rate here is much higher than the 7.2% reported in one large study in a similar age group (342). This raises the possibility that there is an association between cerebrovascular disease and UTI. Since vascular risk factors contribute to chronic LUTS (343, 344), the SIBIMS control population may have been unintentionally biased towards individuals with small vessel disease. Such an association should be explored in future studies, and the nature of possible causation established, as this may represent a novel modifiable risk factor.

Chapter 8 Discussion

8.1 Looking back

This is a quote from a person with MS: *'When I got the water infection, my balance got worse, I couldn't walk, couldn't talk, couldn't think.*' Why should a UTI – where the infection is nowhere near the brain - affect the brain in such a dramatic way? The impact of systemic infection on neurological disease is common, in MS but also in other conditions such as Alzheimer's disease. Understanding this phenomenon is the central question of this thesis.

Hypothesis 1 was that the host inflammatory response to systemic events such as infections is associated with the rate of brain atrophy in people with MS. The SIMS study (Chapter 3) found signals of an association, in that individuals with a high systemic inflammatory response experienced a 62% faster rate of brain atrophy and nearly 10-fold increased odds of significant brain atrophy, versus those with a low response. Those individuals with more severe MS at baseline were more vulnerable to this effect, and in this group a high inflammatory response was associated with more than a doubling in the rate of brain atrophy. This led to an investigation of the BBB as a possible mechanism for communication between systemic events and the brain.

Hypothesis 2 was that K_i as measured by DCE-MRI conforms to the expectations of a BBB permeability marker. Testing this hypothesis was required to establish DCE-MRI as a suitable tool for study of the human BBB. The null hypothesis was rejected in Chapter 4 and again in Chapter 6, as the pre-defined biological expectations of BBB permeability marker were demonstrated to be met, specifically the dependence on vascular surface area and the independence from perfusion. Importantly, it was also shown that DCE-MRI can resolve subtle permeability changes invisible to conventional imaging, for example in the normal-appearing brain tissue of pwMS. Systematic optimisation work was conducted to improve the performance of DCE-MRI, and to establish the measurement variability of the technique.

Hypothesis 3 was that an episode of systemic infection, specifically UTI, is associated with BBB disruption detectable by DCE-MRI. Signals of an association were shown in the SIBIMS study (Chapter 7), as a 53% increase in whole brain K_i was seen at the time of infection. Sickness behaviour and MS symptom worsening were also demonstrated, though a link to BBB disruption was not demonstrated.

8.2 Looking forwards

The SIMS and SIBIMS studies explored novel hypotheses, and the data from these can inform sample size calculations for definitive studies. If these signals are confirmed, the suppression of systemic inflammatory stimuli may become an important avenue for the treatment of MS, and agents which protect the BBB against the effect of systemic inflammation (and/or inflammation within the CNS) may become priorities for investigation (345-347).

If disruption of the BBB does indeed play a role in the communication of systemic events to the brain, then future studies should examine the precise molecular signals and mechanisms which mediate this disruption. In terms of molecular signals, several candidate pathways have been reported in animal and *in vitro* studies (reviewed in Section 1.6), and the relevance of these in humans needs to be clarified. In terms of mechanisms, it is not clear what elements of BBB disruption (outlined in Figure 3) are most relevant. Since serum samples have been saved from all the individuals in this study, preliminary work to investigate serum mediators correlated with BBB permeability will be possible and may inform the priorities of further studies. Identification of these mediators may in the future aid the targeted development of strategies for BBB protection and repair.

It is unlikely, however, that the BBB is the only pathway through which systemic events impact the brain. The 'neuro-immune axes' include the neural pathway (311) as well as the hypothalamic-pituitary-adrenal axis (348). Where important BBB changes do occur, these may be non-disruptive (outlined in Figure 3) and hence unsuitable for detection by DCE-MRI. It is likely that both host and stimulus factors contribute to the relative prominence of these pathways during the response to systemic inflammation. For example, BBB disruption during systemic inflammation may reflect vulnerability of the diseased brain, as shown in one animal study (80). Therefore DCE-MRI can only be one tool in a comprehensive effort to unpick the mechanisms of neuro-immune communication, in health and disease.

Meanwhile, the current COVID-19 pandemic makes further study into the effect of infections on MS all the more relevant. Also, as immunosuppressive drugs which predispose to infections begin to be widely used in people with progressive MS, understanding the role of infections in disease progression will better inform treatment decisions. The course of the pandemic and therefore the completion of the measurement variability and SIBIMS studies are uncertain, however steps will be taken to secure the integrity of the data already collected, for example by analysing stored biosamples. Recruitment to the measurement variability study may be able to restart sooner than SIBIMS, since this involves neither infections nor people with MS who are clinically vulnerable; if

possible, this data will be essential to inform the minimum detectable effect size of future longitudinal studies and ensure that such studies are appropriately powered.

There are other questions which can be answered using the data generated in this thesis. People with MS want to know their long-term prognosis (349), and analyses of the baseline variables in both the SIMS and SIBIMS studies may provide useful clinical, biochemical, or radiological markers. This is especially important as we are now entering the era of treatments for progressive MS (166, 350), and personalised treatment will be important in balancing the risks and benefits of these drugs.

DCE-MRI holds potential for future studies into the human BBB, to gain biological insights and to study conditions such as cerebrovascular disease (100) and dementia (351). Extensive technical work has been done in this thesis to validate and optimise DCE-MRI. One challenge of DCE-MRI is the masses of data it produces – in this study over 8 million dynamic voxels per scan. Recent developments have leveraged exponential increases in computational power and deep learning technologies to increase automation whilst reducing acquisition and analysis time (352-354). Particularly novel is the application of generative adversarial neural networks (the technology behind thispersondoesnotexist.com) to accelerate acquisition (355). Automating input function detection, as shown in this study, may make DCE-MRI more practical for clinical use. However, this thesis has shown that there are still fundamental methodological issues which need addressing such as patient movement during the scan, excitation, and spoiling for example. Combining advances in acquisition and computation with robust data on measurement variability may unlock the full potential of this tool for studying the human BBB in health and disease. This could be a valuable tool for personalised medicine (105, 106, 291), and potentially a useful adjunct to novel therapies which use BBB opening to enhance drug delivery (356, 357). Indeed, it has even been suggested that systemic inflammation could be used to induce transient BBB disruption for drug delivery (358), though this is clearly not without its risks.

In conclusion, this thesis generates two calls to action. The first is to translate the signal of a link between systemic inflammation and MS into an effective intervention to halt this currently incurable disease. The second is to use DCE-MRI to bring accurate, precise, and non-invasive measurements of BBB permeability into the clinical practice of personalised medicine. Both are ambitious, but achievable.

Appendix A SIMS Study Infection Diary

SIMS Study infection diary

Infections

Please recall if any of the following events have occurred in the last week and provide the details as accurately as you can remember. Please add any related comments or notes in the final section.

Question 1.

Have you had an infection in the last week?

Yes☐/No☐

Was this a new infection or a carry-over from previous week?

☐ New infection

☐ Carry-over from previous week

Please specify the location of this infection (select all that apply).

☐ Chest

☐ Throat

☐ Ear

☐ Sinuses

☐ Dental

☐ Eyes

☐ Bladder

☐ Stomach

☐ Bowel

☐ Skin

☐ Nails

☐ Genital

☐ Anus

☐ Joints

☐ Breast

When did this infection start?

How long did this infection last?

☐ 1 day

☐ 2 days

☐ 3 days

☐ 4 days

☐ 5 days

☐ 6 days

☐ 7 days

☐ I still have this infection

Were you prescribed antibiotics for this infection?

Yes☐/No☐

What was the name of the antibiotic you were prescribed?

Have you had another infection in the last week?

Vaccinations

Question 1.

Have you had a vaccination in the last week?

Yes☐/No☐

Please specify (e.g. flu jab).

What was the date of the vaccination?

Have you had another vaccination in the last week?

Yes☐/No☐

Surgery

Question 1.

Have you had a surgical procedure in the last week (either minor or major)?

Yes☐/No☐

Please specify (e.g. stitches, removal of skin mole, injection, appendix, gall bladder etc.).

What was the date of this procedure?

Have you had another surgical procedure in the last week (either minor or major)?

Yes☐/No☐

Injury

Question 1.

Have you had any physical injuries in the last week?

Yes☐/No☐

Please specify (e.g. bone fracture, head injury, skin etc.).

When did this injury occur?

Have you had another injury in the last week?

Yes☐/No☐

Appendix B SIMS Study MRI Exam Card

SIEMENS MAGNETOM Skyra

Geometry - Saturation

Saturation mode	Standard
Fat suppr.	None
Water suppr.	None
Special sat.	None

Geometry - Tim Planning Suite

Set-n-Go Protocol	Off
Table position	F
Table position	65 mm
Inline Composing	Off

System - Miscellaneous

Positioning mode	ISO
Table position	F
Table position	65 mm
MSMA	S - C - T
Sagittal	R >> L
Coronal	A >> P
Transversal	H >> F
Coil Combine Mode	Sum of Squares
Save uncombined	Off
Matrix Optimization	Off
Coil Focus	Flat
AutoAlign	---
Coil Select Mode	On - AutoCoilSelect

System - Adjustments

B0 Shim mode	Tune up
B1 Shim mode	TrueForm
Adjust with body coil	Off
Confirm freq. adjustment	Off
Assume Dominant Fat	Off
Assume Silicone	Off
Adjustment Tolerance	Auto

System - Adjust Volume

Position	Isocenter
Orientation	Transversal
Rotation	0.00 deg
A >> P	263 mm
R >> L	350 mm
F >> H	350 mm
Reset	Off

System - Tx/Rx

Frequency 1H	123.252197 MHz
Correction factor	1
Gain	High
Img. Scale Cor.	1.000
Reset	Off
? Ref. amplitude 1H	0.000 V

Physio - Signal1

1st Signal/Mode	None
TR	7.8 ms
Concatenations	8
Segments	1

Physio - Cardiac

Tagging	None
Magn. preparation	None
Fat suppr.	None
Dark blood	Off

Physio - Cardiac

FoV read	300 mm
FoV phase	100.0 %
Phase resolution	80 %

Physio - PACE

Resp. control	Off
Concatenations	8

Inline - Common

Subtract	Off
Measurements	1
StdDev	Off
Liver registration	Off
Save original images	On

Inline - MIP

MIP-Sag	Off
MIP-Cor	Off
MIP-Tra	Off
MIP-Time	Off
Save original images	On

Inline - Soft Tissue

Wash - In	Off
Wash - Out	Off
TTP	Off
PEI	Off
MIP - time	Off
Measurements	1

Inline - Composing

Inline Composing	Off
Distortion Corr.	On
Mode	2D
Unfiltered images	Off

Inline - MapIt

Save original images	On
MapIt	None
Flip angle	20 deg
Measurements	1
Contrasts	1
TR	7.8 ms
TE	3.69 ms

Sequence - Part 1

Introduction	On
Dimension	2D
Phase stabilisation	Off
Asymmetric echo	Off
Contrasts	1
Flow comp.	No
Multi-slice mode	Sequential
Bandwidth	320 Hz/Px

Sequence - Part 2

Segments	1
Acoustic noise reduction	None
RF pulse type	Normal
Gradient mode	Normal
Excitation	Slice-sel.
RF spoiling	On

SIEMENS MAGNETOM Skyra

\\RESEARCH & Physics\RESEARCH\SIMS\protocol\t1_mprage_sag_p2_iso_1.0

TA: 5:38 PM: ISO Voxel size: 1.0×1.0×1.0 mmPAT: 2 Rel. SNR: 1.00 : tfl

Properties

Prio recon	Off
Load images to viewer	On
Inline movie	Off
Auto store images	On
Load images to stamp segments	Off
Load images to graphic segments	Off
Auto open inline display	Off
Auto close inline display	Off
Start measurement without further preparation	Off
Wait for user to start	Off
Start measurements	Single measurement

Routine

Slab group	1
Slabs	1
Dist. factor	50 %
Position	L0.0 P31.7 H1.7 mm
Orientation	Sagittal
Phase enc. dir.	A >> P
AutoAlign	---
Phase oversampling	10 %
Slice oversampling	27.3 %
Slices per slab	176
FoV read	250 mm
FoV phase	100.0 %
Slice thickness	1.00 mm
TR	2200.0 ms
TE	2.45 ms
Averages	1
Concatenations	1
Filter	Distortion Corr.(2D), Prescan Normalize, Image Filter
Coil elements	HE1-4

Contrast - Common

TR	2200.0 ms
TE	2.45 ms
Magn. preparation	Non-sel. IR
TI	900 ms
Flip angle	8 deg
Fat suppr.	None
Water suppr.	None

Contrast - Dynamic

Averages	1
Averaging mode	Long term
Reconstruction	Magnitude
Measurements	1
Multiple series	Each measurement

Resolution - Common

FoV read	250 mm
FoV phase	100.0 %
Slice thickness	1.00 mm
Base resolution	256
Phase resolution	100 %
Slice resolution	100 %
Phase partial Fourier	Off
Slice partial Fourier	Off

Resolution - Common

Interpolation	Off

Resolution - iPAT

PAT mode	GRAPPA
Accel. factor PE	2
Ref. lines PE	24
Accel. factor 3D	1
Reference scan mode	Integrated

Resolution - Filter Image

Image Filter	On
! Intensity	Medium
Edge Enhancement	3
Smoothing	2
Unfiltered images	Off
Distortion Corr.	On
Mode	2D
Unfiltered images	Off
Prescan Normalize	On
Unfiltered images	Off
Normalize	Off
B1 filter	Off

Resolution - Filter Rawdata

Raw filter	Off
Elliptical filter	Off

Geometry - Common

Slab group	1
Slabs	1
Dist. factor	50 %
Position	L0.0 P31.7 H1.7 mm
Orientation	Sagittal
Phase enc. dir.	A >> P
Slice oversampling	27.3 %
Slices per slab	176
FoV read	250 mm
FoV phase	100.0 %
Slice thickness	1.00 mm
TR	2200.0 ms
Multi-slice mode	Single shot
Series	Ascending
Concatenations	1

Geometry - AutoAlign

Slab group	1
Position	L0.0 P31.7 H1.7 mm
Orientation	Sagittal
Phase enc. dir.	A >> P
AutoAlign	---
Initial Position	Isocenter
L	0.0 mm
P	0.0 mm
H	0.0 mm
Initial Rotation	0.00 deg
Initial Orientation	Transversal

Geometry - Navigator

SIEMENS MAGNETOM Skyra

Sequence - Assistant

Mode	Off
Allowed delay	0 s

SIEMENS MAGNETOM Skyra

\\RESEARCH & Physics\RESEARCH\SIMS\protocol\t1_mprage_sag_p2_iso_1.0

TA: 5:38 PM: ISO Voxel size: 1.0×1.0×1.0 mmPAT: 2 Rel. SNR: 1.00 : tfl

Properties

Prio recon	Off
Load images to viewer	On
Inline movie	Off
Auto store images	On
Load images to stamp segments	Off
Load images to graphic segments	Off
Auto open inline display	Off
Auto close inline display	Off
Start measurement without further preparation	Off
Wait for user to start	Off
Start measurements	Single measurement

Routine

Slab group	1
Slabs	1
Dist. factor	50 %
Position	L0.0 P31.7 H1.7 mm
Orientation	Sagittal
Phase enc. dir.	A >> P
AutoAlign	---
Phase oversampling	10 %
Slice oversampling	27.3 %
Slices per slab	176
FoV read	250 mm
FoV phase	100.0 %
Slice thickness	1.00 mm
TR	2200.0 ms
TE	2.45 ms
Averages	1
Concatenations	1
Filter	Distortion Corr.(2D), Prescan Normalize, Image Filter
Coil elements	HE1-4

Contrast - Common

TR	2200.0 ms
TE	2.45 ms
Magn. preparation	Non-sel. IR
TI	900 ms
Flip angle	8 deg
Fat suppr.	None
Water suppr.	None

Contrast - Dynamic

Averages	1
Averaging mode	Long term
Reconstruction	Magnitude
Measurements	1
Multiple series	Each measurement

Resolution - Common

FoV read	250 mm
FoV phase	100.0 %
Slice thickness	1.00 mm
Base resolution	256
Phase resolution	100 %
Slice resolution	100 %
Phase partial Fourier	Off
Slice partial Fourier	Off

Resolution - Common

Interpolation	Off

Resolution - iPAT

PAT mode	GRAPPA
Accel. factor PE	2
Ref. lines PE	24
Accel. factor 3D	1
Reference scan mode	Integrated

Resolution - Filter Image

Image Filter	On
! Intensity	Medium
Edge Enhancement	3
Smoothing	2
Unfiltered images	Off
Distortion Corr.	On
Mode	2D
Unfiltered images	Off
Prescan Normalize	On
Unfiltered images	Off
Normalize	Off
B1 filter	Off

Resolution - Filter Rawdata

Raw filter	Off
Elliptical filter	Off

Geometry - Common

Slab group	1
Slabs	1
Dist. factor	50 %
Position	L0.0 P31.7 H1.7 mm
Orientation	Sagittal
Phase enc. dir.	A >> P
Slice oversampling	27.3 %
Slices per slab	176
FoV read	250 mm
FoV phase	100.0 %
Slice thickness	1.00 mm
TR	2200.0 ms
Multi-slice mode	Single shot
Series	Ascending
Concatenations	1

Geometry - AutoAlign

Slab group	1
Position	L0.0 P31.7 H1.7 mm
Orientation	Sagittal
Phase enc. dir.	A >> P
AutoAlign	---
Initial Position	Isocenter
L	0.0 mm
P	0.0 mm
H	0.0 mm
Initial Rotation	0.00 deg
Initial Orientation	Transversal

Geometry - Navigator

SIEMENS MAGNETOM Skyra

Geometry - Tim Planning Suite

Set-n-Go Protocol	Off
Table position	H
Table position	2 mm
Inline Composing	Off

System - Miscellaneous

Positioning mode	ISO
Table position	H
Table position	2 mm
MSMA	S - C - T
Sagittal	R >> L
Coronal	A >> P
Transversal	F >> H
Coil Combine Mode	Adaptive Combine
Save uncombined	Off
Matrix Optimization	Off
AutoAlign	---
Coil Select Mode	On - AutoCoilSelect

System - Adjustments

B0 Shim mode	Tune up
B1 Shim mode	TrueForm
Adjust with body coil	Off
Confirm freq. adjustment	Off
Assume Dominant Fat	Off
Assume Silicone	Off
Adjustment Tolerance	Auto

System - Adjust Volume

Position	Isocenter
Orientation	Transversal
Rotation	0.00 deg
A >> P	263 mm
R >> L	350 mm
F >> H	350 mm
Reset	Off

System - Tx/Rx

Frequency 1H	123.252197 MHz
Correction factor	1
Gain	Low
Img. Scale Cor.	1.000
Reset	Off
? Ref. amplitude 1H	0.000 V

Physio - Signal1

1st Signal/Mode	None
TR	2200.0 ms
Concatenations	1

Physio - Cardiac

Magn. preparation	Non-sel. IR
TI	900 ms
Fat suppr.	None
Dark blood	Off
FoV read	250 mm
FoV phase	100.0 %
Phase resolution	100 %

Physio - PACE

Resp. control	Off
Concatenations	1

Inline - Common

Subtract	Off
Measurements	1
StdDev	Off
Save original images	On

Inline - MIP

MIP-Sag	Off
MIP-Cor	Off
MIP-Tra	Off
MIP-Time	Off
Save original images	On

Inline - Composing

Inline Composing	Off
Distortion Corr.	On
Mode	2D
Unfiltered images	Off

Inline - MapIt

Save original images	On
MapIt	None
Flip angle	8 deg
Measurements	1
TR	2200.0 ms
TE	2.45 ms

Sequence - Part 1

Introduction	On
Dimension	3D
Elliptical scanning	Off
Reordering	Linear
Asymmetric echo	Allowed
Flow comp.	No
Multi-slice mode	Single shot
Echo spacing	6 ms
Bandwidth	250 Hz/Px

Sequence - Part 2

RF pulse type	Fast
Gradient mode	Normal
Excitation	Slab-sel.
RF spoiling	On
Incr. Gradient spoiling	Off
Turbo factor	224

Sequence - Assistant

Mode	Off

SIEMENS MAGNETOM Skyra

\\RESEARCH & Physics\RESEARCH\SIMS\protocol\localizer

TA: 0:14 PM: FIX Voxel size: 0.5×0.5×7.0 mmPAT: Off Rel. SNR: 1.00 : fl

Properties

Prio recon	On
Load images to viewer	On
Inline movie	Off
Auto store images	On
Load images to stamp segments	On
Load images to graphic segments	On
Auto open inline display	Off
Auto close inline display	Off
Start measurement without further preparation	On
Wait for user to start	Off
Start measurements	Single measurement

Routine

Slice group	1
Slices	1
Dist. factor	20 %
Position	Isocenter
Orientation	Sagittal
Phase enc. dir.	A >> P
Slice group	2
Slices	1
Dist. factor	20 %
Position	L0.0 P30.0 H0.0 mm
Orientation	Transversal
Phase enc. dir.	A >> P
Slice group	3
Slices	1
Dist. factor	20 %
Position	L0.0 P30.0 H0.0 mm
Orientation	Coronal
Phase enc. dir.	R >> L
AutoAlign	---
Phase oversampling	0 %
FoV read	250 mm
FoV phase	100.0 %
Slice thickness	7.0 mm
TR	8.6 ms
TE	4.00 ms
Averages	2
Concatenations	3
Filter	Distortion Corr.(2D), Prescan Normalize, Elliptical filter
Coil elements	HE1-4

Contrast - Common

TR	8.6 ms
TE	4.00 ms
TD	0 ms
MTC	Off
Magn. preparation	None
Flip angle	20 deg
Fat suppr.	None
Water suppr.	None
SWI	Off

Contrast - Dynamic

Averages	2
Averaging mode	Short term
Reconstruction	Magnitude

Contrast - Dynamic

Measurements	1
Multiple series	Each measurement

Resolution - Common

FoV read	250 mm
FoV phase	100.0 %
Slice thickness	7.0 mm
Base resolution	256
Phase resolution	91 %
Phase partial Fourier	Off
Interpolation	On

Resolution - iPAT

PAT mode	None

Resolution - Filter Image

Image Filter	Off
Distortion Corr.	On
Mode	2D
Unfiltered images	Off
Prescan Normalize	On
Unfiltered images	Off
Normalize	Off
B1 filter	Off

Resolution - Filter Rawdata

Raw filter	Off
Elliptical filter	On

Geometry - Common

Slice group	1
Slices	1
Dist. factor	20 %
Position	Isocenter
Orientation	Sagittal
Phase enc. dir.	A >> P
Slice group	2
Slices	1
Dist. factor	20 %
Position	L0.0 P30.0 H0.0 mm
Orientation	Transversal
Phase enc. dir.	A >> P
Slice group	3
Slices	1
Dist. factor	20 %
Position	L0.0 P30.0 H0.0 mm
Orientation	Coronal
Phase enc. dir.	R >> L
FoV read	250 mm
FoV phase	100.0 %
Slice thickness	7.0 mm
TR	8.6 ms
Multi-slice mode	Sequential
Series	Interleaved
Concatenations	3

Geometry - AutoAlign

Slice group	1
Position	Isocenter
Orientation	Sagittal

SIEMENS MAGNETOM Skyra

Geometry - AutoAlign

Phase enc. dir.	A >> P
Slice group	2
Position	L0.0 P30.0 H0.0 mm
Orientation	Transversal
Phase enc. dir.	A >> P
Slice group	3
Position	L0.0 P30.0 H0.0 mm
Orientation	Coronal
Phase enc. dir.	R >> L
AutoAlign	---
Initial Position	Isocenter
L	0.0 mm
P	0.0 mm
H	0.0 mm
Initial Rotation	0.00 deg
Initial Orientation	Transversal

Geometry - Saturation

Saturation mode	Standard
Fat suppr.	None
Water suppr.	None
Special sat.	None

Geometry - Tim Planning Suite

Set-n-Go Protocol	Off
Table position	H
Table position	0 mm
Inline Composing	Off

System - Miscellaneous

Positioning mode	FIX
Table position	H
Table position	0 mm
MSMA	S - C - T
Sagittal	R >> L
Coronal	A >> P
Transversal	F >> H
Coil Combine Mode	Adaptive Combine
Save uncombined	Off
Matrix Optimization	Off
AutoAlign	---
Coil Select Mode	Off - AutoCoilSelect

System - Adjustments

B0 Shim mode	Tune up
B1 Shim mode	TrueForm
Adjust with body coil	Off
Confirm freq. adjustment	Off
Assume Dominant Fat	Off
Assume Silicone	Off
Adjustment Tolerance	Auto

System - Adjust Volume

Position	Isocenter
Orientation	Transversal
Rotation	0.00 deg
A >> P	263 mm
R >> L	350 mm
F >> H	350 mm
Reset	Off

System - Tx/Rx

Frequency 1H	123.252197 MHz
Correction factor	1

System - Tx/Rx

Gain	High
Img. Scale Cor.	1.000
Reset	Off
? Ref. amplitude 1H	0.000 V

Physio - Signal1

1st Signal/Mode	None
TR	8.6 ms
Concatenations	3
Segments	1

Physio - Cardiac

Tagging	None
Magn. preparation	None
Fat suppr.	None
Dark blood	Off
FoV read	250 mm
FoV phase	100.0 %
Phase resolution	91 %

Physio - PACE

Resp. control	Off
Concatenations	3

Inline - Common

Subtract	Off
Measurements	1
StdDev	Off
Liver registration	Off
Save original images	On

Inline - MIP

MIP-Sag	Off
MIP-Cor	Off
MIP-Tra	Off
MIP-Time	Off
Save original images	On

Inline - Soft Tissue

Wash - In	Off
Wash - Out	Off
TTP	Off
PEI	Off
MIP - time	Off
Measurements	1

Inline - Composing

Inline Composing	Off
Distortion Corr.	On
Mode	2D
Unfiltered images	Off

Inline - MapIt

Save original images	On
MapIt	None
Flip angle	20 deg
Measurements	1
Contrasts	1
TR	8.6 ms
TE	4.00 ms

Sequence - Part 1

Introduction	On

SIEMENS MAGNETOM Skyra

Sequence - Part 1

Dimension	2D
Phase stabilisation	Off
Asymmetric echo	Allowed
Contrasts	1
Flow comp.	No
Multi-slice mode	Sequential
Bandwidth	320 Hz/Px

Sequence - Part 2

Segments	1
Acoustic noise reduction	None
RF pulse type	Normal
Gradient mode	Normal
Excitation	Slice-sel.
RF spoiling	On

Sequence - Assistant

Mode	Off
Allowed delay	0 s

SIEMENS MAGNETOM Skyra

\\RESEARCH & Physics\RESEARCH\SIMS\protocol\t1_mprage_ax_p2_iso_1.0

TA: 5:38 PM: FIX Voxel size: 1.0×1.0×1.0 mmPAT: 2 Rel. SNR: 1.00 : tfl

Properties

Prio recon	Off
Load images to viewer	On
Inline movie	Off
Auto store images	On
Load images to stamp segments	Off
Load images to graphic segments	Off
Auto open inline display	Off
Auto close inline display	Off
Start measurement without further preparation	Off
Wait for user to start	Off
Start measurements	Single measurement

Routine

Slab group	1
Slabs	1
Dist. factor	50 %
Position	L0.0 P8.7 H2.3 mm
Orientation	T > C-12.7
Phase enc. dir.	A >> P
AutoAlign	---
Phase oversampling	10 %
Slice oversampling	27.3 %
Slices per slab	176
FoV read	250 mm
FoV phase	100.0 %
Slice thickness	1.00 mm
TR	2200.0 ms
TE	2.45 ms
Averages	1
Concatenations	1
Filter	Distortion Corr.(2D), Prescan Normalize, Image Filter
Coil elements	HE1-4

Contrast - Common

TR	2200.0 ms
TE	2.45 ms
Magn. preparation	Non-sel. IR
TI	900 ms
Flip angle	8 deg
Fat suppr.	None
Water suppr.	None

Contrast - Dynamic

Averages	1
Averaging mode	Long term
Reconstruction	Magnitude
Measurements	1
Multiple series	Each measurement

Resolution - Common

FoV read	250 mm
FoV phase	100.0 %
Slice thickness	1.00 mm
Base resolution	256
Phase resolution	100 %
Slice resolution	100 %
Phase partial Fourier	Off
Slice partial Fourier	Off

Resolution - Common

Interpolation	Off

Resolution - iPAT

PAT mode	GRAPPA
Accel. factor PE	2
Ref. lines PE	24
Accel. factor 3D	1
Reference scan mode	Integrated

Resolution - Filter Image

Image Filter	On
! Intensity	Medium
Edge Enhancement	3
Smoothing	2
Unfiltered images	Off
Distortion Corr.	On
Mode	2D
Unfiltered images	Off
Prescan Normalize	On
Unfiltered images	Off
Normalize	Off
B1 filter	Off

Resolution - Filter Rawdata

Raw filter	Off
Elliptical filter	Off

Geometry - Common

Slab group	1
Slabs	1
Dist. factor	50 %
Position	L0.0 P8.7 H2.3 mm
Orientation	T > C-12.7
Phase enc. dir.	A >> P
Slice oversampling	27.3 %
Slices per slab	176
FoV read	250 mm
FoV phase	100.0 %
Slice thickness	1.00 mm
TR	2200.0 ms
Multi-slice mode	Single shot
Series	Ascending
Concatenations	1

Geometry - AutoAlign

Slab group	1
Position	L0.0 P8.7 H2.3 mm
Orientation	T > C-12.7
Phase enc. dir.	A >> P
AutoAlign	---
Initial Position	Isocenter
L	0.0 mm
P	0.0 mm
H	0.0 mm
Initial Rotation	0.00 deg
Initial Orientation	Transversal

Geometry - Navigator

SIEMENS MAGNETOM Skyra

Geometry - Tim Planning Suite

Set-n-Go Protocol	Off
Table position	H
Table position	2 mm
Inline Composing	Off

System - Miscellaneous

Positioning mode	FIX
Table position	H
Table position	2 mm
MSMA	S - C - T
Sagittal	R >> L
Coronal	A >> P
Transversal	F >> H
Coil Combine Mode	Adaptive Combine
Save uncombined	Off
Matrix Optimization	Off
AutoAlign	---
Coil Select Mode	Off - AutoCoilSelect

System - Adjustments

B0 Shim mode	Tune up
B1 Shim mode	TrueForm
Adjust with body coil	Off
Confirm freq. adjustment	Off
Assume Dominant Fat	Off
Assume Silicone	Off
Adjustment Tolerance	Auto

System - Adjust Volume

Position	Isocenter
Orientation	Transversal
Rotation	0.00 deg
A >> P	263 mm
R >> L	350 mm
F >> H	350 mm
Reset	Off

System - Tx/Rx

Frequency 1H	123.252197 MHz
Correction factor	1
Gain	Low
Img. Scale Cor.	1.000
Reset	Off
? Ref. amplitude 1H	0.000 V

Physio - Signal1

1st Signal/Mode	None
TR	2200.0 ms
Concatenations	1

Physio - Cardiac

Magn. preparation	Non-sel. IR
TI	900 ms
Fat suppr.	None
Dark blood	Off
FoV read	250 mm
FoV phase	100.0 %
Phase resolution	100 %

Physio - PACE

Resp. control	Off
Concatenations	1

Inline - Common

Subtract	Off
Measurements	1
StdDev	Off
Save original images	On

Inline - MIP

MIP-Sag	Off
MIP-Cor	Off
MIP-Tra	Off
MIP-Time	Off
Save original images	On

Inline - Composing

Inline Composing	Off
Distortion Corr.	On
Mode	2D
Unfiltered images	Off

Inline - MapIt

Save original images	On
MapIt	None
Flip angle	8 deg
Measurements	1
TR	2200.0 ms
TE	2.45 ms

Sequence - Part 1

Introduction	On
Dimension	3D
Elliptical scanning	Off
Reordering	Linear
Asymmetric echo	Allowed
Flow comp.	No
Multi-slice mode	Single shot
Echo spacing	6 ms
Bandwidth	250 Hz/Px

Sequence - Part 2

RF pulse type	Fast
Gradient mode	Normal
Excitation	Slab-sel.
RF spoiling	On
Incr. Gradient spoiling	Off
Turbo factor	224

Sequence - Assistant

Mode	Off

SIEMENS MAGNETOM Skyra

\\RESEARCH & Physics\RESEARCH\SIMS\protocol\pd+t2_tse_ax

TA: 3:11 PM: FIX Voxel size: 1.0×1.0×3.0 mmPAT: Off Rel. SNR: 1.00 : tse

Properties

Prio recon	Off
Load images to viewer	On
Inline movie	Off
Auto store images	On
Load images to stamp segments	On
Load images to graphic segments	On
Auto open inline display	Off
Auto close inline display	Off
Start measurement without further preparation	Off
Wait for user to start	Off
Start measurements	Single measurement

Routine

Slice group	1
Slices	45
Dist. factor	10 %
Position	L0.0 P8.7 H2.3 mm
Orientation	T > C-12.7
Phase enc. dir.	R >> L
AutoAlign	---
Phase oversampling	0 %
FoV read	250 mm
FoV phase	81.3 %
Slice thickness	3.0 mm
TR	4400.0 ms
TE 1	9 ms
TE 2	90 ms
Averages	1
Concatenations	1
Filter	Distortion Corr.(2D), Prescan Normalize, Elliptical filter
Coil elements	HE1-4

Contrast - Common

TR	4400.0 ms
TE 1	9 ms
TE 2	90 ms
MTC	Off
Magn. preparation	None
Flip angle	160 deg
Fat suppr.	None
Water suppr.	None
Restore magn.	Off

Contrast - Dynamic

Averages	1
Averaging mode	Long term
Reconstruction	Magnitude
Measurements	1
Multiple series	Each measurement

Resolution - Common

FoV read	250 mm
FoV phase	81.3 %
Slice thickness	3.0 mm
Base resolution	256
Phase resolution	100 %
Phase partial Fourier	Off
Trajectory	Cartesian

Resolution - Common

Interpolation	Off

Resolution - iPAT

PAT mode	None

Resolution - Filter Image

Image Filter	Off
Distortion Corr.	On
Mode	2D
Unfiltered images	Off
Prescan Normalize	On
Unfiltered images	Off
Normalize	Off
B1 filter	Off

Resolution - Filter Rawdata

Raw filter	Off
Elliptical filter	On

Geometry - Common

Slice group	1
Slices	45
Dist. factor	10 %
Position	L0.0 P8.7 H2.3 mm
Orientation	T > C-12.7
Phase enc. dir.	R >> L
FoV read	250 mm
FoV phase	81.3 %
Slice thickness	3.0 mm
TR	4400.0 ms
Multi-slice mode	Interleaved
Series	Interleaved
Concatenations	1

Geometry - AutoAlign

Slice group	1
Position	L0.0 P8.7 H2.3 mm
Orientation	T > C-12.7
Phase enc. dir.	R >> L
AutoAlign	---
Initial Position	Isocenter
L	0.0 mm
P	0.0 mm
H	0.0 mm
Initial Rotation	90.00 deg
Initial Orientation	Transversal

Geometry - Saturation

Fat suppr.	None
Water suppr.	None
Restore magn.	Off
Special sat.	None

Geometry - Navigator

Geometry - Tim Planning Suite

Set-n-Go Protocol	Off
Table position	H
Table position	2 mm

SIEMENS MAGNETOM Skyra

Geometry - Tim Planning Suite

Inline Composing	Off

System - Miscellaneous

Positioning mode	FIX
Table position	H
Table position	2 mm
MSMA	S - C - T
Sagittal	R >> L
Coronal	A >> P
Transversal	F >> H
Coil Combine Mode	Adaptive Combine
Save uncombined	Off
Matrix Optimization	Off
AutoAlign	---
Coil Select Mode	Off - AutoCoilSelect

System - Adjustments

B0 Shim mode	Tune up
B1 Shim mode	TrueForm
Adjust with body coil	Off
Confirm freq. adjustment	Off
Assume Dominant Fat	Off
Assume Silicone	Off
Adjustment Tolerance	Auto

System - Adjust Volume

Position	Isocenter
Orientation	Transversal
Rotation	0.00 deg
A >> P	263 mm
R >> L	350 mm
F >> H	350 mm
Reset	Off

System - Tx/Rx

Frequency 1H	123.252197 MHz
Correction factor	1
Gain	High
Img. Scale Cor.	1.000
Reset	Off
? Ref. amplitude 1H	0.000 V

Physio - Signal1

1st Signal/Mode	None
TR	4400.0 ms
Concatenations	1

Physio - Cardiac

Magn. preparation	None
Fat suppr.	None
Dark blood	Off
FoV read	250 mm
FoV phase	81.3 %
Phase resolution	100 %
Trajectory	Cartesian

Physio - PACE

Resp. control	Off
Concatenations	1

Inline - Common

Subtract	Off
Measurements	1

Inline - Common

StdDev	Off
Save original images	On

Inline - MIP

MIP-Sag	Off
MIP-Cor	Off
MIP-Tra	Off
MIP-Time	Off
Save original images	On

Inline - Composing

Inline Composing	Off
Distortion Corr.	On
Mode	2D
Unfiltered images	Off

Sequence - Part 1

Introduction	On
Dimension	2D
Compensate T2 decay	Off
Reduce Motion Sens.	On
Contrasts	2
Flow comp.	No
Multi-slice mode	Interleaved
Free echo spacing	Off
Echo spacing	8.96 ms
Bandwidth	250 Hz/Px

Sequence - Part 2

Define	Turbo factor
Echo trains per slice	42
Phase correction	Automatic
Acoustic noise reduction	None
RF pulse type	Normal
Gradient mode	Normal
Hyperecho	Off
WARP	Off
Red. EC sensitivity	Off
Turbo factor	5

Sequence - Assistant

Mode	Min flip angle
Min flip angle	130 deg
Allowed delay	60 s

SIEMENS MAGNETOM Skyra

\\RESEARCH & Physics\RESEARCH\SIMS\protocol\t2_spc_da-fl_ax_p2

TA: 5:12 PM: FIX Voxel size: 1.0×1.0×1.1 mmPAT: 2 Rel. SNR: 1.00 : spcir

Properties

Prio recon	Off
Load images to viewer	On
Inline movie	Off
Auto store images	On
Load images to stamp segments	Off
Load images to graphic segments	Off
Auto open inline display	Off
Auto close inline display	Off
Start measurement without further preparation	Off
Wait for user to start	Off
Start measurements	Single measurement

Routine

Slab group	1
Slabs	1
Position	L0.0 P8.7 H2.3 mm
Orientation	T > C-12.7
Phase enc. dir.	A >> P
AutoAlign	---
Phase oversampling	0 %
Slice oversampling	0.0 %
Slices per slab	176
FoV read	256 mm
FoV phase	96.9 %
Slice thickness	1.10 mm
TR	5000 ms
TE	397 ms
Averages	1.0
Concatenations	1
Filter	Raw filter, Prescan Normalize
Coil elements	HE1-4

Contrast - Common

TR	5000 ms
TE	397 ms
MTC	Off
Magn. preparation	Non-sel. T2-IR
TI 1	1800 ms
Fat suppr.	None
Blood suppr.	Off
Restore magn.	Off

Contrast - Dynamic

Averages	1.0
Reconstruction	Magnitude
Measurements	1
Multiple series	Each measurement

Resolution - Common

FoV read	256 mm
FoV phase	96.9 %
Slice thickness	1.10 mm
Base resolution	256
Phase resolution	100 %
Slice resolution	83 %
Phase partial Fourier	Allowed
Slice partial Fourier	7/8
Interpolation	Off

Resolution - iPAT

PAT mode	GRAPPA
Accel. factor PE	2
Ref. lines PE	24
Accel. factor 3D	1
Reference scan mode	Integrated

Resolution - Filter Image

Image Filter	Off
Distortion Corr.	Off
Prescan Normalize	On
Unfiltered images	Off
Normalize	Off
B1 filter	Off

Resolution - Filter Rawdata

Raw filter	On
Elliptical filter	Off

Geometry - Common

Slab group	1
Slabs	1
Position	L0.0 P8.7 H2.3 mm
Orientation	T > C-12.7
Phase enc. dir.	A >> P
Slice oversampling	0.0 %
Slices per slab	176
FoV read	256 mm
FoV phase	96.9 %
Slice thickness	1.10 mm
TR	5000 ms
Series	Interleaved
Concatenations	1

Geometry - AutoAlign

Slab group	1
Position	L0.0 P8.7 H2.3 mm
Orientation	T > C-12.7
Phase enc. dir.	A >> P
AutoAlign	---
Initial Position	Isocenter
L	0.0 mm
P	0.0 mm
H	0.0 mm
Initial Rotation	0.00 deg
Initial Orientation	Transversal

Geometry - Saturation

Fat suppr.	None
Restore magn.	Off
Special sat.	None

Geometry - Navigator

Geometry - Tim Planning Suite

Set-n-Go Protocol	Off
Table position	H
Table position	2 mm
Inline Composing	Off

SIEMENS MAGNETOM Skyra

System - Miscellaneous

Positioning mode	FIX
Table position	H
Table position	2 mm
MSMA	S - C - T
Sagittal	R >> L
Coronal	A >> P
Transversal	F >> H
Coil Combine Mode	Adaptive Combine
Save uncombined	Off
Matrix Optimization	Off
AutoAlign	---
Coil Select Mode	Off - AutoCoilSelect

System - Adjustments

B0 Shim mode	Standard
B1 Shim mode	TrueForm
Adjust with body coil	Off
Confirm freq. adjustment	Off
Assume Dominant Fat	Off
Assume Silicone	Off
Adjustment Tolerance	Auto

System - Adjust Volume

Position	L0.0 P8.7 H2.3 mm
Orientation	T > C-12.7
Rotation	0.00 deg
A >> P	248 mm
R >> L	256 mm
F >> H	194 mm
Reset	Off

System - Tx/Rx

Frequency 1H	123.252197 MHz
Correction factor	1
Gain	High
Img. Scale Cor.	1.000
Reset	Off
? Ref. amplitude 1H	0.000 V

Physio - Signal1

1st Signal/Mode	None
Trigger delay	0 ms
TR	5000 ms
Concatenations	1

Physio - Cardiac

Magn. preparation	Non-sel. T2-IR
TI 1	1800 ms
Fat suppr.	None
Dark blood	Off
FoV read	256 mm
FoV phase	96.9 %
Phase resolution	100 %

Physio - PACE

Resp. control	Off
Concatenations	1

Inline - Common

Subtract	Off
Measurements	1
StdDev	Off
Save original images	On

Inline - MIP

MIP-Sag	Off
MIP-Cor	Off
MIP-Tra	Off
MIP-Time	Off
Save original images	On

Inline - Composing

Inline Composing	Off
Distortion Corr.	Off

Sequence - Part 1

Introduction	On
Dimension	3D
Elliptical scanning	Off
Reordering	Linear
Flow comp.	No
Echo spacing	3.42 ms
Adiabatic-mode	Off
Bandwidth	781 Hz/Px

Sequence - Part 2

Echo train duration	879 ms
RF pulse type	Normal
Gradient mode	Fast
Excitation	Non-sel.
Flip angle mode	T2 var
Turbo factor	284

Sequence - Assistant

Allowed delay	30 s

Appendix C Clinical measures used in SIMS and SIBIMS

The material in this Appendix cannot be reproduced for copyright reasons. The full text can be viewed at the sources cited in the following sections.

C.1 Expanded Disability Status Scale (EDSS)

Reproduced from Kurtzke (160).

This page is blank for copyright reasons.

This page is blank for copyright reasons.

This page is blank for copyright reasons.

C.2 Multiple Sclerosis Functional Composite (MSFC)

Proforma based on that described by Polman et al (162).

This page is blank for copyright reasons.

This page is blank for copyright reasons.

This page is blank for copyright reasons.

This page is blank for copyright reasons.

Appendix C

This page is blank for copyright reasons.

C.3 Multiple Sclerosis Impact Scale (MSIS)

Proforma based on that described by Hobart et al (163).

This page is blank for copyright reasons.

C.4 Chalder Fatigue Scale (FS)

Proforma based on that described by Chalder et al (164).

This page is blank for copyright reasons.

C.5 Beck Depression Inventory (BDI)

Proforma based on that described by Beck et al (359).

This page is blank for copyright reasons.

Appendix C

This page is blank for copyright reasons.

This page is blank for copyright reasons.

C.6 Activities of daily living (ADLs)

This was the proforma devised for this study.

Has this infection affected your ability to …	**Yes**	**No**	**n/a**	**Explain further if you like**
Work?				
Drive?				
Feed yourself?				
Dress yourself?				
Wash yourself?				
Get in and out of bed?				
Use the toilet?				
Use the stairs?				

C.7 Patient Global Impression of Improvement (PGI-I)

Proforma based on that described by Yalcin et al (360).

This page is blank for copyright reasons.

C.8 Multiple Sclerosis Symptoms and Impact Diary (MSSID)

Proforma based on that described by Greenhalgh et al (301), and modified for this study with the help of Dr Joanne Greenhalgh.

This page is blank for copyright reasons.

This page is blank for copyright reasons.

This page is blank for copyright reasons.

This page is blank for copyright reasons.

C.9 SicknessQ

Proforma reproduced from Andreasson et al (276).

This page is blank for copyright reasons.

C.10 Non-steroid anti-inflammatory drug (NSAID) score

Proforma based on that described by Dougados et al (277).

This page is blank for copyright reasons.

C.11 Lower urinary tract symptom (LUTS) score

Proforma based on that kindly provided by Professor James Malone-Lee, and originally described by Khasriya et al (54).

This page is blank for copyright reasons.

This page is blank for copyright reasons.

C.12 Spasticity self-score

Proforma based on that described by Farrar et al (298).

This page is blank for copyright reasons.

C.13 Ashworth spasticity score

Proforma based on that described by Bohannon et al (299).

This page is blank for copyright reasons.

Appendix D Testing of ZEFRAM

In a repeated measures ANOVA there were no differences in brain atrophy measurements according to the three methods of analysis (P = 0.73), namely with Popescu's recommendations (127), with lesion filling, and with ZEFRAM. Brain atrophy measurements by ZEFRAM correlated well with clinical disability progression as assessed by MSFC (ρ = 0.38 P = 0.005), however this correlation was absent when using the two standard brain atrophy measurement methods (see Table 43). Brain atrophy did not correlate with EDSS progression, by any method.

Table 43 Correlation of brain atrophy with clinical progression, by analysis method.

All by Spearman's, values are ρ and P-value.
EDSS = Expanded Disability Status Scale, MSFC = Multiple Sclerosis Functional Composite, ZEFRAM = ZEro-Filled Robust Atrophy Measurement.

SIENA method	**Correlation with MSFC change**	**Correlation with EDSS change**
ZEFRAM	0.38 0.005	0.02 0.88
Popescu	-0.03 0.86	0.02 0.92
Lesion filling	-0.04 0.76	0.03 0.83

A previous study reported that longitudinal brain atrophy measurements with SIENA are insensitive to the presence of lesions (136), and is often cited as a rationale for ignoring lesions in atrophy measurement. However, what the investigators actually found was that when lesions with an intensity equal to CSF (i.e. obvious black holes) were artificially added to an image, these would not influence the atrophy measurement until their volume reached 60 ml. Lesser lesion volumes or lesions with an intensity between CSF and GM, which should be classed as black holes (133-135), did not influence volume measurements. For comparison, the mean baseline black hole volume in this study was 4.2 ml, and these participants had established disability. Since black holes may play an important role in the pathogenesis of disability (15), ignoring their contribution to brain volume loss may blunt sensitivity to change. This technique is under development but may be especially important for clinical trials of new agents designed to slow progression, which may rely on radiological outcomes. Further work should examine the performance of ZEFRAM in

diverse cohorts of pwMS to replicate this finding, investigate the effect of the signal threshold used to define black holes, and explore the possibility of black hole regression over time.

Appendix E Protocol optimisations

Table 44 Declarations regarding the optimisations described in Chapter 5.

Optimisation	**Declaration**
B1 correction	Sequence described in literature (239). Adapted by Siemens and analysed using MATLAB code written by me. Tested by me in experiments described in Section 5.6 and 6.5.2.
Baudrexel correction	Described in literature (243) and implemented using MATLAB code written by me. Tested by me in experiments described in Section 5.7 and 6.5.2.
Motion correction	Developed and tested by me in experiments described in Section 5.8 and 6.5.2. MATLAB code written by me. I used FSL commands routinely used for image registration.
Arterio-venous scaling of input function	Described in literature and implemented using MATLAB code adapted by me from that written by Professor Henrik Larsson, University of Copenhagen. Tested by me in experiments described in Section 5.10 and 6.5.2.
Automatic input function measurement	Developed and tested by me in experiments described in Section 5.10 and 6.5.2. Parameters to guide the search were adapted from those described in literature (256). MATLAB code written by me. I used FSL commands routinely used for image registration.

Appendix F SIBIMS Study MRI Exam Card

SIEMENS MAGNETOM Skyra

\\RESEARCH & Physics\RESEARCH\Sibims-2\SIBIMS-2 v7 21/02/2019\localizer

TA: 0:26 PM: FIX Voxel size: 0.6×0.6×6.0 mmPAT: Off Rel. SNR: 1.00 : fl

Properties

Prio recon	Off
Load images to viewer	On
Inline movie	Off
Auto store images	On
Load images to stamp segments	On
Load images to graphic segments	On
Auto open inline display	Off
Auto close inline display	Off
Start measurement without further preparation	On
Wait for user to start	Off
Start measurements	Single measurement

Routine

Slice group	1
Slices	5
Dist. factor	300 %
Position	L0.0 P7.7 H0.8 mm
Orientation	Coronal
Phase enc. dir.	R >> L
Slice group	2
Slices	3
Dist. factor	50 %
Position	L0.0 P19.1 F2.2 mm
Orientation	Sagittal
Phase enc. dir.	A >> P
Slice group	3
Slices	3
Dist. factor	300 %
Position	L0.0 P6.3 H8.1 mm
Orientation	T > C-13.5
Phase enc. dir.	A >> P
AutoAlign	---
Phase oversampling	38 %
FoV read	300 mm
FoV phase	100.0 %
Slice thickness	6.0 mm
TR	7.8 ms
TE	3.69 ms
Averages	1
Concatenations	11
Filter	Distortion Corr.(2D), Prescan Normalize
Coil elements	HE1-4;NE1,2

Contrast - Common

TR	7.8 ms
TE	3.69 ms
TD	0 ms
MTC	Off
Magn. preparation	None
Flip angle	20 deg
Fat suppr.	None
Water suppr.	None
SWI	Off

Contrast - Dynamic

Averages	1
Averaging mode	Short term
Reconstruction	Magnitude
Measurements	1

Contrast - Dynamic

Multiple series	Each measurement

Resolution - Common

FoV read	300 mm
FoV phase	100.0 %
Slice thickness	6.0 mm
Base resolution	256
Phase resolution	80 %
Phase partial Fourier	Off
Interpolation	On

Resolution - iPAT

PAT mode	None

Resolution - Filter Image

Image Filter	Off
Distortion Corr.	On
Mode	2D
Unfiltered images	Off
Prescan Normalize	On
Unfiltered images	Off
Normalize	Off
B1 filter	Off

Resolution - Filter Rawdata

Raw filter	Off
Elliptical filter	Off

Geometry - Common

Slice group	1
Slices	5
Dist. factor	300 %
Position	L0.0 P7.7 H0.8 mm
Orientation	Coronal
Phase enc. dir.	R >> L
Slice group	2
Slices	3
Dist. factor	50 %
Position	L0.0 P19.1 F2.2 mm
Orientation	Sagittal
Phase enc. dir.	A >> P
Slice group	3
Slices	3
Dist. factor	300 %
Position	L0.0 P6.3 H8.1 mm
Orientation	T > C-13.5
Phase enc. dir.	A >> P
FoV read	300 mm
FoV phase	100.0 %
Slice thickness	6.0 mm
TR	7.8 ms
Multi-slice mode	Sequential
Series	Interleaved
Concatenations	11

Geometry - AutoAlign

Slice group	1
Position	L0.0 P7.7 H0.8 mm
Orientation	Coronal
Phase enc. dir.	R >> L

SIEMENS MAGNETOM Skyra

Geometry - AutoAlign

Slice group	2
Position	L0.0 P19.1 F2.2 mm
Orientation	Sagittal
Phase enc. dir.	A >> P
Slice group	3
Position	L0.0 P6.3 H8.1 mm
Orientation	T > C-13.5
Phase enc. dir.	A >> P
AutoAlign	---
Initial Position	L0.0 P7.7 H1.8
L	0.0 mm
P	7.7 mm
H	1.8 mm
Initial Rotation	0.00 deg
Initial Orientation	Coronal

Geometry - Saturation

Saturation mode	Standard
Fat suppr.	None
Water suppr.	None
Special sat.	None

Geometry - Tim Planning Suite

Set-n-Go Protocol	Off
Table position	F
Table position	1 mm
Inline Composing	Off

System - Miscellaneous

Positioning mode	FIX
Table position	F
Table position	1 mm
MSMA	S - C - T
Sagittal	R >> L
Coronal	A >> P
Transversal	H >> F
Coil Combine Mode	Sum of Squares
Save uncombined	Off
Matrix Optimization	Off
AutoAlign	---
Coil Select Mode	On - AutoCoilSelect

System - Adjustments

B0 Shim mode	Tune up
B1 Shim mode	TrueForm
Adjust with body coil	Off
Confirm freq. adjustment	Off
Assume Dominant Fat	Off
Assume Silicone	Off
Adjustment Tolerance	Auto

System - Adjust Volume

Position	Isocenter
Orientation	Transversal
Rotation	0.00 deg
A >> P	263 mm
R >> L	350 mm
F >> H	350 mm
Reset	Off

System - Tx/Rx

Frequency 1H	123.253591 MHz
Correction factor	1
Gain	High

System - Tx/Rx

Img. Scale Cor.	1.000
Reset	Off
? Ref. amplitude 1H	0.000 V

Physio - Signal1

1st Signal/Mode	None
TR	7.8 ms
Concatenations	11
Segments	1

Physio - Cardiac

Tagging	None
Magn. preparation	None
Fat suppr.	None
Dark blood	Off
FoV read	300 mm
FoV phase	100.0 %
Phase resolution	80 %

Physio - PACE

Resp. control	Off
Concatenations	11

Inline - Common

Subtract	Off
Measurements	1
StdDev	Off
Liver registration	Off
Save original images	On

Inline - MIP

MIP-Sag	Off
MIP-Cor	Off
MIP-Tra	Off
MIP-Time	Off
Save original images	On

Inline - Soft Tissue

Wash - In	Off
Wash - Out	Off
TTP	Off
PEI	Off
MIP - time	Off
Measurements	1

Inline - Composing

Inline Composing	Off
Distortion Corr.	On
Mode	2D
Unfiltered images	Off

Inline - MapIt

Save original images	On
MapIt	None
Flip angle	20 deg
Measurements	1
Contrasts	1
TR	7.8 ms
TE	3.69 ms

Sequence - Part 1

Introduction	On
Dimension	2D

SIEMENS MAGNETOM Skyra

Sequence - Part 1

Phase stabilisation	Off
Asymmetric echo	Off
Contrasts	1
Flow comp.	No
Multi-slice mode	Sequential
Bandwidth	320 Hz/Px

Sequence - Part 2

Segments	1
Acoustic noise reduction	None
RF pulse type	Normal
Gradient mode	Normal
Excitation	Slice-sel.
RF spoiling	On

Sequence - Assistant

Mode	Off
Allowed delay	0 s

SIEMENS MAGNETOM Skyra

\\RESEARCH & Physics\RESEARCH\Sibims-2\SIBIMS-2 v7 21/02/2019\ax_pd+t2_tse

TA: 3:12 PM: FIX Voxel size: 0.3×0.3×4.0 mmPAT: Off Rel. SNR: 1.00 : tse

Properties

Prio recon	Off
Load images to viewer	On
Inline movie	Off
Auto store images	On
Load images to stamp segments	On
Load images to graphic segments	On
Auto open inline display	Off
Auto close inline display	Off
Start measurement without further preparation	Off
Wait for user to start	Off
Start measurements	Single measurement

Routine

Slice group	1
Slices	35
Dist. factor	10 %
Position	Isocenter
Orientation	T > C-5.4
Phase enc. dir.	R >> L
AutoAlign	Head > Brain
Phase oversampling	0 %
FoV read	220 mm
FoV phase	81.3 %
Slice thickness	4.0 mm
TR	3600.0 ms
TE 1	9.4 ms
TE 2	94 ms
Averages	1
Concatenations	1
Filter	Distortion Corr.(2D), Prescan Normalize, Elliptical filter
Coil elements	HE1-4

Contrast - Common

TR	3600.0 ms
TE 1	9.4 ms
TE 2	94 ms
MTC	Off
Magn. preparation	None
Flip angle	160 deg
Fat suppr.	None
Water suppr.	None
Restore magn.	Off

Contrast - Dynamic

Averages	1
Averaging mode	Long term
Reconstruction	Magnitude
Measurements	1
Multiple series	Each measurement

Resolution - Common

FoV read	220 mm
FoV phase	81.3 %
Slice thickness	4.0 mm
Base resolution	320
Phase resolution	100 %
Phase partial Fourier	Off
Trajectory	Cartesian

Resolution - Common

Interpolation	On

Resolution - iPAT

PAT mode	None

Resolution - Filter Image

Image Filter	Off
Distortion Corr.	On
Mode	2D
Unfiltered images	Off
Prescan Normalize	On
Unfiltered images	Off
Normalize	Off
B1 filter	Off

Resolution - Filter Rawdata

Raw filter	Off
Elliptical filter	On

Geometry - Common

Slice group	1
Slices	35
Dist. factor	10 %
Position	Isocenter
Orientation	T > C-5.4
Phase enc. dir.	R >> L
FoV read	220 mm
FoV phase	81.3 %
Slice thickness	4.0 mm
TR	3600.0 ms
Multi-slice mode	Interleaved
Series	Ascending
Concatenations	1

Geometry - AutoAlign

Slice group	1
Position	Isocenter
Orientation	T > C-5.4
Phase enc. dir.	R >> L
AutoAlign	Head > Brain
Initial Position	Isocenter
L	0.0 mm
P	0.0 mm
H	0.0 mm
Initial Rotation	90.54 deg
Initial Orientation	T > C
T > C	-5.4
> S	0.0

Geometry - Saturation

Fat suppr.	None
Water suppr.	None
Restore magn.	Off
Special sat.	None

Geometry - Navigator

Geometry - Tim Planning Suite

Set-n-Go Protocol	Off

SIEMENS MAGNETOM Skyra

Geometry - Tim Planning Suite

Table position	H
Table position	0 mm
Inline Composing	Off

System - Miscellaneous

Positioning mode	FIX
Table position	H
Table position	0 mm
MSMA	S - C - T
Sagittal	R >> L
Coronal	A >> P
Transversal	F >> H
Coil Combine Mode	Adaptive Combine
Save uncombined	Off
Matrix Optimization	Off
AutoAlign	Head > Brain
Coil Select Mode	On - AutoCoilSelect

System - Adjustments

B0 Shim mode	Tune up
B1 Shim mode	TrueForm
Adjust with body coil	Off
Confirm freq. adjustment	Off
Assume Dominant Fat	Off
Assume Silicone	Off
Adjustment Tolerance	Auto

System - Adjust Volume

Position	Isocenter
Orientation	Transversal
Rotation	0.00 deg
A >> P	263 mm
R >> L	350 mm
F >> H	350 mm
Reset	Off

System - Tx/Rx

Frequency 1H	123.253591 MHz
Correction factor	1
Gain	High
Img. Scale Cor.	1.000
Reset	Off
? Ref. amplitude 1H	0.000 V

Physio - Signal1

1st Signal/Mode	None
TR	3600.0 ms
Concatenations	1

Physio - Cardiac

Magn. preparation	None
Fat suppr.	None
Dark blood	Off
FoV read	220 mm
FoV phase	81.3 %
Phase resolution	100 %
Trajectory	Cartesian

Physio - PACE

Resp. control	Off
Concatenations	1

Inline - Common

Subtract	Off
Measurements	1
StdDev	Off
Save original images	On

Inline - MIP

MIP-Sag	Off
MIP-Cor	Off
MIP-Tra	Off
MIP-Time	Off
Save original images	On

Inline - Composing

Inline Composing	Off
Distortion Corr.	On
Mode	2D
Unfiltered images	Off

Sequence - Part 1

Introduction	On
Dimension	2D
Compensate T2 decay	Off
Reduce Motion Sens.	On
Contrasts	2
Flow comp.	No
Multi-slice mode	Interleaved
Free echo spacing	Off
Echo spacing	9.36 ms
Bandwidth	252 Hz/Px

Sequence - Part 2

Define	Turbo factor
Echo trains per slice	52
Phase correction	Automatic
Acoustic noise reduction	None
RF pulse type	Normal
Gradient mode	Normal
Hyperecho	Off
WARP	Off
Red. EC sensitivity	Off
Turbo factor	5

Sequence - Assistant

Mode	Min flip angle
Min flip angle	130 deg
Allowed delay	60 s

SIEMENS MAGNETOM Skyra

\\RESEARCH & Physics\RESEARCH\Sibims-2\SIBIMS-2 v7 21/02/2019\t2_spc_da-fl_ax_p2

TA: 5:12 PM: FIX Voxel size: 1.0×1.0×1.1 mmPAT: 2 Rel. SNR: 1.00 : spcir

Properties

Prio recon	Off
Load images to viewer	On
Inline movie	Off
Auto store images	On
Load images to stamp segments	Off
Load images to graphic segments	Off
Auto open inline display	Off
Auto close inline display	Off
Start measurement without further preparation	Off
Wait for user to start	Off
Start measurements	Single measurement

Routine

Slab group	1
Slabs	1
Position	Isocenter
Orientation	T > C-5.4
Phase enc. dir.	A >> P
AutoAlign	Head > Brain
Phase oversampling	0 %
Slice oversampling	0.0 %
Slices per slab	176
FoV read	256 mm
FoV phase	96.9 %
Slice thickness	1.10 mm
TR	5000 ms
TE	397 ms
Averages	1.0
Concatenations	1
Filter	Raw filter, Prescan Normalize
Coil elements	HE1-4

Contrast - Common

TR	5000 ms
TE	397 ms
MTC	Off
Magn. preparation	Non-sel. T2-IR
TI 1	1800 ms
Fat suppr.	None
Blood suppr.	Off
Restore magn.	Off

Contrast - Dynamic

Averages	1.0
Reconstruction	Magnitude
Measurements	1
Multiple series	Each measurement

Resolution - Common

FoV read	256 mm
FoV phase	96.9 %
Slice thickness	1.10 mm
Base resolution	256
Phase resolution	100 %
Slice resolution	83 %
Phase partial Fourier	Allowed
Slice partial Fourier	7/8
Interpolation	Off

Resolution - iPAT

PAT mode	GRAPPA
Accel. factor PE	2
Ref. lines PE	24
Accel. factor 3D	1
Reference scan mode	Integrated

Resolution - Filter Image

Image Filter	Off
Distortion Corr.	Off
Prescan Normalize	On
Unfiltered images	Off
Normalize	Off
B1 filter	Off

Resolution - Filter Rawdata

Raw filter	On
Elliptical filter	Off

Geometry - Common

Slab group	1
Slabs	1
Position	Isocenter
Orientation	T > C-5.4
Phase enc. dir.	A >> P
Slice oversampling	0.0 %
Slices per slab	176
FoV read	256 mm
FoV phase	96.9 %
Slice thickness	1.10 mm
TR	5000 ms
Series	Interleaved
Concatenations	1

Geometry - AutoAlign

Slab group	1
Position	Isocenter
Orientation	T > C-5.4
Phase enc. dir.	A >> P
AutoAlign	Head > Brain
Initial Position	Isocenter
L	0.0 mm
P	0.0 mm
H	0.0 mm
Initial Rotation	0.54 deg
Initial Orientation	T > C
T > C	-5.4
> S	0.0

Geometry - Saturation

Fat suppr.	None
Restore magn.	Off
Special sat.	None

Geometry - Navigator

Geometry - Tim Planning Suite

Set-n-Go Protocol	Off
Table position	H
Table position	0 mm
Inline Composing	Off

SIEMENS MAGNETOM Skyra

System - Miscellaneous

Positioning mode	FIX
Table position	H
Table position	0 mm
MSMA	S - C - T
Sagittal	R >> L
Coronal	A >> P
Transversal	F >> H
Coil Combine Mode	Adaptive Combine
Save uncombined	Off
Matrix Optimization	Off
AutoAlign	Head > Brain
Coil Select Mode	Off - AutoCoilSelect

System - Adjustments

B0 Shim mode	Standard
B1 Shim mode	TrueForm
Adjust with body coil	Off
Confirm freq. adjustment	Off
Assume Dominant Fat	Off
Assume Silicone	Off
Adjustment Tolerance	Auto

System - Adjust Volume

Position	Isocenter
Orientation	T > C-5.4
Rotation	0.54 deg
A >> P	248 mm
R >> L	256 mm
F >> H	194 mm
Reset	Off

System - Tx/Rx

Frequency 1H	123.253591 MHz
Correction factor	1
Gain	High
Img. Scale Cor.	1.000
Reset	Off
? Ref. amplitude 1H	0.000 V

Physio - Signal1

1st Signal/Mode	None
Trigger delay	0 ms
TR	5000 ms
Concatenations	1

Physio - Cardiac

Magn. preparation	Non-sel. T2-IR
TI 1	1800 ms
Fat suppr.	None
Dark blood	Off
FoV read	256 mm
FoV phase	96.9 %
Phase resolution	100 %

Physio - PACE

Resp. control	Off
Concatenations	1

Inline - Common

Subtract	Off
Measurements	1
StdDev	Off
Save original images	On

Inline - MIP

MIP-Sag	Off
MIP-Cor	Off
MIP-Tra	Off
MIP-Time	Off
Save original images	On

Inline - Composing

Inline Composing	Off
Distortion Corr.	Off

Sequence - Part 1

Introduction	On
Dimension	3D
Elliptical scanning	Off
Reordering	Linear
Flow comp.	No
Echo spacing	3.42 ms
Adiabatic-mode	Off
Bandwidth	781 Hz/Px

Sequence - Part 2

Echo train duration	879 ms
RF pulse type	Normal
Gradient mode	Fast
Excitation	Non-sel.
Flip angle mode	T2 var
Turbo factor	284

Sequence - Assistant

Allowed delay	30 s

SIEMENS MAGNETOM Skyra

\\RESEARCH & Physics\RESEARCH\Sibims-2\SIBIMS-2 v7 21/02/2019\B1 map

TA: 0:18 PM: FIX Voxel size: 3.9×3.9×8.0 mmPAT: Off Rel. SNR: 1.00 : tfl

Properties

Prio recon	Off
Load images to viewer	On
Inline movie	Off
Auto store images	On
Load images to stamp segments	Off
Load images to graphic segments	Off
Auto open inline display	Off
Auto close inline display	Off
Start measurement without further preparation	Off
Wait for user to start	Off
Start measurements	Single measurement

Routine

Slice group	1
Slices	15
Dist. factor	25 %
Position	Isocenter
Orientation	T > C-5.4
Phase enc. dir.	A >> P
AutoAlign	Head > Brain
Phase oversampling	0 %
FoV read	250 mm
FoV phase	100.0 %
Slice thickness	8.0 mm
TR	8190.0 ms
TE	1.83 ms
Averages	1
Concatenations	1
Filter	None
Coil elements	HE1-4

Contrast - Common

TR	8190.0 ms
TE	1.83 ms
Magn. preparation	None
Flip angle	8 deg
Fat suppr.	None
Water suppr.	None

Contrast - Dynamic

Averages	1
Reconstruction	Magnitude
Measurements	1
Multiple series	Each measurement

Resolution - Common

FoV read	250 mm
FoV phase	100.0 %
Slice thickness	8.0 mm
Base resolution	64
Phase resolution	100 %
Phase partial Fourier	Off
Interpolation	Off

Resolution - iPAT

PAT mode	None

Resolution - Filter Image

Image Filter	Off
Distortion Corr.	Off
Prescan Normalize	Off
Normalize	Off
B1 filter	Off

Resolution - Filter Rawdata

Raw filter	Off
Elliptical filter	Off

Geometry - Common

Slice group	1
Slices	15
Dist. factor	25 %
Position	Isocenter
Orientation	T > C-5.4
Phase enc. dir.	A >> P
FoV read	250 mm
FoV phase	100.0 %
Slice thickness	8.0 mm
TR	8190.0 ms
Multi-slice mode	Interleaved
Series	Interleaved
Concatenations	1

Geometry - AutoAlign

Slice group	1
Position	Isocenter
Orientation	T > C-5.4
Phase enc. dir.	A >> P
AutoAlign	Head > Brain
Initial Position	Isocenter
L	0.0 mm
P	0.0 mm
H	0.0 mm
Initial Rotation	0.54 deg
Initial Orientation	T > C
T > C	-5.4
> S	0.0

Geometry - Tim Planning Suite

Set-n-Go Protocol	Off
Table position	H
Table position	0 mm
Inline Composing	Off

System - Miscellaneous

Positioning mode	FIX
Table position	H
Table position	0 mm
MSMA	S - C - T
Sagittal	R >> L
Coronal	A >> P
Transversal	F >> H
Coil Combine Mode	Sum of Squares
Save uncombined	Off
Matrix Optimization	Off
AutoAlign	Head > Brain
Coil Select Mode	Default

SIEMENS MAGNETOM Skyra

System - Adjustments

B0 Shim mode	Tune up
B1 Shim mode	TrueForm
Adjust with body coil	Off
Confirm freq. adjustment	Off
Assume Dominant Fat	Off
Assume Silicone	Off
Adjustment Tolerance	Auto

System - Adjust Volume

Position	Isocenter
Orientation	Transversal
Rotation	0.00 deg
A >> P	263 mm
R >> L	350 mm
F >> H	350 mm
Reset	Off

System - Tx/Rx

Frequency 1H	123.253591 MHz
Correction factor	1
Gain	High
Img. Scale Cor.	1.000
Reset	Off
? Ref. amplitude 1H	0.000 V

Inline - Common

Subtract	Off
Measurements	1
StdDev	Off
Save original images	On

Inline - MIP

MIP-Sag	Off
MIP-Cor	Off
MIP-Tra	Off
MIP-Time	Off
Save original images	On

Inline - Composing

Inline Composing	Off
Distortion Corr.	Off

Sequence - Part 1

Introduction	On
Dimension	2D
Asymmetric echo	Allowed
Flow comp.	No
Multi-slice mode	Interleaved
Echo spacing	4.1 ms
Bandwidth	490 Hz/Px

Sequence - Part 2

RF pulse type	Low SAR
Gradient mode	Normal
Excitation	Slice-sel.
RF spoiling	On
Turbo factor	64

Sequence - Assistant

Mode	Off

SIEMENS MAGNETOM Skyra

\\RESEARCH & Physics\RESEARCH\Sibims-2\SIBIMS-2 v7 21/02/2019\t1_mprage_sag_p2_iso_1.0_pre

TA: 5:38 PM: FIX Voxel size: 1.0×1.0×1.0 mmPAT: 2 Rel. SNR: 1.00 : tfl

Properties

Prio recon	Off
Load images to viewer	On
Inline movie	Off
Auto store images	On
Load images to stamp segments	Off
Load images to graphic segments	Off
Auto open inline display	Off
Auto close inline display	Off
Start measurement without further preparation	Off
Wait for user to start	Off
Start measurements	Single measurement

Routine

Slab group	1
Slabs	1
Dist. factor	50 %
Position	L3.4 P2.3 F24.9 mm
Orientation	Sagittal
Phase enc. dir.	A >> P
AutoAlign	---
Phase oversampling	10 %
Slice oversampling	27.3 %
Slices per slab	176
FoV read	250 mm
FoV phase	100.0 %
Slice thickness	1.00 mm
TR	2200.0 ms
TE	2.45 ms
Averages	1
Concatenations	1
Filter	Distortion Corr.(2D), Prescan Normalize, Image Filter
Coil elements	HE1-4;NE1,2

Contrast - Common

TR	2200.0 ms
TE	2.45 ms
Magn. preparation	Non-sel. IR
TI	900 ms
Flip angle	8 deg
Fat suppr.	None
Water suppr.	None

Contrast - Dynamic

Averages	1
Averaging mode	Long term
Reconstruction	Magnitude
Measurements	1
Multiple series	Each measurement

Resolution - Common

FoV read	250 mm
FoV phase	100.0 %
Slice thickness	1.00 mm
Base resolution	256
Phase resolution	100 %
Slice resolution	100 %

Resolution - Common

Phase partial Fourier	Off
Slice partial Fourier	Off
Interpolation	Off

Resolution - iPAT

PAT mode	GRAPPA
Accel. factor PE	2
Ref. lines PE	24
Accel. factor 3D	1
Reference scan mode	Integrated

Resolution - Filter Image

Image Filter	On
! Intensity	Medium
Edge Enhancement	3
Smoothing	2
Unfiltered images	Off
Distortion Corr.	On
Mode	2D
Unfiltered images	Off
Prescan Normalize	On
Unfiltered images	Off
Normalize	Off
B1 filter	Off

Resolution - Filter Rawdata

Raw filter	Off
Elliptical filter	Off

Geometry - Common

Slab group	1
Slabs	1
Dist. factor	50 %
Position	L3.4 P2.3 F24.9 mm
Orientation	Sagittal
Phase enc. dir.	A >> P
Slice oversampling	27.3 %
Slices per slab	176
FoV read	250 mm
FoV phase	100.0 %
Slice thickness	1.00 mm
TR	2200.0 ms
Multi-slice mode	Single shot
Series	Ascending
Concatenations	1

Geometry - AutoAlign

Slab group	1
Position	L3.4 P2.3 F24.9 mm
Orientation	Sagittal
Phase enc. dir.	A >> P
AutoAlign	---
Initial Position	L3.4 P2.3 F24.9
L	3.4 mm
P	2.3 mm
F	24.9 mm
Initial Rotation	-15.10 deg
Initial Orientation	Sagittal

SIEMENS MAGNETOM Skyra

Geometry - Navigator

Geometry - Tim Planning Suite

Set-n-Go Protocol	Off
Table position	H
Table position	0 mm
Inline Composing	Off

System - Miscellaneous

Positioning mode	FIX
Table position	H
Table position	0 mm
MSMA	S - C - T
Sagittal	R >> L
Coronal	A >> P
Transversal	F >> H
Coil Combine Mode	Adaptive Combine
Save uncombined	Off
Matrix Optimization	Off
AutoAlign	---
Coil Select Mode	Off - AutoCoilSelect

System - Adjustments

B0 Shim mode	Tune up
B1 Shim mode	TrueForm
Adjust with body coil	Off
Confirm freq. adjustment	Off
Assume Dominant Fat	Off
Assume Silicone	Off
Adjustment Tolerance	Auto

System - Adjust Volume

Position	Isocenter
Orientation	Transversal
Rotation	0.00 deg
A >> P	263 mm
R >> L	350 mm
F >> H	350 mm
Reset	Off

System - Tx/Rx

Frequency 1H	123.253591 MHz
Correction factor	1
Gain	Low
Img. Scale Cor.	1.000
Reset	Off
? Ref. amplitude 1H	0.000 V

Physio - Signal1

1st Signal/Mode	None
TR	2200.0 ms
Concatenations	1

Physio - Cardiac

Magn. preparation	Non-sel. IR
TI	900 ms
Fat suppr.	None
Dark blood	Off
FoV read	250 mm
FoV phase	100.0 %
Phase resolution	100 %

Physio - PACE

Resp. control	Off

Physio - PACE

Concatenations	1

Inline - Common

Subtract	Off
Measurements	1
StdDev	Off
Save original images	On

Inline - MIP

MIP-Sag	Off
MIP-Cor	Off
MIP-Tra	Off
MIP-Time	Off
Save original images	On

Inline - Composing

Inline Composing	Off
Distortion Corr.	On
Mode	2D
Unfiltered images	Off

Inline - MapIt

Save original images	On
MapIt	None
Flip angle	8 deg
Measurements	1
TR	2200.0 ms
TE	2.45 ms

Sequence - Part 1

Introduction	On
Dimension	3D
Elliptical scanning	Off
Reordering	Linear
Asymmetric echo	Allowed
Flow comp.	No
Multi-slice mode	Single shot
Echo spacing	6 ms
Bandwidth	250 Hz/Px

Sequence - Part 2

RF pulse type	Fast
Gradient mode	Normal
Excitation	Slab-sel.
RF spoiling	On
Incr. Gradient spoiling	Off
Turbo factor	224

Sequence - Assistant

Mode	Off

SIEMENS MAGNETOM Skyra

\\RESEARCH & Physics\RESEARCH\Sibims-2\SIBIMS-2 v7 21/02/2019\Angio3D_ax_dyn_FA5_4av

TA: 0:25 PM: FIX Voxel size: 1.3×1.3×5.0 mmPAT: 2 Rel. SNR: 1.00 : fl

Properties

Prio recon	Off
Load images to viewer	On
Inline movie	Off
Auto store images	On
Load images to stamp segments	On
Load images to graphic segments	On
Auto open inline display	Off
Auto close inline display	Off
Start measurement without further preparation	Off
Wait for user to start	Off
Start measurements	Single measurement

Routine

Slab group	1
Slabs	1
Dist. factor	20 %
Position	Isocenter
Orientation	T > C-5.4
Phase enc. dir.	R >> L
AutoAlign	Head > Brain
Phase oversampling	0 %
Slice oversampling	0.0 %
Slices per slab	30
FoV read	250 mm
FoV phase	75.0 %
Slice thickness	5.00 mm
TR	2.48 ms
TE	0.99 ms
Averages	4
Filter	Distortion Corr.(2D), Prescan Normalize
Coil elements	HE1-4

Contrast - Common

TR	2.48 ms
TE	0.99 ms
Magn. preparation	None
Flip angle	5 deg
Fat suppr.	Fat sat.

Contrast - Dynamic

Averages	4
Averaging mode	Short term
Reconstruction	Magn./Phase
Measurements	2
Pause after meas. 1	0.0 s
Multiple series	Off

Resolution - Common

FoV read	250 mm
FoV phase	75.0 %
Slice thickness	5.00 mm
Base resolution	192
Phase resolution	75 %
Slice resolution	73 %
Phase partial Fourier	6/8
Slice partial Fourier	6/8
Interpolation	Off

Resolution - iPAT

PAT mode	GRAPPA
Accel. factor PE	2
Ref. lines PE	24
Accel. factor 3D	1
Reference scan mode	Integrated

Resolution - Filter Image

Image Filter	Off
Distortion Corr.	On
Mode	2D
Unfiltered images	Off
Prescan Normalize	On
Unfiltered images	Off
Normalize	Off
B1 filter	Off

Resolution - Filter Rawdata

Raw filter	Off
Elliptical filter	Off

Geometry - Common

Slab group	1
Slabs	1
Dist. factor	20 %
Position	Isocenter
Orientation	T > C-5.4
Phase enc. dir.	R >> L
Slice oversampling	0.0 %
Slices per slab	30
FoV read	250 mm
FoV phase	75.0 %
Slice thickness	5.00 mm
TR	2.48 ms
Multi-slice mode	Sequential
Series	Ascending

Geometry - AutoAlign

Slab group	1
Position	Isocenter
Orientation	T > C-5.4
Phase enc. dir.	R >> L
AutoAlign	Head > Brain
Initial Position	Isocenter
L	0.0 mm
P	0.0 mm
H	0.0 mm
Initial Rotation	90.54 deg
Initial Orientation	T > C
T > C	-5.4
> S	0.0

Geometry - Saturation

Fat suppr.	Fat sat.
Special sat.	None

Geometry - Tim Planning Suite

Set-n-Go Protocol	Off
Table position	H
Table position	0 mm
Inline Composing	Off

SIEMENS MAGNETOM Skyra

System - Miscellaneous

Positioning mode	FIX
Table position	H
Table position	0 mm
MSMA	S - C - T
Sagittal	R >> L
Coronal	A >> P
Transversal	F >> H
Coil Combine Mode	Sum of Squares
Save uncombined	Off
Matrix Optimization	Off
AutoAlign	Head > Brain
Coil Select Mode	On - AutoCoilSelect

System - Adjustments

B0 Shim mode	Standard
B1 Shim mode	TrueForm
Adjust with body coil	Off
Confirm freq. adjustment	Off
Assume Dominant Fat	Off
Assume Silicone	Off
Adjustment Tolerance	Maximum

System - Adjust Volume

Position	Isocenter
Orientation	T > C-5.4
Rotation	90.54 deg
R >> L	188 mm
A >> P	250 mm
F >> H	150 mm
Reset	Off

System - Tx/Rx

Frequency 1H	123.253591 MHz
Correction factor	1
Gain	Low
Img. Scale Cor.	1.000
Reset	Off
? Ref. amplitude 1H	0.000 V

Physio - Signal1

1st Signal/Mode	None
TR	2.48 ms
Segments	1

Angio - Common

Flip angle	5 deg
Measurements	2
Pause after meas. 1	0.0 s
3D centric reordering	Off
Time to center	1.2 s

Angio - Inline

Subtract	Off
Measurements	2
StdDev	Off
Motion Correction	None
Save original images	On

Angio - MIP

MIP-Sag	Off
MIP-Cor	Off
MIP-Tra	Off
MIP-Time	Off

Angio - MIP

Save original images	On

Angio - Composing

Inline Composing	Off
Distortion Corr.	On
Mode	2D
Unfiltered images	Off

Sequence - Part 1

Introduction	Off
Dimension	3D
Elliptical scanning	Off
Asymmetric echo	Allowed
Optimization	None
Multi-slice mode	Sequential
Bandwidth	930 Hz/Px

Sequence - Part 2

Segments	1
RF pulse type	Fast
Gradient mode	Fast
Excitation	Slab-sel.
RF spoiling	On
Phase Enc. Rewinder	On

Sequence - Assistant

Mode	Off
Allowed delay	0 s

SIEMENS MAGNETOM Skyra

\\RESEARCH & Physics\RESEARCH\Sibims-2\SIBIMS-2 v7 21/02/2019\Angio3D_ax_dyn_FA5_4av_TR10

TA: 1:25 PM: FIX Voxel size: 1.3×1.3×5.0 mmPAT: 2 Rel. SNR: 1.00 : fl

Properties

Prio recon	Off
Load images to viewer	On
Inline movie	Off
Auto store images	On
Load images to stamp segments	On
Load images to graphic segments	On
Auto open inline display	Off
Auto close inline display	Off
Start measurement without further preparation	Off
Wait for user to start	Off
Start measurements	Single measurement

Routine

Slab group	1
Slabs	1
Dist. factor	20 %
Position	Isocenter
Orientation	T > C-5.4
Phase enc. dir.	R >> L
AutoAlign	Head > Brain
Phase oversampling	0 %
Slice oversampling	0.0 %
Slices per slab	30
FoV read	250 mm
FoV phase	75.0 %
Slice thickness	5.00 mm
TR	10.00 ms
TE	0.99 ms
Averages	4
Filter	Distortion Corr.(2D), Prescan Normalize
Coil elements	HE1-4

Contrast - Common

TR	10.00 ms
TE	0.99 ms
Magn. preparation	None
Flip angle	5 deg
Fat suppr.	Fat sat.

Contrast - Dynamic

Averages	4
Averaging mode	Short term
Reconstruction	Magn./Phase
Measurements	2
Pause after meas. 1	0.0 s
Multiple series	Off

Resolution - Common

FoV read	250 mm
FoV phase	75.0 %
Slice thickness	5.00 mm
Base resolution	192
Phase resolution	75 %
Slice resolution	73 %
Phase partial Fourier	6/8
Slice partial Fourier	6/8
Interpolation	Off

Resolution - iPAT

PAT mode	GRAPPA
Accel. factor PE	2
Ref. lines PE	24
Accel. factor 3D	1
Reference scan mode	Integrated

Resolution - Filter Image

Image Filter	Off
Distortion Corr.	On
Mode	2D
Unfiltered images	Off
Prescan Normalize	On
Unfiltered images	Off
Normalize	Off
B1 filter	Off

Resolution - Filter Rawdata

Raw filter	Off
Elliptical filter	Off

Geometry - Common

Slab group	1
Slabs	1
Dist. factor	20 %
Position	Isocenter
Orientation	T > C-5.4
Phase enc. dir.	R >> L
Slice oversampling	0.0 %
Slices per slab	30
FoV read	250 mm
FoV phase	75.0 %
Slice thickness	5.00 mm
TR	10.00 ms
Multi-slice mode	Sequential
Series	Ascending

Geometry - AutoAlign

Slab group	1
Position	Isocenter
Orientation	T > C-5.4
Phase enc. dir.	R >> L
AutoAlign	Head > Brain
Initial Position	Isocenter
L	0.0 mm
P	0.0 mm
H	0.0 mm
Initial Rotation	90.54 deg
Initial Orientation	T > C
T > C	-5.4
> S	0.0

Geometry - Saturation

Fat suppr.	Fat sat.
Special sat.	None

Geometry - Tim Planning Suite

Set-n-Go Protocol	Off
Table position	H
Table position	0 mm

SIEMENS MAGNETOM Skyra

Geometry - Tim Planning Suite

Inline Composing	Off

System - Miscellaneous

Positioning mode	FIX
Table position	H
Table position	0 mm
MSMA	S - C - T
Sagittal	R >> L
Coronal	A >> P
Transversal	F >> H
Coil Combine Mode	Sum of Squares
Save uncombined	Off
Matrix Optimization	Off
AutoAlign	Head > Brain
Coil Select Mode	On - AutoCoilSelect

System - Adjustments

B0 Shim mode	Standard
B1 Shim mode	TrueForm
Adjust with body coil	Off
Confirm freq. adjustment	Off
Assume Dominant Fat	Off
Assume Silicone	Off
Adjustment Tolerance	Maximum

System - Adjust Volume

Position	Isocenter
Orientation	T > C-5.4
Rotation	90.54 deg
R >> L	188 mm
A >> P	250 mm
F >> H	150 mm
Reset	Off

System - Tx/Rx

Frequency 1H	123.253591 MHz
Correction factor	1
Gain	Low
Img. Scale Cor.	1.000
Reset	Off
? Ref. amplitude 1H	0.000 V

Physio - Signal1

1st Signal/Mode	None
TR	10.00 ms
Segments	1

Angio - Common

Flip angle	5 deg
Measurements	2
Pause after meas. 1	0.0 s
3D centric reordering	Off
Time to center	4.1 s

Angio - Inline

Subtract	Off
Measurements	2
StdDev	Off
Motion Correction	None
Save original images	On

Angio - MIP

MIP-Sag	Off

Angio - MIP

MIP-Cor	Off
MIP-Tra	Off
MIP-Time	Off
Save original images	On

Angio - Composing

Inline Composing	Off
Distortion Corr.	On
Mode	2D
Unfiltered images	Off

Sequence - Part 1

Introduction	Off
Dimension	3D
Elliptical scanning	Off
Asymmetric echo	Allowed
Optimization	None
Multi-slice mode	Sequential
Bandwidth	930 Hz/Px

Sequence - Part 2

Segments	1
RF pulse type	Fast
Gradient mode	Fast
Excitation	Slab-sel.
RF spoiling	On
Phase Enc. Rewinder	On

Sequence - Assistant

Mode	Off
Allowed delay	0 s

SIEMENS MAGNETOM Skyra

\\RESEARCH & Physics\RESEARCH\Sibims-2\SIBIMS-2 v7 21/02/2019\Angio3D_ax_dyn_FA7_4av

TA: 0:25 PM: FIX Voxel size: 1.3×1.3×5.0 mmPAT: 2 Rel. SNR: 1.00 : fl

Properties

Prio recon	Off
Load images to viewer	On
Inline movie	Off
Auto store images	On
Load images to stamp segments	On
Load images to graphic segments	On
Auto open inline display	Off
Auto close inline display	Off
Start measurement without further preparation	Off
Wait for user to start	Off
Start measurements	Single measurement

Routine

Slab group	1
Slabs	1
Dist. factor	20 %
Position	Isocenter
Orientation	T > C-5.4
Phase enc. dir.	R >> L
AutoAlign	Head > Brain
Phase oversampling	0 %
Slice oversampling	0.0 %
Slices per slab	30
FoV read	250 mm
FoV phase	75.0 %
Slice thickness	5.00 mm
TR	2.48 ms
TE	0.99 ms
Averages	4
Filter	Distortion Corr.(2D), Prescan Normalize
Coil elements	HE1-4

Contrast - Common

TR	2.48 ms
TE	0.99 ms
Magn. preparation	None
Flip angle	7 deg
Fat suppr.	Fat sat.

Contrast - Dynamic

Averages	4
Averaging mode	Short term
Reconstruction	Magn./Phase
Measurements	2
Pause after meas. 1	0.0 s
Multiple series	Off

Resolution - Common

FoV read	250 mm
FoV phase	75.0 %
Slice thickness	5.00 mm
Base resolution	192
Phase resolution	75 %
Slice resolution	73 %
Phase partial Fourier	6/8
Slice partial Fourier	6/8
Interpolation	Off

Resolution - iPAT

PAT mode	GRAPPA
Accel. factor PE	2
Ref. lines PE	24
Accel. factor 3D	1
Reference scan mode	Integrated

Resolution - Filter Image

Image Filter	Off
Distortion Corr.	On
Mode	2D
Unfiltered images	Off
Prescan Normalize	On
Unfiltered images	Off
Normalize	Off
B1 filter	Off

Resolution - Filter Rawdata

Raw filter	Off
Elliptical filter	Off

Geometry - Common

Slab group	1
Slabs	1
Dist. factor	20 %
Position	Isocenter
Orientation	T > C-5.4
Phase enc. dir.	R >> L
Slice oversampling	0.0 %
Slices per slab	30
FoV read	250 mm
FoV phase	75.0 %
Slice thickness	5.00 mm
TR	2.48 ms
Multi-slice mode	Sequential
Series	Ascending

Geometry - AutoAlign

Slab group	1
Position	Isocenter
Orientation	T > C-5.4
Phase enc. dir.	R >> L
AutoAlign	Head > Brain
Initial Position	Isocenter
L	0.0 mm
P	0.0 mm
H	0.0 mm
Initial Rotation	90.54 deg
Initial Orientation	T > C
T > C	-5.4
> S	0.0

Geometry - Saturation

Fat suppr.	Fat sat.
Special sat.	None

Geometry - Tim Planning Suite

Set-n-Go Protocol	Off
Table position	H
Table position	0 mm
Inline Composing	Off

SIEMENS MAGNETOM Skyra

System - Miscellaneous

Positioning mode	FIX
Table position	H
Table position	0 mm
MSMA	S - C - T
Sagittal	R >> L
Coronal	A >> P
Transversal	F >> H
Coil Combine Mode	Sum of Squares
Save uncombined	Off
Matrix Optimization	Off
AutoAlign	Head > Brain
Coil Select Mode	On - AutoCoilSelect

System - Adjustments

B0 Shim mode	Standard
B1 Shim mode	TrueForm
Adjust with body coil	Off
Confirm freq. adjustment	Off
Assume Dominant Fat	Off
Assume Silicone	Off
Adjustment Tolerance	Maximum

System - Adjust Volume

Position	Isocenter
Orientation	T > C-5.4
Rotation	90.54 deg
R >> L	188 mm
A >> P	250 mm
F >> H	150 mm
Reset	Off

System - Tx/Rx

Frequency 1H	123.253591 MHz
Correction factor	1
Gain	Low
Img. Scale Cor.	1.000
Reset	Off
? Ref. amplitude 1H	0.000 V

Physio - Signal1

1st Signal/Mode	None
TR	2.48 ms
Segments	1

Angio - Common

Flip angle	7 deg
Measurements	2
Pause after meas. 1	0.0 s
3D centric reordering	Off
Time to center	1.2 s

Angio - Inline

Subtract	Off
Measurements	2
StdDev	Off
Motion Correction	None
Save original images	On

Angio - MIP

MIP-Sag	Off
MIP-Cor	Off
MIP-Tra	Off
MIP-Time	Off

Angio - MIP

Save original images	On

Angio - Composing

Inline Composing	Off
Distortion Corr.	On
Mode	2D
Unfiltered images	Off

Sequence - Part 1

Introduction	Off
Dimension	3D
Elliptical scanning	Off
Asymmetric echo	Allowed
Optimization	None
Multi-slice mode	Sequential
Bandwidth	930 Hz/Px

Sequence - Part 2

Segments	1
RF pulse type	Fast
Gradient mode	Fast
Excitation	Slab-sel.
RF spoiling	On
Phase Enc. Rewinder	On

Sequence - Assistant

Mode	Off
Allowed delay	0 s

SIEMENS MAGNETOM Skyra

\\RESEARCH & Physics\RESEARCH\Sibims-2\SIBIMS-2 v7 21/02/2019\Angio3D_ax_dyn_FA15_4av

TA: 0:25 PM: FIX Voxel size: 1.3×1.3×5.0 mmPAT: 2 Rel. SNR: 1.00 : fl

Properties

Prio recon	Off
Load images to viewer	On
Inline movie	Off
Auto store images	On
Load images to stamp segments	On
Load images to graphic segments	On
Auto open inline display	Off
Auto close inline display	Off
Start measurement without further preparation	Off
Wait for user to start	Off
Start measurements	Single measurement

Routine

Slab group	1
Slabs	1
Dist. factor	20 %
Position	Isocenter
Orientation	T > C-5.4
Phase enc. dir.	R >> L
AutoAlign	Head > Brain
Phase oversampling	0 %
Slice oversampling	0.0 %
Slices per slab	30
FoV read	250 mm
FoV phase	75.0 %
Slice thickness	5.00 mm
TR	2.48 ms
TE	0.99 ms
Averages	4
Filter	Distortion Corr.(2D), Prescan Normalize
Coil elements	HE1-4

Contrast - Common

TR	2.48 ms
TE	0.99 ms
Magn. preparation	None
Flip angle	15 deg
Fat suppr.	Fat sat.

Contrast - Dynamic

Averages	4
Averaging mode	Short term
Reconstruction	Magn./Phase
Measurements	2
Pause after meas. 1	0.0 s
Multiple series	Off

Resolution - Common

FoV read	250 mm
FoV phase	75.0 %
Slice thickness	5.00 mm
Base resolution	192
Phase resolution	75 %
Slice resolution	73 %
Phase partial Fourier	6/8
Slice partial Fourier	6/8
Interpolation	Off

Resolution - iPAT

PAT mode	GRAPPA
Accel. factor PE	2
Ref. lines PE	24
Accel. factor 3D	1
Reference scan mode	Integrated

Resolution - Filter Image

Image Filter	Off
Distortion Corr.	On
Mode	2D
Unfiltered images	Off
Prescan Normalize	On
Unfiltered images	Off
Normalize	Off
B1 filter	Off

Resolution - Filter Rawdata

Raw filter	Off
Elliptical filter	Off

Geometry - Common

Slab group	1
Slabs	1
Dist. factor	20 %
Position	Isocenter
Orientation	T > C-5.4
Phase enc. dir.	R >> L
Slice oversampling	0.0 %
Slices per slab	30
FoV read	250 mm
FoV phase	75.0 %
Slice thickness	5.00 mm
TR	2.48 ms
Multi-slice mode	Sequential
Series	Ascending

Geometry - AutoAlign

Slab group	1
Position	Isocenter
Orientation	T > C-5.4
Phase enc. dir.	R >> L
AutoAlign	Head > Brain
Initial Position	Isocenter
L	0.0 mm
P	0.0 mm
H	0.0 mm
Initial Rotation	90.54 deg
Initial Orientation	T > C
T > C	-5.4
> S	0.0

Geometry - Saturation

Fat suppr.	Fat sat.
Special sat.	None

Geometry - Tim Planning Suite

Set-n-Go Protocol	Off
Table position	H
Table position	0 mm
Inline Composing	Off

SIEMENS MAGNETOM Skyra

System - Miscellaneous

Positioning mode	FIX
Table position	H
Table position	0 mm
MSMA	S - C - T
Sagittal	R >> L
Coronal	A >> P
Transversal	F >> H
Coil Combine Mode	Sum of Squares
Save uncombined	Off
Matrix Optimization	Off
AutoAlign	Head > Brain
Coil Select Mode	On - AutoCoilSelect

System - Adjustments

B0 Shim mode	Standard
B1 Shim mode	TrueForm
Adjust with body coil	Off
Confirm freq. adjustment	Off
Assume Dominant Fat	Off
Assume Silicone	Off
Adjustment Tolerance	Maximum

System - Adjust Volume

Position	Isocenter
Orientation	T > C-5.4
Rotation	90.54 deg
R >> L	188 mm
A >> P	250 mm
F >> H	150 mm
Reset	Off

System - Tx/Rx

Frequency 1H	123.253591 MHz
Correction factor	1
Gain	Low
Img. Scale Cor.	1.000
Reset	Off
? Ref. amplitude 1H	0.000 V

Physio - Signal1

1st Signal/Mode	None
TR	2.48 ms
Segments	1

Angio - Common

Flip angle	15 deg
Measurements	2
Pause after meas. 1	0.0 s
3D centric reordering	Off
Time to center	1.2 s

Angio - Inline

Subtract	Off
Measurements	2
StdDev	Off
Motion Correction	None
Save original images	On

Angio - MIP

MIP-Sag	Off
MIP-Cor	Off
MIP-Tra	Off
MIP-Time	Off

Angio - MIP

Save original images	On

Angio - Composing

Inline Composing	Off
Distortion Corr.	On
Mode	2D
Unfiltered images	Off

Sequence - Part 1

Introduction	Off
Dimension	3D
Elliptical scanning	Off
Asymmetric echo	Allowed
Optimization	None
Multi-slice mode	Sequential
Bandwidth	930 Hz/Px

Sequence - Part 2

Segments	1
RF pulse type	Fast
Gradient mode	Fast
Excitation	Slab-sel.
RF spoiling	On
Phase Enc. Rewinder	On

Sequence - Assistant

Mode	Off
Allowed delay	0 s

SIEMENS MAGNETOM Skyra

\\RESEARCH & Physics\RESEARCH\Sibims-2\SIBIMS-2 v7 21/02/2019\Angio3D_ax_dyn_FA15_4av_TR10

TA: 1:25 PM: FIX Voxel size: 1.3×1.3×5.0 mmPAT: 2 Rel. SNR: 1.00 : fl

Properties

Prio recon	Off
Load images to viewer	On
Inline movie	Off
Auto store images	On
Load images to stamp segments	On
Load images to graphic segments	On
Auto open inline display	Off
Auto close inline display	Off
Start measurement without further preparation	Off
Wait for user to start	Off
Start measurements	Single measurement

Routine

Slab group	1
Slabs	1
Dist. factor	20 %
Position	Isocenter
Orientation	T > C-5.4
Phase enc. dir.	R >> L
AutoAlign	Head > Brain
Phase oversampling	0 %
Slice oversampling	0.0 %
Slices per slab	30
FoV read	250 mm
FoV phase	75.0 %
Slice thickness	5.00 mm
TR	10.00 ms
TE	0.99 ms
Averages	4
Filter	Distortion Corr.(2D), Prescan Normalize
Coil elements	HE1-4

Contrast - Common

TR	10.00 ms
TE	0.99 ms
Magn. preparation	None
Flip angle	15 deg
Fat suppr.	Fat sat.

Contrast - Dynamic

Averages	4
Averaging mode	Short term
Reconstruction	Magn./Phase
Measurements	2
Pause after meas. 1	0.0 s
Multiple series	Off

Resolution - Common

FoV read	250 mm
FoV phase	75.0 %
Slice thickness	5.00 mm
Base resolution	192
Phase resolution	75 %
Slice resolution	73 %
Phase partial Fourier	6/8
Slice partial Fourier	6/8
Interpolation	Off

Resolution - iPAT

PAT mode	GRAPPA
Accel. factor PE	2
Ref. lines PE	24
Accel. factor 3D	1
Reference scan mode	Integrated

Resolution - Filter Image

Image Filter	Off
Distortion Corr.	On
Mode	2D
Unfiltered images	Off
Prescan Normalize	On
Unfiltered images	Off
Normalize	Off
B1 filter	Off

Resolution - Filter Rawdata

Raw filter	Off
Elliptical filter	Off

Geometry - Common

Slab group	1
Slabs	1
Dist. factor	20 %
Position	Isocenter
Orientation	T > C-5.4
Phase enc. dir.	R >> L
Slice oversampling	0.0 %
Slices per slab	30
FoV read	250 mm
FoV phase	75.0 %
Slice thickness	5.00 mm
TR	10.00 ms
Multi-slice mode	Sequential
Series	Ascending

Geometry - AutoAlign

Slab group	1
Position	Isocenter
Orientation	T > C-5.4
Phase enc. dir.	R >> L
AutoAlign	Head > Brain
Initial Position	Isocenter
L	0.0 mm
P	0.0 mm
H	0.0 mm
Initial Rotation	90.54 deg
Initial Orientation	T > C
T > C	-5.4
> S	0.0

Geometry - Saturation

Fat suppr.	Fat sat.
Special sat.	None

Geometry - Tim Planning Suite

Set-n-Go Protocol	Off
Table position	H
Table position	0 mm

SIEMENS MAGNETOM Skyra

Geometry - Tim Planning Suite

Inline Composing	Off

System - Miscellaneous

Positioning mode	FIX
Table position	H
Table position	0 mm
MSMA	S - C - T
Sagittal	R >> L
Coronal	A >> P
Transversal	F >> H
Coil Combine Mode	Sum of Squares
Save uncombined	Off
Matrix Optimization	Off
AutoAlign	Head > Brain
Coil Select Mode	On - AutoCoilSelect

System - Adjustments

B0 Shim mode	Standard
B1 Shim mode	TrueForm
Adjust with body coil	Off
Confirm freq. adjustment	Off
Assume Dominant Fat	Off
Assume Silicone	Off
Adjustment Tolerance	Maximum

System - Adjust Volume

Position	Isocenter
Orientation	T > C-5.4
Rotation	90.54 deg
R >> L	188 mm
A >> P	250 mm
F >> H	150 mm
Reset	Off

System - Tx/Rx

Frequency 1H	123.253591 MHz
Correction factor	1
Gain	Low
Img. Scale Cor.	1.000
Reset	Off
? Ref. amplitude 1H	0.000 V

Physio - Signal1

1st Signal/Mode	None
TR	10.00 ms
Segments	1

Angio - Common

Flip angle	15 deg
Measurements	2
Pause after meas. 1	0.0 s
3D centric reordering	Off
Time to center	4.1 s

Angio - Inline

Subtract	Off
Measurements	2
StdDev	Off
Motion Correction	None
Save original images	On

Angio - MIP

MIP-Sag	Off

Angio - MIP

MIP-Cor	Off
MIP-Tra	Off
MIP-Time	Off
Save original images	On

Angio - Composing

Inline Composing	Off
Distortion Corr.	On
Mode	2D
Unfiltered images	Off

Sequence - Part 1

Introduction	Off
Dimension	3D
Elliptical scanning	Off
Asymmetric echo	Allowed
Optimization	None
Multi-slice mode	Sequential
Bandwidth	930 Hz/Px

Sequence - Part 2

Segments	1
RF pulse type	Fast
Gradient mode	Fast
Excitation	Slab-sel.
RF spoiling	On
Phase Enc. Rewinder	On

Sequence - Assistant

Mode	Off
Allowed delay	0 s

SIEMENS MAGNETOM Skyra

\\RESEARCH & Physics\RESEARCH\Sibims-2\SIBIMS-2 v7 21/02/2019\Angio3D_ax_dyn_300meas_2.5_fatsat_3.2

TA: 15:55 PM: FIX Voxel size: 1.3×1.3×5.0 mmPAT: 2 Rel. SNR: 1.00 : fl

Properties

Prio recon	Off
Load images to viewer	On
Inline movie	Off
Auto store images	On
Load images to stamp segments	On
Load images to graphic segments	On
Auto open inline display	Off
Auto close inline display	Off
Start measurement without further preparation	Off
Wait for user to start	On
Start measurements	Single measurement

Routine

Slab group	1
Slabs	1
Dist. factor	20 %
Position	Isocenter
Orientation	T > C-5.4
Phase enc. dir.	R >> L
AutoAlign	Head > Brain
Phase oversampling	0 %
Slice oversampling	0.0 %
Slices per slab	30
FoV read	250 mm
FoV phase	75.0 %
Slice thickness	5.00 mm
TR	2.48 ms
TE	0.99 ms
Averages	1
Filter	Distortion Corr.(2D), Prescan Normalize
Coil elements	HE1-4

Contrast - Common

TR	2.48 ms
TE	0.99 ms
Magn. preparation	None
Flip angle	15 deg
Fat suppr.	Fat sat.

Contrast - Dynamic

Averages	1
Averaging mode	Short term
Reconstruction	Magn./Phase
Measurements	300
Pause after meas.	0.0 s
Multiple series	Off

Resolution - Common

FoV read	250 mm
FoV phase	75.0 %
Slice thickness	5.00 mm
Base resolution	192
Phase resolution	75 %
Slice resolution	73 %
Phase partial Fourier	6/8
Slice partial Fourier	6/8
Interpolation	Off

Resolution - iPAT

PAT mode	GRAPPA
Accel. factor PE	2
Ref. lines PE	24
Accel. factor 3D	1
Reference scan mode	Integrated

Resolution - Filter Image

Image Filter	Off
Distortion Corr.	On
Mode	2D
Unfiltered images	Off
Prescan Normalize	On
Unfiltered images	Off
Normalize	Off
B1 filter	Off

Resolution - Filter Rawdata

Raw filter	Off
Elliptical filter	Off

Geometry - Common

Slab group	1
Slabs	1
Dist. factor	20 %
Position	Isocenter
Orientation	T > C-5.4
Phase enc. dir.	R >> L
Slice oversampling	0.0 %
Slices per slab	30
FoV read	250 mm
FoV phase	75.0 %
Slice thickness	5.00 mm
TR	2.48 ms
Multi-slice mode	Sequential
Series	Ascending

Geometry - AutoAlign

Slab group	1
Position	Isocenter
Orientation	T > C-5.4
Phase enc. dir.	R >> L
AutoAlign	Head > Brain
Initial Position	Isocenter
L	0.0 mm
P	0.0 mm
H	0.0 mm
Initial Rotation	90.54 deg
Initial Orientation	T > C
T > C	-5.4
> S	0.0

Geometry - Saturation

Fat suppr.	Fat sat.
Special sat.	None

Geometry - Tim Planning Suite

Set-n-Go Protocol	Off
Table position	H
Table position	0 mm

SIEMENS MAGNETOM Skyra

Geometry - Tim Planning Suite

Inline Composing	Off

System - Miscellaneous

Positioning mode	FIX
Table position	H
Table position	0 mm
MSMA	S - C - T
Sagittal	R >> L
Coronal	A >> P
Transversal	F >> H
Coil Combine Mode	Sum of Squares
Save uncombined	Off
Matrix Optimization	Off
AutoAlign	Head > Brain
Coil Select Mode	On - AutoCoilSelect

System - Adjustments

B0 Shim mode	Standard
B1 Shim mode	TrueForm
Adjust with body coil	Off
Confirm freq. adjustment	Off
Assume Dominant Fat	Off
Assume Silicone	Off
Adjustment Tolerance	Maximum

System - Adjust Volume

Position	Isocenter
Orientation	T > C-5.4
Rotation	90.54 deg
R >> L	188 mm
A >> P	250 mm
F >> H	150 mm
Reset	Off

System - Tx/Rx

Frequency 1H	123.253591 MHz
Correction factor	1
Gain	Low
Img. Scale Cor.	1.000
Reset	Off
? Ref. amplitude 1H	0.000 V

Physio - Signal1

1st Signal/Mode	None
TR	2.48 ms
Segments	1

Angio - Common

Flip angle	15 deg
Measurements	300
Pause after meas.	0.0 s
3D centric reordering	Off
Time to center	1.2 s

Angio - Inline

Subtract	Off
Measurements	300
StdDev	Off
Motion Correction	None
Save original images	On

Angio - MIP

MIP-Sag	Off

Angio - MIP

MIP-Cor	Off
MIP-Tra	Off
MIP-Time	Off
Save original images	On

Angio - Composing

Inline Composing	Off
Distortion Corr.	On
Mode	2D
Unfiltered images	Off

Sequence - Part 1

Introduction	Off
Dimension	3D
Elliptical scanning	Off
Asymmetric echo	Allowed
Optimization	None
Multi-slice mode	Sequential
Bandwidth	930 Hz/Px

Sequence - Part 2

Segments	1
RF pulse type	Fast
Gradient mode	Fast
Excitation	Slab-sel.
RF spoiling	On
Phase Enc. Rewinder	On

Sequence - Assistant

Mode	Off
Allowed delay	0 s

SIEMENS MAGNETOM Skyra

\\RESEARCH & Physics\RESEARCH\Sibims-2\SIBIMS-2 v7 21/02/2019\t1_mprage_sag_p2_iso_1.0_post

TA: 5:38 PM: FIX Voxel size: 1.0×1.0×1.0 mmPAT: 2 Rel. SNR: 1.00 : tfl

Properties

Prio recon	Off
Load images to viewer	On
Inline movie	Off
Auto store images	On
Load images to stamp segments	Off
Load images to graphic segments	Off
Auto open inline display	Off
Auto close inline display	Off
Start measurement without further preparation	Off
Wait for user to start	Off
Start measurements	Single measurement

Routine

Slab group	1
Slabs	1
Dist. factor	50 %
Position	L3.4 P2.3 F24.9 mm
Orientation	Sagittal
Phase enc. dir.	A >> P
AutoAlign	---
Phase oversampling	10 %
Slice oversampling	27.3 %
Slices per slab	176
FoV read	250 mm
FoV phase	100.0 %
Slice thickness	1.00 mm
TR	2200.0 ms
TE	2.45 ms
Averages	1
Concatenations	1
Filter	Distortion Corr.(2D), Prescan Normalize, Image Filter
Coil elements	HE1-4;NE1,2

Contrast - Common

TR	2200.0 ms
TE	2.45 ms
Magn. preparation	Non-sel. IR
TI	900 ms
Flip angle	8 deg
Fat suppr.	None
Water suppr.	None

Contrast - Dynamic

Averages	1
Averaging mode	Long term
Reconstruction	Magnitude
Measurements	1
Multiple series	Each measurement

Resolution - Common

FoV read	250 mm
FoV phase	100.0 %
Slice thickness	1.00 mm
Base resolution	256
Phase resolution	100 %
Slice resolution	100 %

Resolution - Common

Phase partial Fourier	Off
Slice partial Fourier	Off
Interpolation	Off

Resolution - iPAT

PAT mode	GRAPPA
Accel. factor PE	2
Ref. lines PE	24
Accel. factor 3D	1
Reference scan mode	Integrated

Resolution - Filter Image

Image Filter	On
! Intensity	Medium
Edge Enhancement	3
Smoothing	2
Unfiltered images	Off
Distortion Corr.	On
Mode	2D
Unfiltered images	Off
Prescan Normalize	On
Unfiltered images	Off
Normalize	Off
B1 filter	Off

Resolution - Filter Rawdata

Raw filter	Off
Elliptical filter	Off

Geometry - Common

Slab group	1
Slabs	1
Dist. factor	50 %
Position	L3.4 P2.3 F24.9 mm
Orientation	Sagittal
Phase enc. dir.	A >> P
Slice oversampling	27.3 %
Slices per slab	176
FoV read	250 mm
FoV phase	100.0 %
Slice thickness	1.00 mm
TR	2200.0 ms
Multi-slice mode	Single shot
Series	Ascending
Concatenations	1

Geometry - AutoAlign

Slab group	1
Position	L3.4 P2.3 F24.9 mm
Orientation	Sagittal
Phase enc. dir.	A >> P
AutoAlign	---
Initial Position	L3.4 P2.3 F24.9
L	3.4 mm
P	2.3 mm
F	24.9 mm
Initial Rotation	-15.10 deg
Initial Orientation	Sagittal

SIEMENS MAGNETOM Skyra

Geometry - Navigator

Geometry - Tim Planning Suite

Set-n-Go Protocol	Off
Table position	H
Table position	0 mm
Inline Composing	Off

System - Miscellaneous

Positioning mode	FIX
Table position	H
Table position	0 mm
MSMA	S - C - T
Sagittal	R >> L
Coronal	A >> P
Transversal	F >> H
Coil Combine Mode	Adaptive Combine
Save uncombined	Off
Matrix Optimization	Off
AutoAlign	---
Coil Select Mode	Off - All

System - Adjustments

B0 Shim mode	Tune up
B1 Shim mode	TrueForm
Adjust with body coil	Off
Confirm freq. adjustment	Off
Assume Dominant Fat	Off
Assume Silicone	Off
Adjustment Tolerance	Auto

System - Adjust Volume

Position	Isocenter
Orientation	Transversal
Rotation	0.00 deg
A >> P	263 mm
R >> L	350 mm
F >> H	350 mm
Reset	Off

System - Tx/Rx

Frequency 1H	123.253591 MHz
Correction factor	1
Gain	Low
Img. Scale Cor.	1.000
Reset	Off
? Ref. amplitude 1H	0.000 V

Physio - Signal1

1st Signal/Mode	None
TR	2200.0 ms
Concatenations	1

Physio - Cardiac

Magn. preparation	Non-sel. IR
TI	900 ms
Fat suppr.	None
Dark blood	Off
FoV read	250 mm
FoV phase	100.0 %
Phase resolution	100 %

Physio - PACE

Resp. control	Off

Physio - PACE

Concatenations	1

Inline - Common

Subtract	Off
Measurements	1
StdDev	Off
Save original images	On

Inline - MIP

MIP-Sag	Off
MIP-Cor	Off
MIP-Tra	Off
MIP-Time	Off
Save original images	On

Inline - Composing

Inline Composing	Off
Distortion Corr.	On
Mode	2D
Unfiltered images	Off

Inline - MapIt

Save original images	On
MapIt	None
Flip angle	8 deg
Measurements	1
TR	2200.0 ms
TE	2.45 ms

Sequence - Part 1

Introduction	On
Dimension	3D
Elliptical scanning	Off
Reordering	Linear
Asymmetric echo	Allowed
Flow comp.	No
Multi-slice mode	Single shot
Echo spacing	6 ms
Bandwidth	250 Hz/Px

Sequence - Part 2

RF pulse type	Fast
Gradient mode	Normal
Excitation	Slab-sel.
RF spoiling	On
Incr. Gradient spoiling	Off
Turbo factor	224

Sequence - Assistant

Mode	Off

List of References

1. Mackenzie IS, Morant SV, Bloomfield GA, MacDonald TM, O'Riordan J. Incidence and prevalence of multiple sclerosis in the UK 1990-2010: a descriptive study in the General Practice Research Database. J Neurol Neurosurg Psychiatry. 2014;85(1):76-84.

2. Compston A, Coles A. Multiple sclerosis. The Lancet. 2008;372(9648):1502-17.

3. Galea I, Ward-Abel N, Heesen C. Relapse in multiple sclerosis. BMJ. 2015;350:h1765.

4. Scalfari A, Neuhaus A, Daumer M, Muraro PA, Ebers GC. Onset of secondary progressive phase and long-term evolution of multiple sclerosis. J Neurol Neurosurg Psychiatry. 2014;85(1):67-75.

5. Scalfari A, Neuhaus A, Degenhardt A, Rice GP, Muraro PA, Daumer M, et al. The natural history of multiple sclerosis: a geographically based study 10: relapses and long-term disability. Brain. 2010;133(Pt 7):1914-29.

6. Lassmann H. Multiple Sclerosis Pathology. Cold Spring Harb Perspect Med. 2018;8(3).

7. Lassmann H, van Horssen J, Mahad D. Progressive multiple sclerosis: pathology and pathogenesis. Nat Rev Neurol. 2012;8(11):647-56.

8. Serafini B, Rosicarelli B, Magliozzi R, Stigliano E, Aloisi F. Detection of Ectopic B-cell Follicles with Germinal Centers in the Meninges of Patients with Secondary Progressive Multiple Sclerosis. Brain Pathology. 2004;14(2):164-74.

9. Tremlett H, Yousefi M, Devonshire V, Rieckmann P, Zhao Y, Neurologists UBC. Impact of multiple sclerosis relapses on progression diminishes with time. Neurology. 2009;73(20):1616-23.

10. International Multiple Sclerosis Genetics Consortium. Multiple sclerosis genomic map implicates peripheral immune cells and microglia in susceptibility. Science. 2019;365(6460).

11. Rovira A, Wattjes MP, Tintore M, Tur C, Yousry TA, Sormani MP, et al. Evidence-based guidelines: MAGNIMS consensus guidelines on the use of MRI in multiple sclerosis-clinical implementation in the diagnostic process. Nat Rev Neurol. 2015;11(8):471-82.

12. Wattjes MP, Rovira A, Miller D, Yousry TA, Sormani MP, de Stefano MP, et al. Evidence-based guidelines: MAGNIMS consensus guidelines on the use of MRI in multiple sclerosis--establishing disease prognosis and monitoring patients. Nat Rev Neurol. 2015;11(10):597-606.

13. Barkhof F. MRI in multiple sclerosis: correlation with expanded disability status scale (EDSS). Mult Scler. 1999;5(4):283-6.

14. Kermode AG, Thompson AJ, Tofts P, MacManus DG, Kendall BE, Kingsley DP, et al. Breakdown of the blood-brain barrier precedes symptoms and other MRI signs of new lesions in multiple sclerosis. Pathogenetic and clinical implications. Brain. 1990;113 (Pt 5):1477-89.

15. Sahraian MA, Radue EW, Haller S, Kappos L. Black holes in multiple sclerosis: definition, evolution, and clinical correlations. Acta Neurol Scand. 2010;122(1):1-8.

16. Khaleeli Z, Ciccarelli O, Manfredonia F, Barkhof F, Brochet B, Cercignani M, et al. Predicting progression in primary progressive multiple sclerosis: a 10-year multicenter study. Ann Neurol. 2008;63(6):790-3.

17. Fabis MJ, Scott GS, Kean RB, Koprowski H, Hooper DC. Loss of blood-brain barrier integrity in the spinal cord is common to experimental allergic encephalomyelitis in knockout mouse models. Proc Natl Acad Sci U S A. 2007;104(13):5656-61.

18. Fabis MJ, Phares TW, Kean RB, Koprowski H, Hooper DC. Blood-brain barrier changes and cell invasion differ between therapeutic immune clearance of neurotrophic virus and CNS autoimmunity. Proc Natl Acad Sci U S A. 2008;105(40):15511-6.

19. Wolburg H, Wolburg-Buchholz K, Kraus J, Rascher-Eggstein G, Liebner S, Hamm S, et al. Localization of claudin-3 in tight junctions of the blood-brain barrier is selectively lost during experimental autoimmune encephalomyelitis and human glioblastoma multiforme. Acta Neuropathol. 2003;105(6):586-92.

20. Minagar A, Alexander JS. Blood-brain barrier disruption in multiple sclerosis. Mult Scler. 2003;9(6):540-9.

21. Junker A, Krumbholz M, Eisele S, Mohan H, Augstein F, Bittner R, et al. MicroRNA profiling of multiple sclerosis lesions identifies modulators of the regulatory protein CD47. Brain. 2009;132(Pt 12):3342-52.

22. Lopez-Ramirez MA, Wu D, Pryce G, Simpson JE, Reijerkerk A, King-Robson J, et al. MicroRNA-155 negatively affects blood-brain barrier function during neuroinflammation. FASEB J. 2014;28(6):2551-65.

23. Cramer SP, Simonsen H, Frederiksen JL, Rostrup E, Larsson HB. Abnormal blood-brain barrier permeability in normal appearing white matter in multiple sclerosis investigated by MRI. Neuroimage Clin. 2014;4:182-9.

24. Alvarez JI, Saint-Laurent O, Godschalk A, Terouz S, Briels C, Larouche S, et al. Focal disturbances in the blood-brain barrier are associated with formation of neuroinflammatory lesions. Neurobiol Dis. 2015;74:14-24.

25. Filippi M, Rossi P, Campi A, Colombo B, Pereira C, Comi G. Serial contrast-enhanced MR in patients with multiple sclerosis and varying levels of disability. AJNR Am J Neuroradiol. 1997;18(8):1549-56.

26. Thompson AJ, Kermode AG, Wicks D, MacManus DG, Kendall BE, Kingsley DP, et al. Major differences in the dynamics of primary and secondary progressive multiple sclerosis. Ann Neurol. 1991;29(1):53-62.

27. McLean BN, Zeman AZ, Barnes D, Thompson EJ. Patterns of blood-brain barrier impairment and clinical features in multiple sclerosis. J Neurol Neurosurg Psychiatry. 1993;56(4):356-60.

28. Akaishi T, Narikawa K, Suzuki Y, Mitsuzawa S, Tsukita K, Kuroda H, et al. Importance of the quotient of albumin, quotient of immunoglobulin G and Reibergram in inflammatory neurological disorders with disease-specific patterns of blood–brain barrier permeability. Neurology and Clinical Neuroscience. 2015;3(3):94-100.

29. Jongen PJ, Lamers KJ, Doesburg WH, Lemmens WA, Hommes OR. Cerebrospinal fluid analysis differentiates between relapsing-remitting and secondary progressive multiple sclerosis. J Neurol Neurosurg Psychiatry. 1997;63(4):446-51.

30. Hochmeister S, Grundtner R, Bauer J, Engelhardt B, Lyck R, Gordon G, et al. Dysferlin is a new marker for leaky brain blood vessels in multiple sclerosis. J Neuropathol Exp Neurol. 2006;65(9):855-65.

31. Kirk J, Plumb J, Mirakhur M, McQuaid S. Tight junctional abnormality in multiple sclerosis white matter affects all calibres of vessel and is associated with blood-brain barrier leakage and active demyelination. J Pathol. 2003;201(2):319-27.

32. Leech S, Kirk J, Plumb J, McQuaid S. Persistent endothelial abnormalities and blood-brain barrier leak in primary and secondary progressive multiple sclerosis. Neuropathol Appl Neurobiol. 2007;33(1):86-98.

33. Eilaghi A, Kassner A, Sitartchouk I, Francis PL, Jakubovic R, Feinstein A, et al. Normal-appearing white matter permeability distinguishes poor cognitive performance in processing speed and working memory. AJNR Am J Neuroradiol. 2013;34(11):2119-24.

34. Akaishi T, Takahashi T, Fujihara K, Misu T, Nishiyama S, Takai Y, et al. Impact of intrathecal IgG synthesis on neurological disability in patients with multiple sclerosis. Mult Scler Relat Disord. 2020;45:102382.

35. Uher T, Horakova D, Tyblova M, Zeman D, Krasulova E, Mrazova K, et al. Increased albumin quotient (QAlb) in patients after first clinical event suggestive of multiple sclerosis is associated with development of brain atrophy and greater disability 48 months later. Mult Scler. 2016;22(6):770-81.

36. Willis MD, Robertson NP. Multiple sclerosis and the risk of infection: considerations in the threat of the novel coronavirus, COVID-19/SARS-CoV-2. J Neurol. 2020;267(5):1567-9.

37. Andersen O, Lygner PE, Bergstrom T, Andersson M, Vahlne A. Viral infections trigger multiple sclerosis relapses: a prospective seroepidemiological study. J Neurol. 1993;240(7):417-22.

38. Edwards S, Zvartau M, Clarke H, Irving W, Blumhardt LD. Clinical relapses and disease activity on magnetic resonance imaging associated with viral upper respiratory tract infections in multiple sclerosis. J Neurol Neurosurg Psychiatry. 1998;64(6):736-41.

39. Correale J, Fiol M, Gilmore W. The risk of relapses in multiple sclerosis during systemic infections. Neurology. 2006;67(4):652-9.

40. Panitch HS. Influence of infection on exacerbations of multiple sclerosis. Ann Neurol. 1994;36 Suppl:S25-8.

41. Buljevac D, Flach HZ, Hop WC, Hijdra D, Laman JD, Savelkoul HF, et al. Prospective study on the relationship between infections and multiple sclerosis exacerbations. Brain. 2002;125(Pt 5):952-60.

42. Sibley W. Clinical Viral Infections and Multiple Sclerosis. The Lancet. 1985;325(8441):1313-5.

43. Moreno B, Jukes JP, Vergara-Irigaray N, Errea O, Villoslada P, Perry VH, et al. Systemic inflammation induces axon injury during brain inflammation. Ann Neurol. 2011;70(6):932-42.

44. Serres S, Anthony DC, Jiang Y, Broom KA, Campbell SJ, Tyler DJ, et al. Systemic inflammatory response reactivates immune-mediated lesions in rat brain. J Neurosci. 2009;29(15):4820-8.

45. Flores-Mireles AL, Walker JN, Caparon M, Hultgren SJ. Urinary tract infections: epidemiology, mechanisms of infection and treatment options. Nat Rev Microbiol. 2015;13(5):269-84.

46. Medeiros Junior WLG, Demore CC, Mazaro LP, de Souza MFN, Parolin LF, Melo LH, et al. Urinary tract infection in patients with multiple sclerosis: An overview. Mult Scler Relat Disord. 2020;46:102462.

47. de Seze M, Ruffion A, Denys P, Joseph PA, Perrouin-Verbe B, Genulf. The neurogenic bladder in multiple sclerosis: review of the literature and proposal of management guidelines. Mult Scler. 2007;13(7):915-28.

48. Jick SS, Li L, Falcone GJ, Vassilev ZP, Wallander MA. Epidemiology of multiple sclerosis: results from a large observational study in the UK. J Neurol. 2015;262(9):2033-41.

49. Marrie RA, Elliott L, Marriott J, Cossoy M, Blanchard J, Tennakoon A, et al. Dramatically changing rates and reasons for hospitalization in multiple sclerosis. Neurology. 2014;83(10):929-37.

50. Stamm WE. Measurement of pyuria and its relation to bacteriuria. Am J Med. 1983;75(1B):53-8.

51. Sathiananthamoorthy S, Malone-Lee J, Gill K, Tymon A, Nguyen TK, Gurung S, et al. Reassessment of Routine Midstream Culture in Diagnosis of Urinary Tract Infection. J Clin Microbiol. 2019;57(3).

52. Bent S, Nallamothu BK, Simel DL, Fihn SD, Saint S. Does this woman have an acute uncomplicated urinary tract infection? JAMA. 2002;287(20):2701-10.

53. Kupelian AS, Horsley H, Khasriya R, Amussah RT, Badiani R, Courtney AM, et al. Discrediting microscopic pyuria and leucocyte esterase as diagnostic surrogates for infection in patients with lower urinary tract symptoms: results from a clinical and laboratory evaluation. BJU Int. 2013;112(2):231-8.

54. Khasriya R, Barcella W, De Iorio M, Swamy S, Gill K, Kupelian A, et al. Lower urinary tract symptoms that predict microscopic pyuria. Int Urogynecol J. 2018;29(7):1019-28.

55. Gadeholt H. Quantitative estimation of cells in urine. An evaluation of the Addis count. Acta Med Scand. 1968;183(4):369-74.

56. Public Health England. Diagnosis of urinary tract infections: Quick reference tool for primary care for consultation and local adaptation. 2020 [Available from: https://assets.publishing.service.gov.uk/government/uploads/system/uploads/attachment_data/file/927195/UTI_diagnostic_flowchart_NICE-October_2020-FINAL.pdf.

57. Abbott NJ, Patabendige AA, Dolman DE, Yusof SR, Begley DJ. Structure and function of the blood-brain barrier. Neurobiol Dis. 2010;37(1):13-25.

58. Reese TS, Karnovsky MJ. Fine structural localization of a blood-brain barrier to exogenous peroxidase. J Cell Biol. 1967;34(1):207-17.

59. Simpson IA, Carruthers A, Vannucci SJ. Supply and demand in cerebral energy metabolism: the role of nutrient transporters. J Cereb Blood Flow Metab. 2007;27(11):1766-91.

60. Moore SA, Spector AA, Hart MN. Eicosanoid metabolism in cerebromicrovascular endothelium. Am J Physiol. 1988;254(1 Pt 1):C37-44.

61. Abbott NJ. Inflammatory mediators and modulation of blood-brain barrier permeability. Cell Mol Neurobiol. 2000;20(2):131-47.

62. Varatharaj A, Galea I. The blood-brain barrier in systemic inflammation. Brain Behav Immun. 2017;60:1-12.

63. de Vries HE, Blom-Roosemalen MC, van Oosten M, de Boer AG, van Berkel TJ, Breimer DD, et al. The influence of cytokines on the integrity of the blood-brain barrier in vitro. J Neuroimmunol. 1996;64(1):37-43.

64. Tunkel AR, Rosser SW, Hansen EJ, Scheld WM. Blood-brain barrier alterations in bacterial meningitis: development of an in vitro model and observations on the effects of lipopolysaccharide. In Vitro Cell Dev Biol. 1991;27A(2):113-20.

65. Deo AK, Theil FP, Nicolas JM. Confounding parameters in preclinical assessment of blood-brain barrier permeation: an overview with emphasis on species differences and effect of disease states. Mol Pharm. 2013;10(5):1581-95.

66. Banks WA. The blood-brain barrier in neuroimmunology: Tales of separation and assimilation. Brain Behav Immun. 2015;44:1-8.

67. Cao C, Matsumura K, Yamagata K, Watanabe Y. Induction by lipopolysaccharide of cyclooxygenase-2 mRNA in rat brain; its possible role in the febrile response. Brain Res. 1995;697(1-2):187-96.

68. Minami T, Okazaki J, Kawabata A, Kuroda R, Okazaki Y. Penetration of cisplatin into mouse brain by lipopolysaccharide. Toxicology. 1998;130(2-3):107-13.

69. Wong D, Dorovini-Zis K, Vincent SR. Cytokines, nitric oxide, and cGMP modulate the permeability of an in vitro model of the human blood-brain barrier. Exp Neurol. 2004;190(2):446-55.

70. Qin LH, Huang W, Mo XA, Chen YL, Wu XH. LPS Induces Occludin Dysregulation in Cerebral Microvascular Endothelial Cells via MAPK Signaling and Augmenting MMP-2 Levels. Oxid Med Cell Longev. 2015;2015:120641.

71. Yu HY, Cai YB, Liu Z. Activation of AMPK improves lipopolysaccharide-induced dysfunction of the blood-brain barrier in mice. Brain Inj. 2015;29(6):777-84.

72. Karahashi H, Michelsen KS, Arditi M. Lipopolysaccharide-induced apoptosis in transformed bovine brain endothelial cells and human dermal microvessel endothelial cells: the role of JNK. J Immunol. 2009;182(11):7280-6.

73. Wiesinger A, Peters W, Chappell D, Kentrup D, Reuter S, Pavenstadt H, et al. Nanomechanics of the endothelial glycocalyx in experimental sepsis. PLoS One. 2013;8(11):e80905.

74. Chappell D, Hofmann-Kiefer K, Jacob M, Rehm M, Briegel J, Welsch U, et al. TNF-alpha induced shedding of the endothelial glycocalyx is prevented by hydrocortisone and antithrombin. Basic Res Cardiol. 2009;104(1):78-89.

75. Moseley R, Waddington RJ, Embery G. Degradation of glycosaminoglycans by reactive oxygen species derived from stimulated polymorphonuclear leukocytes. Biochim Biophys Acta. 1997;1362(2-3):221-31.

76. Lipowsky HH. Protease Activity and the Role of the Endothelial Glycocalyx in Inflammation. Drug Discov Today Dis Models. 2011;8(1):57-62.

77. Cardoso FL, Brites D, Brito MA. Looking at the blood-brain barrier: molecular anatomy and possible investigation approaches. Brain Res Rev. 2010;64(2):328-63.

78. Biesmans S, Meert TF, Bouwknecht JA, Acton PD, Davoodi N, De Haes P, et al. Systemic immune activation leads to neuroinflammation and sickness behavior in mice. Mediators Inflamm. 2013;2013:271359.

79. Zamanian JL, Xu L, Foo LC, Nouri N, Zhou L, Giffard RG, et al. Genomic analysis of reactive astrogliosis. J Neurosci. 2012;32(18):6391-410.

80. Takeda S, Sato N, Ikimura K, Nishino H, Rakugi H, Morishita R. Increased blood-brain barrier vulnerability to systemic inflammation in an Alzheimer disease mouse model. Neurobiol Aging. 2013;34(8):2064-70.

81. Perry VH, Holmes C. Microglial priming in neurodegenerative disease. Nat Rev Neurol. 2014;10(4):217-24.

82. Haruwaka K, Ikegami A, Tachibana Y, Ohno N, Konishi H, Hashimoto A, et al. Dual microglia effects on blood brain barrier permeability induced by systemic inflammation. Nat Commun. 2019;10(1):5816.

83. Elwood E, Lim Z, Naveed H, Galea I. The effect of systemic inflammation on human brain barrier function. Brain Behav Immun. 2017;62:35-40.

84. van Vliet EA, da Costa Araujo S, Redeker S, van Schaik R, Aronica E, Gorter JA. Blood-brain barrier leakage may lead to progression of temporal lobe epilepsy. Brain. 2007;130(Pt 2):521-34.

85. Kapural M, Krizanac-Bengez L, Barnett G, Perl J, Masaryk T, Apollo D, et al. Serum S-100beta as a possible marker of blood-brain barrier disruption. Brain Res. 2002;940(1-2):102-4.

86. Iannotti F, Fieschi C, Alfano B, Picozzi P, Mansi L, Pozzilli C, et al. Simplified, noninvasive PET measurement of blood-brain barrier permeability. J Comput Assist Tomogr. 1987;11(3):390-7.

87. Liebert A, Milej D, Weigl W, Gerega A, Kacprzak M, Maniewski R. Fluorescence-based method for assessment of blood-brain barrier disruption. Annu Int Conf IEEE Eng Med Biol Soc. 2013;2013:3040-2.

88. Knudsen GM. Application of the double-indicator technique for measurement of blood-brain barrier permeability in humans. Cerebrovasc Brain Metab Rev. 1994;6(1):1-30.

89. Gregori J, Schuff N, Kern R, Gunther M. T2-based arterial spin labeling measurements of blood to tissue water transfer in human brain. J Magn Reson Imaging. 2013;37(2):332-42.

90. Patlak CS, Blasberg RG, Fenstermacher JD. Graphical evaluation of blood-to-brain transfer constants from multiple-time uptake data. J Cereb Blood Flow Metab. 1983;3(1):1-7.

91. Cramer SP, Larsson HB. Accurate determination of blood-brain barrier permeability using dynamic contrast-enhanced T1-weighted MRI: a simulation and in vivo study on healthy subjects and multiple sclerosis patients. J Cereb Blood Flow Metab. 2014;34(10):1655-65.

92. Heye AK, Thrippleton MJ, Armitage PA, Valdes Hernandez MDC, Makin SD, Glatz A, et al. Tracer kinetic modelling for DCE-MRI quantification of subtle blood-brain barrier permeability. Neuroimage. 2016;125:446-55.

93. Barber TW, Brockway JA, Higgins LS. The density of tissues in and about the head. Acta Neurol Scand. 1970;46(1):85-92.

94. Larsson HB, Courivaud F, Rostrup E, Hansen AE. Measurement of brain perfusion, blood volume, and blood-brain barrier permeability, using dynamic contrast-enhanced T(1)-weighted MRI at 3 tesla. Magn Reson Med. 2009;62(5):1270-81.

95. Renkin EM. Transport of potassium-42 from blood to tissue in isolated mammalian skeletal muscles. Am J Physiol. 1959;197:1205-10.

96. Crone C. The Permeability of Capillaries in Various Organs as Determined by Use of the 'Indicator Diffusion' Method. Acta Physiol Scand. 1963;58:292-305.

97. Tofts PS, Kermode AG. Measurement of the blood-brain barrier permeability and leakage space using dynamic MR imaging. 1. Fundamental concepts. Magn Reson Med. 1991;17(2):357-67.

98. Tofts PS. Modeling tracer kinetics in dynamic Gd-DTPA MR imaging. J Magn Reson Imaging. 1997;7(1):91-101.

99. Carare RO, Aldea R, Agarwal N, Bacskai BJ, Bechman I, Boche D, et al. Clearance of interstitial fluid (ISF) and CSF (CLIC) group-part of Vascular Professional Interest Area (PIA): Cerebrovascular disease and the failure of elimination of Amyloid-beta from the brain and retina with age and Alzheimer's disease-Opportunities for Therapy. Alzheimers Dement (Amst). 2020;12(1):e12053.

100. Thrippleton MJ, Backes WH, Sourbron S, Ingrisch M, van Osch MJP, Dichgans M, et al. Quantifying blood-brain barrier leakage in small vessel disease: Review and consensus recommendations. Alzheimers Dement. 2019;15(6):840-58.

101. DCE-MRI Technical Committee. DCE-MRI Quantification Profile, Quantitative Imaging Biomarkers Alliance, Version 1.0 [Available from: https://www.rsna.org/uploadedFiles/RSNA/Content/Science_and_Education/QIBA/DCE-MRI_Quantification_Profile_v1%200-ReviewedDraft%208-8-12.pdf.

102. Koenig SH, Spiller M, Brown RD, 3rd, Wolf GL. Relaxation of water protons in the intra- and extracellular regions of blood containing Gd(DTPA). Magn Reson Med. 1986;3(5):791-5.

103. Saremi F. Perfusion Imaging in Clinical Practice: A Multimodality Approach to Tissue Perfusion Analysis: Wolters Kluwer; 2015.

104. Tofts PS, Brix G, Buckley DL, Evelhoch JL, Henderson E, Knopp MV, et al. Estimating kinetic parameters from dynamic contrast-enhanced T(1)-weighted MRI of a diffusable tracer: standardized quantities and symbols. J Magn Reson Imaging. 1999;10(3):223-32.

105. Cramer SP, Modvig S, Simonsen HJ, Frederiksen JL, Larsson HB. Permeability of the blood-brain barrier predicts conversion from optic neuritis to multiple sclerosis. Brain. 2015;138(Pt 9):2571-83.

106. Cramer SP, Simonsen HJ, Varatharaj A, Galea I, Frederiksen JL, Larsson HBW. Permeability of the blood-brain barrier predicts no evidence of disease activity at 2 years after natalizumab or fingolimod treatment in relapsing-remitting multiple sclerosis. Ann Neurol. 2018;83(5):902-14.

107. Calamante F, Ahlgren A, van Osch MJ, Knutsson L. A novel approach to measure local cerebral haematocrit using MRI. J Cereb Blood Flow Metab. 2016;36(4):768-80.

108. Okazawa H, Yonekura Y, Fujibayashi Y, Yamauchi H, Ishizu K, Nishizawa S, et al. Measurement of regional cerebral plasma pool and hematocrit with copper-62-labeled HSA-DTS. J Nucl Med. 1996;37(7):1080-5.

109. Lammertsma AA, Brooks DJ, Beaney RP, Turton DR, Kensett MJ, Heather JD, et al. In vivo measurement of regional cerebral haematocrit using positron emission tomography. J Cereb Blood Flow Metab. 1984;4(3):317-22.

110. Brooks DJ, Beaney RP, Lammertsma AA, Turton DR, Marshall J, Thomas DG, et al. Studies on regional cerebral haematocrit and blood flow in patients with cerebral tumours using positron emission tomography. Microvasc Res. 1986;31(3):267-76.

111. Sowa P, Bjornerud A, Nygaard GO, Damangir S, Spulber G, Celius EG, et al. Reduced perfusion in white matter lesions in multiple sclerosis. Eur J Radiol. 2015;84(12):2605-12.

112. Doche E, Lecocq A, Maarouf A, Duhamel G, Soulier E, Confort-Gouny S, et al. Hypoperfusion of the thalamus is associated with disability in relapsing remitting multiple sclerosis. J Neuroradiol. 2017;44(2):158-64.

113. de la Pena MJ, Pena IC, Garcia PG, Gavilan ML, Malpica N, Rubio M, et al. Early perfusion changes in multiple sclerosis patients as assessed by MRI using arterial spin labeling. Acta Radiol Open. 2019;8(12):2058460119894214.

114. Rashid W, Parkes LM, Ingle GT, Chard DT, Toosy AT, Altmann DR, et al. Abnormalities of cerebral perfusion in multiple sclerosis. J Neurol Neurosurg Psychiatry. 2004;75(9):1288-93.

115. European Federation of Clinical Chemistry and Laboratory Medicine. Biological variation in haematocrit [Available from: https://biologicalvariation.eu/search?q=haematocrit.

116. Rivers E, Nguyen B, Havstad S, Ressler J, Muzzin A, Knoblich B, et al. Early goal-directed therapy in the treatment of severe sepsis and septic shock. N Engl J Med. 2001;345(19):1368-77.

117. Stuart CM, Zotova E, Koster G, Varatharaj A, Richardson G, Cornick FR, et al. High-Throughput Urinary Neopterin-to-Creatinine Ratio Monitoring of Systemic Inflammation. J Appl Lab Med. 2020;5(1):101-13.

118. Zha Z, Bucher F, Nejatfard A, Zheng T, Zhang H, Yea K, et al. Interferon-gamma is a master checkpoint regulator of cytokine-induced differentiation. Proc Natl Acad Sci U S A. 2017;114(33):E6867-E74.

119. Fredrikson S, Link H, Eneroth P. CSF neopterin as marker of disease activity in multiple sclerosis. Acta Neurol Scand. 1987;75(5):352-5.

120. Raghavan K, Healy BC, Carruthers RL, Chitnis T. Progression rates and sample size estimates for PPMS based on the CLIMB study population. Mult Scler. 2015;21(2):180-8.

121. Barkhof F, Calabresi PA, Miller DH, Reingold SC. Imaging outcomes for neuroprotection and repair in multiple sclerosis trials. Nat Rev Neurol. 2009;5(5):256-66.

122. Vrenken H, Jenkinson M, Horsfield MA, Battaglini M, van Schijndel RA, Rostrup E, et al. Recommendations to improve imaging and analysis of brain lesion load and atrophy in longitudinal studies of multiple sclerosis. J Neurol. 2013;260(10):2458-71.

123. Miller DH, Barkhof F, Frank JA, Parker GJ, Thompson AJ. Measurement of atrophy in multiple sclerosis: pathological basis, methodological aspects and clinical relevance. Brain. 2002;125(Pt 8):1676-95.

124. Smith SM, Zhang Y, Jenkinson M, Chen J, Matthews PM, Federico A, et al. Accurate, robust, and automated longitudinal and cross-sectional brain change analysis. Neuroimage. 2002;17(1):479-89.

125. Smith SM, Jenkinson M, Woolrich MW, Beckmann CF, Behrens TE, Johansen-Berg H, et al. Advances in functional and structural MR image analysis and implementation as FSL. Neuroimage. 2004;23 Suppl 1:S208-19.

126. Smith SM. Fast robust automated brain extraction. Hum Brain Mapp. 2002;17(3):143-55.

127. Popescu V, Battaglini M, Hoogstrate WS, Verfaillie SC, Sluimer IC, van Schijndel RA, et al. Optimizing parameter choice for FSL-Brain Extraction Tool (BET) on 3D T1 images in multiple sclerosis. Neuroimage. 2012;61(4):1484-94.

128. Battaglini M, Smith SM, Brogi S, De Stefano N. Enhanced brain extraction improves the accuracy of brain atrophy estimation. Neuroimage. 2008;40(2):583-9.

129. Jenkinson M, Bannister P, Brady M, Smith S. Improved optimization for the robust and accurate linear registration and motion correction of brain images. Neuroimage. 2002;17(2):825-41.

130. Zhang Y, Brady M, Smith S. Segmentation of brain MR images through a hidden Markov random field model and the expectation-maximization algorithm. IEEE Trans Med Imaging. 2001;20(1):45-57.

131. van Walderveen MA, Kamphorst W, Scheltens P, van Waesberghe JH, Ravid R, Valk J, et al. Histopathologic correlate of hypointense lesions on T1-weighted spin-echo MRI in multiple sclerosis. Neurology. 1998;50(5):1282-8.

132. Beadnall HN, Wang C, Van Hecke W, Ribbens A, Billiet T, Barnett MH. Comparing longitudinal brain atrophy measurement techniques in a real-world multiple sclerosis clinical practice cohort: towards clinical integration? Ther Adv Neurol Disord. 2019;12:1756286418823462.

133. Enzinger C, Ropele S, Smith S, Strasser-Fuchs S, Poltrum B, Schmidt H, et al. Accelerated evolution of brain atrophy and "black holes" in MS patients with APOE-epsilon 4. Ann Neurol. 2004;55(4):563-9.

134. Giorgio A, Stromillo ML, Bartolozzi ML, Rossi F, Battaglini M, De Leucio A, et al. Relevance of hypointense brain MRI lesions for long-term worsening of clinical disability in relapsing multiple sclerosis. Mult Scler. 2014;20(2):214-9.

135. Fazekas F, Strasser-Fuchs S, Schmidt H, Enzinger C, Ropele S, Lechner A, et al. Apolipoprotein E genotype related differences in brain lesions of multiple sclerosis. J Neurol Neurosurg Psychiatry. 2000;69(1):25-8.

136. Battaglini M, Jenkinson M, De Stefano N. Evaluating and reducing the impact of white matter lesions on brain volume measurements. Hum Brain Mapp. 2012;33(9):2062-71.

137. Guo C, Ferreira D, Fink K, Westman E, Granberg T. Repeatability and reproducibility of FreeSurfer, FSL-SIENAX and SPM brain volumetric measurements and the effect of lesion filling in multiple sclerosis. Eur Radiol. 2019;29(3):1355-64.

138. NeuroImaging & Surgical Technologies Lab. Atlases [Available from: http://nist.mni.mcgill.ca/?page_id=714.

139. Eshaghi A, Prados F, Brownlee WJ, Altmann DR, Tur C, Cardoso MJ, et al. Deep gray matter volume loss drives disability worsening in multiple sclerosis. Ann Neurol. 2018;83(2):210-22.

140. Schmidt P, Gaser C, Arsic M, Buck D, Forschler A, Berthele A, et al. An automated tool for detection of FLAIR-hyperintense white-matter lesions in Multiple Sclerosis. Neuroimage. 2012;59(4):3774-83.

141. Egger C, Opfer R, Wang C, Kepp T, Sormani MP, Spies L, et al. MRI FLAIR lesion segmentation in multiple sclerosis: Does automated segmentation hold up with manual annotation? Neuroimage Clin. 2017;13:264-70.

142. Nijeholt GJ, van Walderveen MA, Castelijns JA, van Waesberghe JH, Polman C, Scheltens P, et al. Brain and spinal cord abnormalities in multiple sclerosis. Correlation between MRI parameters, clinical subtypes and symptoms. Brain. 1998;121 (Pt 4):687-97.

143. DeLuca GC, Ebers GC, Esiri MM. Axonal loss in multiple sclerosis: a pathological survey of the corticospinal and sensory tracts. Brain. 2004;127(Pt 5):1009-18.

144. Daams M, Weiler F, Steenwijk MD, Hahn HK, Geurts JJ, Vrenken H, et al. Mean upper cervical cord area (MUCCA) measurement in long-standing multiple sclerosis: relation to brain findings and clinical disability. Mult Scler. 2014;20(14):1860-5.

145. Kearney H, Rocca MA, Valsasina P, Balk L, Sastre-Garriga J, Reinhardt J, et al. Magnetic resonance imaging correlates of physical disability in relapse onset multiple sclerosis of long disease duration. Mult Scler. 2014;20(1):72-80.

146. Lukas C, Sombekke MH, Bellenberg B, Hahn HK, Popescu V, Bendfeldt K, et al. Relevance of spinal cord abnormalities to clinical disability in multiple sclerosis: MR imaging findings in a large cohort of patients. Radiology. 2013;269(2):542-52.

147. Losseff NA, Webb SL, O'Riordan JI, Page R, Wang L, Barker GJ, et al. Spinal cord atrophy and disability in multiple sclerosis. A new reproducible and sensitive MRI method with potential to monitor disease progression. Brain. 1996;119 (Pt 3):701-8.

148. Moccia M, Prados F, Filippi M, Rocca MA, Valsasina P, Brownlee WJ, et al. Longitudinal spinal cord atrophy in multiple sclerosis using the generalized boundary shift integral. Ann Neurol. 2019;86(5):704-13.

149. Agosta F, Absinta M, Sormani MP, Ghezzi A, Bertolotto A, Montanari E, et al. In vivo assessment of cervical cord damage in MS patients: a longitudinal diffusion tensor MRI study. Brain. 2007;130(Pt 8):2211-9.

150. Lin X, Tench CR, Turner B, Blumhardt LD, Constantinescu CS. Spinal cord atrophy and disability in multiple sclerosis over four years: application of a reproducible automated technique in monitoring disease progression in a cohort of the interferon beta-1a (Rebif) treatment trial. J Neurol Neurosurg Psychiatry. 2003;74(8):1090-4.

151. Ingle GT, Stevenson VL, Miller DH, Thompson AJ. Primary progressive multiple sclerosis: a 5-year clinical and MR study. Brain. 2003;126(Pt 11):2528-36.

152. Rashid W, Davies GR, Chard DT, Griffin CM, Altmann DR, Gordon R, et al. Increasing cord atrophy in early relapsing-remitting multiple sclerosis: a 3 year study. J Neurol Neurosurg Psychiatry. 2006;77(1):51-5.

153. Horsfield MA, Sala S, Neema M, Absinta M, Bakshi A, Sormani MP, et al. Rapid semi-automatic segmentation of the spinal cord from magnetic resonance images: application in multiple sclerosis. Neuroimage. 2010;50(2):446-55.

154. Amann M, Pezold S, Naegelin Y, Fundana K, Andelova M, Weier K, et al. Reliable volumetry of the cervical spinal cord in MS patient follow-up data with cord image analyzer (Cordial). J Neurol. 2016;263(7):1364-74.

155. De Leener B, Kadoury S, Cohen-Adad J. Robust, accurate and fast automatic segmentation of the spinal cord. Neuroimage. 2014;98:528-36.

156. De Leener B, Levy S, Dupont SM, Fonov VS, Stikov N, Louis Collins D, et al. SCT: Spinal Cord Toolbox, an open-source software for processing spinal cord MRI data. Neuroimage. 2017;145(Pt A):24-43.

157. Yiannakas MC, Mustafa AM, De Leener B, Kearney H, Tur C, Altmann DR, et al. Fully automated segmentation of the cervical cord from T1-weighted MRI using PropSeg: Application to multiple sclerosis. Neuroimage Clin. 2016;10:71-7.

158. Healy BC, Arora A, Hayden DL, Ceccarelli A, Tauhid SS, Neema M, et al. Approaches to normalization of spinal cord volume: application to multiple sclerosis. J Neuroimaging. 2012;22(3):e12-9.

159. Jasperse B, Valsasina P, Neacsu V, Knol DL, De Stefano N, Enzinger C, et al. Intercenter agreement of brain atrophy measurement in multiple sclerosis patients using manually-edited SIENA and SIENAX. J Magn Reson Imaging. 2007;26(4):881-5.

160. Kurtzke JF. Rating neurologic impairment in multiple sclerosis: an expanded disability status scale (EDSS). Neurology. 1983;33(11):1444-52.

161. Hobart J, Freeman J, Thompson A. Kurtzke scales revisited: the application of psychometric methods to clinical intuition. Brain. 2000;123 (Pt 5):1027-40.

162. Polman CH, Rudick RA. The multiple sclerosis functional composite: a clinically meaningful measure of disability. Neurology. 2010;74 Suppl 3:S8-15.

163. Hobart J, Lamping D, Fitzpatrick R, Riazi A, Thompson A. The Multiple Sclerosis Impact Scale (MSIS-29): a new patient-based outcome measure. Brain. 2001;124(Pt 5):962-73.

164. Chalder T, Berelowitz G, Pawlikowska T, Watts L, Wessely S, Wright D, et al. Development of a fatigue scale. Journal of Psychosomatic Research. 1993;37(2):147-53.

165. Benedict RH, Fishman I, McClellan MM, Bakshi R, Weinstock-Guttman B. Validity of the Beck Depression Inventory-Fast Screen in multiple sclerosis. Mult Scler. 2003;9(4):393-6.

166. Montalban X, Hauser SL, Kappos L, Arnold DL, Bar-Or A, Comi G, et al. Ocrelizumab versus Placebo in Primary Progressive Multiple Sclerosis. N Engl J Med. 2017;376(3):209-20.

167. Rudick RA, Polman CH, Cohen JA, Walton MK, Miller AE, Confavreux C, et al. Assessing disability progression with the Multiple Sclerosis Functional Composite. Mult Scler. 2009;15(8):984-97.

168. Costelloe L, O'Rourke K, Kearney H, McGuigan C, Gribbin L, Duggan M, et al. The patient knows best: significant change in the physical component of the Multiple Sclerosis Impact Scale (MSIS-29 physical). J Neurol Neurosurg Psychiatry. 2007;78(8):841-4.

169. McGuigan C, Hutchinson M. The multiple sclerosis impact scale (MSIS-29) is a reliable and sensitive measure. J Neurol Neurosurg Psychiatry. 2004;75(2):266-9.

170. Chataway J, Schuerer N, Alsanousi A, Chan D, MacManus D, Hunter K, et al. Effect of high-dose simvastatin on brain atrophy and disability in secondary progressive multiple sclerosis (MS-STAT): a randomised, placebo-controlled, phase 2 trial. The Lancet. 2014;383(9936):2213-21.

171. Polman CH, Reingold SC, Banwell B, Clanet M, Cohen JA, Filippi M, et al. Diagnostic criteria for multiple sclerosis: 2010 revisions to the McDonald criteria. Ann Neurol. 2011;69(2):292-302.

172. Office for National Statistics. Population estimates for UK, England and Wales, Scotland, and Northern Ireland [Available from: https://www.ons.gov.uk/peoplepopulationandcommunity/populationandmigration/populationestimates/datasets/populationestimatesforukenglandandwalesscotlandandnorthernireland.

173. Office for National Statistics. Multiple sclerosis: prevalence, incidence, and smoking status [Available from: https://www.gov.uk/government/publications/multiple-sclerosis-prevalence-

incidence-and-smoking-status/multiple-sclerosis-prevalence-incidence-and-smoking-status-data-briefing.

174. Altmann DR, Jasperse B, Barkhof F, Beckmann K, Filippi M, Kappos LD, et al. Sample sizes for brain atrophy outcomes in trials for secondary progressive multiple sclerosis. Neurology. 2009;72(7):595-601.

175. Wood J, Freemantle N, King M, Nazareth I. Trap of trends to statistical significance: likelihood of near significant P value becoming more significant with extra data. BMJ. 2014;348:g2215.

176. Vandenbroucke JP, von Elm E, Altman DG, Gotzsche PC, Mulrow CD, Pocock SJ, et al. Strengthening the Reporting of Observational Studies in Epidemiology (STROBE): explanation and elaboration. PLoS Med. 2007;4(10):e297.

177. FMRIB. FSLeyes [Available from: https://zenodo.org/record/3937147#.X5_WTIj7SUk.

178. De Stefano N, Stromillo ML, Giorgio A, Bartolozzi ML, Battaglini M, Baldini M, et al. Establishing pathological cut-offs of brain atrophy rates in multiple sclerosis. J Neurol Neurosurg Psychiatry. 2016;87(1):93-9.

179. Azevedo CJ, Cen SY, Jaberzadeh A, Zheng L, Hauser SL, Pelletier D. Contribution of normal aging to brain atrophy in MS. Neurol Neuroimmunol Neuroinflamm. 2019;6(6).

180. Gur RC, Mozley PD, Resnick SM, Gottlieb GL, Kohn M, Zimmerman R, et al. Gender differences in age effect on brain atrophy measured by magnetic resonance imaging. Proc Natl Acad Sci U S A. 1991;88(7):2845-9.

181. Rudick RA, Cutter G, Baier M, Fisher E, Dougherty D, Weinstock-Guttman B, et al. Use of the Multiple Sclerosis Functional Composite to predict disability in relapsing MS. Neurology. 2001;56(10):1324-30.

182. Pittas F, Ponsonby AL, van der Mei IA, Taylor BV, Blizzard L, Groom P, et al. Smoking is associated with progressive disease course and increased progression in clinical disability in a prospective cohort of people with multiple sclerosis. J Neurol. 2009;256(4):577-85.

183. Miller DH, Lublin FD, Sormani MP, Kappos L, Yaldizli O, Freedman MS, et al. Brain atrophy and disability worsening in primary progressive multiple sclerosis: insights from the INFORMS study. Ann Clin Transl Neurol. 2018;5(3):346-56.

184. Elliott C, Belachew S, Wolinsky JS, Hauser SL, Kappos L, Barkhof F, et al. Chronic white matter lesion activity predicts clinical progression in primary progressive multiple sclerosis. Brain. 2019;142(9):2787-99.

185. Gallinat J, Meisenzahl E, Jacobsen LK, Kalus P, Bierbrauer J, Kienast T, et al. Smoking and structural brain deficits: a volumetric MR investigation. Eur J Neurosci. 2006;24(6):1744-50.

186. Kalkers NF, Vrenken H, Uitdehaag BM, Polman CH, Barkhof F. Brain atrophy in multiple sclerosis: impact of lesions and of damage of whole brain tissue. Mult Scler. 2002;8(5):410-4.

187. Gawne-Cain ML, O'Riordan JI, Coles A, Newell B, Thompson AJ, Miller DH. MRI lesion volume measurement in multiple sclerosis and its correlation with disability: a comparison of fast fluid attenuated inversion recovery (fFLAIR) and spin echo sequences. J Neurol Neurosurg Psychiatry. 1998;64(2):197-203.

188. Denz H, Fuchs D, Hausen A, Huber H, Nachbaur D, Reibnegger G, et al. Value of urinary neopterin in the differential diagnosis of bacterial and viral infections. Klin Wochenschr. 1990;68(4):218-22.

189. Amiri H, de Sitter A, Bendfeldt K, Battaglini M, Gandini Wheeler-Kingshott CAM, Calabrese M, et al. Urgent challenges in quantification and interpretation of brain grey matter atrophy in individual MS patients using MRI. Neuroimage Clin. 2018;19:466-75.

190. Kolasa M, Hakulinen U, Brander A, Hagman S, Dastidar P, Elovaara I, et al. Diffusion tensor imaging and disability progression in multiple sclerosis: A 4-year follow-up study. Brain Behav. 2019;9(1):e01194.

191. Azevedo CJ, Kornak J, Chu P, Sampat M, Okuda DT, Cree BA, et al. In vivo evidence of glutamate toxicity in multiple sclerosis. Ann Neurol. 2014;76(2):269-78.

192. Kearney H, Altmann DR, Samson RS, Yiannakas MC, Wheeler-Kingshott CA, Ciccarelli O, et al. Cervical cord lesion load is associated with disability independently from atrophy in MS. Neurology. 2015;84(4):367-73.

193. Caramanos Z, Fonov VS, Francis SJ, Narayanan S, Pike GB, Collins DL, et al. Gradient distortions in MRI: characterizing and correcting for their effects on SIENA-generated measures of brain volume change. Neuroimage. 2010;49(2):1601-11.

194. Narayanan S, Nakamura K, Fonov VS, Maranzano J, Caramanos Z, Giacomini PS, et al. Brain volume loss in individuals over time: Source of variance and limits of detectability. Neuroimage. 2020;214:116737.

195. Nakamura K, Brown RA, Araujo D, Narayanan S, Arnold DL. Correlation between brain volume change and T2 relaxation time induced by dehydration and rehydration: implications for monitoring atrophy in clinical studies. Neuroimage Clin. 2014;6:166-70.

196. Sampat MP, Healy BC, Meier DS, Dell'Oglio E, Liguori M, Guttmann CR. Disease modeling in multiple sclerosis: assessment and quantification of sources of variability in brain parenchymal fraction measurements. Neuroimage. 2010;52(4):1367-73.

197. Austin PC, Brunner LJ. Inflation of the type I error rate when a continuous confounding variable is categorized in logistic regression analyses. Stat Med. 2004;23(7):1159-78.

198. Ramaglia V, Hughes TR, Donev RM, Ruseva MM, Wu X, Huitinga I, et al. C3-dependent mechanism of microglial priming relevant to multiple sclerosis. Proc Natl Acad Sci U S A. 2012;109(3):965-70.

199. O'Loughlin E, Madore C, Lassmann H, Butovsky O. Microglial Phenotypes and Functions in Multiple Sclerosis. Cold Spring Harb Perspect Med. 2018;8(2).

200. Romme Christensen J, Bornsen L, Ratzer R, Piehl F, Khademi M, Olsson T, et al. Systemic inflammation in progressive multiple sclerosis involves follicular T-helper, Th17- and activated B-cells and correlates with progression. PLoS One. 2013;8(3):e57820.

201. Fisher E, Rudick RA, Simon JH, Cutter G, Baier M, Lee JC, et al. Eight-year follow-up study of brain atrophy in patients with MS. Neurology. 2002;59(9):1412-20.

202. Mahadeva A, Tanasescu R, Gran B. Urinary tract infections in multiple sclerosis: under-diagnosed and under-treated? A clinical audit at a large University Hospital. Am J Clin Exp Immunol. 2014;3(1):57-67.

203. Fowler CJ, Panicker JN, Drake M, Harris C, Harrison SC, Kirby M, et al. A UK consensus on the management of the bladder in multiple sclerosis. J Neurol Neurosurg Psychiatry. 2009;80(5):470-7.

204. Hess MJ, Hess PE, Sullivan MR, Nee M, Yalla SV. Evaluation of cranberry tablets for the prevention of urinary tract infections in spinal cord injured patients with neurogenic bladder. Spinal Cord. 2008;46(9):622-6.

205. Santa Eulalia-Troisfontaines E, Martinez-Perez EM, Miegimolle-Herrero M, Planells-Del Pozo P. Oral health status of a population with multiple sclerosis. Med Oral Patol Oral Cir Bucal. 2012;17(2):e223-7.

206. Furutama D, Matsuda S, Yamawaki Y, Hatano S, Okanobu A, Memida T, et al. IL-6 Induced by Periodontal Inflammation Causes Neuroinflammation and Disrupts the Blood-Brain Barrier. Brain Sci. 2020;10(10).

207. Kim-Hellmuth S, Bechheim M, Putz B, Mohammadi P, Nedelec Y, Giangreco N, et al. Genetic regulatory effects modified by immune activation contribute to autoimmune disease associations. Nat Commun. 2017;8(1):266.

208. Aw D, Silva AB, Palmer DB. Immunosenescence: emerging challenges for an ageing population. Immunology. 2007;120(4):435-46.

209. Mokry LE, Ross S, Ahmad OS, Forgetta V, Smith GD, Goltzman D, et al. Vitamin D and Risk of Multiple Sclerosis: A Mendelian Randomization Study. PLoS Med. 2015;12(8):e1001866.

210. Kreutz M, Andreesen R, Krause SW, Szabo A, Ritz E, Reichel H. 1,25-dihydroxyvitamin D3 production and vitamin D3 receptor expression are developmentally regulated during differentiation of human monocytes into macrophages. Blood. 1993;82(4):1300-7.

211. Liu PT, Stenger S, Li H, Wenzel L, Tan BH, Krutzik SR, et al. Toll-like receptor triggering of a vitamin D-mediated human antimicrobial response. Science. 2006;311(5768):1770-3.

212. Lierse W, Horstmann E. Quantitative anatomy of the cerebral vascular bed with especial emphasis on homogeneity and inhomogeneity in small ports of the gray and white matter. Acta Neurol Scand Suppl. 1965;14:15-9.

213. Vos CM, Geurts JJ, Montagne L, van Haastert ES, Bo L, van der Valk P, et al. Blood-brain barrier alterations in both focal and diffuse abnormalities on postmortem MRI in multiple sclerosis. Neurobiol Dis. 2005;20(3):953-60.

214. Silver NC, Tofts PS, Symms MR, Barker GJ, Thompson AJ, Miller DH. Quantitative contrast-enhanced magnetic resonance imaging to evaluate blood-brain barrier integrity in multiple sclerosis: a preliminary study. Mult Scler. 2001;7(2):75-82.

215. Taheri S, Rosenberg GA, Ford C. Quantification of blood-to-brain transfer rate in multiple sclerosis. Mult Scler Relat Disord. 2013;2(2):124-32.

216. Lund H, Krakauer M, Skimminge A, Sellebjerg F, Garde E, Siebner HR, et al. Blood-brain barrier permeability of normal appearing white matter in relapsing-remitting multiple sclerosis. PLoS One. 2013;8(2):e56375.

217. Montagne A, Barnes SR, Sweeney MD, Halliday MR, Sagare AP, Zhao Z, et al. Blood-brain barrier breakdown in the aging human hippocampus. Neuron. 2015;85(2):296-302.

218. Tofts PS, Berkowitz B, Schnall MD. Quantitative analysis of dynamic Gd-DTPA enhancement in breast tumors using a permeability model. Magn Reson Med. 1995;33(4):564-8.

219. Parry A, Clare S, Jenkinson M, Smith S, Palace J, Matthews PM. White matter and lesion T1 relaxation times increase in parallel and correlate with disability in multiple sclerosis. J Neurol. 2002;249(9):1279-86.

220. Brookes JA, Redpath TW, Gilbert FJ, Needham G, Murray AD. Measurement of spin-lattice relaxation times with FLASH for dynamic MRI of the breast. Br J Radiol. 1996;69(819):206-14.

221. Schick F. Whole-body MRI at high field: technical limits and clinical potential. Eur Radiol. 2005;15(5):946-59.

222. Bojorquez JZ, Bricq S, Acquitter C, Brunotte F, Walker PM, Lalande A. What are normal relaxation times of tissues at 3 T? Magn Reson Imaging. 2017;35:69-80.

223. Gulani V, Calamante F, Shellock FG, Kanal E, Reeder SB. Gadolinium deposition in the brain: summary of evidence and recommendations. The Lancet Neurology. 2017;16(7):564-70.

224. Shen Y, Goerner FL, Snyder C, Morelli JN, Hao D, Hu D, et al. T1 relaxivities of gadolinium-based magnetic resonance contrast agents in human whole blood at 1.5, 3, and 7 T. Invest Radiol. 2015;50(5):330-8.

225. Ashburner J, Friston KJ. Voxel-based morphometry--the methods. Neuroimage. 2000;11(6 Pt 1):805-21.

226. Larsson HB, Hansen AE, Berg HK, Rostrup E, Haraldseth O. Dynamic contrast-enhanced quantitative perfusion measurement of the brain using T1-weighted MRI at 3T. J Magn Reson Imaging. 2008;27(4):754-62.

227. Zaki R, Bulgiba A, Ismail R, Ismail NA. Statistical methods used to test for agreement of medical instruments measuring continuous variables in method comparison studies: a systematic review. PLoS One. 2012;7(5):e37908.

228. Koo TK, Li MY. A Guideline of Selecting and Reporting Intraclass Correlation Coefficients for Reliability Research. J Chiropr Med. 2016;15(2):155-63.

229. Ferrier MC, Sarin H, Fung SH, Schatlo B, Pluta RM, Gupta SN, et al. Validation of dynamic contrast-enhanced magnetic resonance imaging-derived vascular permeability measurements using quantitative autoradiography in the RG2 rat brain tumor model. Neoplasia. 2007;9(7):546-55.

230. Klein B, Kuschinsky W, Schrock H, Vetterlein F. Interdependency of local capillary density, blood flow, and metabolism in rat brains. Am J Physiol. 1986;251(6 Pt 2):H1333-40.

231. Carroll TJ, Horowitz S, Shin W, Mouannes J, Sawlani R, Ali S, et al. Quantification of cerebral perfusion using the "bookend technique": an evaluation in CNS tumors. Magn Reson Imaging. 2008;26(10):1352-9.

232. Leenders KL, Perani D, Lammertsma AA, Heather JD, Buckingham P, Healy MJ, et al. Cerebral blood flow, blood volume and oxygen utilization. Normal values and effect of age. Brain. 1990;113 (Pt 1):27-47.

233. Gorgolewski KJ, Poldrack RA. A Practical Guide for Improving Transparency and Reproducibility in Neuroimaging Research. PLoS Biol. 2016;14(7):e1002506.

234. Sengupta A, Gupta RK, Singh A. Evaluation of B1 inhomogeneity effect on DCE-MRI data analysis of brain tumor patients at 3T. J Transl Med. 2017;15(1):242.

235. Naik P, Cucullo L. In vitro blood-brain barrier models: current and perspective technologies. J Pharm Sci. 2012;101(4):1337-54.

236. Captur G, Gatehouse P, Keenan KE, Heslinga FG, Bruehl R, Prothmann M, et al. A medical device-grade T1 and ECV phantom for global T1 mapping quality assurance-the T1 Mapping and ECV Standardization in cardiovascular magnetic resonance (T1MES) program. J Cardiovasc Magn Reson. 2016;18(1):58.

237. Deoni SC, Rutt BK, Peters TM. Rapid combined T1 and T2 mapping using gradient recalled acquisition in the steady state. Magn Reson Med. 2003;49(3):515-26.

238. Insko EK, Bolinger L. Mapping of the Radiofrequency Field. Journal of Magnetic Resonance, Series A. 1993;103(1):82-5.

239. Chung S, Kim D, Breton E, Axel L. Rapid B1+ mapping using a preconditioning RF pulse with TurboFLASH readout. Magn Reson Med. 2010;64(2):439-46.

240. Boudreau M, Tardif CL, Stikov N, Sled JG, Lee W, Pike GB. B1 mapping for bias-correction in quantitative T1 imaging of the brain at 3T using standard pulse sequences. J Magn Reson Imaging. 2017;46(6):1673-82.

241. Wansapura J, Holland S, Scott Dunn R, Ball Jr W. NMR Relaxation Times in the Human Brain at 3.0 Tesla. Journal of Magnetic Resonance Imaging. 1999;9:531-9.

242. Preibisch C, Deichmann R. Influence of RF spoiling on the stability and accuracy of T1 mapping based on spoiled FLASH with varying flip angles. Magn Reson Med. 2009;61(1):125-35.

243. Baudrexel S, Noth U, Schure JR, Deichmann R. T1 mapping with the variable flip angle technique: A simple correction for insufficient spoiling of transverse magnetization. Magn Reson Med. 2018;79(6):3082-92.

244. Wylie GR, Genova H, DeLuca J, Chiaravalloti N, Sumowski JF. Functional magnetic resonance imaging movers and shakers: does subject-movement cause sampling bias? Hum Brain Mapp. 2014;35(1):1-13.

245. Godenschweger F, Kagebein U, Stucht D, Yarach U, Sciarra A, Yakupov R, et al. Motion correction in MRI of the brain. Phys Med Biol. 2016;61(5):R32-56.

246. Jansen MJA, Kuijf HJ, Veldhuis WB, Wessels FJ, van Leeuwen MS, Pluim JPW. Evaluation of motion correction for clinical dynamic contrast enhanced MRI of the liver. Phys Med Biol. 2017;62(19):7556-68.

247. Vos SB, Tax CM, Luijten PR, Ourselin S, Leemans A, Froeling M. The importance of correcting for signal drift in diffusion MRI. Magn Reson Med. 2017;77(1):285-99.

248. Roberts C, Buckley DL, Parker GJ. Comparison of errors associated with single- and multi-bolus injection protocols in low-temporal-resolution dynamic contrast-enhanced tracer kinetic analysis. Magn Reson Med. 2006;56(3):611-9.

249. Grant EG, Benson CB, Moneta GL, Alexandrov AV, Baker JD, Bluth EI, et al. Carotid artery stenosis: gray-scale and Doppler US diagnosis--Society of Radiologists in Ultrasound Consensus Conference. Radiology. 2003;229(2):340-6.

250. Choudhry FA, Grantham JT, Rai AT, Hogg JP. Vascular geometry of the extracranial carotid arteries: an analysis of length, diameter, and tortuosity. J Neurointerv Surg. 2016;8(5):536-40.

251. Filice S, Crisi G. Dynamic Contrast-Enhanced Perfusion MRI of High Grade Brain Gliomas Obtained with Arterial or Venous Waveform Input Function. J Neuroimaging. 2016;26(1):124-9.

252. Hansen AE, Pedersen H, Rostrup E, Larsson HB. Partial volume effect (PVE) on the arterial input function (AIF) in T1-weighted perfusion imaging and limitations of the multiplicative rescaling approach. Magn Reson Med. 2009;62(4):1055-9.

253. Forkert ND, Fiehler J, Suniaga S, Wersching H, Knecht S, Kemmling A. A statistical cerebroarterial atlas derived from 700 MRA datasets. Methods Inf Med. 2013;52(6):467-74.

254. Huck J, Wanner Y, Fan AP, Jager AT, Grahl S, Schneider U, et al. High resolution atlas of the venous brain vasculature from 7 T quantitative susceptibility maps. Brain Struct Funct. 2019;224(7):2467-85.

255. Andersson J, Jenkinson M, Smith S. FMRIB Technical Report TR07JA2 [Available from: https://www.fmrib.ox.ac.uk/datasets/techrep/tr07ja2/tr07ja2.pdf.

256. Mouridsen K, Christensen S, Gyldensted L, Ostergaard L. Automatic selection of arterial input function using cluster analysis. Magn Reson Med. 2006;55(3):524-31.

257. Bink A, Schmitt M, Gaa J, Mugler JP, 3rd, Lanfermann H, Zanella FE. Detection of lesions in multiple sclerosis by 2D FLAIR and single-slab 3D FLAIR sequences at 3.0 T: initial results. Eur Radiol. 2006;16(5):1104-10.

258. Heinen R, Steenwijk MD, Barkhof F, Biesbroek JM, van der Flier WM, Kuijf HJ, et al. Performance of five automated white matter hyperintensity segmentation methods in a multicenter dataset. Sci Rep. 2019;9(1):16742.

259. van Westen D, Lindqvist D, Blennow K, Minthon L, Nagga K, Stomrud E, et al. Cerebral white matter lesions - associations with Abeta isoforms and amyloid PET. Sci Rep. 2016;6:20709.

260. Fujishima M, Maikusa N, Nakamura K, Nakatsuka M, Matsuda H, Meguro K. Mild cognitive impairment, poor episodic memory, and late-life depression are associated with cerebral cortical thinning and increased white matter hyperintensities. Front Aging Neurosci. 2014;6:306.

261. Thrippleton MJ. MRI measurement of blood-brain barrier leakage: minding the gaps. J Physiol. 2019;597(3):667-8.

262. International Organisation for Standardization. ISO 21748:2017 Guidance for the use of repeatability, reproducibility and trueness estimates in measurement uncertainty evaluation [Available from: https://www.iso.org/standard/71615.html.

263. Maggioli E, McArthur S, Mauro C, Kieswich J, Kusters DH, Reutelingsperger CP, et al. Estrogen protects the blood-brain barrier from inflammation-induced disruption and increased lymphocyte trafficking. Brain Behav Immun. 2016;51:212-22.

264. Pallebage-Gamarallage MM, Takechi R, Lam V, Galloway S, Dhaliwal S, Mamo JC. Post-prandial lipid metabolism, lipid-modulating agents and cerebrovascular integrity: implications for dementia risk. Atheroscler Suppl. 2010;11(1):49-54.

265. Chen X, Ghribi O, Geiger JD. Caffeine protects against disruptions of the blood-brain barrier in animal models of Alzheimer's and Parkinson's diseases. J Alzheimers Dis. 2010;20 Suppl 1:S127-41.

266. Malkiewicz MA, Szarmach A, Sabisz A, Cubala WJ, Szurowska E, Winklewski PJ. Blood-brain barrier permeability and physical exercise. J Neuroinflammation. 2019;16(1):15.

267. Tarbell JM, Pahakis MY. Mechanotransduction and the glycocalyx. J Intern Med. 2006;259(4):339-50.

268. Ernst E, Schroeder M, Saradeth T, Bergmann H. Analytical and physiological variations of some hemorheological and hematological blood tests. Clinical Hemorheology and Microcirculation. 1990;10(5):525-33.

269. Ismaili ARA, Vestergaard MB, Hansen AE, Larsson HBW, Johannesen HH, Law I, et al. Components of day-to-day variability of cerebral perfusion measurements - Analysis of phase contrast mapping magnetic resonance imaging measurements in healthy volunteers. PLoS One. 2018;13(6):e0197807.

270. Eurachem. Quantifying Uncertainty in Analytical Measurement [Available from: https://eurachem.org/images/stories/Guides/pdf/QUAM2012_P1.pdf.

271. Aarsand AK, Roraas T, Fernandez-Calle P, Ricos C, Diaz-Garzon J, Jonker N, et al. The Biological Variation Data Critical Appraisal Checklist: A Standard for Evaluating Studies on Biological Variation. Clin Chem. 2018;64(3):501-14.

272. Electronic Medicines Compendium. SmPC Gadovist [Available from: https://www.medicines.org.uk/emc/product/2876/smpc.

273. Freed M, de Zwart JA, Hariharan P, Myers MR, Badano A. Development and characterization of a dynamic lesion phantom for the quantitative evaluation of dynamic contrast-enhanced MRI. Med Phys. 2011;38(10):5601-11.

274. Wong SM, Jansen JFA, Zhang CE, Staals J, Hofman PAM, van Oostenbrugge RJ, et al. Measuring subtle leakage of the blood-brain barrier in cerebrovascular disease with DCE-MRI: Test-retest reproducibility and its influencing factors. J Magn Reson Imaging. 2017;46(1):159-66.

275. Huisa BN, Caprihan A, Thompson J, Prestopnik J, Qualls CR, Rosenberg GA. Long-Term Blood-Brain Barrier Permeability Changes in Binswanger Disease. Stroke. 2015;46(9):2413-8.

276. Andreasson A, Wicksell RK, Lodin K, Karshikoff B, Axelsson J, Lekander M. A global measure of sickness behaviour: Development of the Sickness Questionnaire. J Health Psychol. 2018;23(11):1452-63.

277. Dougados M, Simon P, Braun J, Burgos-Vargas R, Maksymowych WP, Sieper J, et al. ASAS recommendations for collecting, analysing and reporting NSAID intake in clinical trials/epidemiological studies in axial spondyloarthritis. Ann Rheum Dis. 2011;70(2):249-51.

278. van de Haar HJ, Jansen JFA, van Osch MJP, van Buchem MA, Muller M, Wong SM, et al. Neurovascular unit impairment in early Alzheimer's disease measured with magnetic resonance imaging. Neurobiol Aging. 2016;45:190-6.

279. Sullivan DC, Obuchowski NA, Kessler LG, Raunig DL, Gatsonis C, Huang EP, et al. Metrology Standards for Quantitative Imaging Biomarkers. Radiology. 2015;277(3):813-25.

280. Van Belle G. Statistical rules of thumb. New York: Wiley-Interscience; 2002. xviii, 221 p. p.

281. Jackson A, Jayson GC, Li KL, Zhu XP, Checkley DR, Tessier JJ, et al. Reproducibility of quantitative dynamic contrast-enhanced MRI in newly presenting glioma. Br J Radiol. 2003;76(903):153-62.

282. Roberts C, Issa B, Stone A, Jackson A, Waterton JC, Parker GJ. Comparative study into the robustness of compartmental modeling and model-free analysis in DCE-MRI studies. J Magn Reson Imaging. 2006;23(4):554-63.

283. Rennings A, Chen L, Otto S, Erni D, editors. B1-field inhomogeneity problem of MRI: Basic investigations on a head-tissue-simulating cylinder phantom excited by a birdcage-mode. 42nd European Microwave Conference; 2012; Amsterdam.

284. Parkes LM, Rashid W, Chard DT, Tofts PS. Normal cerebral perfusion measurements using arterial spin labeling: reproducibility, stability, and age and gender effects. Magn Reson Med. 2004;51(4):736-43.

285. Pozzilli C, Bernardi S, Mansi L, Picozzi P, Iannotti F, Alfano B, et al. Quantitative assessment of blood-brain barrier permeability in multiple sclerosis using 68-Ga-EDTA and positron emission tomography. J Neurol Neurosurg Psychiatry. 1988;51(8):1058-62.

286. Wang Y, Spiller M, Caravan P. Evidence for weak protein binding of commercial extracellular gadolinium contrast agents. Magn Reson Med. 2010;63(3):609-16.

287. While PT, Forbes LK, Crozier S. Designing gradient coils with reduced hot spot temperatures. J Magn Reson. 2010;203(1):91-9.

288. Morgan B, Utting JF, Higginson A, Thomas AL, Steward WP, Horsfield MA. A simple, reproducible method for monitoring the treatment of tumours using dynamic contrast-enhanced MR imaging. Br J Cancer. 2006;94(10):1420-7.

289. Galbraith SM, Lodge MA, Taylor NJ, Rustin GJ, Bentzen S, Stirling JJ, et al. Reproducibility of dynamic contrast-enhanced MRI in human muscle and tumours: comparison of quantitative and semi-quantitative analysis. NMR Biomed. 2002;15(2):132-42.

290. Koopman T, Martens RM, Lavini C, Yaqub M, Castelijns JA, Boellaard R, et al. Repeatability of arterial input functions and kinetic parameters in muscle obtained by dynamic contrast enhanced MR imaging of the head and neck. Magn Reson Imaging. 2020;68:1-8.

291. Fu F, Sun X, Li Y, Liu Y, Shan Y, Ji N, et al. Dynamic contrast-enhanced magnetic resonance imaging biomarkers predict chemotherapeutic responses and survival in primary central-nervous-system lymphoma. Eur Radiol. 2020.

292. Shahim P, Holleran L, Kim JH, Brody DL. Test-retest reliability of high spatial resolution diffusion tensor and diffusion kurtosis imaging. Sci Rep. 2017;7(1):11141.

293. Hougaard A, Amin FM, Christensen CE, Younis S, Wolfram F, Cramer SP, et al. Increased brainstem perfusion, but no blood-brain barrier disruption, during attacks of migraine with aura. Brain. 2017;140(6):1633-42.

294. Giovannoni G, Lai M, Kidd D, Thorpe JW, Miller DH, Thompson AJ, et al. Daily urinary neopterin excretion as an immunological marker of disease activity in multiple sclerosis. Brain. 1997;120 (Pt 1):1-13.

295. Fox RJ, Thompson A, Baker D, Baneke P, Brown D, Browne P, et al. Setting a research agenda for progressive multiple sclerosis: the International Collaborative on Progressive MS. Mult Scler. 2012;18(11):1534-40.

296. Kass EH. How important is bacteriuria? Rev Infect Dis. 1982;4(2):434-7.

297. Little P, Turner S, Rumsby K, Jones R, Warner G, Moore M, et al. Validating the prediction of lower urinary tract infection in primary care: sensitivity and specificity of urinary dipsticks and clinical scores in women. Br J Gen Pract. 2010;60(576):495-500.

298. Farrar JT, Troxel AB, Stott C, Duncombe P, Jensen MP. Validity, reliability, and clinical importance of change in a 0-10 numeric rating scale measure of spasticity: a post hoc analysis of a randomized, double-blind, placebo-controlled trial. Clin Ther. 2008;30(5):974-85.

299. Bohannon RW, Smith MB. Interrater reliability of a modified Ashworth scale of muscle spasticity. Phys Ther. 1987;67(2):206-7.

300. Sacco E, Bientinesi R, Marangi F, Totaro A, D'Addessi A, Racioppi M, et al. Patient-reported outcomes in men with lower urinary tract symptoms (LUTS) due to benign prostatic hyperplasia (BPH) treated with intraprostatic OnabotulinumtoxinA: 3-month results of a prospective single-armed cohort study. BJU Int. 2012;110(11 Pt C):E837-44.

301. Greenhalgh J, Ford H, Long AF, Hurst K. The MS Symptom and Impact Diary (MSSID): psychometric evaluation of a new instrument to measure the day to day impact of multiple sclerosis. J Neurol Neurosurg Psychiatry. 2004;75(4):577-82.

302. Fazekas F, Chawluk JB, Alavi A, Hurtig HI, Zimmerman RA. MR signal abnormalities at 1.5 T in Alzheimer's dementia and normal aging. AJR Am J Roentgenol. 1987;149(2):351-6.

303. Bouman PM, Steenwijk MD, Pouwels PJW, Schoonheim MM, Barkhof F, Jonkman LE, et al. Histopathology-validated recommendations for cortical lesion imaging in multiple sclerosis. Brain. 2020;143(10):2988-97.

304. Banks WA, Gray AM, Erickson MA, Salameh TS, Damodarasamy M, Sheibani N, et al. Lipopolysaccharide-induced blood-brain barrier disruption: roles of cyclooxygenase, oxidative stress, neuroinflammation, and elements of the neurovascular unit. J Neuroinflammation. 2015;12:223.

305. Poldrack RA, Fletcher PC, Henson RN, Worsley KJ, Brett M, Nichols TE. Guidelines for reporting an fMRI study. Neuroimage. 2008;40(2):409-14.

306. Eklund A, Nichols TE, Knutsson H. Cluster failure: Why fMRI inferences for spatial extent have inflated false-positive rates. Proc Natl Acad Sci U S A. 2016;113(28):7900-5.

307. Zhang J, Chen Y, Zhang Y, Zhang E, Yu HJ, Yuan H, et al. Diagnosis of spinal lesions using perfusion parameters measured by DCE-MRI and metabolism parameters measured by PET/CT. Eur Spine J. 2020;29(5):1061-70.

308. Osei-Bimpong A, Meek JH, Lewis SM. ESR or CRP? A comparison of their clinical utility. Hematology. 2007;12(4):353-7.

309. Plata-Nazar K, Luczak G, Liberek A, Dudzinska-Gehrmann J, Sznurkowska K, Landowski P, et al. Evaluation of clinical usefulness of serum neopterin determination in children with bacterial infections. Acta Biochim Pol. 2015;62(1):133-7.

310. Tsao N, Hsu HP, Wu CM, Liu CC, Lei HY. Tumour necrosis factor-alpha causes an increase in blood-brain barrier permeability during sepsis. J Med Microbiol. 2001;50(9):812-21.

311. Chavan SS, Pavlov VA, Tracey KJ. Mechanisms and Therapeutic Relevance of Neuro-immune Communication. Immunity. 2017;46(6):927-42.

312. Bluthe RM, Michaud B, Kelley KW, Dantzer R. Vagotomy blocks behavioural effects of interleukin-1 injected via the intraperitoneal route but not via other systemic routes. Neuroreport. 1996;7(15-17):2823-7.

313. Hosoi T, Okuma Y, Matsuda T, Nomura Y. Novel pathway for LPS-induced afferent vagus nerve activation: possible role of nodose ganglion. Auton Neurosci. 2005;120(1-2):104-7.

314. Fowler CJ, Griffiths D, de Groat WC. The neural control of micturition. Nat Rev Neurosci. 2008;9(6):453-66.

315. Erickson MA, Wilson ML, Banks WA. In vitro modeling of blood-brain barrier and interface functions in neuroimmune communication. Fluids Barriers CNS. 2020;17(1):26.

316. Hoogervorst EL, Eikelenboom MJ, Uitdehaag BM, Polman CH. One year changes in disability in multiple sclerosis: neurological examination compared with patient self report. J Neurol Neurosurg Psychiatry. 2003;74(4):439-42.

317. Costelloe L, O'Rourke K, McGuigan C, Walsh C, Tubridy N, Hutchinson M. The longitudinal relationship between the patient-reported Multiple Sclerosis Impact Scale and the clinician-assessed Multiple Sclerosis Functional Composite. Mult Scler. 2008;14(2):255-8.

318. The Lancet N. Patient-reported outcomes in the spotlight. Lancet Neurol. 2019;18(11):981.

319. Massa LM, Hoffman JM, Cardenas DD. Validity, accuracy, and predictive value of urinary tract infection signs and symptoms in individuals with spinal cord injury on intermittent catheterization. J Spinal Cord Med. 2009;32(5):568-73.

320. Cotton F, Weiner HL, Jolesz FA, Guttmann CR. MRI contrast uptake in new lesions in relapsing-remitting MS followed at weekly intervals. Neurology. 2003;60(4):640-6.

321. Khaleeli Z, Ciccarelli O, Mizskiel K, Altmann D, Miller DH, Thompson AJ. Lesion enhancement diminishes with time in primary progressive multiple sclerosis. Mult Scler. 2010;16(3):317-24.

322. Berkowitz FE. Hemolysis and infection: categories and mechanisms of their interrelationship. Rev Infect Dis. 1991;13(6):1151-62.

323. Legros N, Dusny S, Humpf HU, Pohlentz G, Karch H, Muthing J. Shiga toxin glycosphingolipid receptors and their lipid membrane ensemble in primary human blood-brain barrier endothelial cells. Glycobiology. 2017;27(1):99-109.

324. Amran MY, Fujii J, Suzuki SO, Kolling GL, Villanueva SY, Kainuma M, et al. Investigation of encephalopathy caused by Shiga toxin 2c-producing Escherichia coli infection in mice. PLoS One. 2013;8(3):e58959.

325. D'Alessio L, Pinto A, Cangelosi A, Geoghegan PA, Tironi-Farinati C, Brener GJ, et al. Sub-Lethal Dose of Shiga Toxin 2 from Enterohemorrhagic Escherichia coli Affects Balance and Cerebellar Cytoarchitecture. Front Microbiol. 2016;7:133.

326. Toval F, Schiller R, Meisen I, Putze J, Kouzel IU, Zhang W, et al. Characterization of urinary tract infection-associated Shiga toxin-producing Escherichia coli. Infect Immun. 2014;82(11):4631-42.

327. Toval F, Kohler CD, Vogel U, Wagenlehner F, Mellmann A, Fruth A, et al. Characterization of Escherichia coli isolates from hospital inpatients or outpatients with urinary tract infection. J Clin Microbiol. 2014;52(2):407-18.

328. Nagamatsu K, Hannan TJ, Guest RL, Kostakioti M, Hadjifrangiskou M, Binkley J, et al. Dysregulation of Escherichia coli alpha-hemolysin expression alters the course of acute and persistent urinary tract infection. Proc Natl Acad Sci U S A. 2015;112(8):E871-80.

329. Abraham SN, Miao Y. The nature of immune responses to urinary tract infections. Nat Rev Immunol. 2015;15(10):655-63.

330. Kuriakose M, Younger D, Ravula AR, Alay E, Rama Rao KV, Chandra N. Synergistic Role of Oxidative Stress and Blood-Brain Barrier Permeability as Injury Mechanisms in the Acute Pathophysiology of Blast-induced Neurotrauma. Sci Rep. 2019;9(1):7717.

331. Plumb J, McQuaid S, Mirakhur M, Kirk J. Abnormal endothelial tight junctions in active lesions and normal-appearing white matter in multiple sclerosis. Brain Pathol. 2002;12(2):154-69.

332. Cannistraro RJ, Badi M, Eidelman BH, Dickson DW, Middlebrooks EH, Meschia JF. CNS small vessel disease: A clinical review. Neurology. 2019;92(24):1146-56.

333. Zhang CE, Wong SM, van de Haar HJ, Staals J, Jansen JF, Jeukens CR, et al. Blood-brain barrier leakage is more widespread in patients with cerebral small vessel disease. Neurology. 2017;88(5):426-32.

334. Wardlaw JM, Smith EE, Biessels GJ, Cordonnier C, Fazekas F, Frayne R, et al. Neuroimaging standards for research into small vessel disease and its contribution to ageing and neurodegeneration. Lancet Neurol. 2013;12(8):822-38.

335. Palladino R, Marrie RA, Majeed A, Chataway J. Evaluating the Risk of Macrovascular Events and Mortality Among People With Multiple Sclerosis in England. JAMA Neurol. 2020;77(7):820-8.

336. Filippi M, Preziosa P, Banwell BL, Barkhof F, Ciccarelli O, De Stefano N, et al. Assessment of lesions on magnetic resonance imaging in multiple sclerosis: practical guidelines. Brain. 2019;142(7):1858-75.

337. Tran KA, Zhang X, Predescu D, Huang X, Machado RF, Gothert JR, et al. Endothelial beta-Catenin Signaling Is Required for Maintaining Adult Blood-Brain Barrier Integrity and Central Nervous System Homeostasis. Circulation. 2016;133(2):177-86.

338. Fancy SP, Baranzini SE, Zhao C, Yuk DI, Irvine KA, Kaing S, et al. Dysregulation of the Wnt pathway inhibits timely myelination and remyelination in the mammalian CNS. Genes Dev. 2009;23(13):1571-85.

339. Lengfeld JE, Lutz SE, Smith JR, Diaconu C, Scott C, Kofman SB, et al. Endothelial Wnt/beta-catenin signaling reduces immune cell infiltration in multiple sclerosis. Proc Natl Acad Sci U S A. 2017;114(7):E1168-E77.

340. Mietani K, Sumitani M, Ogata T, Shimojo N, Inoue R, Abe H, et al. Dysfunction of the blood-brain barrier in postoperative delirium patients, referring to the axonal damage biomarker phosphorylated neurofilament heavy subunit. PLoS One. 2019;14(10):e0222721.

341. Erikson K, Tuominen H, Vakkala M, Liisanantti JH, Karttunen T, Syrjala H, et al. Brain tight junction protein expression in sepsis in an autopsy series. Crit Care. 2020;24(1):385.

342. Vernooij MW, Ikram MA, Tanghe HL, Vincent AJ, Hofman A, Krestin GP, et al. Incidental findings on brain MRI in the general population. N Engl J Med. 2007;357(18):1821-8.

343. Ponholzer A, Temml C, Wehrberger C, Marszalek M, Madersbacher S. The association between vascular risk factors and lower urinary tract symptoms in both sexes. Eur Urol. 2006;50(3):581-6.

344. Tsui A, Kuh D, Cardozo L, Davis D. Vascular risk factors for male and female urgency urinary incontinence at age 68 years from a British birth cohort study. BJU Int. 2018;122(1):118-25.

345. Kasatkina LA, Heinemann A, Hudz YA, Thomas D, Sturm EM. Stearoylethanolamide interferes with retrograde endocannabinoid signalling and supports the blood-brain barrier integrity under acute systemic inflammation. Biochem Pharmacol. 2020;174:113783.

346. Logsdon AF, Erickson MA, Chen X, Qiu J, Lim YP, Stonestreet BS, et al. Inter-alpha inhibitor proteins attenuate lipopolysaccharide-induced blood-brain barrier disruption and downregulate circulating interleukin 6 in mice. J Cereb Blood Flow Metab. 2020;40(5):1090-102.

347. Yang CH, Kao MC, Shih PC, Li KY, Tsai PS, Huang CJ. Simvastatin attenuates sepsis-induced blood-brain barrier integrity loss. J Surg Res. 2015;194(2):591-8.

348. Haddad JJ, Saade NE, Safieh-Garabedian B. Cytokines and neuro-immune-endocrine interactions: a role for the hypothalamic-pituitary-adrenal revolving axis. J Neuroimmunol. 2002;133(1-2):1-19.

349. Dennison L, Brown M, Kirby S, Galea I. Do people with multiple sclerosis want to know their prognosis? A UK nationwide study. PLoS One. 2018;13(2):e0193407.

350. Kappos L, Bar-Or A, Cree BAC, Fox RJ, Giovannoni G, Gold R, et al. Siponimod versus placebo in secondary progressive multiple sclerosis (EXPAND): a double-blind, randomised, phase 3 study. Lancet. 2018;391(10127):1263-73.

351. Montagne A, Nation DA, Sagare AP, Barisano G, Sweeney MD, Chakhoyan A, et al. APOE4 leads to blood-brain barrier dysfunction predicting cognitive decline. Nature. 2020;581(7806):71-6.

352. Choi KS, You SH, Han Y, Ye JC, Jeong B, Choi SH. Improving the Reliability of Pharmacokinetic Parameters at Dynamic Contrast-enhanced MRI in Astrocytomas: A Deep Learning Approach. Radiology. 2020;297(1):178-88.

353. Bliesener Y, Acharya J, Nayak KS. Efficient DCE-MRI Parameter and Uncertainty Estimation Using a Neural Network. IEEE Trans Med Imaging. 2020;39(5):1712-23.

354. Nalepa J, Ribalta Lorenzo P, Marcinkiewicz M, Bobek-Billewicz B, Wawrzyniak P, Walczak M, et al. Fully-automated deep learning-powered system for DCE-MRI analysis of brain tumors. Artif Intell Med. 2020;102:101769.

355. Shaul R, David I, Shitrit O, Riklin Raviv T. Subsampled brain MRI reconstruction by generative adversarial neural networks. Med Image Anal. 2020;65:101747.

356. Abrahao A, Meng Y, Llinas M, Huang Y, Hamani C, Mainprize T, et al. First-in-human trial of blood-brain barrier opening in amyotrophic lateral sclerosis using MR-guided focused ultrasound. Nat Commun. 2019;10(1):4373.

357. Rezai AR, Ranjan M, D'Haese PF, Haut MW, Carpenter J, Najib U, et al. Noninvasive hippocampal blood-brain barrier opening in Alzheimer's disease with focused ultrasound. Proc Natl Acad Sci U S A. 2020;117(17):9180-2.

358. Barton SM, Janve VA, McClure R, Anderson A, Matsubara JA, Gore JC, et al. Lipopolysaccharide Induced Opening of the Blood Brain Barrier on Aging 5XFAD Mouse Model. J Alzheimers Dis. 2019;67(2):503-13.

359. Beck AT, Ward CH, Mendelson M, Mock J, Erbaugh J. An inventory for measuring depression. Arch Gen Psychiatry. 1961;4:561-71.

360. Yalcin I, Bump RC. Validation of two global impression questionnaires for incontinence. Am J Obstet Gynecol. 2003;189(1):98-101.

Bibliography

McRobbie DW, Moore, EA, Graves MJ, Prince MR. MRI from picture to proton 2nd Edition. Cambridge: Cambridge University Press; 2007.

Buxton RB. Introduction to functional magnetic resonance imaging. Cambridge: Cambridge University Press; 2002.

Krishna DR, Klotz U. Clinical pharmacokinetics. Berlin: Springer-Verlag; 1990.